

On the conjugate heat transfer method:

Numerical study and
an application case of an
optimization for a
gas turbine transition piece cooling

MSc Thesis Report
Svetoslav Angelov

On the conjugate heat transfer method

Numerical study and an
application case of optimization for a
gas turbine transition piece cooling

S. Angelov

to obtain the degree of Master of Science
at the Delft University of Technology,
to be defended publicly on Friday April 30, 2021 at 01:00 PM.

Student number: 4909615
Project duration: February 3, 2020 – April 30, 2021
Thesis committee: Prof. dr. ir. S. Klein, TU Delft, supervisor
Dr. R. Pecnik, TU Delft, co-supervisor
Dr. S. Hermeth, Siemens Energy, co-supervisor
Dr. B. Wegner, Siemens Energy, co-supervisor.
Dr. H. Bazyar, TU Delft

This thesis is confidential and cannot be made public until April 30, 2023.

An electronic version of this thesis is available at <http://repository.tudelft.nl/>.

Acknowledgements

*We've come a long long way together,
Through the hard times and the good,
I have to celebrate you baby,
I have to praise you like I should.*

Fatboy Slim, "Praise You"

First, I want to express my deepest gratitude to my supervisor Prof. Sikke Klein, for letting me do my Master's thesis abroad and also for trusting me throughout the entire time. No one could have expected what everyone was going to go through in the past year but his support and concise criticism really helped me steer the project in the right direction, despite the many (physical) roadblocks that just seemed to keep arising.

I would like to also thank my daily supervisor at Siemens, Dr. Sebastian Hermeth. First, for letting me do my thesis in the combustion team, and second, for his generosity in sharing knowledge and industry acumen, which were the key for me in building a wide network of contacts in Germany and US, particularly Landon and Jeffrey, accelerating my progress in gaining crucial software skills and heat transfer knowledge. My gratitude also goes to Dr. Bernhard Wegner. I sometimes wondered how he *managed* (pun intended) to keep such a high level of calmness and professionalism when approaching big uncertainties. My work benefits in big parts of him. I would also like to thank Lukasz for being in the office when no-one else was during the pandemic and the fun daily talks over lunch, gently emphasizing to us, students, that there is, in fact, a life outside of the simulation.

The friendships I built in Delft made the last two and a half years something I will never forget, and I hope that I will meet again most of you soon. To my partner in crime in Berlin, Michael, the person to probably suffer the most from my occasional frustrations. He was there to reassure me, while the "few" beers definitely helped (despite the neighbour's bitterness). Fernando, Giacomo, Herman, Marko, Lim, Stefan, Diego, Akhil, and everyone else in Delft, also played a role in me reaching this point today, and I hope I meet them soon somewhere across the globe.

To my sister and brother-in-law for their relentless support during the uncertain times in Berlin, and also my family at home: it certainly was not easy for them, and I wish that someday I will be able to "pay back" for their support, in one shape or another.

And last but surely not least, to Julia. I am sorry for being empty-headed at times. She made this whole journey a lot more pleasant and I thank her for her endless patience.

Vielen Dank,
Dank je wel,
Thank you,

Svetoslav Angelov,
Burgas, April 2021.

Abstract

Gas turbines (GT) play a crucial role in the transition to fully sustainable energy. Conversely, the expected growth of the GT market is met with more stringent regulatory requirements. Clearly, an increasing turbine inlet temperature (TIT) is beneficial for the efficiency of GT cycles. With increasing TIT, however, the magnitude of the thermal loads becomes unbearable, causing thermal fatigue of the component in a transient setting such as GT start-up or shut-down. Therefore, it is crucial that the thermal loads are well managed, which is typically achievable only by an adequate external and internal cooling. Generally, such cooling systems are modelled in industry using an uncoupled heat transfer (HT) approach, assuming that the heat coefficients (HTCs) are only influenced by the aerodynamics of the flow field: HTCs are obtained in a separate computational fluid dynamics (CFD) simulation and are extracted and mapped on the solid domain of the component.

Firstly, the report presents a comparison between the uncoupled approach and the increasingly popular conjugate heat transfer (CHT) approach, in which the fluid and solid domains are solved in a single simulation. To do so, the commercial code (STAR-CCM+) is first validated for both laminar flat plate and turbulent offset jet in a steady-state setting. The latter is done by comparing three Reynolds-Averaged Navier-Stokes (RANS) models. The popular wall treatment methods: blended and high- y^+ wall functions (WFs) are also compared. The comparison between the two HT methodologies is done by a parameter sensitivity study, involving the thermal conductivity of the solid (for both laminar and turbulent cases), Turbulent Prandtl number and turbulence intensity. It was concluded that the realizable $k - \epsilon$ model is the most accurate for this flow. Conjugation played a marginal role for all parameters, with only a considerable difference in the stagnation regions, when the solid conductivity is low. The results using a high- y^+ WF displayed high numerical dissipation due to the coarse mesh size and hence the difference between the HT methodologies was artificially low. It is therefore advised that the study of the high- y^+ WF is repeated on a different flow arrangement/setting (e.g. increased inlet velocity).

Secondly, the thesis details a study around the internal cooling of Siemens GT transition piece (TP), using CHT. An introduction of perpendicular ribs into a fully developed turbulent channel flow can theoretically significantly increase the heat transfer coefficient through the introduction of large-scale vortices downstream. An optimization routine was run with a hybrid algorithm to study the effect of different rib configurations in a steady RANS simulation, aiming to minimize both mass flow and transition bond coat temperature. The performance is compared to the baseline smooth channels used in the Siemens TP. No better results were achieved for both objective functions in comparison to the baseline case mostly due to the length of the channels. However, a considerable decrease in the coolant consumption was present with a limited increase in the BC temperature. The study showed that the optimization of such ribs can minimize the effect of skin friction (which influences the amount of coolant), and presents a possible further improvement of the TP cooling, without relying solely on the experience of the designer.

Keywords: *conjugate heat transfer, optimization, combustion equipment, cooling, channel turbulence.*

Contents

Acknowledgements

Abstract i

List of Figures v

List of Tables x

1	Introduction	1
1.1	Motivation	1
1.1.1	Gas turbine introduction	1
1.1.2	Novel computational methods	2
1.2	Project scope	4
1.2.1	Objectives	4
1.2.2	Research questions	5
1.3	Methodology	5
2	Literature study	7
2.1	Gas turbine combustion system basics	7
2.1.1	Structural basics	8
2.1.2	Flow arrangement	9
2.1.3	Heat transfer in combustion systems	9
2.1.4	Thermal loads	13
2.2	Conjugate heat transfer problems	15
2.2.1	Flat plate	16
2.2.2	Turbulent offset jet	18
2.3	Combustion systems cooling	20
2.3.1	Internal cooling	20
2.3.2	External cooling	23
2.4	Low cycle fatigue	24
2.4.1	Lifespan calculation	26
3	Optimization Terminology	29
3.1	Optimization algorithms	29
3.1.1	Simplex programming	31
3.1.2	Deterministic and stochastic programming	32
3.1.3	Genetic optimization	32
3.1.4	SHERPA [®]	33
3.2	Multi-disciplinary Optimization	34
3.3	Screening and Design of Experiments	36

4	Numerical Methodology	39
4.1	Numerics of conjugate heat transfer	39
4.2	Reynolds-Averaged Navier-Stokes Modelling	42
4.2.1	Standard $k - \varepsilon$ model	42
4.2.2	Realizable $k - \varepsilon$ model	43
4.2.3	SST $k - \omega$ model	44
4.3	Calculation of heat transfer coefficients	44
4.4	Wall treatment functions	46
I	Part	50
5	Numerical validation cases	51
5.1	Laminar flat plate	51
5.1.1	Analytical solution	51
5.1.2	CFD setup and boundary conditions	55
5.1.3	Results and discussion	58
5.1.4	Summary	62
5.2	Turbulent offset jet	63
5.2.1	CFD setup and boundary conditions	63
5.2.2	Results and discussion	65
5.2.3	Summary	69
6	Heat transfer methodology comparison	70
6.1	Flat plate	70
6.2	Turbulent offset jet	77
6.2.1	Turbulent Prandtl number	79
6.2.2	Turbulence intensity	82
6.2.3	Thermal conductivity ratio	85
6.3	Summary	88
II	Part	89
7	Gas Turbine Transition Piece Analysis	90
7.1	Computational domain	90
7.2	Reynolds Analogy	94
7.3	Parametrization of cooling topology	95
7.3.1	Mesh study	96
7.4	Flow validation	99
7.5	Preliminary baseline comparison	100
8	Ribs Optimization Study	106
8.1	Optimization set-up	106
8.1.1	Optimization objectives	106
8.1.2	Optimization parameters & range	107
8.2	Results & analysis	108
8.3	Recommendations	117
9	Conclusion	118
9.1	Conclusions	118
9.2	Recommendations	120
	Appendices	121

Appendix A Gas turbine basics	122
Appendix B Luikov solution	123
B.1 Direct heat transfer solution method	123
B.2 Boundary layer approximation	123
B.3 Numerical solution	124
Appendix C Turbulent offset jet mesh study	128
Appendix D Auxiliary contracted inlets study	132
D.1 Concept introduction	132
D.2 Constant cross-section	133
D.3 Adjusted cross-section	133
Appendix E More on numerical methodology	135
E.1 Interpolation methods & coupling	135
E.1.1 Interpolation stencils	135
E.1.2 CHT coupling algorithms	138
E.2 More on turbulence models	141
E.2.1 Derivation of the RANS equations	141
E.2.2 Realizable $k - \varepsilon$ Damping function	142
E.2.3 Two-layer modification of the $k - \varepsilon$ model	142
E.2.4 Shear and stretching modification in the $k - \omega$ SST model	142
E.3 CFD roughness	143
Appendix Bibliography	144

List of Figures

1.1	Illustration of the Siemens SGT-8000H gas turbine. The term 'PCS' stands for Platform Combustion System and was proposed by Siemens in 2005. [109]	1
1.2	Overall evolution over the years of the TIT. Obtained from Rao [128].	2
1.3	The decoupled approach (top) versus the conjugate approach (bottom). Dashed line is used to indicate necessity for manual data extraction and mapping between simulation tools.	3
1.4	Flow schematic in a reverse flow arrangement combustor, with a typical diffuser, plenum chamber, and transition piece. Original unannotated image obtained from [103]	4
1.5	Thesis outline	5
2.1	Main components in the combustion system of the Siemens SGT5-8000H [38]	8
2.2	Typical transition piece geometries	9
2.3	Schematic of heat transfer loads in a combustor liner. Extracted from [6]	14
2.4	The one-dimensional CHT problem schematic	15
2.5	Temperature gradients at low and high Biot number settings in fluid and solid regions	16
2.6	The turbulent offset jet problem. Extracted from [95].	18
2.7	Dimensionless wall temperature on the wall as a function of offset ratio ($\theta_w = (T_{wall} - T_\infty)/(T_{ex} - T_\infty)$, $x' = xI_r$) for a conjugate heat transfer case [47].	19
2.8	Two examples of internal cooling design for GT turbine vanes; for reference, vane length is 12.75mm [15].	20
2.9	The three configurations used in the study of Siw et al. (top to bottom: triangular, semicircular, circular) and the dimensional heat transfer coefficient distributions (domain dimensions width, $W=63.5\text{mm}$; height, $H=25.4\text{mm}$; length, $L=101.6\text{mm}$) [111]	21
2.10	Rib shape configurations reported in [41]	22
2.11	Turbulence intensity contour plot from [17], indicating three key recirculation regions of low HTC where hot spots occur, for flows over ribs ($Re = 3 \cdot 10^4$, $e/D_h = 0.3$, $p/e = 10$)	22
2.12	Comparison of heat transfer performance (heat transfer augmentation \overline{Nu}/Nu_o on y-coordinate versus friction factor f/f_o) for various types of internal cooling. Extracted from [77]	23
2.13	A typical array of a jet-impingement geometry.	24
2.14	Schematic of a cross-flow. G_c and G_j are the cross-flow and impingement jet velocities respectively	24
2.15	Schematic of a film cooling process, illustrating the mixing process of a coolant with mainstream flow. [91]	24
2.16	Von Mises yield surface, along with the yield criterion function f , along with the increment in plastic strain normal to the surface, and the resultant stress-strain curve obtained for uniaxial straining (no hardening). Note at the yield surface, $f = 0$.	25
2.17	Neuber shakedown method	26
2.18	Wöhler SN curve (log-scale)	27
2.19	Effect of mean stress presence on fatigue life [115].	27

2.20	Constant mean strain ϵ_m effect on the mean stress levels σ_m . The relaxation is due to the plastic deformation, and hence the relaxation rate depends on strain amplitude [115].	27
3.1	Families and classes of optimization algorithms (adapted from [80])	30
3.2	A polyhedron \mathcal{P} and an extremum, highlighted in red.	31
3.3	Genetic evolutionary process [5].	33
3.4	Simplified Pareto front illustration of a multi-objective trade-off study.	33
3.5	Results from benchmark comparison of different optimization algorithms. SHERPA yielded better results even at a very low number of evaluations [116].	34
3.6	Pareto front of a MO (2 objectives) optimization and the equivalent optimization using a weighted sum in a single-objective optimization. The dashed lines represent values of the converted MO calculation. The resultant penalty decreases as the dashed line approaches the Pareto front.	35
3.7	Linear effect a), quadratic effect b), and interaction c).	36
3.8	A schematic of a full-factorial design with three factors and two levels each.	37
3.9	Illustrative representation of the effects of factor x_1	37
4.1	Domains and boundaries in a typical conjugate heat transfer problem	40
4.2	Typical velocity profile of a turbulent boundary layer	47
4.3	Velocity (a) and temperature (b) as a function of non dimensional wall distance displaying wall treatment for viscous sub-layer, log layer, and the blending approach covering the buffer layer	48
5.1	Schematic of boundary conditions and respective notation used for the analytical solution of Luikov.[81]	52
5.2	Problem domain schematic and boundary conditions.	56
5.3	Heat transfer coefficient along the plate surface for $\overline{Bi} = 0.1$, and $\overline{Bi} = 1$ for each of the two solution methods by Luikov [81].	57
5.4	Mesh used in the validation and HT methodology comparison. Grid is of size 60x120 and a first cell height of $\Delta y_{\min} = 7.2e-05\text{m}$ with a logarithmic stretching factor of 1.061	57
5.5	Interface temperature and heat transfer coefficient comparison with the differential heat transfer approach [81], at $\overline{Bi} = 0.1$	59
5.6	Temperature distribution across the fluid region (left) and solid (right) and comparison to Luikov solution, with a $\overline{Bi} = 0.1$	59
5.7	Comparison of velocity profiles to Blasius solution [106], at $\overline{Bi} = 0.1$	60
5.8	Interface temperature and heat transfer coefficient comparison with the differential heat transfer approach [81], at $\overline{Bi} = 1$	61
5.9	Temperature distribution across the fluid region (left) and solid (right) and comparison to Luikov solution, with a $\overline{Bi} = 1.0$	61
5.10	Comparison of velocity profiles to Blasius solution [106], at $\overline{Bi} = 1$	62
5.11	Close-up of dark gray region in Figure C.2: schematic of boundary conditions used in the turbulent offset jet problem. Domain width is 150mm (identical to experiment)	64
5.12	Interface temperature variation using countermeasures on the realizable $k - \epsilon$ model	66
5.13	Comparison of eddy viscosity for all three models	66
5.14	Comparison of interfacial temperature profile for all three models using finer mesh (M2) and blended wall function approach	67
5.15	Nondimensional temperature in the wall-normal direction at (a) 3mm in front of the exit nozzle and (b) $X = 6.69$ (midway in the recirculation region in the experiment).	67
5.16	Decay of the maximum jet temperature downstream (SST model in red and $k - \epsilon$ model in black).	68
5.17	Comparison of interfacial temperature profile for all three models using coarse mesh (M6) and high- y^+ wall function approach	68
6.1	Wall interface temperature (solid side) as a function of all conductivity ratios consider.	71

6.2	Velocity profile comparison for all thermal conductivity ratios at four different axial locations.	72
6.3	Nondimensional (a) velocity and (b) thermal boundary layers for all cases.	73
6.4	Critical z criterion for all cases	73
6.5	Averaged Nusselt number, derived from Eq.5.23 (shape-preserving interpolant)	74
6.6	Effect of thermal conductivity ratio on boundary layer ratio (shape-preserving interpolant)	74
6.7	Comparison of interface temperatures using a decreased bottom plate surface temperature, for all conductivities (a) - (e).	75
6.8	Comparison of resultant wall y^+ profiles from the validation case and the methodology comparison with increased jet velocity. The value of the wall y^+ is still ≤ 10 for the blended WF approach, which is beneficial for the consistency of the study.	77
6.9	Local wall interface temperature (solid side) as a function of Pr_t .	78
6.10	Local wall interface temperature (solid side) as a function of Pr_t .	78
6.11	Local wall interface temperature (solid side) as a function of Pr_t .	79
6.12	HTC as a function of Pr_t .	79
6.13	Local wall interface temperature (solid side) as a function of Pr_t .	80
6.14	HTC as a function of Pr_t .	80
6.15	Influence on surface averaged values of (a) temperature, (b) reattachment length, (c) specified- y^+ heat transfer coefficient	81
6.16	Local wall interface temperature (solid side) as a function of Tu(%).	82
6.17	HTC as a function of Tu(%).	82
6.18	Turbulent kinetic energy for (a) Tu = 2%, (b) Tu = 15% using a fine mesh (M2) and the blended wall function approach.	83
6.19	Turbulent kinetic energy for (a) Tu = 2%, (b) Tu = 15% using a coarse mesh (M6) and the high- y^+ wall function.	83
6.20	Local wall interface temperature (solid side) as a function of Tu(%).	83
6.21	HTC as a function of Tu(%).	84
6.22	Influence on surface averaged values of (a) temperature, (b) reattachment length, (c) specified- y^+ heat transfer coefficient	84
6.23	Local wall interface temperature (solid side) as a function of λ^* .	85
6.24	HTC as a function of λ^* .	85
6.25	Local wall interface temperature (solid side) as a function of λ^* .	86
6.26	HTC as a function of λ^* .	86
6.27	Influence on surface averaged values of (a) temperature, (b) reattachment length, (c) specified- y^+ heat transfer coefficient	87
7.1	Illustration of approach used for discretizing the transition piece geometry into a parametric slide of two channels.	90
7.2	Top panel schematic and boundary conditions used, along with a close-up view of the channels, where relevant interfaces are illustrated using dashed lines. Red and blue are used to indicate fluid region (hot and cold flows, respectively), whereas gray is the transition metal region. Channel flow is shown in purple.	91
7.3	Bottom panel schematic and boundary conditions used.	92
7.4	Types of HTC BCs and interfaces in the transition piece set-up.	92
7.5	Mapped HTC on hot and cold sides of the top and bottom panels, extracted from a full midframe simulation.	93
7.6	Roughness benchmarking for AM-channels of various build directions: friction factor f , Nusselt number (b) as a function of Re , and f and heat transfer augmentation for all tested channels (c) from Snyder [112].	95
7.7	Schematic representation of key parameters used in the rib geometry	95
7.8	Resultant flow structure in the rib geometry used (top panel used for illustrative purposes). The structure closely resembles the flow structure commonly found in literature, see Fig.2.11, with the exception of a recirculation region on top of the rib structure.	96
7.9	Comparison of mesh resolution: M1 (a) and M5 (b), channel shown in blue.	97

7.10	Mesh convergence tracked in surface averaged temperatures: Bond coating (i.e. hot side of transition metal) (a), thermal barrier coating (b), channel surface (c).	98
7.11	Outer-layer scaling at four locations downstream in one of the cooling channels inside the bottom panel.	99
7.12	Schematic of a square duct with transverse ribs used by Wang [84]. The duct uses a blockage ratio of 0.2 and pitch-to-height ratio of 4.	99
7.13	Comparison to DNS data of nondimensional streamwise velocity at three downstream locations of the rib.	100
7.14	Effect of HLP on cooling effectiveness, and the ratio of passive to active cooling requirement as a function of the cold side convective heat transfer coefficient.	101
7.15	Local wall temperatures for bottom (a) and top (b) panels, with and without rib turbulators.	102
7.16	Nondimensional bulk velocity and bulk nondimensional temperature along the two channels for both geometries.	103
7.17	Bulk heat transfer coefficients on both panels for each channel: (a)-(b) top panel, (c)-(d) bottom panel.	104
8.1	Flowchart of the automated design workflow in HEEDS.	107
8.2	SHERPA Design performance.	108
8.3	Evolution of temperature OF	109
8.4	Evolution of nondimensionalized cooling mass flow	109
8.5	Pareto front of top panel.	111
8.6	Pareto front of bottom panel.	111
8.7	Influence of rib parameters on bottom panel temperature and cooling	113
8.8	Influence of rib parameters on top panel temperature and cooling	114
8.9	Nusselt number increase with Reynolds number	115
8.10	Skin friction increase with Reynolds number	115
8.11	Nusselt number against skin friction	116
8.12	Z-score (scatter and distribution) of (a) Nusselt number and (b) Skin friction coefficient.	116
B.1	All five meshes used for the independence study of the flat plate problem, in the vicinity above the plate (no rear and front fluid extensions)	125
B.2	Temperature, energy, and thermal load residual values from M1 and M2, until iteration number 120 (convergence for M1 reached at 260 iterations)	126
B.3	Comparison of friction coefficient to Blasius analytical solution, along with heat transfer coefficient, heat flux, and temperature at the interface with Luikov analytical solution ($\overline{Bi} = 0.1$).	126
B.4	Mesh M1 with x-refinement (incl. extensions in fluid region).	127
B.5	Comparison of interface temperature obtained from refined mesh in the x-direction w.r.t mesh without refinement and the analytical solution from Luikov ($\overline{Bi} = 0.1$).	127
C.1	Schematic of experimental arrangement, extracted from [95]	128
C.2	Entire CFD domain with relevant dimensions (m) (light gray region is not included in Figure 5.11, i.e. ambient room region in the experimental domain, having a width of 3.0m)	128
C.3	All five meshes used for the independence study of the flat plate problem, in the vicinity above the plate (no rear and front fluid extensions)	130
C.4	Convergence for M1, M2, M3, M4 and M5	130
C.5	Axial velocity component convergence with experimental data at five downstream location	131
D.1	Schematic of the setup: auxiliary inlets are place downstream for both counter current channels.	132
D.2	Illustrative depiction of the idea of contracting the inlets downstream.	133
D.3	Effect of number of inlets and inlet angle on average, maximum temperatures and coolant consumption (nondimensionalized).	133

D.4	Influence of the amount of contraction on the average, maximum temperatures and coolant consumption (nondimensionalized).	134
D.5	Kriging fits of numerical data: (a) nondimensionalized mass flow and (b) average bond coating temperature.	134
E.1	Nearest neighbour interpolation method illustration.	136
E.2	Least square interpolation schematic.	137
E.3	Flow chart of the hFTB method.	139
E.4	Flow chart of the hFFTB method.	140

List of Tables

2.1	Review of CHT studies on flat plates	17
3.1	Brief comparison of full-factorial and partial-factorial designs	38
4.1	Model coefficients used in the standard formulation of the $k - \varepsilon$ model, according to Launder and Sharma [70]	43
4.2	Model coefficients used in the realizable formulation of the $k - \varepsilon$ model	44
4.3	Model coefficients used in the SST $k - \omega$ model	44
4.4	Summary of available heat transfer coefficients.	46
4.5	Wall functions for both approaches for turbulence parameters required by the RANS model	49
5.1	Calculated properties of air at 1000K. [65]	55
5.2	Resultant solid thermal conductivity from the two average Biot numbers	55
5.3	Summary of average values for temperature and heat transfer coefficient from both simulations and the analytical solution [81].	62
5.4	Sources of errors and unknowns in the numerical procedure followed for the CHT validation.	65
6.1	Resultant Biot numbers from heat conductivity ratios	71
6.2	Summary of average heat transfer coefficient, and boundary layers comparison for all conductivities at $T_b = 600K$	76
6.3	Error comparison for average interface temperature for baseline and increased critical temperature difference ($T_\infty - T_b$)	76
7.1	Non-dimensionalized transition channels effective area (A_{eff}/A_{ch}): validation of pressure drop calculation versus test measurements.	93
7.2	Thermal conductivities used in the model.	94
7.3	Cross section of baseline (circular) and ribbed baseline (rectangular) channels used.	96
7.4	Mesh settings used for the top panel study. The channel with an inlet upstream is denoted with 1, and vice versa.	97
7.5	Computational cost comparison between all meshes.	98
7.6	Maximum allowable temperatures and design margins	102
7.7	Comparison of two baseline cooling schemes	104
8.1	Comparison of maximum and minimum values achieved by SHERPA for both panels to the values with baseline channel configuration (BR - baseline ribbed, BCIRC - baseline circular).	109
B.1	Interface boundary condition settings	124
B.2	Properties of meshes used for laminar flat plate study	124
C.1	Specification of mesh settings on target surfaces for M2	129
C.2	Mesh attributes of all meshes in the mesh independence study	129

E.1 Different interpolation methods in accordance to the source and target stencils. 135
E.2 Values and settings of the mapped interface tolerance 137

Chapter 1

Introduction

1.1 Motivation

1.1.1 Gas turbine introduction

While renewable technologies are becoming more and more popular, the gas turbine (GT) market was responsible for roughly 30% of worlds' energy production as of October 2020¹, and is expected to grow by at least 5.4% yearly by 2027 due the increased foreseen energy demand in the near future [79]. GTs also offer flexibility compared to alternative power generation methods (easy start/stop operation). This can be further employed to serve as a back up for intermittent renewable power, or potential to switch to zero carbon fuels like hydrogen.

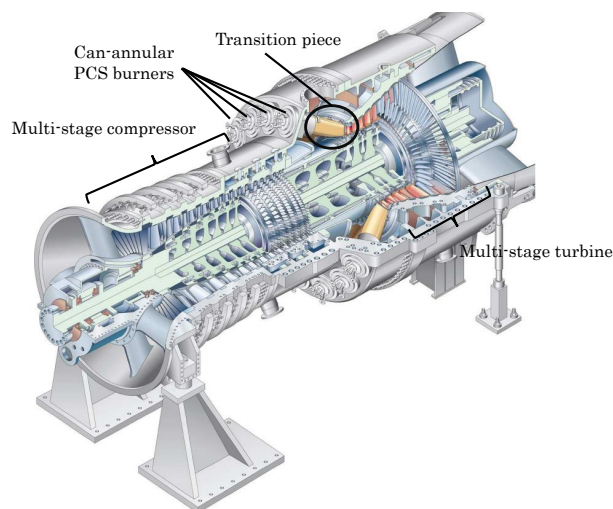


Figure 1.1: Illustration of the Siemens SGT-8000H gas turbine. The term 'PCS' stands for Platform Combustion System and was proposed by Siemens in 2005. [109]

On the other hand, governmental regulations on gas turbine components have increasingly become more and more stringent in terms of emissions and pollutant levels. Thereby, in order to be able to adhere to these regulations and remain competitive by adapting to rapidly changing demands, turbomachine manufacturers face a multi-faceted problem, the main two challenges of it being the shortening of the design cycle and the necessary increase in the performance of their products.

¹Data provided by Organisation for Economic Co-operation and Development (OECD)

The latter could be achieved by addressing the improvement of various systems of the gas turbine. An illustration of large a gas turbine is given in Figure 1.1, where the main stages in a gas-turbine cycle are given: namely the compressor stage, combustion chamber, and turbine stage. From a societal point of view, it can be mathematically shown that gas turbine cycles should be operated at a turbine inlet temperature (TIT) as high as possible in order to maximize its thermodynamic efficiency. For the case of the Joule-Brayton cycle (the idealized thermodynamic process in the gas turbine), at **optimum pressure ratio**, the *thermodynamic* efficiency can be thus read as:

$$\eta_{th-dynamic} = 1 - \sqrt{\frac{T_2}{T_4}}, \quad (1.1)$$

where T_2 is the compressor inlet temperature and T_4 is the TIT. the full derivation of the equation is given in Appendix A. Clearly, the cooling requirement within gas turbines are hence also increased, due to the resultant increase in heat flux on components at higher TIT, and the melting temperature of the turbine material being lower. In addition to this, GT components exposed to such high temperatures are more susceptible to a secondary failure mechanism, arising from temperature differentials developed during the starting and stopping of the turbine. The resultant thermal expansion and contractions produce thermal stresses, the cycling of which causes thermal fatigue. The overall trend of the further increase of TIT in the industry is to remain, as shown in Fig.1.2, which amplifies the importance of novel approaches to tackle the challenge.

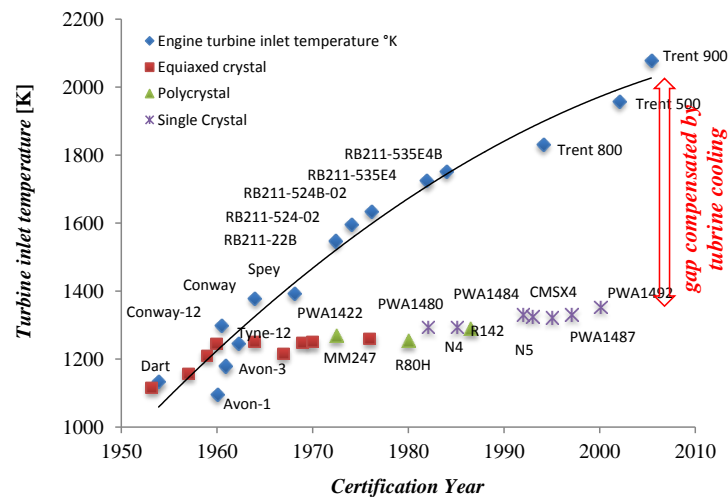


Figure 1.2: Overall evolution over the years of the TIT. Obtained from Rao [128].

A possible solution to the problem is simply increasing the cooling air rates until the cooling requirements are met. The known issue with increasing cooling air flow, however, is in the penalty on *thermal efficiency* ($\eta_{thermal} = \text{Shaft power}/\text{Heat addition}$), which is mainly a result of two factors: (1) entropy generation from coolant and hot burnt gas mixing, and (2) irrecoverability of the increased compression work on bleed air in the expansion process, due to its usage in combustor and turbine cooling. The coolant mass flow (compressor bleed air) needs to be hence kept at a minimum.

1.1.2 Novel computational methods

In today's age of digitization, the challenge of higher TIT can be solved by both the rapidly changing manufacturing and design processes. In order to exploit the full potential of the newly emerging manufacturing process such as additive manufacturing for example, the design and production methods must also develop further in the field of gas turbines. Such novel methodologies allow for the employment of

cooling designs, and eventually deliver even better GTs.

With regards to the aforementioned improvement of such design cycles, computer-aided calculation methods, mainly computational fluid dynamics (CFD) and computational structural mechanics (CSM) have solidified their presence into the design process of modern manufacturers, together however with the increased complexity of the simulations and computational demand. In addition, the fundamentals in heat transfer in the design process are often neglected for the sake of reduction in computational cost and also time efficiency of projects, and the iterative manner of the entire process has remained. Thereby, it is important to introduce the topic of conjugate heat transfer (CHT), i.e. the simultaneous solution of both solid and fluid regions, allowing for an enhanced design methodology that makes the multiple-step process of calculating thermal stresses considerably shorter. Currently, the well established practice consists of calculating heat transfer coefficients on all solid walls in adiabatic CFD simulations, and later imposing the results along with the respective ambient temperature setting on the solid walls in a separate CSM simulation as a *convective boundary condition*, with the overall procedure presented schematically in Figure 1.3.

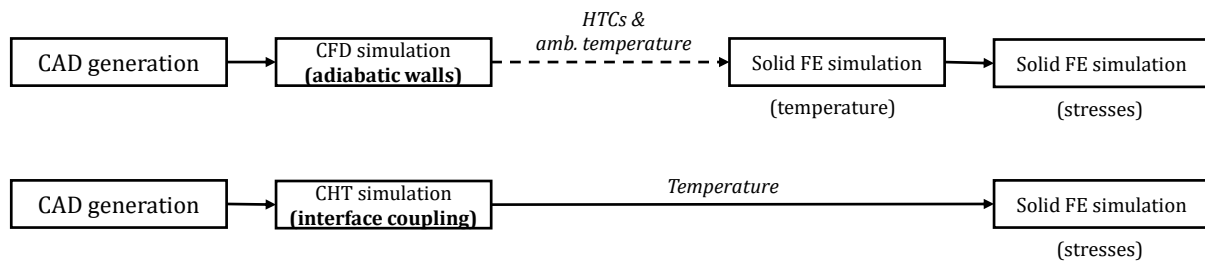


Figure 1.3: The decoupled approach (top) versus the conjugate approach (bottom). Dashed line is used to indicate necessity for manual data extraction and mapping between simulation tools.

This methodology is only applicable if the assumption that the heat transfer profile on the solid walls is solely determined by the aerodynamics of the flow is valid. Thereby, by relying only on CFD-based simulations, the heat loads are calculated with the assumption of a constant adiabatic temperature on the solid region, which then leads to the arise of multiple concerns. The use of non-conjugate methods completely omits the reality of fluid-structure interaction [83]. It is worthwhile mentioning that this assumption may actually be a valid one in some cases, but the complete understanding of the effects of conjugation require sound reasoning when and why the difference between the two approaches occur. The use of one-way interaction between fluid and the solid neglects what happens in reality. Additionally, it can be argued that the heat transfer coefficient does not depends only on the wall temperature level, but also the upstream history of the boundary layer on the wall, which also could greatly influence the uniformity on the wall temperature profile. The CHT method also eliminates the need for manual heat transfer data from one finite volume (FV) mesh to solid finite element mesh (FEM), hence decreasing component lead time. In this work, this is addressed by evaluating the difference between the two approaches on two separate cases under various physical and numerical conditions.

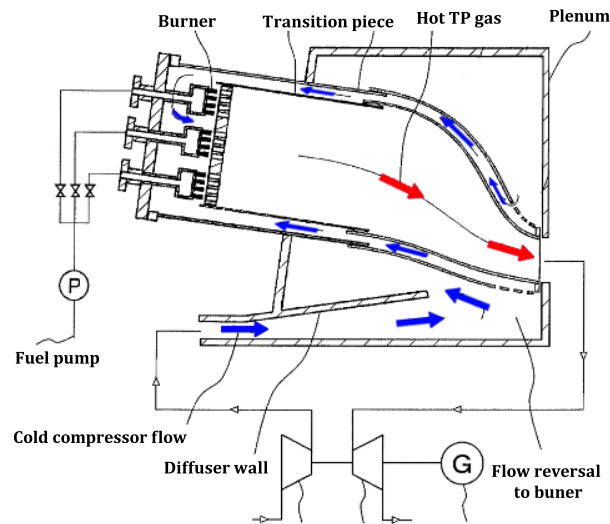


Figure 1.4: Flow schematic in a reverse flow arrangement combustor, with a typical diffuser, plenum chamber, and transition piece. Original unannotated image obtained from [103]

With regards to the mutual connection between the two challenges (design cycle improvement and gas turbine performance), the term multi-disciplinary optimization (MDO) has gained traction in recent years. As previously mentioned, one way to meet such GT performance requirements, which is in the scope of this project, is to enhance the cooling performance of the transition piece of one of Siemens Heavy Duty GTs combustion systems (CS), visible in Figure 1.1, whereas the typical flow arrangement is presented in Fig. 1.4. The optimization of the cooling topology would ideally lead to a reduction in maximum and average temperatures on the hot side surface, and thus also increasing the lifetime of the component. The multiobjective (MO) nature of such practices comes from the fact that the requirement for minimizing the coolant mass flow rate is also present for reasons discussed earlier.

1.2 Project scope

1.2.1 Objectives

Given the widespread applicability of the uncoupled approach described above, a comprehensive comparison with the CHT method under a variety of conditions, to author's knowledge, has not been performed, which presents viable research field for this thesis. In addition, with regards to topologies used for internal cooling of GT components, a number of surface devices such as ribs, dimples and fins are commonly used in order to increase turbulent kinetic energy and mixing, which plays a crucial part of effective convective heat transfer. The compromise between heat transfer augmentation and friction can be achieved by a multi-objective optimization on the geometry parameters of the turbulence using a novel hybrid algorithm. The main objectives of this thesis can be thereby formulated as:

1. Validate the CHT procedure in a commercial software package against canonical cases for both laminar and turbulent flow and determine under what conditions the CHT methodology is recommended over the commonly used uncoupled approach (e.g. adiabatic/isothermal heat transfer coefficient method)
2. Develop an optimization methodology using CHT for the design of the cooling of a preselected GT transition piece, and evaluate whether channel turbulence parameters can be optimized so that the skin friction losses are minimized.

1.2.2 Research questions

To reach the two objectives mentioned, the following set of research questions was deduced:

1. Does the numerical CHT methodology in the CFD code used results in an accurate solution w.r.t temperature profiles on the solid region on canonical test cases?
2. What is the best turbulence model for CHT in flows exhibiting similar characteristics as in a GT transition piece (recirculation, reattachment)?
3. Do wall treatment methods and the physical properties of the flow affect the difference between the CHT and decoupled approaches?
4. Can the internal cooling design of the transition piece be improved in terms of lifing and coolant consumption compared to a baseline case using an optimized channel turbulation?

1.3 Methodology

The first three chapters (**Chapter 2**, **Chapter 3**, and **Chapter 4**) contain an elaborative literature review, optimization terminology and numerical methodologies summaries necessary for the understanding of the thesis contents. The literature review entails heat transfer mechanisms in combustion systems, cooling techniques for gas turbines, with an emphasis on internal cooling, and calculation methods for low-cycle fatigue.

The thesis paper can be split into two parts: the first part focuses on validation of the conjugate heat transfer methodology and computational comparison between the two heat transfer approaches (uncoupled and conjugate). The findings of the validation studies (wall treatment and turbulence model) were then applied to the GT transition piece, and subsequently the optimization of the cooling design of the transition piece was performed. This is in the scope of the second part of this report. The structure is presented schematically in Figure 1.5

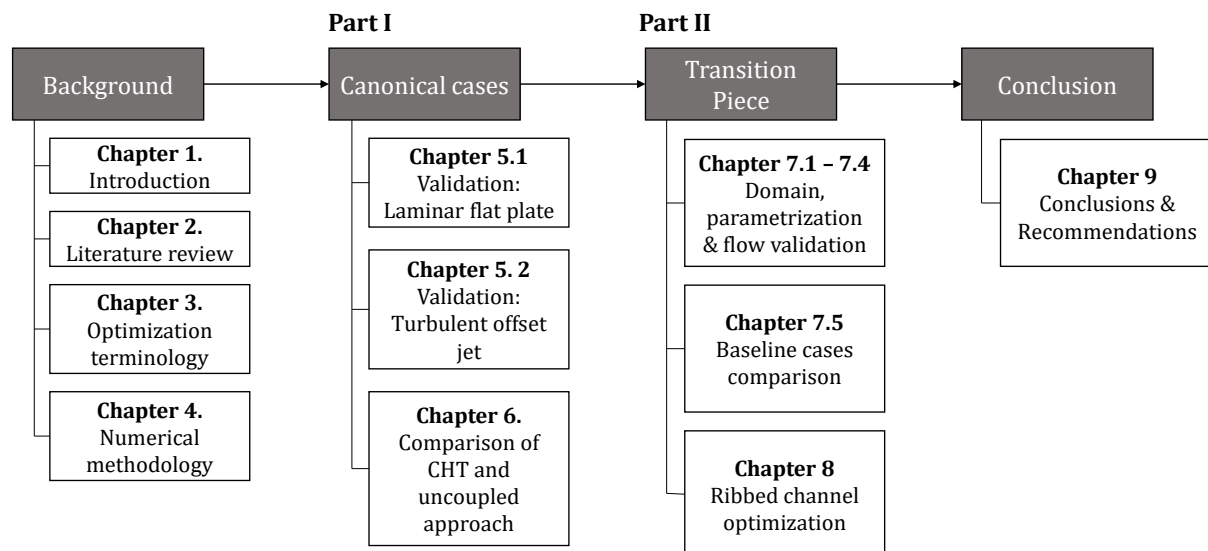


Figure 1.5: Thesis outline

In more detail, in **Chapter 5**, first, validation cases are introduced. The first validation study consists of a simple laminar flow over a flat plate of finite thickness. The results at two physical settings are compared to analytical solutions presented in literature. The second validation study is based on experimental data of a turbulent offset jet over a flat plate. The study includes a comparison of popular

turbulence models (without parameter tuning) and the use of different wall treatment methods. The resulting difference is discussed and recommendations are given and later used for the real-life case of the TP. The next chapter (**Chapter 6**) includes a numerical comparison study on the two aforementioned cases, where relevant physical or turbulence parameters are changed for the purpose of evaluating the CHT solver's sensitivity. The chapter ends by a discussion on the resultant differences between the coupled and decoupled approach, by comparing relevant scalar fields in the vicinity of the wall and main stream. To the author's knowledge, no previous studies were conducted specifically for the comparison between the uncoupled and conjugate method on a turbulent offset jet.

The second part of the study deals with the use of optimization methods for the design of an enhanced cooling on a turbomachinery component. This is done by first comparing baseline cases of the currently employed design by Siemens and new proposed turbulated channels, shown in **Chapter 7**. The turbulence parameters are then fed into a proprietary hybrid optimization algorithm with the two competing objectives of minimizing coolant consumption, and minimizing the surface averaged temperature of the hot side of the component. The results are presented and discussed in **Chapter 8**. The second part ends by proposing an adjustment in the cooling design that might lead to cooling enhancement. This is done by the introduction of two design parameters, namely number of auxiliary cooling channels inlets, and reduction of the area of the respective inlet downstream. Since the study is beyond the main two objectives of the project, the results are presented in **Appendix D**.

Finally, the conclusions for this thesis will be drawn in **Chapter 9**. Also, possible areas of improvement are indicated in the form of recommendations for future research both in the field of cooling optimization and CHT methods.

Chapter 2

Literature study

The aim of this literature study is to establish the current state-of-the-art research and practices, relevant to the field of heat transfer in gas turbine combustion, conjugate heat transfer, and the subsequent influence thermal loads resulting from combustion have on lifing in such components. Papers addressing the life prolongation of such components, potentially by the enhancement or optimization of some commonly used cooling techniques are discussed as well.

The study begins with basic overview of combustion systems and the resultant types of heat transfers and heat loads which will effectively be applied to components in combustion systems, requiring novel cooling methodologies. It further contains the history and techniques used for solving conjugate heat transfer problems, namely a laminar flow over a flat plate and a turbulent offset jet. A proprietary optimization algorithm is used in the thesis but it is important to keep track of what also has been achieved in the past in the field of thermo(-mechanical) optimization and what frameworks have been used in similar multidisciplinary investigations, and how do they compare to the approach and optimization algorithm employed in this study. Fields and topics of potential research, where resources tend to be deficient, are also pointed out.

The terminology of optimization and the most common types of optimization algorithms are outside the scope of this chapter and are presented in detail in Chapter 3.

Herein after, purely resources depicting methods used in the heat transfer analysis performed by the broad scientific community and research engineers in gas turbines are explained. Explanations of important terms is included where deemed necessary.

2.1 Gas turbine combustion system basics

Gas turbines are internal combustion engines through which compressible fluids flow. They have a high energy density and are used, for example, in the aviation and shipping sectors, or used as a mobile drive system, and in stationary areas for generating electricity. A gas turbine basically consists at least of a compressor, a combustion system and a turbine. Ambient air is sucked in in the compressor and through several compressor stages it is compressed to a high temperature. The compressed air is mixed with fuel in the combustion system and burned under almost isobaric conditions. The enthalpy of the combustion gas is then extracted through the expansion of the gas in the turbine stage. The enthalpy contained in the fluid is hence partially converted into rotational energy. Some of the energy is required to drive the compressor, while any remaining usable rotational energy can be converted into electrical energy with the help of a generator.

2.1.1 Structural basics

To analyse the heat loading and heat transfer mechanisms inside a combustion system, the system structure and sequence of undergoing processes has to be understood first. Therefore, the combustion system of interest in this project which is of the Siemens SGT5-8000H Heavy Duty Gas Turbine is shown in the schematic below to illustrate key components and help visualize its operating cycle.

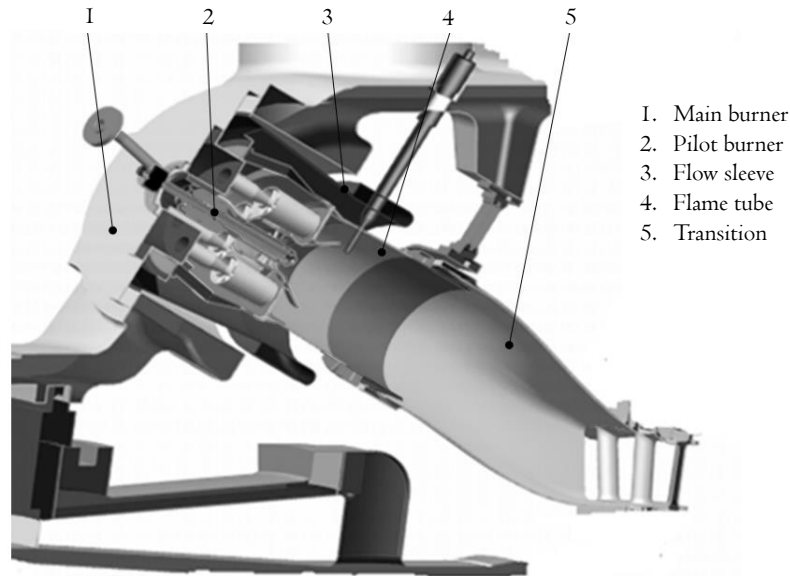


Figure 2.1: Main components in the combustion system of the Siemens SGT5-8000H [38]

The combustion system in Figure 2.1 is comprised of sixteen ring-shaped burners in total, arranged circumferentially around the gas turbine. First, compressor air goes through the flow sleeve to the main and pilot cone burners. Then, fuel is injected and mixed with the compressor air through the interior of the pilot cone and swirled through the blades of a mixer, maximizing the homogeneity of the fuel-air mixture and reducing the amount of pollutants released upon burning [131]. The purpose of the pilot burner located in the center of the combustion system is generally speaking to suppress the inherent combustion instabilities [76], which as a result leads to high frequency pressure fluctuations that exert an additional strain on the structures of the combustion system. The mixture is then burned in the flame tube. The transition piece (TP) is connected to the combustion basket (and hence flame tube), from which the hot burnt gases are emitted. They are then guided and flow through the transition into the first stage of the turbine blades. Hence, the purpose of the transition piece is to simply navigate and accelerate the burnt hot gases into the turbine stage. The cross-section of a typical transition piece, incl. the one used in this study changes from a circular to a quadrangle, the main purpose of which is to enhance the uniformity of the temperature distribution at the outlet region of the transition piece.

A detailed look on the exact transition piece is not presented for confidentiality reasons. Similar TP geometries to the one used in the study are found in open literature and are shown in Figure 2.2.

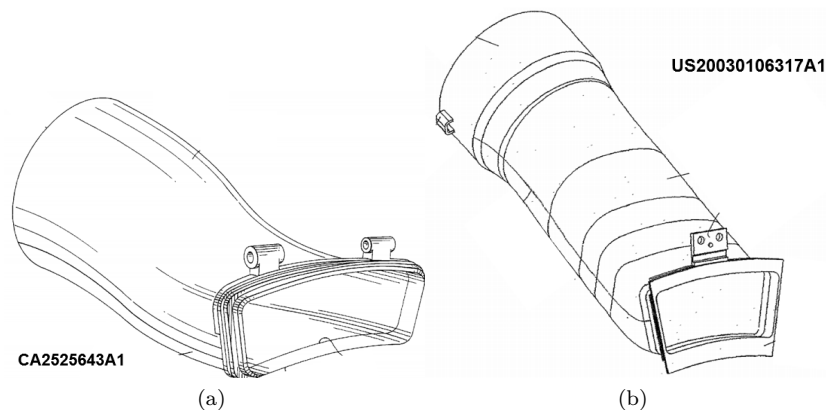


Figure 2.2: Typical transition piece geometries

2.1.2 Flow arrangement

The combustor system of the studied TP employs the so-called reverse-flow arrangement, which has been reported to lead to weight reductions and other technical benefits such as compactness and enhanced maintainability [25]. This plays a large role in the thermal management of the TP due to the complexity of the cold compressor flow in the region outside the transition piece, commonly referred to as the *dump diffuser*.

When it comes to literature regarding heat transfer inside the dump diffuser section in such an arrangement, relatively limited studies are present. The oldest study found dates back to 1996 done by Kapat [61] and Zhou et al. [132]. In the former a sub-scale diffuser model was used to study experimentally the cold flow of the diffuser section reporting various causes of pressure losses and features of the flow in key regions. The first computational study presented [132] yielded useful fundamental information regarding the complicated flow structures present within a dump diffuser. The following study of Kapat reported that air extraction does not accentuate flow nonuniformities, necessary in the avoidance of hot spots on TPs [60]. Wang et al. later investigated the effect of extraction and concluded that the propensity for flow reversal increases if the location and amount of air extraction is not optimized for [124]. The most prominent recent studies available are performed by Wang et al. [122], in a two-part paper with an experimental study and a numerical simulation part. In the former, Wang et al. showed that the usage of a perforated sleeve (sheath), forming impingement cooling on the surface of the transition results in a considerable reduction of transition wall temperature at the expense of an equal increase in pressure drop, and in [123] it was shown that a similar sleeve can help harness temperatures especially on the upper section near the turbine end.

The subsequent subsections will address the topic of types of heat transfer and the magnitude of heat loads on combustion equipment for gas turbines of similar power output as the one of this study, ending with a short discussion on the few key studies of transition piece heat transfer.

2.1.3 Heat transfer in combustion systems

Due to the comparatively low interest in research in gas turbine TPs, the section provides an overview on heat transfer mechanisms found in the entirety of the gas turbine combustor, and not exclusively in TPs. Hence, for the sake of this literature study, papers discussed entail heat transfer research aimed at all components exposed to combustion gases (excluding turbine vanes). It is also worthwhile mentioning that due to the extensiveness of the field of heat transfer, generally only a small proportion is focused exclusively on the subject of combustion. The majority of these studies are conducted on a completely practical point of view. Therefore, a short discussion on the fundamental physics is of benefit and pre-

sented in the upcoming subsections. Moreover, the main focus when considering combustion processes in industrial applications lies solely on gaseous radiation heat transfer and not heat transfer in general. Chapter 3 of the book given in [57] by Buakal et al. presents a concise summary of heat transfer in industrial combustion processes. A book by Schulz [44] lays a review in Chapter 4 mostly focused on radiative heat transfer and convective *cooling* instead, with a brief discussion on numerical modelling approaches.

Combustion flows are inherently of considerable complexity. They consist of a multitude of phenomena. According to Viskanta [120], the processes can be summarized as: convective and radiation heat transfer, molecular diffusion, turbulent/laminar multiphase fluid dynamics, chemical kinetics, nucleation, phase change heat transfer (i.e. condensation and evaporation), and surface effects. Each of these processes can be treated separately in order to produce an accurate mathematical combustion model. This has received substantial research interest in the recent years and state-of-the-art combustion models are present in literature [27], [52]. Each of the aforementioned mechanisms plays a partial contribution in accordance to the specific case and conditions, and will therefore be examined separately.

Convection

In the case of heat transfer between solid and fluid, in cases where their respective temperatures differ, one speaks of heat transfer by convection. It is a combination of energy transport by a macroscopic movement of a fluid and individual random movements of molecules. Convection is driven by temperature difference and the process can be simply expressed by Newton's law of cooling:

$$q = h \cdot (T_w - T_f). \quad (2.1)$$

The heat transfer coefficient (from here after referred to as HTC) h determines the intensity of the heat transfer at an interface. The HTC is a related heat flux density, i.e. a quantity that is shared by all variables of the process under consideration is influenced. Important influencing variables are geometric conditions, flow speed, type of flow and surface properties. [33]. At the wall one can express the heat flux balance as:

$$h \cdot (T_w - T_f) = -\lambda \cdot \left(\frac{\partial T}{\partial n} \right) \Big|_{\text{wall}}, \quad (2.2)$$

and hence

$$h = \frac{-\lambda(\partial T/\partial y)|_{y=0}}{T_w - T_f}. \quad (2.3)$$

The first principal dimensionless number which is essential for heat transfer analysis is the Nusselt number. Heat transfer coefficient is proportional to the Nusselt number, which characterises the thermal boundary layer, typically expressed as:

$$h = \frac{\lambda}{l} \cdot Nu(Re, Pr), \quad (2.4)$$

with λ as the thermal conductivity of the fluid, l as the characteristic length, Re as the Reynolds number and Pr as the Prandtl number:

$$Re = \frac{\rho v l}{\mu} \sim \frac{\text{Inertial forces}}{\text{Viscous forces}}. \quad (2.5)$$

$$Pr = \frac{c_p \mu}{k} \sim \frac{\text{Momentum diffusivity}}{\text{Thermal diffusivity}} \quad (2.6)$$

Traditionally, the Nusselt number is the ratio of:

$$Nu = \frac{h \cdot l}{\lambda} \sim \frac{\text{Stagnant fluid conductive resistance}}{\text{Convective resistance}} \quad (2.7)$$

and if the temperature gradient given in Eq.2.3 is nondimensionalized, and the resultant expression for α is used, the following expression is obtained

$$Nu = \frac{d \left(\frac{T_f - T_w}{T_f - T_w} \right)}{d \left(\frac{n}{l} \right)} \Bigg|_{\text{wall}} \quad (2.8)$$

Hence, the Nusselt number can also be regarded as the non-dimensional temperature gradient at the wall [85].

The calculation of the heat transfer coefficient in reality of combustion flow is fairly complicated and most often a correct definition does not exist for the exact configuration of interest. Some heat transfer correlations related to combustion are mentioned below, but such empirical formulations are only useful in preliminary design *if ever*, as they provide only averaged quantities over the combustor walls, and in most industrial cases, a more detailed temperature distribution along the wall is needed. This is only achievable by numerical models for combustion applied with the appropriate level of sophistication.

Relatively little research interest is present when it comes to convective heat transfer correlations for (can-)annular combustion systems. The convective heat load in such an arrangement is non-uniform and strongly depends on reaction and swirling flow dynamics. Lefebvre et al. ([72], [74]) performed the first attempts to derive semi-empirical correlations aimed at heat transfer along combustor liner walls. However, Lefebvre also stated that the the airflow in combustor liners exhibits a great amount of uncertainties, including “the state of boundary layer development, and effective gas temperature”, which effectively makes the choice “of a realistic model almost arbitrary”. Generally, same applies to TPs as well. Hence, it was argued that when no film cooling is applied for the liner/TP, the correlation should be comparable to fully developed turbulent channel flow. Lefebvre and Ballal hence proposed [74]:

$$h_c = 0.02 Re_{c,\infty}^{0.8} \frac{k_\infty}{D_c}. \quad (2.9)$$

The vast majority of heat transfer studies in reactive flows for industrial applications are in fact belong to the popular jet impingement problem, which has a wide variety of industrial applications and can be considered to some extent analogous to processes in gas turbine combustors. For a turbulent impingement jet, the correlation is given by Hustad [49]:

$$Nu = \frac{l_j}{\lambda_e} \left\{ 0.41 Re_{b,e}^{0.6} Pr_e^{0.35} Tu^{0.15} \left(\frac{Pr_e}{Pr_w} \right)^{0.25} \right\} \quad (2.10)$$

particularly intended for flames by jets of CH_4 and C_3H_8 . A full comprehensive summary of various jet impingement studies of flame flows prior to 2005 under a great variety of flow conditions and geometry properties is presented by Chander and Ray, [20]. Griswold proposed a correlation for the heat transfer coefficient for forced convection from the outside of a combustor wall, with a velocity of v against the surface, in his book *Fuels, Combustion and Furnaces* [37]:

$$h_c = \frac{1 + 0.225v}{(t_w - t_\infty)} \quad (2.11)$$

The author also proposes an empirical formula for natural convection from outside combustor wall as well:

$$h_c = \frac{0.53C (T_w - T_\infty)^{0.27}}{[(T_w + T_\infty)/2]^{0.18}} \quad (2.12)$$

where C is a shape constant (e.g. 1.79 for an arch, and 1.39 for a vertical wall).

A more commonly used correlation in design of gas turbine combustors makes use of a modified form of the well-known Dittus-Boelter correlation [11], which is the empirical relation for heat transfer coefficient in a fully developed turbulent flow in a circular tube:

$$\text{Nu}_{\text{Dittus-Boelter}} = 0.0235 \text{Re}_{C,f}^{0.8} \text{Pr}_f^{n_t} \quad (2.13)$$

The exponent n_t is set to 0.3 in cases where the wall temperature is lower than the free-stream temperature. Otherwise it is 0.4. The correlation holds well for flows between $10,000 < Re < 120,000$, and temperature differences of wall to gas of only 56K, and flows properties also being taken as temperature independent [75]. The gas properties are then evaluated at the film temperature. Lefebvre and Ballal state that such modifications can vary from one use-case to another, and it should also be noted that the correlation they derived (see Eq.2.9) is closely comparable to the Dittus-Boelter relation [74]. It has been reported that the Dittus-Boelter correlation underpredicts the heat transfer coefficient in real combustion processes, which is the case of the work of Patil et al. [94], where the author studies reactive flow in a simulated scaled up annular combustor.

Since the formulation of the Dittus-Boelter correlation (published in 1930), a considerable understanding has been gained when it comes to turbulent pipe flow heat transfer correlations. The addition of flow swirl also helped understanding the characterization of heat transfer, particularly in gas turbine combustors [127]. Heat transfer enhancement due to abrupt flow expansions has also been an insightful endeavour in the understanding of heat transfer in combustors, mainly due to the presence of corner recirculation regions upstream of the flow reattachment points ([7], [26]).

Conduction

When it comes to the heat transfer in the form of conduction, it is usually considered to be of smaller influence on the calculation of heat transfer in combustion systems. Conduction is physically described as the energy transfer occurring due to collisions of more-energetic particles with lower-energy particles [23]. It can occur in gases, liquids and solids, where in each medium the underlying principles behind the conduction process differ [23]. It is generally expressed with Fourier's law of heat conduction, which in three dimensions reads:

$$q = -\lambda_s \nabla T \quad (2.14)$$

where λ_s is the thermal conductivity of the solid region (e.g. combustor walls). The process is overwhelmingly omitted in gas turbine combustion studies. On the other hand, it can become crucial when calculating the heat losses through the outer wall of the combustor to the ambient. Conduction is in the basis of conjugate heat transfer studies, as it will be shown later, but as explained earlier, such studies are relatively few in the field of gas turbine combustor design.

Conduction is usually more carefully examined in microturbine combustion systems or when the surface-area-to-volume ratio of the system examined is considerably larger than in large gas turbines. In such systems the heat loss from the outer wall can become large and hence sensible calculation of thermal efficiency becomes possible only when conduction is included in the analysis [16].

Again, similarly to convection heat transfer, conduction has been more widely studied in problems involving flame impingement. Arrangement with internally cooled ([8], [9], and others) and uncooled target surfaces ([32], [42], [108]) have been used for such studies, where a steady-state conduction through the target surface has been produced.

Furthermore, Baukal [57] also noted that transient effects of conduction is usually also neglected, however it should be subjected to more research particularly in the firing up phase of the combustor. Other studies that deal with conduction in gas turbine combustion systems focus on the field of contact thermal resistance, which is closely related to the study of thermal barrier coatings (TBCs) and thermal delamination, macro-cracking or spallation. Some studies reported in open literature entailing the use of ceramic composites for gas turbine combustion applications are present in the works of Corman et al. [24], Miriyala et al. [86], Nelson and Orenstein [89], Price [98], and others.

Radiation

Radiation is a fairly complicated subject and has received substantial amount of research interest over the years. Viskanta and Menguc [120] noted that the main reasons behind the complexity of radiation in combustors is the coupled nature of multiple phenomena: (i) as the system undergoes different operation conditions, the surface effects change as well, (ii) turbulent mixing of gases and particles, and finally (iii) irregularities in the temperature field. Soot formation, particle size distribution and agglomeration have also been discussed as relevant factors too [66]. As pointed out above, radiation heat transfer is often times discounted in thermal analyses of combustion systems, and are of little to no relevance in TPs. Studies that validate such a choice are in [8], [20], and [110]. For that reason, herein, only a very basic overview of the physics behind radiation is described, and the reader can refer to the review of Baukal [57] for a more detailed study, where a variety of cases are discussed.

Radiation in general is the energy emission by a matter in solid, fluid or even gas state, primarily due to the change of electron configuration in the molecules, which as a results reduces its internal energy. This release of energy is done by a discrete energy quanta, i.e. photons, with an energy of $hf = hc/\lambda$, where h is Plank's constant and f is the frequency of the energy. Additional efforts were put by Viskanta [120] in the understanding of radiative heat transfer (described briefly in the upcoming paragraphs) along the contribution of Lefebvre [73].

$$q = \sigma T^4 \quad (2.15)$$

$$\sigma = 5.67 \cdot 10^{-8} \text{W/m}^2 \text{K}. \quad (2.16)$$

The maximum heat flux from radiation is described by the law of Stefan-Boltzmann, and its magnitude depend sheerly on its temperature, given in Eq.2.15

The upcoming subsection is solely focused on (semi-)empirical methods for estimating the resultant heat loads of the previously described heat transfer mechanisms.

2.1.4 Thermal loads

While a considerable level of understanding on heat transfer phenomena has been gained over the years, less light has been shed on combustor heat loads. With the growth of numerical methods over the years, simulation models have become increasingly better and the application of Reynolds-Average Navier Stokes (RANS) models to simple domains allow for quick results regarding heat loads in combustors. When combined with supporting experimental measurements for validation, this has become a strong toolchain for designers of gas turbine combustors.

To the author's knowledge, the works of Lefebvre [74] and Gosselin et al. [36] present the only empirical calculation methods of the heat loads on combustion components. A schematic is presented in Figure 2.3. Using the assumption of a steady-state heat transfer on the wall, the heat transfer into the wall can be balanced out by the heat transfer leaving, as given in Eq. 2.17. The empirical analysis is summarized in the subsequent equations.

$$R_1 + C_1 = R_2 + C_2 = K_{1-2} \quad (2.17)$$

$$K_{1-2} = \frac{\lambda_w}{t_w} (T_{w1} - T_{w2}) \quad (2.18)$$

$$R_1 = 0.5\sigma (1 + \varepsilon_w) \varepsilon_g T_g^{1.5} (T_g^{2.5} - T_{w1}^{2.5}) \quad (2.19)$$

$$T_g = T_3 + \Delta T_{\text{comb}} \quad (2.20)$$

$$T_g = T_3 + \Delta T_{\text{comb}} \varepsilon_g = 1 - e^{-290PL(q'l_b)^{0.5} T_3^{-1.5}} \quad (2.21)$$

$$L = 0.0691(C/H - 1.82)^{2.71} \quad (2.22)$$

$$R_2 = Z\sigma (T_{w2}^4 - T_3^4) \quad (2.23)$$

$$C_1 = 0.020 \frac{\lambda_g}{D_L^{0.2}} \left(\frac{\dot{m}_g}{A_L \mu_g} \right)^{0.8} (T_g - T_{w1}) \quad (2.24)$$

$$C_2 = 0.020 \frac{\lambda_a}{D_{an}^{0.2}} \left(\frac{\dot{m}_{an}}{A_{an} \mu_a} \right)^{0.8} (T_{w2} - T_3) \quad (2.25)$$

The term of the internal radiation is also comprised of soot and gas, as indicated in the schematic. The two emissivities, of the wall and gas, respectively, are ϵ_w and ϵ_g . The temperature of the combustion gas T_g is found by the sum of the annulus (compressor air) temperature and the resultant temperature rise from the combustion process (ΔT_{comb}), available in standard combustion tables for this purpose. The value of the constant Z is dependent on the liner casing emissivity, which is interchangeable from one material to another (0.4 for aluminium alloys and 0.6 for steel).

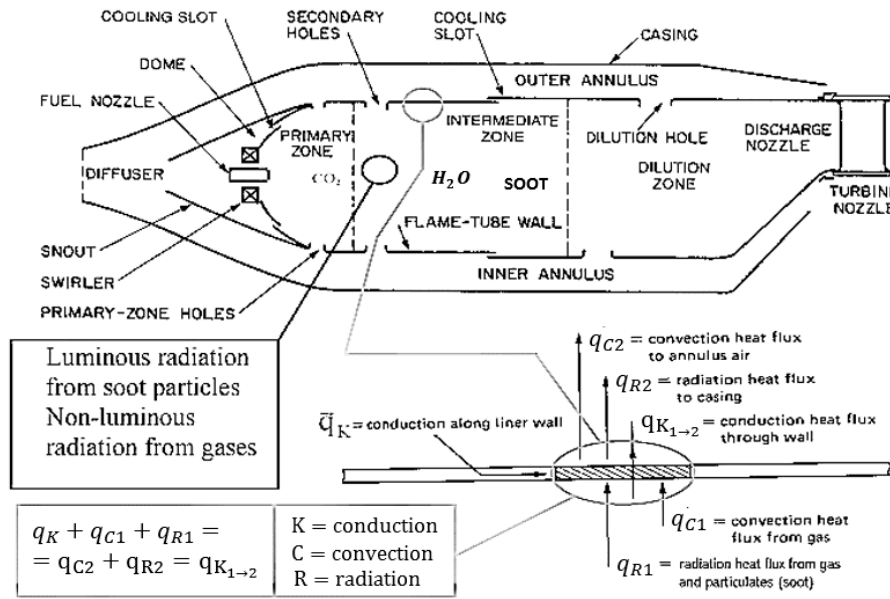


Figure 2.3: Schematic of heat transfer loads in a combustor liner. Extracted from [6]

The equation above hold only if the liner is uncooled. Thereby, in cases where film cooling is utilized, only the convective heat load on the inside changes (C_1), due to the resultant changes in the flow characteristics in the vicinity of the wall [74]:

$$m = \frac{(\rho U)_a}{(\rho U)_g} \quad , \quad Re_x = U_a \rho_a \frac{x}{\mu_a} \quad (2.26)$$

$$\text{if } 0.5 < m < 1.3 : \quad C_1 = 0.069 \frac{\lambda_a}{x} Re_x^{0.7} (T_{w,ad} - T_{w1}) \quad (2.27)$$

$$m > 1.3 : \quad C_1 = 0.10 \frac{\lambda_a}{x} Re_x^{0.8} \left(\frac{x}{s} \right)^{-0.36} (T_{w,ad} - T_{w1}) \quad (2.28)$$

The adiabatic wall temperature is calculated using the cooling effectiveness:

$$T_{w,ad} = T_g - \eta(T_g - T_a) \quad (2.29)$$

Lefebvre proposes two approaches for the calculation of the cooling effectiveness: turbulent-boundary-layer-based or wall-jet-model-based.

The empirical relations concerning the final energy balance was also validated by Lefebvre and Herbert [71], in which both internal and external radiation were accounted for. The results were compared to engine wall temperatures from an experiment on the primary zone. The resultant agreement was good at various operating conditions. On the other hand, the validation study did not include an analysis on the peak heat loads or distribution of the temperature field, caused by limited experimental data.

The approach from Gosselin et al. [36] does not alter the empirical relations used until now. Only a small modification is that the combustor was divided into four zones in their study: recirculation zone, primary zone, dilution zone. The loads were thereby calculated for each zone.

The complexity of the equations in both approaches accentuates the challenge of the selection of appropriate reference mass flows, velocities and temperatures for relatively accurate calculations. For example, in the early analysis of Lefebvre and Herbert [71], the mass flow in all crucial zones (combustor inlet flow, primary zone flow, and swirler mass flow) was either estimated or calculated, which was in fact crucial for the good agreement. Such data however most often is not available without prior experimental or simulation work. The relations however, are still useful and are used to this day at early design stages (e.g. work of Ramierz [102]).

2.2 Conjugate heat transfer problems

The term conjugate heat transfer (CHT) was first coined in 1961 by Perelman [96], addressing the problem of heat transfer between a fluid and a solid, with an unknown initial interface condition, evaluated from the solution of the heat transfer problem. The term conjugate heat transfer entails the simultaneous solution of both conduction and convection, within the solid and in the thermal boundary layer close to the wall, respectively. A one-dimensional CHT problem is depicted in Figure 2.4.

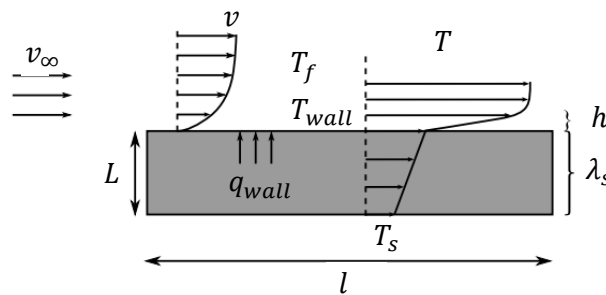


Figure 2.4: The one-dimensional CHT problem schematic

In addition to the Nusselt number described in Eq. 2.7, the second characteristic non-dimensional number for CHT problems is the Biot number. It describes the ratio of the conductive over the convective *thermal resistances* of the problem.

$$Bi = \frac{h \cdot L}{\lambda_s} \sim \frac{\text{Conductive resistance}}{\text{Convective resistance}} \quad (2.30)$$

Consequently, a large Biot number could be used to indicate a high temperature gradient in the wall, whereas in case of a low Biot number the temperature gradient in the boundary layer is the highest due to the high convective thermal resistance. This is also illustrated in the figure below.

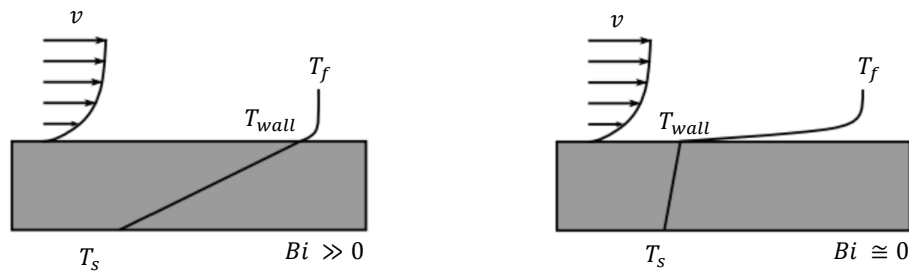


Figure 2.5: Temperature gradients at low and high Biot number settings in fluid and solid regions

The fundamental difference with the Nusselt number is that in the latter case, the resistances are related entirely to the *fluid* region, whereas for the former, it is the convective resistance of the *fluid* and the conduction resistance of the *solid* region.

A comprehensive summary of all CHT work prior to 2018 is well presented by John [54], where analytical studies are discussed with relevant theory, and a set of some of the most important computational studies is included, along with a strong direction to their application envelope. According to the author, more emphasis is put on the computational side of CHT and presents various coupling techniques in more detail. The review exhibits CHT as a great approach for achieving high-fidelity results for complex problems, where analytical solutions do not work. The author also identifies the coupling algorithms as critical part of the solution and distinguishes two types of coupling: (i) monolithic, and (ii) partitioned. For a more mathematically-focused explanation of the conjugate heat transfer, the reader can skip to Section 4.1.

2.2.1 Flat plate

The analysis of conjugate heat transfer problem using a solid plate of finite thickness has been the subject of research for a plethora of authors over the years, particularly in the early stages of CHT problems where the first analytical solutions were derived. The variety in proposed analytical solutions is mainly due to the assumptions made for the velocity and temperature profiles in the boundary layer, the most popular assumption of which is a linear velocity profile within the boundary layer. The complexity of the solutions increased with more complicated geometries and hence did not present any practical feasibility. In this section, both laminar and turbulent studies are included.

The first found publication with an experimental setup was published by Soliman [114]. The author reported transient temperature responses with varying Reynolds numbers in the range of $500,000 < Re < 2,000,000$. A well known problem in open literature is the Luikov problem [1], in which an analytical solution was derived for a laminar flow over a plate with a bottom surface set at constant temperature. The nondimensional Brun number ($Br_x = (\lambda_f/\lambda_s)(b/x)Pr^m Re_x^n$) was introduced, and it was noted that for Brun numbers > 0.1 (ratio between thermal resistance of the plate to that of the convective boundary layer), the problem should be solved using the CHT method. The author also later derived expressions for laminar flow in circular and planar tubes. Karvinen [62] derived new results for conjugated heat transfer in a plate for both laminar and turbulent flow regimes. The author presented an approximate method based on simplifications of the governing equations. The model was then compared to experimental data by Sohal and Howel [113], in which the influence of radiation heat transfer was taken into account. Later, Yu et al. [125]. derived a new solution method, which proved to be effective for any Prandtl number. A proposed Nusselt number correlation was also compared to numerical data. In the following study of Yu [129], additional conjugation parameters were introduced that seemed to match well with numerical data from Keller's box method differencing scheme [19]. Vynnycky, M. et al. [121] proposed two analytical methods: an averaging method and a boundary-layer-based method, both compared to numerical solutions at a wide range of three non-dimensional parameters (Pr, Re, λ). The methods allowed for a two-dimensional conduction in the plate, compared to Luikov's solution where

the assumption for one-dimensional conduction is held. Mosaad, M. [87] proposed another analytical solution based on the observation that the upper surface temperature of the plate is independent of the Prandtl number. The condition for the Brun number above which conjugation is important was hence adjusted from 0.1 (Luikov) to 0.15.

In this report, a laminar case is considered for the analysis. However, turbulence is of utmost practical importance in industry, and a summary of the work on turbulent CHT over flat plates is included in the following paragraph.

Ames & Moffat [3] performed an experimental turbulence investigation over a flat plate problem including conjugate heat transfer measurements. Thirty three years later Karvinen's publication mentioned above, the author presented a new semi-analytical solution for a class of flat plate conjugate convective heat transfer problems [63]. These included the popular Luikov problem, uniformly generated heat on one surface, and a modified Luikov problem where both surfaces are under a convection boundary condition. The author used the superposition principle and analytical expressions to couple the heat flux and temperature distributions. A similar approach was followed by Shariatzadeh [56], where the author also provided a semi-analytical solution for a conjugate turbulent forced convection boundary layer flow over plates. The solution was based on the Differential Transform Method (DTM) used for solving a non-linear integro-differential equation. Later, Hajmohammadi [39], using a temperature-dependent thermal conductivity for the plate, performed numerical simulations for the sake of validating the model of Shariatzadeh. In the paper, the author reported a single case in which a horizontal plate is heated with uniform heat flux at the lower surface while being cooled at the upper surface under a laminar forced convection flow. Lastly, Lindstedt & Karvinen [78] presented a new simpler semi-analytical solution for problems with a surface at a constant temperature and forced/natural cooling applied on the other. It is reported that the simplicity is achieved by assuming only one-dimensional conduction in the solid, which leads only to small deviations from previous studies very near the leading edge, which in practical engineering cases can be ignored.

Summary

The conjugate heat transfer problem over a flat plate has received considerable attention due to the inherent geometric simplicity. An overview of the key papers discussed above is presented in Table 2.1 below.

Table 2.1: Review of CHT studies on flat plates

Author	Analysis	Flow type	Comments
Soliman (1967)	Experimental	Turbulent	Transient temperature response with $5e5 < Re < 2e6$
Luikov (1972)	Fully analytical	Laminar	Analytical solution for a plate with a constant temperature profile on the bottom surface
R. Karvinen (1978)	Semi-analytical	Turbulent/Laminar	Comparison to experimental data by Sohal, combining conduction, convection and radiation heat exchange
K. Cole (1996)	Fully analytical	Laminar	Laminar shear flow over a small heated strip for electronic cooling; new scaling law using Pe number
Karvinen (2011)	Analytical	Turbulent/Laminar	Power sum series for different configurations
Shariatzadeh (2013)	Semi-analytical	Turbulent	Analytical solution using DTM
Hajmohammadi (2013)	Numerical	Turbulent/Laminar	Numerical FVM comparison to DTM analytical calculation
Lindstedt & Karvinen (2013)	Analytical	Turbulent/laminar	Bottom isothermal surface, comparison with previous studies

- (Semi-)analytical models developed over the years for turbulent and laminar CHT over flat plates yield good agreement with numerical and experimental data.
- At the groundwork of the models however lie fundamental assumptions, which lead to discrepancies more apparent at the leading edge of the plate

No specific criterion was found w.r.t a conjugation requirement: most of the studies entail a comparison with the uncoupled approach using a narrow range of parameter variation.

2.2.2 Turbulent offset jet

The turbulent offset jet is a comparatively well researched problem with a multitude of experimental research data, including turbulence and flow characteristics, heat transfer and conjugation set-ups. To the author's knowledge, the majority of available CHT data comes from practical experimental sources. Plenty of computational studies, however, exist in open literature too. Some of the key studies including a conjugate heat transfer approach are included below.

The first reported experimental study found in literature was by Nizou [90], where experimental investigation of a wall jet (i.e. offset ratio = 0) with a constant wall heat flux condition was conducted. The heat transfer and momentum transfer for such arrangement were correlated and the difference between a wall jet boundary layer and turbulent boundary layer. In the same year, Hoch and Jiji [45] studied the same problem with an additional imposition of freestream velocity, later providing an analytical solution for a laminar case. One of the most insightful studies in the matter was published later by Pelfrey and Liburdy [95], with a detailed analysis of the mean flow and turbulent characteristics at multitude of offset ratios (OR).

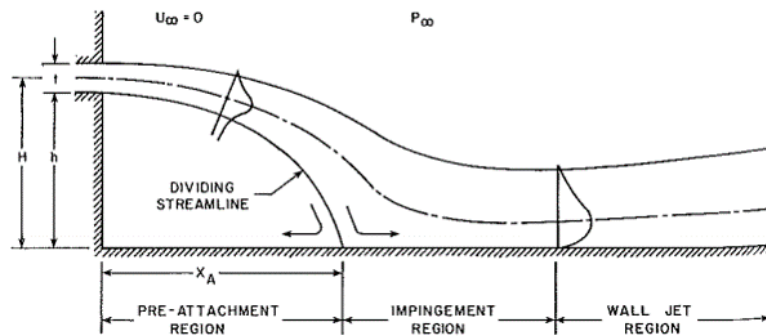


Figure 2.6: The turbulent offset jet problem. Extracted from [95]. The flow can be characterized by three regions where the flow exhibits different behaviour. The recirculation zone (which is upstream from the reattachment point), the impingement region, where the reattachment length is measured, and the wall jet region where the flow is practically identical to a turbulent jet with an OR of 0. The wall jet region is free of gradients of mean pressure, and is where the flow decelerates and spreads.

Briefly after the study of Pelfrey and Liburdy, Holland and Liburdy [47] used the same experimental setup to study the thermal characteristics of offset jets. The key findings of the study concern the reattachment length (RL), and resultant interface temperature profiles, Nusselt numbers, and jet velocity decay. RLs were found to coincide with the maximum Nusselt number locations, whereas the maximum temperature location depends on the offset ratio, and approaches the RL with increasing ORs. The interface temperature reduces/increases rapidly up to the reattachment point and thereafter it increases/decreases. A typical profile is shown in Figure 2.7 below. The term I_r was introduced to scale the axial location with respect to the RL for an OR=7 (i.e. for $OR = 3$, $I_r = 1.77$, as $RL = 7.02$, and $RL = 12.42$ for $OR = 7$). Moreover, thermal energy within the recirculation zone is relatively uniform for all ORs.

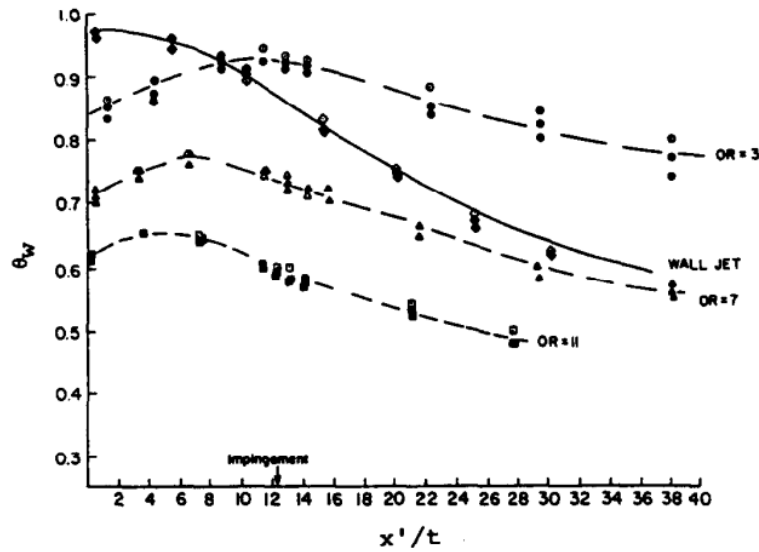


Figure 2.7: Dimensionless wall temperature on the wall as a function of offset ratio ($\theta_w = (T_{wall} - T_\infty)/(T_{ex} - T_\infty)$, $x' = xI_r$) for a conjugate heat transfer case [47].

Vishnuvardhanarao and Das [118] performed an extensive numerical study by simulating the experimental work of Holland and Liburdy using solely a $k - \epsilon$ turbulence model, with a detailed discussion on velocity and temperature distribution in the domain are discussed. The same authors [119] then performed another CHT on the same domain by imposing constant flux at bottom surface and sweeping a number nondimensional numbers. The third paper from the sequence of studies by Vishnuvardhanarao [29] was a CHT computation with a constant bottom wall temperature, investigating the influence of Pr number, offset ratio, thickness ratio, and conductivity ratio on the thermal and flow fields. A more recent study using CHT was done by Fu [31] where results from various two-dimensional RANS models were compared to LES data using STAR-CCM+. The author expressed a slight favour in the face of the standard $k - \epsilon$ model.

Summary

Overall, the problem of a turbulent offset jet is wall established and a multitude of key findings w.r.t heat transfer and flow behaviour have been solidified over the years of research. This includes:

- The static pressure distribution in the recirculation region is independent at sufficiently large Reynolds numbers ($Re > 11 \cdot 10^3$).
- The reattachment length does not depend on Re above $Re = 15,000$.
- Not much focus on flow physics in the impingement region; studies agree on a rapid decay of local maximum streamwise mean velocity U_m , and an increase in wall-normal jet half-width $y_{0.5}$; increasing OR seemed to lead to an increase in the streamwise velocity decay rate.
- Both lateral on wall-normal jet spreading are generally independent on OR.
- Overall, both $k - \epsilon$ and $SST - \omega$ models are able to predict the recirculation region extent reasonably well; turbulence modelling predict the loci of the maximum streamwise velocity decay, wall-normal location of U_m , wall-normal half-width in the outer shear layer and the wall static pressure distribution, partly due to the isotropic assumptions made in the models.
- The location of maximum Nusselt number coincides with the reattachment point for OR = 5, and decreases downstream; a second increase is present upstream near the corner region. The maximum

and minimum locations of the Nusselt numbers, however, shift progressively downstream as the offset ratio is increased.

In general, the amount of **conjugate** heat transfer studies is low, compared to the flat plate case. To author's knowledge, no comparison between the uncoupled and conjugate approach has been performed in the past, particularly for the case of an turbulent offset jet.

2.3 Combustion systems cooling

The field of cooling studies in the field of gas turbines is one of the major research pillars in convective heat transfer in general, with the age-old goal of augmenting heat transfer capabilities without resulting in a penalty from a pressure drop point of view (the increase in pressure drop Δp , however, directly proportionate to the coolant mass flow rate, such that $\dot{m}_c \propto \Delta p$). According to Bunker [15], the field comprises of five main subfields: (i) internal convective cooling, (ii) external surface film cooling, (iii) materials selection, (iv) thermo-mechanical design, and (v) selection/conditioning of the coolant. The subsection below would only focus on internal and external cooling geometries. Before more detailed specifications of the geometries are given, it is worthwhile mentioning that in most gas turbine cooling cases, both external and internal coolant flows are fully turbulent. It is a well-established fact that turbulence enhances mixing [4] and hence accelerates heat transfer which is fully exploited in the design of such components. A large proportion of studies on convective cooling in gas turbine components focuses on turbine vanes, but the techniques used are also applicable to other moving or stationary components in a combustion system (e.g. combustion liner or **transition piece**).

2.3.1 Internal cooling

Arguably, the most common mechanism reported in literature for internal channel cooling techniques is the use of different turbulation topologies. With the advent of additive manufacturing, and the resultant dimensionality reduction of the cooling, some turbulator arrangements have become increasingly more complex [15]. Examples of internal cooling topologies achievable only by non-conventional methods like AM are shown in Figure 2.8.

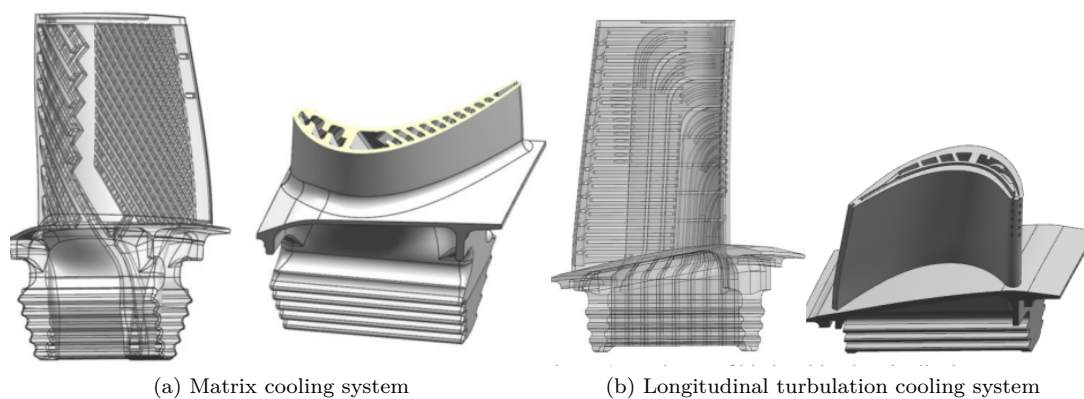


Figure 2.8: Two examples of internal cooling design for GT turbine vanes; for reference, vane length is 12.75mm [15].

A fully detailed summary is given in the works of Ligrani [77]. The article mentions a multitude of rib, fins, dimple and swirl generator geometries with a full comparison and discussion on relevant papers. The review article eventually concludes that from the comparison between the cooling methodologies obtained prior and after 2003, based on their respective thermal performance and friction factors, a only a minimal improvement has been achieved in providing a better “spatially-averaged thermal protection.”

The main types can be divided into the following sections: (i) pin fin arrays, (ii) dimples, (iii) rib turbulators, (iv) swirl chambers, (v) and combination devices, where swirl chambers have not undergone major developments since 2003.

With regards to pin fins specifically, the geometry can be described as a pedestals generally arranged into arrays and extending between two opposite walls of an internal cooling passage. Studies report comparatively high pressure drop compared to other turbulators. Multiple types of cross-sections are investigated in literature. Some studies suggest that “the highest overall heat transfer coefficients, which are spatially averaged over all pin fin and endwall surfaces, is produced by the triangular pin fin arrangement” [111]. Siw et al. explains this by the increased shear and wake shedding caused by the sharp edges on the triangular elements. The author examined the thermal performance of pin fins of three cross sections, shown in Figure 2.9. This in turn enhances flow mixing, and thus an increase in the turbulence transport is achieved.

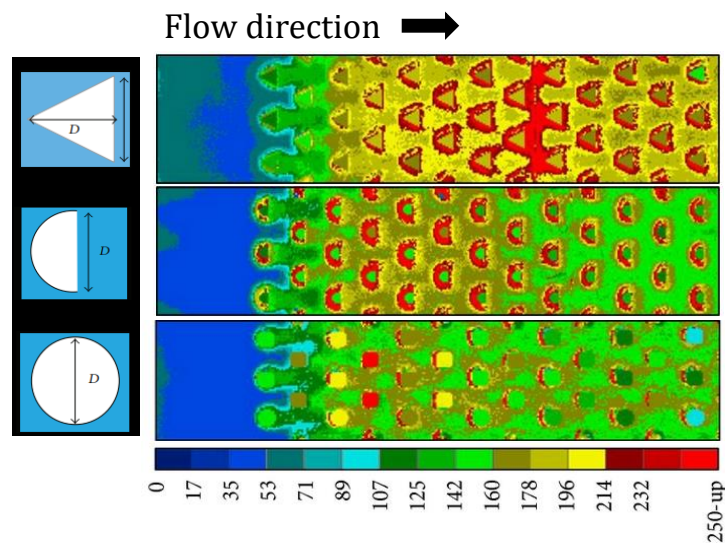


Figure 2.9: The three configurations used in the study of Siw et al. (top to bottom: triangular, semi-circular, circular) and the dimensional heat transfer coefficient distributions (domain dimensions width, $W=63.5\text{mm}$; height, $H=25.4\text{mm}$; length, $L=101.6\text{mm}$) [111]

Tabulated ribs are similar to rectangular (not exclusively) bars mounted along a surface, at a certain angle with respect to the bulk flow. Flow recirculation around a single rib are positioned just downstream of each rib, and cover a considerable portion of the ribbed wall depending on the pitch/height ratio of the ribs. Studies suggested that each of the recirculation zones is often considered to be a potential hot spot because it is associated with locally lower surface Nusselt numbers. Parameters that influence the performance of ribbed channels are namely the channel aspect ratio (w_c/h_c), the rib blockage ratio (the rib height to channel height e/D_h), the spacing expressed using the pitch-to-height ratio (p/e), the cross sectional shape of the rib, the orientation of the ribs on the opposite wall, and the shape of the rib across the channel (straight, V-shaped etc.). An example configuration of a study by Casarsa [17], is shown in Figure 2.11.

The angle with respect to the bulk flow has been the subject of multiple studies. Some studies of Lau et al. [68], [69] suggested that the best heat transfer augmentation is achieved when the angle is equal to 45° , due to the stronger secondary flow induction, compared to other angles. With regards to the cross section for the rib, it has been reported that the best cooling performance is achieved by the so called backward-aligned delta-shaped ribs. The shape resulted in the lowest pressure drop and highest Nusselt number augmentation (Nu/Nu_o). Alternatively, wedge-shaped ribs also exhibit promising results in studies. However they remain outperformed by backward-aligned delta-shaped ribs. The two

types are presented in Figure 2.10 below.

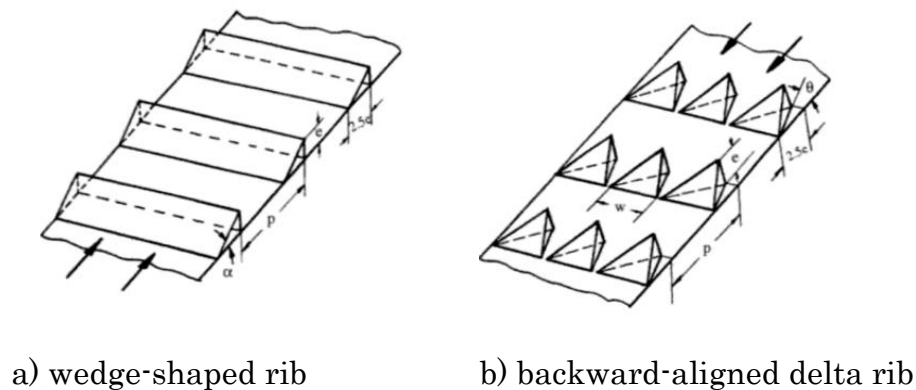


Figure 2.10: Rib shape configurations reported in [41]

Dimples on surfaces can also be protrusions, whereas multiple studies on flow structure resultant from various shape of the dimple/protrusion are given in literature. An agreement on the flow structure on dimples is lacking and is still an ongoing research, yet all studies reported an increase in heat transfer. Generally, an increase in relative dimple depth produces increases in surface heat transfer rates, as well as increases in pressure penalties downstream. Multiple papers however report the same overall key features responsible for local heat transfer augmentation: (i) shedding of multiple vortex pairs, (ii) strong secondary fluid motions within the vortex pairs, (iii) shear layer reattachment within the dimples.

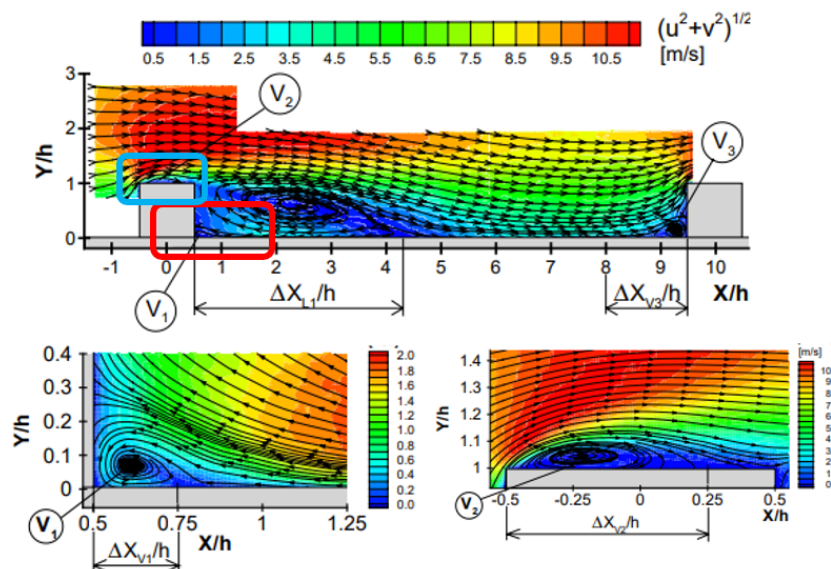


Figure 2.11: Turbulence intensity contour plot from [17], indicating three key recirculation regions of low HTC where hot spots occur, for flows over ribs ($Re = 3 \cdot 10^4$, $e/D_h = 0.3$, $p/e = 10$)

The main recent advancements in the internal cooling of gas turbine components and latest research interest comes with the simultaneous use of different augmentation technologies in one channel. Dimples together with rib-turbulators are for example investigated by Amano et al., whereas pin fins and rib turbulators is given in Siw et al. Combinations of three geometries is also recorded. urata et al. investigates passages with ribs, dimples and protrusions. Other studies also focus on the addition of external cooling to such turbulence topologies. For example Yang et al reports effusion cooling (see

next subsection) with internal ribs. Results indicated that pin fin-dimple channels yielded a higher HTC augmentation than purely pin fin channels. Each combination reported has a unique flow field and the resultant thermal (and hence Nusselt number) fields is explained by the accompanying flow structures. For a more detailed outlook, the reader can refer to the abovementioned studies.

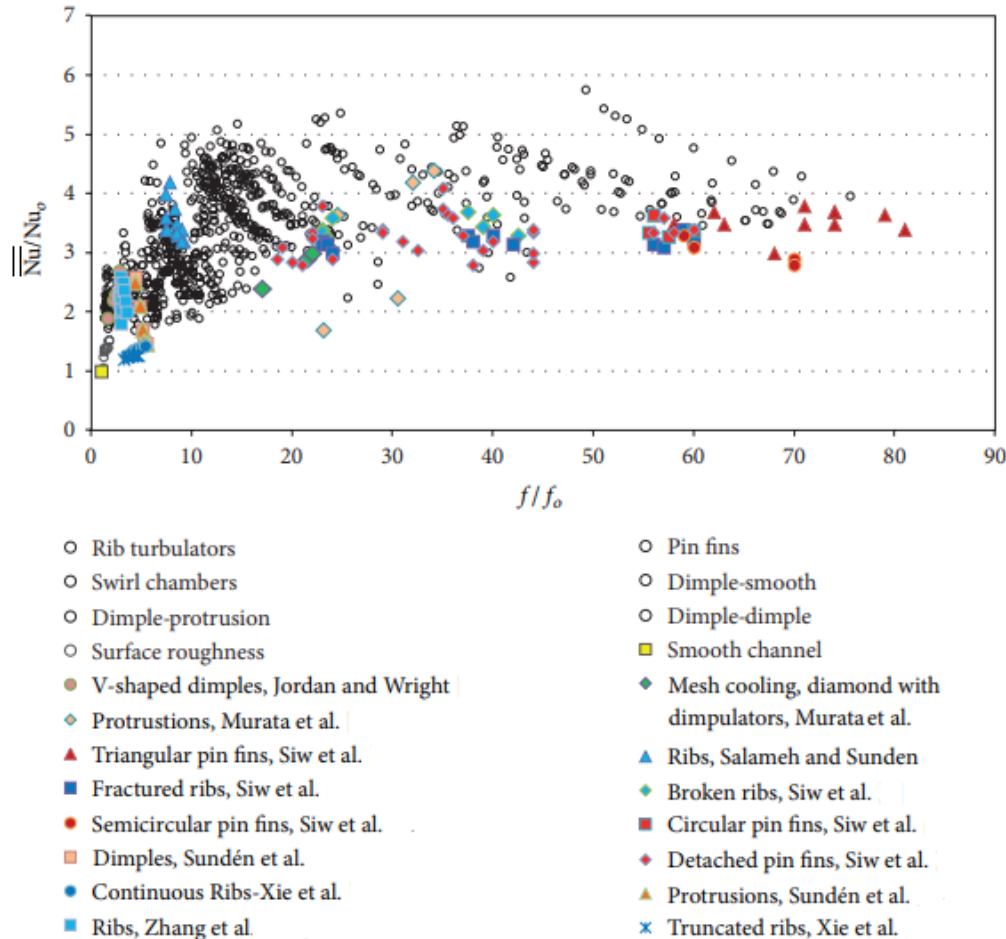


Figure 2.12: Comparison of heat transfer performance (heat transfer augmentation \overline{Nu}/Nu_o on y-coordinate versus friction factor f/f_o) for various types of internal cooling. Extracted from [77]

A direct comparison of each of the arrangement can be easily observed in the scatter plot given by Ligrani et al. [77]. In the plot it becomes evident that the combination devices are not included. This is due to the fact that the abovementioned studies did not include friction factor ratio data. A smooth channel is also given to serve as a reference point for comparison. The scatter plot suggests that the best tradeoff and hence best thermal performance is achieved for the rib geometry presented by Salameh and Stunden [104]. Fractured and truncated ribs on the other hand showed very little increase in pressure drop, but the resultant increase in heat transfer coefficients was not fully satisfactory either. On the far right and middle of the plot are the pin fin arrangements which are more sensitive to pressure drops as mentioned earlier.

2.3.2 External cooling

Since the goal of this study is mainly focused on an optimization of internal cooling passages, the subject of external cooling is of little relevance. For the sake of logical coherence and completeness, a

brief overview is presented here.

The main types of external cooling for gas turbine components reported in literature are film cooling, impingement cooling, and transpiration cooling. Jet impingement is a mechanism that utilises a supply plenum air at an overpressure and impingement holes on an orifice plate, which serves for flow confinement and is located at an offset from the heated surface. Areas of exposure to high thermal loads are often times subjected to impingement cooling as it provides very high heat transfer coefficients. One drawback, however, is that it reportedly could weaken the strength of the structure in the surrounding region [40]. An impingement array is given in Figure 2.13, along with a side-view cut-through in Figure 2.14.

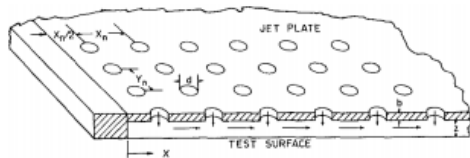


Figure 2.13: A typical array of a jet-impingement geometry.

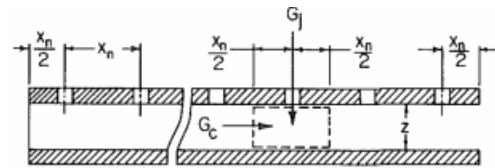


Figure 2.14: Schematic of a cross-flow. G_c and G_j are the cross-flow and impingement jet velocities respectively

An important phenomenon in jet-impingement cooling is cross-flow, which is the interference of the regular cooling air with the impingement cooling air. Hence, the ratio of cross flow velocity to jet velocity is an important parameter in the design of such cooling, along with the spacing in the jet array and hole diameter.

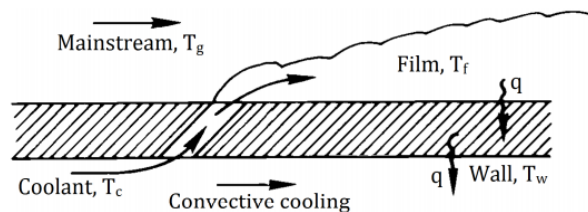


Figure 2.15: Schematic of a film cooling process, illustrating the mixing process of a coolant with mainstream flow. [91]

Film cooling generally refers to a secondary fluid which is injected in the area of interest. The resulting flow structure is of high complexity and is influenced by multiple parameters. The flow mixing is visualized in 2.15. Example parameters include the hole geometry configuration (exit shape, injection angle, hole length and spacing, number of holes), mainstream conditions, such as mass flux ratio M , coolant density ratio DR , approach boundary layer and others. Some authors also investigated slots instead of discrete holes for an injection geometry.

2.4 Low cycle fatigue

The aim of the design of a GT (combustion) component in the low-cyclic fatigue range is to determine the service life under the local influence of cyclic plastic strain. This is done so that the components in GT meet the mechanical integrity requirements, which are influenced by the thermal strain effects that temperature gradients cause from the component's cyclic thermal expansion[1]. The cyclic nature of

¹LCF is also a result of the **mechanical** cyclic stress. Such stresses arise from the mechanical loading of the component, e.g. displacements, pressure loads etc, which most of the time account for the majority of the total stress.

the loading is based on the chosen operating cycles of the components (usually such cycle is the intermittent shutting and starting of the entire GT). Low cycle fatigue arises due to thermal expansions of a component. The two key features of LCF analysis are the use of the total stress or strain amplitude and the use of suitable material data in the form of stress or Wöhler strain curves (sample curve presented in Figure 2.18). The material data used in this work comes from the Siemens internal material database. One duty cycle for the component considered in this work consists, in simplified terms, of the state of rest, starting the Gas turbine, base load operation and shutdown of the gas turbine back to its idle state. Under the assumption of the highest load in base load operation is used in this work to determine a quasi-static analysis of the maximum stresses was carried out. For the hibernation of the system it is generally assumed to be in a stress-free state at ambient temperature. As a general rule, the time-dependent change in load must be determined by transient analyses for the starting and shutdown processes.

The LCF analysis simulates the thermal fatigue of the combustion components; i.e. the thermal expansions and hence stresses caused by temperatures that change over time, which lead to the formation and growth of cracks in the component. ([101], p.202) The real material behaviour shows a non-linear relationship between stress and strain in this area. The multi-axial stress state can be compared with the von Mises equivalent stress failure criterion of the material. The von Mises equivalent stress is calculated according to the following equation, where σ_1 to σ_3 represent the principal stress components:

$$\sigma_{V,Mises} = \frac{1}{\sqrt{2}} \cdot \sqrt{(\sigma_1 - \sigma_2)^2 + (\sigma_2 - \sigma_3)^2 + (\sigma_3 - \sigma_1)^2} \quad (2.31)$$

The Von Mises yield criterion is used to determine when yielding occurs. The criterion function and the plane stress of the Von Mises yield surface is given in Figure 2.16 below.

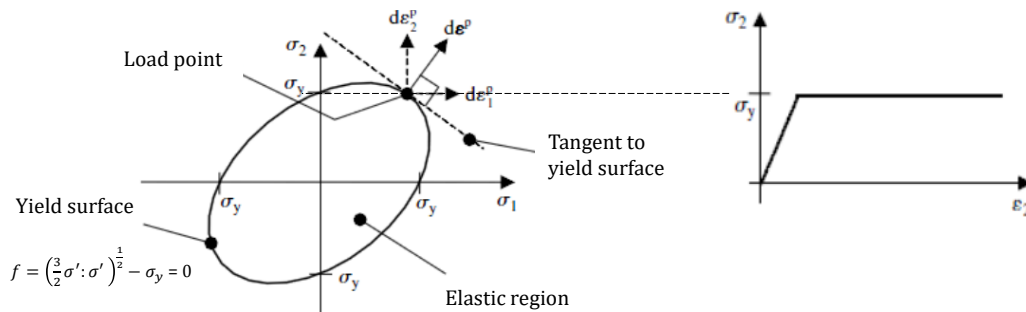


Figure 2.16: Von Mises yield surface, along with the yield criterion function f , along with the increment in plastic strain normal to the surface, and the resultant stress-strain curve obtained for uniaxial straining (no hardening). Note at the yield surface, $f = 0$.

In order to avoid the high computational effort of a nonlinear finite element analysis, a linear-elastic calculation approach is used for simulations in this thesis. The result of the linear calculation method is then approximated to the real elastic-plastic component behavior with a shakedown according to Neuber correction method. The Neuber approximation is given by:

$$\epsilon_{plastic} = \frac{(K_t \sigma_n)^2}{E} = \frac{\sigma^2}{E} + \sigma \left(\frac{\sigma}{K'} \right)^{\frac{1}{n'}}, \quad (2.32)$$

where K_t is the stress concentration factor, σ_n is the nominal stress, σ is the local stress, and K' and n' are the Ramberg-Osgood parameters for cyclic loading. In case the stresses are calculated by a linear elastic analysis, a proper determination of the cyclic loading requires a consideration of the reloading in addition to the Neuber relationship for initial loading.

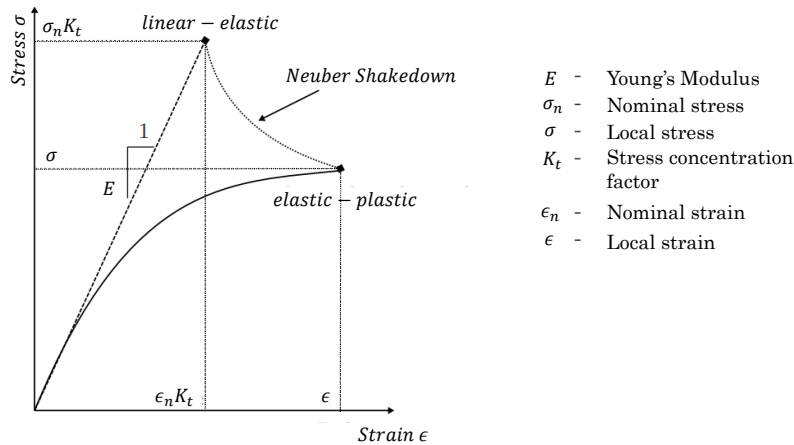


Figure 2.17: Neuber shakedown method

The shakedown for initial loading starts in the linear-elastic stress state and ends at the starting point of the cyclic hysteresis curve, as shown in the figure above. Then, the cyclical process of loading and unloading begins. The stress or strain range corresponds to twice the amplitude value of the stress or strain of the initial load curve. The equation below describes the approximation by Neuber for cyclical reloading;

$$\frac{(K_t \Delta \sigma_n)^2}{E} = \frac{(\Delta \sigma)^2}{E} + 2 \Delta \sigma \left(\frac{\Delta \sigma}{2K'} \right)^{\frac{1}{n'}} \quad (2.33)$$

2.4.1 Lifespan calculation

For the design of cyclically loaded components, the prediction of the service life is of great importance. The stresses, strains and temperatures calculated in a finite element analysis are available for calculating the service life. Furthermore, empirically determined material coefficients from vibration tests are known. Based on this data and the equations described in this section, the expected service life can be thus calculated.

The basic equation describing the relationship between total strain amplitude and service life was described by L. Coffin and S. Manson [115] and is:

$$\varepsilon_a = \underbrace{\frac{\sigma'_f}{E} (2N_i)^b}_{\text{elastic}} + \underbrace{\epsilon'_f (2N_i)^c}_{\text{plastic}}, \quad (2.34)$$

where σ'_f is the so-called vibration resistance coefficient, ϵ'_f represents the cyclic ductility coefficient, b is the fatigue strength component, and c is the cyclic ductility exponent. The factors ϵ'_f and $\frac{\sigma'_f}{E}$ are, per convention, found from the intersection of the elastic or plastic strain Wöhler line with the vertical at $N_i = 0.5$ [100]. N_i is thus also known as the number of tolerable oscillation cycles up to crack formation. Furthermore, the exponents b and c , ϵ , and σ are temperature dependent material properties that are empirically determined by vibration testing.

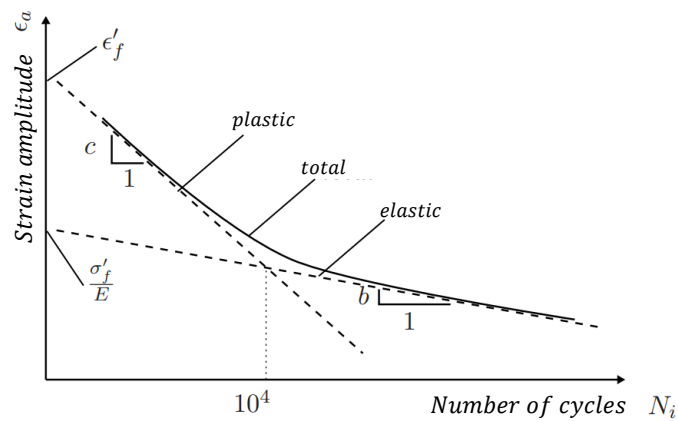


Figure 2.18: Wöhler SN curve (log-scale)

The first term of the equation relates to the elastic strain amplitude, while the second part relates to the plastic strain amplitude and represents a measure of the half-width of the stress-strain hysteresis. Equation 2.34 has to be solved numerically. The Wöhler line is essentially derived from the superposition of the elastic and plastic strain components shown in Figure 2.18 [100].

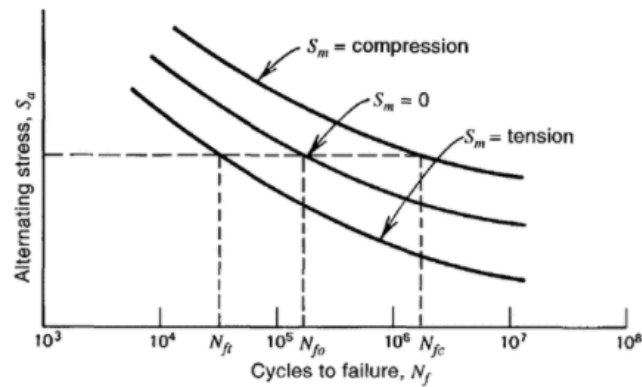


Figure 2.19: Effect of mean stress presence on fatigue life [115].

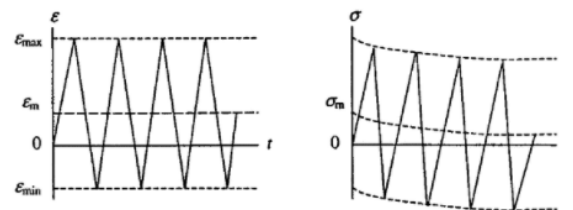


Figure 2.20: Constant mean strain ϵ_m effect on the mean stress levels σ_m . The relaxation is due to the plastic deformation, and hence the relaxation rate depends on strain amplitude [115].

The presence of a mean stress σ_m can have a significant influence on the service life ([115], p.74). Compressive mean stresses increase strength of the component, while on the other hand tensile mean stresses reduce it [100] (refer to Figure 2.19). The mean stress σ_m is read off at the midpoint of the stress-strain hysteresis. Several techniques have been developed in the attempt to incorporate the mean stress influence into the Coffin-Manson equation (equation 2.34). In the following formulation, the mean

stress according to Morrow is taken into account, see equation 2.35. In this method, a mean stress correction is applied to the elastic stress component of the Coffin-Manson equation. ([115], p.113)

$$\varepsilon_a = \frac{\sigma'_f}{E} \left(1 - \frac{\sigma_m}{\sigma'_f} \right) (2N_i)^b + \varepsilon'_f (2N_i)^c \quad (2.35)$$

However, since there is more mean stress relaxation at higher strain amplitudes due to larger plastic strains, low-cycle fatigue region is less influenced by the mean stress effect [115].

Chapter 3

Optimization Terminology

The problem of mathematical optimization is a vast one, expanding over a multitude of scientific disciplines, incl. computational theory, statistic, mathematics etc., and has been studied for a considerably long time: a monograph introducing the concept linear optimization technique for the first time was written in 1939 by Kantonovich [59]. In this chapter, the author's attempt to provide the reader with a very brief overview of current state-of-the-art optimization algorithms, and where possible some relevant mathematical background is herein presented, along with a relevant application envelope of each algorithm. The list of optimization algorithms below is by no means complete and only serves to provide an idea of the vast possibilities and the wide range of methods. The chapter also contains an overview on the proprietary optimization algorithm by Siemens, which is at the groundwork of the optimization analysis in this project. The benefits of using such a *hybrid* optimization algorithm are also touched upon. The chapter includes basic terminology regarding multidisciplinary optimization and, finally, statistical design of experiments, which is presented as a method for efficient planning of simulation series.

3.1 Optimization algorithms

The hybrid nature of the proprietary optimization algorithm used in this project necessitates an ample understanding of the basics of the most fundamental types of optimization algorithms. In its canonical form, an optimization problem can be mathematically formulated as:

$$\text{Minimize: } f(\vec{x}) \quad (3.1)$$

$$\text{Subject to: } g_j(\vec{x}) \leq 0 \quad j = 1..m \quad (3.2)$$

$$h_k(\vec{x}) = 0 \quad k = 1..l \quad (3.3)$$

$$x_i^l(\vec{x}) \leq x_i \leq x_i^u(\vec{x}) \quad i = 1..n \quad (3.4)$$

$$\text{Where } \vec{x} = \begin{Bmatrix} x_1 \\ x_2 \\ \vdots \\ x_n \end{Bmatrix} \quad (3.5)$$

The following notation is used:

- The *objective function* (OF) (less formally put, the goal of the optimizer) is mathematically denoted as $f(\vec{x})$. A common practice is to express the objective as a minimization problem, but the inverse holds too (maximization). From an industrial perspective, the function can consider a wide variety of objectives as long as a mathematical formulation exists.
- All *design variables* that can be modified are contained in the vector \vec{x} . The last equation (3.4) comprises of the lower and upper bounds of each of the respective design variables.

- Optimization can be unconstrained or constrained depending on the problem, expressed in the inequality, i.e. the function $g_i(\vec{x})$.
- The equality of the variable $h_k(\vec{x})$ can be used to express relations between design variables, which tend to be explicit in \vec{x} in most cases. Such relations can be eliminated when the choice and number n of variable is properly selected.

A constrained optimization presents a challenge for direct solvers due to the inequality constraint and can be often translated into an unconstrained pseudo-objective optimization:

$$\tilde{f}(\vec{x}) = f(\vec{x}) + R \cdot \sum_{j=1}^m \delta_j \cdot (g_j(\vec{x}))^2 \tag{3.6}$$

$$\text{Where } \begin{cases} \delta_j = 0 & \text{if } g_j(\vec{x}) \leq 0 \\ \delta_j = 1 & \text{if } g_j(\vec{x}) > 0 \end{cases}$$

Such 'penalty-based' methods use a multiplier R that puts weight to satisfying the constraints (genetic algorithms discussed later for example use this technique). This however remains a *weak* formulation of the problem and sometimes the constraints might remain unsatisfied.

The majority of optimization algorithms base the new design on the previously found one, such that:

$$\vec{x}_{i+1} = \vec{x}_i + \alpha_i \cdot \vec{S}_i, \tag{3.7}$$

where the iteration is indicated with the subscript i , and hence \vec{x}_{i+1} is the new guess for optima on the design space. The search direction can be expressed with \vec{S}_i and α_i is a scalar used for representing the amplitude of the change in the direction of the vector \vec{S}_i . Essentially, the difference in all possible optimization algorithms lies in the manner in which previous iterations compute the amplitude and direction vector in the search of new optimum, given in Equation 3.7.

Generally speaking, optimization algorithms can be classified depending on the order of derivatives used of the OF. For example, zero order methods, sometimes called derivative free optimization (DFO), include only algorithms which evaluate and use directly the value of the OF in search of an optimum. First and second order methods respectively, which lie outside the scope of this report employ first and second order derivatives of $f_i(\vec{x})$. New optimization algorithms however are constantly being developed and can be sometimes grouped into families. Figure 3.1 presents an overview of grouping of some of the most popular optimization algorithms, also indicating the order of the respective algorithm.

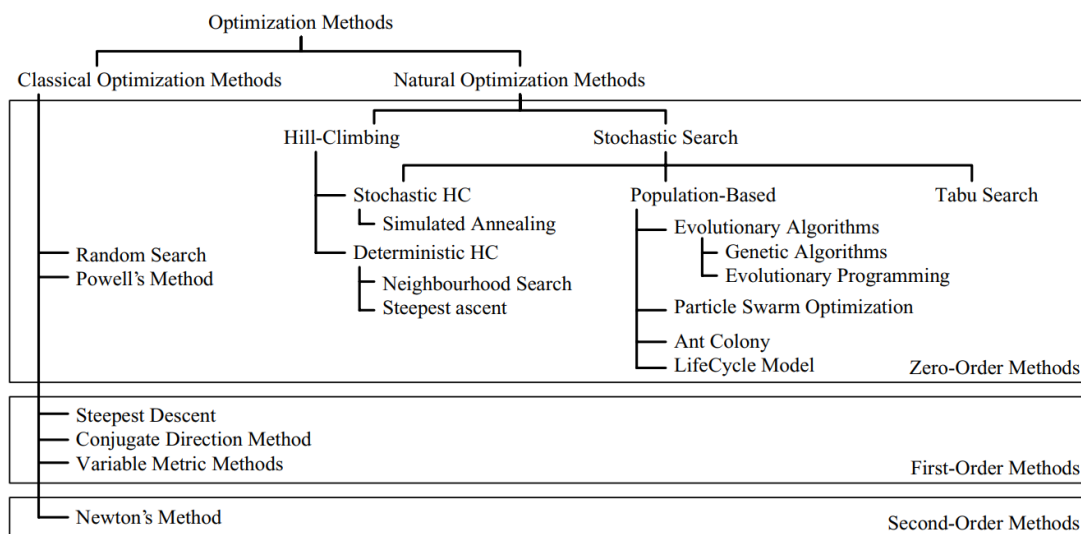


Figure 3.1: Families and classes of optimization algorithms (adapted from [80])

For the sake of conciseness of the report, in the following subsections, only the types of optimization algorithms present in the hybrid algorithm are presented in more detail: (i) simplex programming, (ii) deterministic/stochastic programming, and (iii) genetic optimization. The term *programming* can be used interchangeably with *optimization* in the context of algorithms and is not related to *computer programming* but rather a set of logistic instructions.

3.1.1 Simplex programming

Linear programming refers to the solution approach used to solve optimization problems where all the constraints are linear equalities or inequalities, along with a linear objective function. The most common algorithm for such problems is the Simplex Method, which was first introduced in 1947 by George Dantzig. Linear programs are most commonly expressed as:

$$\text{Minimize: } z = f(\vec{x}) = \vec{c}^T \vec{x} \quad (3.8)$$

$$\text{Subject to: } A \vec{x} \leq \vec{b} \quad (3.9)$$

$$\vec{x} \geq 0 \quad (3.10)$$

where A is an $n \times m$ coefficient matrix, comprised of the constraint coefficient vectors for each variable (\vec{a}_i) and \vec{b} is a vector of coefficients in \mathbb{R}^n (n equations in m unknowns, $m > n$). The constraint set in a linear program defines a feasible region, which is in the form a polyhedron, coming from the intersection of n -number half-spaces ($\vec{a}_i^T \vec{x} \leq b_i$). The constraints set be expressed as $\mathcal{P} := \{x \in \mathbb{R}^n \mid \vec{a}_i^T \vec{x} \leq b_i, i = 1 \dots, \text{right}\}$. An example polyhedron in two-dimensions is given in Figure 3.2 below.

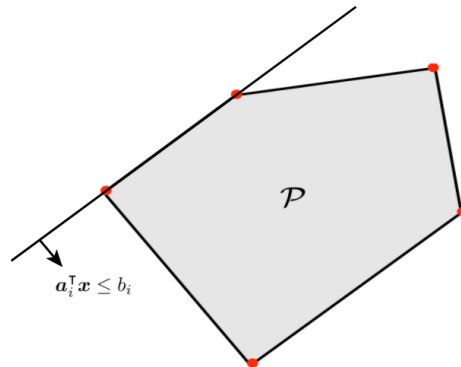


Figure 3.2: A polyhedron \mathcal{P} and an extremum, highlighted in red.

An important mathematical concept in linear programming are the extreme points of the polyhedron. They are defined such that

$$\vec{x}^k = \lambda \vec{x}^1 + (1 - \lambda) \vec{x}^2 \Leftrightarrow \vec{x}^1 = \vec{x}^2 = \vec{x}^k \quad (3.11)$$

where the vectors \vec{x}^1 and $\vec{x}^2 \in \mathcal{P}$, and the equation holds for any $\lambda \in (0,1)$. The fundamental property that follows for a polyhedron is then that it is a convex set. If it is assumed that \vec{P} has p distinct extrema $\vec{x}^1, \dots, \vec{x}^p$. The convexity then is express as:

$$\vec{x} = \sum_{l=1}^p \lambda_l \vec{x}^l, \quad \text{where } \sum_{l=1}^p \lambda_l = 1 \text{ and } \lambda_l \geq 0 \quad l = 1, \dots, p \quad (3.12)$$

Dantzig used this property of convexity, from which the fundamental theorem of linear programming is derived: "Suppose that the feasible region P to a linear program is a non-empty bounded set, i.e., an optimal solution exists. Then the optimal solution \vec{x}^* is an extreme point to the set defined by the

inequalities".

The most important concept in Simplex Programming is another form of representation which states that the Linear program has to be represented in the so called *slack* form, after ensuring that the polyhedron is in its standard form (the mathematical definition of the standard form lies outside the scope of this subsection). The algorithmic flow then consists of converting one slack form into an equivalent slack form whose objective value has not decreased, and has likely increased.

The slack form introduces an additional number of variable corresponding to the number of equations that are present. Such variable are called basic variables, whereas the original variable in are non-basic. The additional variables, hence, represent slack, in the sense that they correspond to how much slack is given in the inequalities present in the original problem. Once a solution is found (called the basic solution) for the set of equations, the iterative search for an optimum begins. It is achieved by searching from vertex to vertex. Each subsequent vertex is chosen such that the search direction is in the steepest feasible direction (based on so called reduced cost calculation), an exercise commonly referred to as *pivoting*.

Simplex Programming is covered in an extensive amount of literature, and for all unknown terms in the paragraphs above, the reader can refer to the following references where it is described in more detail. This includes [12] and [30], and therefore no further quantitative explanation will be given about it.

3.1.2 Deterministic and stochastic programming

The deterministic optimization contains the classical optimization algorithms of mathematics and is largely based on linear algebra. One advantage of deterministic optimization is the faster convergence compared to stochastic methods. This means that fewer simulations of the response variable are necessary to achieve an optimized solution. Since the optimization is consistently based on mathematical formulations and does not contain any random elements, the results are always clear and reproducible. However, deterministic optimization has the disadvantage that by nature it can only optimize for one objective. It is also required to have gradient information of the objective function, which includes a considerable computational effort. The objective function also needs to be continuous and deterministic methods display weak performance in a noisy environment. In addition, the deterministic algorithms look for stationary points of the response variable, so that the solution may converge on a local optimum and overlook a global optimum. ([18], p.77) This fact can be illustrated with a simple optimization that starts at a certain point on a function curve and moves along the gradient to ever smaller function values. If this optimizer reaches a local minimum, it stops because from this point on the function values increase again. An underlying global optimum could hence remain undiscovered.

Stochastic optimization algorithms are methods that are based on chance or contain random elements. Many stochastic algorithms are modeled on natural processes. Simplified mathematical models were generated for various concepts from biology, physics or society, such as evolution, genetics or swarm intelligence. The greatest advantage of stochastic optimization algorithms lies in the possibility of multi-target optimization. So it is possible to optimize for more than one response variable. Furthermore, global optima can also be easily found, since the entire design space is examined with "randomly" placed samples ([18], p.103). The already mentioned slower convergence and the ambiguity of the solution are disadvantageous.

3.1.3 Genetic optimization

One sub-area of stochastic optimization is optimization using genetic algorithms that imitate processes from biological evolution. Genetic algorithms (GA) have the advantage that they can be applied to almost any type of optimization problem. GA-base algorithms have been reportedly the most commonly used for optimization problems involving Navier-Stokes equations in FV domains. Even complex relationships do not pose a problem. The three main components of a genetic algorithm are *crossing*, *mutation*,

and *selection*. Each solution is encoded in what is called a chromosome. The crossing of two parents (chromosomes) produces a new generation of children by interchanging parts of the chromosomes. In the next step, a mutation takes place with a much lower probability.

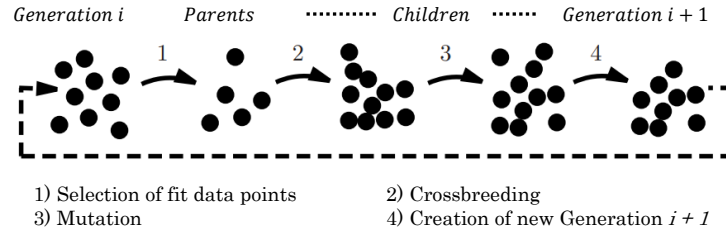


Figure 3.3: Genetic evolutionary process [5].

Individual parts of the chromosome are randomly changed. This ensures that random factor settings are generated again and again and that the algorithm does not converge to a local optimum. The newly generated solutions are sorted out based on their "fitness". Only the best solutions are passed on to the next generation of parents. The iterative process is repeated until the maximum number of iterations or the convergence criterion is reached [18].

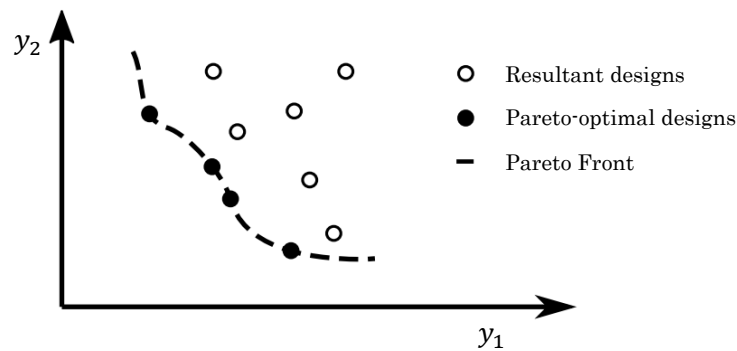


Figure 3.4: Simplified Pareto front illustration of a multi-objective trade-off study. Design points which lie on top of the Pareto line are not dominated, and also do not dominate each other. On the other hand, points that lie outside of the border, are dominated by the Pareto-optimal designs.

With the help of genetic algorithms, an optimization can be carried out for several goals. With multi-objective (MO) optimization, there is no clear optimum, but a set of so-called Pareto optima. A Pareto optimum is defined as the fact that no target variable can be improved without another target variable deteriorating. The so-called Pareto Front is the sum of all Pareto Optima solutions, i.e. if the problem is translated from a multi- to a single-objective optimization, the **weighted** sum of the objectives needs to be minimized. For the sake of this projects optimization objective function this reads:

$$F(\vec{x}) = w_{\text{temperature}} \cdot F_{\text{temperature}}(\vec{x}) + w_{\text{mass}} \cdot F_{\text{mass}}(\vec{x}), \quad (3.13)$$

which is analogous to Equation 3.15, representing the general form for a MO optimization. The relationship is shown schematically in Figure 3.4 above. When the number of objectives in the study however exceeds 2, the Pareto is not simply a single line anymore but a hyperplane. This leads to an increase in the number geometries necessary for analysis, and the visualization becomes less trivial.

3.1.4 SHERPA [®]

As mention earlier in the introduction chapter of this thesis, in this work a proprietary multi-objective optimization algorithm SHERPA is used, which comes within Siemens' Design Exploration Software

MDO HEEDS ®[116]. A very limited number of sources available in open literature makes use of this algorithm. SHERPA’s search method employs a hybrid and adaptive algorithm, that makes use of multiple search strategies at once and adapts to the problem. The name stands for “Simultaneous Hybrid Exploration that is Robust, Progressive, and Adaptive”. Siemens reports that a method’s participation is diminished in the optimization if it is determined to be ineffective for the given search problem. It is also worth mentioning that the developers of the algorithm do not claim that SHERPA is the best approach for all problems. The method, however, has shown convincing efficiency in finding a global optimum for a variety of practical engineering design problems.

A simple benchmark problem (minimizing mass of a cantilever beam while also satisfying a constraint on stress and deflection) is also used to compare the algorithm’s performance to numerous other ‘baseline’ algorithms. The figures below shows that SHERPA manages to find an optimal solution in considerably fewer iterations.

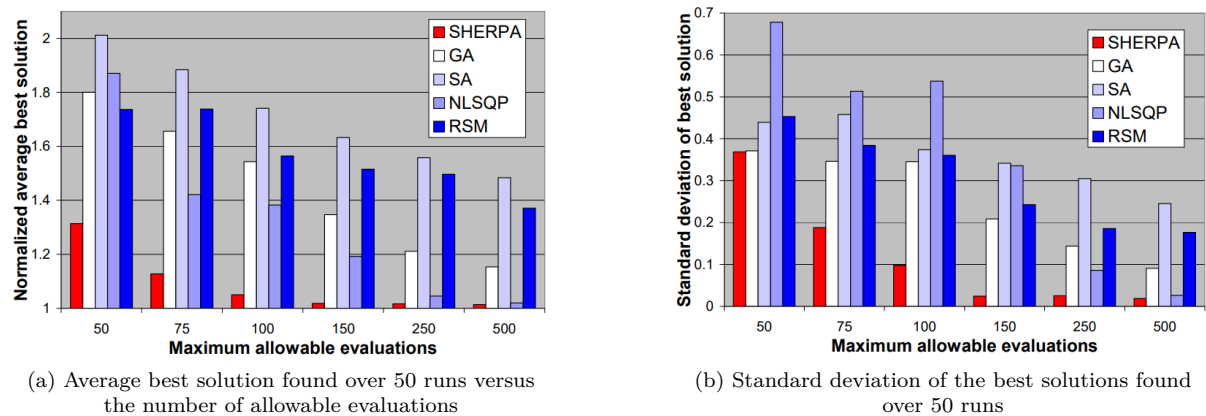


Figure 3.5: Results from benchmark comparison of different optimization algorithms. SHERPA yielded better results even at a very low number of evaluations [116].

Goldin et al. [35] also claimed that SHERPA is a hybrid combination of Nelder-Mead Simplex [88], simulated annealing [50], quadratic programming [105] and a genetic algorithm [34]. Some of the reported advantages include [97]:

- No iterative tuning of optimizer parameters is necessary
- Does not employ approximate response surface models and performs direct optimization
- Multiple strategies ensure that large and complex design space does hinder the efficiency of the global and local optima search

3.2 Multi-disciplinary Optimization

The problem of multi-disciplinary optimization has gain considerable traction over the years, particularly with the commercialization of high-performance computers. As the name suggests, MDO problems are comprised of multiple disciplinary analyses. According to Zadeh [130], the core idea of MDO “pertains to the decomposition of complex engineering systems into a set of smaller and less complex subsystems together with formal approaches of accounting for system interactions and couplings.” While the term multidisciplinary in literature is more relevant for system-level optimization types, the term is sometimes interchangeable with multi-objective optimization. The MDO framework is characterized in [130]. In such systems, it is desired to minimize/maximize several response variables at the same time, such as

the case in this thesis. Thereby, the correct mathematical formulation of such a system reads:

$$\begin{aligned}
& \text{Minimize:} && f_i(\vec{x}) && i = 1..l \\
& \text{Subject to:} && g_j(\vec{x}) \leq 0 && j = 1..m \\
& && h_k(\vec{x}) = 0 && k = 1..n \\
& && x_p^l(\vec{x}) \leq x_p \leq x_p^u(\vec{x}) && p = 1..q
\end{aligned} \tag{3.14}$$

The vector \vec{x} is the vector of design variables, consisting of the parameters of interest that can be modified. The function $f_i(\vec{x})$ is the respective objective function, specified by the subscript i . The constraints of the optimization are given by the inequality equations, whereas the equality constraint contributes the relations between design variables, in an identical manner to a single-object optimization. The only difference lies in the subscript of $f_i(\vec{x})$.

The multi-objective formulation can be easily converted to a single-objective by summing each individual weighted objective:

$$F(\vec{x}) = \sum_{i=1}^l w_i \cdot f_i(\vec{x}) \tag{3.15}$$

The function $F(\vec{x})$ then corresponds to a single point on the Pareto front, depending on the choice of weight values. This approach however diminishes the amount of insight obtained from the optimization problem, despite its computational advantage. The set of equations in Eq. 3.14 are either converted into a pseudo-objective functions (where the constraints are incorporated into a single equation, and hence an unconstrained optimization is solved) or the strong formulation is used with an optimization algorithm.

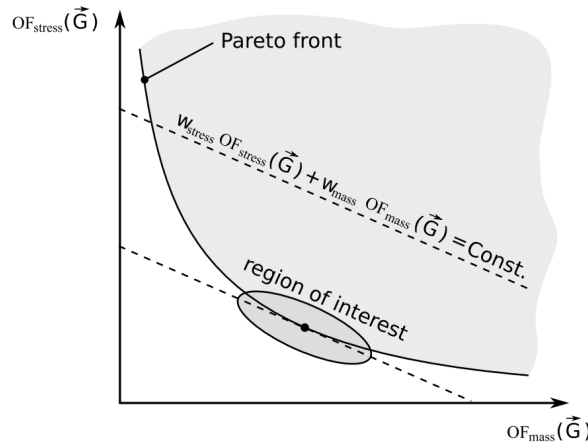


Figure 3.6: Pareto front of a MO (2 objectives) optimization and the equivalent optimization using a weighted sum in a single-objective optimization. The dashed lines represent values of the converted MO calculation. The resultant penalty decreases as the dashed line approaches the Pareto front.

It is worthwhile mentioning that the choice among so-called "Pareto optimal" solutions (solutions lying on the Pareto front) to determine the "favourite solution" is entirely delegated to the decision maker, and is usually performed **after** the MO optimization is finished. The conversion from MO to a single-objective less computations are needed to obtain the minimum, and the designer needs to observe only the region in the vicinity of the optimum (presented as the region near the black dot in Figure 3.6. The difficulty of using this approach comes in the determination of the weights. This becomes particularly ambiguous if the objectives are in different fields (such as the case of the optimization problem in this problem).

3.3 Screening and Design of Experiments

The field of Design of Experiments and screening could be used as an alternative powerful tool for optimization problems. The following contains a brief overview of the basics, necessary for the application of so-called meta models used in optimization.

For a parametric model with n free parameters x , there is a large number of possible parameter combinations. For each of these parameter combinations there is an answer y of the overall system.

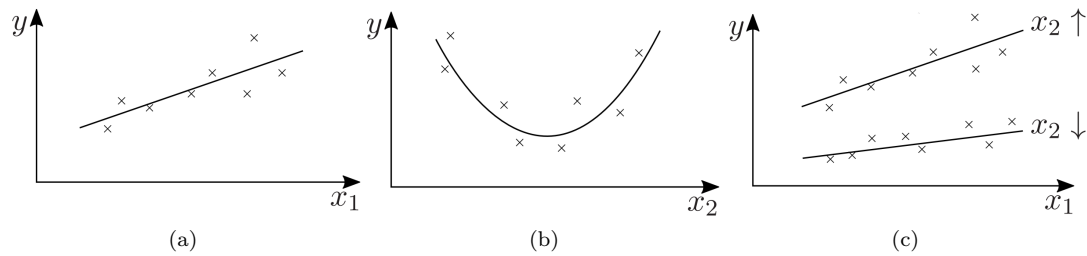


Figure 3.7: Linear effect a), quadratic effect b), and interaction c).

The relationship between a parameter x and the answer y can in many cases be described with a mathematical function. This dependence of the system response on a parameter is called *an effect*. Linear relationships between factors and response variables are called main effects, see Figure 3.7. A quadratic effect can be seen in 3.7 b). If n factors influence one another, one speaks of N^{th} order interaction. Figure 3.7 c) shows the interaction between parameters x_1 and x_2 . For a high value of x_1 , a different function curve arises than for a low value of x_2 : the parameters interact.

The determination of the main effects of many influencing factors is often more efficient, than the exact specification of a higher-order term. Research experience has shown that for the majority of physical problems, only a few interactions and nonlinear effects actually play a role.

In order to determine the answer y for a certain parameter combination, an experiment or a simulation must be carried out. In practice, it is often not useful or either possible to look for every possible parameter combination due to the great computational effort involved. Statistical test planning is therefore used for efficient planning and evaluation of test series, more commonly known as Design of Experiments (or DoE).

A statistical test plan tries to determine the relationship between input parameters x and output parameters y as precisely as possible with the smallest possible number of experiments or simulations. The input parameters of a DoE are also referred to as factors. Factors have at least two levels. The number of levels describes how many different values each parameter x can assume. For a three-level design, each factor x takes three values and one gets three response values for y . With such a test plan, quadratic effects can be mapped, whereas mapping of high-order effects requires more levels, which becomes more computationally expensive [5].

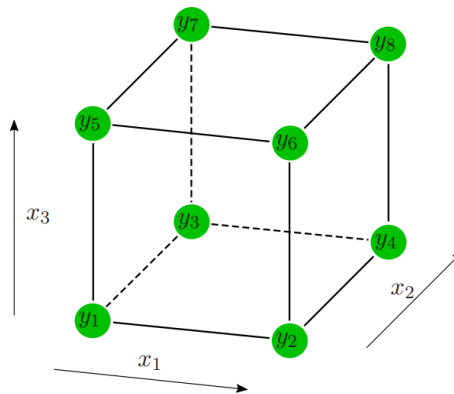


Figure 3.8: A schematic of a full-factorial design with three factors and two levels each.

Figure 3.8 displays a full-factorial design of three parameters. Each parameter in this design has two levels, i.e. it takes on two different values, the minimum value (-) and the maximum value (+) of the selected interval. This plan is sufficient to determine the main effects of the three parameters. The green points represent the support points of the test plan, i.e. the points at which the output parameter y is determined for a parameter combination x_1, x_2, x_3 .

In a statistical test plan, several factors are strategically varied at the same time. The structure of the test plans enables the effects to be clearly assigned to the input parameters despite simultaneous variation. Standardized experimental plans are Orthogonal and Balanced. Orthogonal means that no combination of two columns correlates with one another. Balanced means that the factor levels of any factor and the settings of the other factors are evenly divided [5].

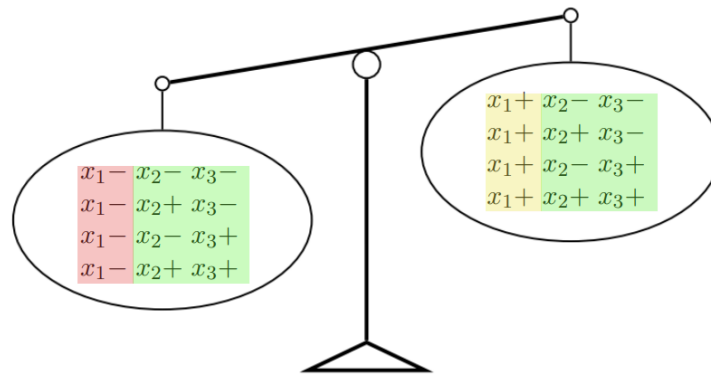
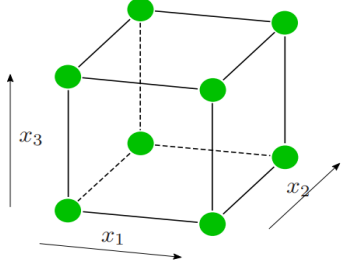
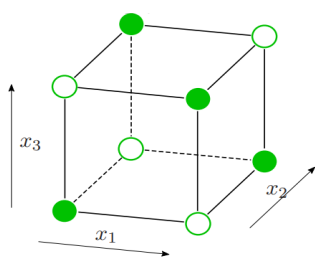


Figure 3.9: Illustrative representation of the effects of factor x_1 .

Figure 3.9 shows that even a small effect of x_1 can easily be determined by balancing the remaining factors x_2 and x_3 . [5] Despite the simultaneous variation of all factors, the green block on the right is the same on both sides of the scale. Hence, the difference between the red and yellow blocks corresponds to the effect of x_1 .

The concept of design screening is well put by Allen [2], according to whom screening is a process that begins with an extensive list of potentially influential factors and ends with a smaller list of factors. Once this process is finished, the remaining factors are likely to have a large effect on the mean response. Screening is useful at the beginning of an examination in order to reduce the number of factors considered and to make follow-up examinations more efficient. In most cases it is based on a partial factorial design. A partial factorial test plan is a reduced, full factorial plan in which individual support points are not

Table 3.1: Brief comparison of full-factorial and partial-factorial designs

Full-factorial design	Partial-factorial design
	
100% effort All main effects All interactions	50% effort Main effects superimposed with interactions

calculated in order to reduce the simulation effort.

In a full factorial test plan, measured values are recorded for all possible combinations of the factor levels. With n_s levels and k factors, n attempts are required:

$$n = n_s^k \quad (3.16)$$

Since the number of tests required increases sharply with the number of factors examined, factorial test plans are often used in screening. The effort of the partial factorial test plan shown in Table 3.1 is half of the full factorial test effort. In the fully factorial test plan shown, all main and interaction effects of the three factors are mapped with eight tests. In this case, these are the main effects of the factors x_1 , x_2 and x_3 , the interactions of the second degree between the factors $x_1 \cdot x_2$, $x_1 \cdot x_3$ and $x_2 \cdot x_3$ as well as the triple interaction $x_1 \cdot x_2 \cdot x_3$. For the partial factorial design, only 50% of the tests are required compared to the full factorial design, i.e. four tests. However, the main effects are overlaid with specific interaction effects. With the reduced effort involved in the experiment, there is also a loss of information. In a test plan with three factors and four tests, the following effects can no longer be separated:

- Main effect of x_1 , and interaction of $x_2 \cdot x_3$;
- Main effect of x_2 , and interaction of $x_1 \cdot x_3$;
- Main effect of x_3 , and interaction of $x_1 \cdot x_2$.

In other words, it is not possible to differentiate between main effects and interaction effects of the second degree. Assuming low interaction effects, the main effects of individual parameters can nevertheless be estimated with a small number of tests [5]

The field of DoE expands further into so-called meta-models. The concept will only be briefly explained, but for a detailed read, one can refer to [107] and [2]. Meta-models are used for an analytical calculation of the response variable over the design space based on the results of the DoE. It thereby, allows for quick and easy optimization without the necessity of running further simulations. They present suitability in cases where the relationship between factors and response variable needs to be determined precisely and when a subsequent optimization ought to be performed. Some meta-models include Central Composite, Box Behnken, Latin hypercube, Optimal Space Filling and others.

Chapter 4

Numerical Methodology

The purpose of this section is to introduce the reader to governing equations used within the STAR-CCM+ solver, starting from the mathematical formulation of the conjugate heat transfer methodology, explaining into further details the available convective heat transfer coefficients, which will be later used for the purpose of conducting a comprehensive comparison between the decoupled and conjugate approach, and finishing off by describing common flow modelling models and wall treatment methods in turbulent flows.

4.1 Numerics of conjugate heat transfer

Before introducing the numerical procedure followed in the commercial software package, first a coherent explanation of the mathematical formulation of conjugate heat transfer is presented.

The three fundamental conservation laws governing the physics of fluids are conservation of mass (continuity equation), conservation of momentum (aka the Navier-Stokes equations), and conservation of energy. If Ω_f is a fluid domain with a boundary $\partial\Omega_f$, then the three laws can be equated in the differential form as:

$$\frac{\partial \rho_f}{\partial t} + \nabla \cdot (\rho_f \vec{v}) = 0 \quad (4.1a)$$

$$\frac{\partial \rho_f \vec{v}}{\partial t} + \nabla \cdot (\rho_f \vec{v} \otimes \vec{v}) = -\nabla p + \rho_f \vec{f} + \nabla \cdot \tau \quad (4.1b)$$

$$\frac{\partial \rho_f E}{\partial t} + \nabla \cdot (\rho_f H \vec{v}) = \rho_f \vec{f} \cdot \vec{v} + \nabla \cdot (\tau \cdot \vec{v}) - \nabla \cdot (\lambda_f \nabla T_f) \quad (4.1c)$$

in which, on the left hand side of the equations stands the density of the fluid, denoted ρ_f , the time t , the velocity vector \vec{v} , comprised of the scalars v_x , v_y , and v_z , respectively, the pressure term p , the total enthalpy and total energy, H and E , respectively. On the right hand side are the the body force vector representing the combined body forces of rotation and gravity \vec{f} , the viscous stress tensor τ can mathematically expressed as:

$$\tau = \mu \left[(\nabla \vec{v} + \nabla \vec{v}^T) - \frac{2}{3} \nabla \cdot \vec{v} \mathbf{I} \right], \quad (4.2)$$

also, the thermal conductivity of the fluid λ_f , and the temperature T_f . The energy term is defined as:

$$E = H - p/\rho, \quad (4.3)$$

where

$$H = \int_{T_{ref}}^T C_p dT + |\vec{v}|^2. \quad (4.4)$$

Based on the schematic shown in Figure 4.1, the contacts (boundaries) where the respective boundary conditions are applied are defined such that $\Gamma_1 \cap \Gamma_2 = \emptyset$, and the fluid boundary not in contact with the solid boundary (i.e. $\partial\Omega_f \setminus \partial\Omega_s$) is equal to $\Gamma_1 \cup \Gamma_2$, which leads to boundary conditions or Dirichlet and Neumann type, applied to $\partial\Omega_f \setminus \partial\Omega_s$:

$$\begin{cases} T_f = f_1 & \text{on } \Gamma_1 \\ \lambda_f \cdot \frac{\partial T_f}{\partial n} = f_2 & \text{on } \Gamma_2 \end{cases} \quad (4.5)$$

with f_1 being the specified temperature on the boundary, and f_2 is the heat flux on Γ_2

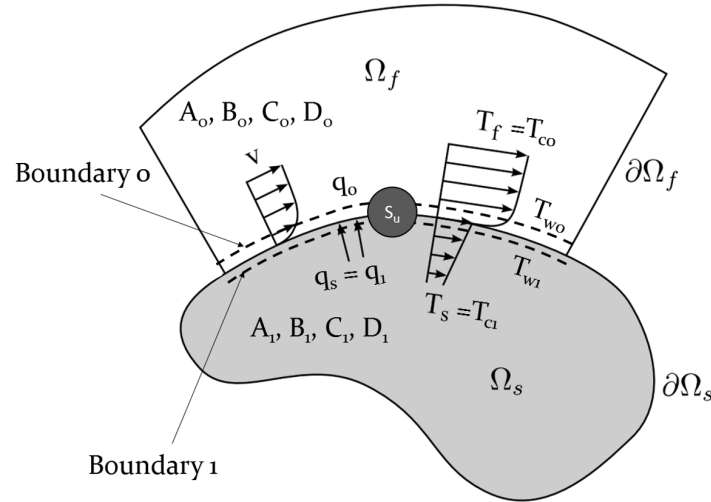


Figure 4.1: Domains and boundaries in a typical conjugate heat transfer problem

The solid region Ω_s , with the domain boundary Ω_s is described by the conservation energy equation only, which in fact simplifies to the popular heat transfer equation. If the velocity is removed along with the transient term, then:

$$\nabla (\lambda_s \nabla T_s) = 0, \quad (4.6)$$

with the thermal conductivity of the solid region λ_s . In a similar fashion, three possible boundary conditions can be applied to the boundary non in contact with the fluid domain, namely Dirichlet, Neumann or Robin, given respectively as:

$$\begin{cases} T_s = g_1 & \text{on } \Delta_1 \\ \lambda_s \cdot \frac{\partial T_s}{\partial n} = g_2 & \text{on } \Delta_2 \\ \lambda_s \cdot \frac{\partial T_s}{\partial n} = h \cdot (T_s - T_\infty) & \text{on } \Delta_3 \end{cases} \quad (4.7)$$

where similarly $\partial\Omega_s \setminus \partial\Omega_f = \Delta_1 \cup \Delta_2 \cup \Delta_3$. The heat transfer coefficient of the fluid is given as h , the ambient temperature T_∞ , specified temperature g_1 and heat flux g_2 on the boundaries Δ_1 and Δ_2 .

Finally, the boundary condition on the boundary where $\partial\Omega_s$ intersects with Ω_f , namely $\partial\Omega_w = \partial\Omega_f \cap \partial\Omega_s$. Thus, two boundary conditions are set: temperature and flux continuity:

$$\text{on } \partial\Omega_w : \begin{cases} T_f = T_s \\ \lambda_f \cdot \frac{\partial T_f}{\partial n} = -\lambda_s \cdot \frac{\partial T_s}{\partial n} \end{cases} \quad (4.8)$$

which finalizes the definition of the mathematical form of conjugate heat transfer, together with the boundary conditions for the momentum conservation on the fluid region.

Now that it has been established that the heat flux is conserved at the interface, one can define two additional boundaries adjacent to Ω_s and write

$$\dot{q}_0 + \dot{q}_1 = -S_u \quad (4.9)$$

where \dot{q}_0 is the heat flux from the fluid through Boundary 0, and \dot{q}_1 is the heat flux leaving through Boundary 1 into the solid (both shown in the schematic in Figure 4.1 as dashed lines, the thickness of the boundary is exaggerated for the purposes of illustration). The term used for a specified heat source is denoted with S_u . Each of the aforementioned heat fluxes is then linearised:

$$\dot{q}_0 = A_0 + B_0T_{c0} + C_0T_{w0} + D_0T_{w0}^4 \quad (4.10a)$$

$$\dot{q}_1 = A_1 + B_1T_{c1} + C_1T_{w1} + D_1T_{w1}^4 \quad (4.10b)$$

with A , B , C , and D being the linearised heat flux coefficients. The subscript c or w indicates either cell or wall value at the respective boundary number. For a single phase flow problem the coefficients are composed of internally pre-calculated and manually specified coefficients (kept at 0 for all computations in this study)

$$A = A_{internal} + A_{specified} \quad (4.11a)$$

$$B = B_{internal} + B_{specified} \quad (4.11b)$$

$$C = C_{internal} + C_{specified} \quad (4.11c)$$

The internal coefficients are evaluated in accordance to the physical processes undergoing in the system. They are found using the equation for the diffusion flux at an interior cell face:

$$k\nabla T = k[\nabla T_c - (\nabla T_c \cdot \mathbf{ds}) \vec{\alpha}] - k\vec{\alpha}T_c + k\vec{\alpha}T_w + 0T_w^4. \quad (4.12)$$

The discretization of the diffusion flux and the derivation of Eq.4.12 is omitted here, but a full derivation and more detailed explanation of the finite volume method could be found in the Appendix. where

$$\vec{\alpha} = \frac{\mathbf{a}}{\mathbf{a} \cdot \mathbf{ds}}, \quad (4.13a)$$

$$\mathbf{ds} = \mathbf{x}_f - \mathbf{x}_0. \quad (4.13b)$$

The surface area vector of the respective cell is denoted with \mathbf{a} and the vectors \mathbf{x}_f and \mathbf{x}_0 are used to indicate the face vector and cell centroid vector from the coordinate frame origin, respectively.

$$A_{internal} = k[\nabla T_c - (\nabla T_c \cdot \mathbf{ds}) \vec{\alpha}] \quad (4.13c)$$

$$B_{internal} = -k\vec{\alpha} \quad (4.13d)$$

$$C_{internal} = k\vec{\alpha} \quad (4.13e)$$

In cases where the temperature is different across the interface (e.g. a thermal barrier coating is included without physically modelling the coating), an interface thermal resistance is set:

$$\dot{q}_0 = -\frac{S_u}{2} + \frac{T_{w1} - T_{w0}}{R}, \quad (4.14)$$

where the denominator in the second term on the right hand side of the equation is the resistance (K/W). The last term in Eq.4.12 representing radiation is set intentionally to zero for the purposes of this explanation. Finally, the set of equations (4.9)-(4.10b) and (4.14) are solved for the four unknowns either analytically or numerically. If the radiation term is included, STAR-CCM+ performs a numerical calculation. If not, a linear system of equations is obtained and solved.

4.2 Reynolds-Averaged Navier-Stokes Modelling

In the present work, Reynolds-Averaged Navier Stokes (RANS) models are compared. The concept of Reynolds-Averaging comes from replacing the standard solution variables, ϕ , by a mean (averaged) component and a fluctuation part

$$\phi = \bar{\phi} + \phi' \quad (4.15)$$

Upon substitution in Eq. 4.1b and in Eq. 4.1c, new terms are obtained, namely the Reynolds Stress term:

$$\boldsymbol{\tau} = - \begin{pmatrix} \overline{u'u'} & \overline{u'v'} & \overline{u'w'} \\ \overline{u'v'} & \overline{v'v'} & \overline{v'w'} \\ \overline{u'w'} & \overline{v'w'} & \overline{w'w'} \end{pmatrix} \quad (4.16)$$

These new unknown quantities pose the challenge of the *closure model*, which is a fundamental part of the theoretical description of turbulence, i.e. requiring another relationship to solve the problem. RANS models are one approach to close the two terms and are based on the Boussinesq hypothesis. In the Boussinesq hypothesis, the intrinsic assumption is made that the Reynolds stress anisotropy tensor, \mathbf{A} , is determined by the mean velocity gradients and the specific assumption is made that there is an alignment between the Reynolds stress anisotropy tensor and the mean rate-of-strain tensor \mathbf{S} , hence, the following equation should hold:

$$\mathbf{A} = \boldsymbol{\tau} + \frac{2}{3}k\mathbf{I} \approx 2\nu_t\mathbf{S} \quad (4.17)$$

$$\mathbf{S} = \frac{1}{2}(\nabla\bar{\mathbf{v}} + \nabla\bar{\mathbf{v}}^T) \quad (4.18)$$

where most importantly, ν_t is the **eddy viscosity**, and $k = \text{tr}(\boldsymbol{\tau})$ is the turbulent kinetic energy. RANS models rely on the Boussinesq hypothesis due to the fact that it gives acceptable results in simple shear flows (Pope [2000]) as these flows match the specific assumption, but also, due to the added numerical stability to the model from the Boussinesq approximation. However, it is known that in many engineering applications and flow topologies, the Boussinesq assumption does not work for specific flow regions. The RANS model used in this study are briefly explained in the upcoming sections below.

4.2.1 Standard $k - \varepsilon$ model

The RANS models used in the project, employ the two-equation approach, i.e. two additional differential equations are solved for the transport of turbulence quantities, namely the turbulent kinetic energy k and turbulent dissipation η . The formulation of the standard $k - \varepsilon$ model, implemented in the CFD code is the one by Jones and Launder [55], which for k and ε respectively reads:

$$\frac{Dk}{Dt} = \frac{\partial k}{\partial t} + \nabla \cdot (k\bar{\mathbf{v}}) = \nabla \cdot \left[\left(\nu + \frac{\nu_t}{\sigma_k} \right) \nabla k \right] + P_k - (\varepsilon - \varepsilon_0) + S_k \quad (4.19)$$

$$\frac{D\varepsilon}{Dt} = \frac{\partial \varepsilon}{\partial t} + \nabla \cdot (\varepsilon\bar{\mathbf{v}}) = \nabla \cdot \left[\left(\nu + \frac{\nu_t}{\sigma_\varepsilon} \right) \nabla \varepsilon \right] + \frac{1}{T_e} C_{\varepsilon 1} P_\varepsilon - C_{\varepsilon 2} \left(\frac{\varepsilon}{T_e} - \frac{\varepsilon_0}{T_0} \right) + S_\varepsilon \quad (4.20)$$

where S is a manually specified source term for both equations, $T_e = k/\varepsilon$ is the large-eddy time scale, and P_k is the turbulence source term, comprised of turbulent and buoyancy production terms:

$$P_k = \nu_t \mathcal{S}^2 - \frac{2}{3}k(\nabla \cdot \bar{\mathbf{v}}) - \frac{2}{3}\nu_t(\nabla \cdot \bar{\mathbf{v}})^2 + \beta \frac{\nu_t}{Pr_t} (\nabla \bar{T} \cdot \mathbf{g}) \quad (4.21)$$

$$P_\varepsilon = \nu_t \mathcal{S}^2 - \frac{2}{3}k(\nabla \cdot \bar{\mathbf{v}}) - \frac{2}{3}\nu_t(\nabla \cdot \bar{\mathbf{v}})^2 + C_{\varepsilon 3} \beta \frac{\nu_t}{Pr_t} (\nabla \bar{T} \cdot \mathbf{g}) \quad (4.22)$$

with \mathcal{S} being the modulus of the mean rate-of-strain tensor, $\mathcal{S} = |\mathbf{S}| = \sqrt{2\mathbf{S} : \mathbf{S}^T} = \sqrt{2\mathbf{S} : \mathbf{S}}$. Following the Boussinesq approximation, the turbulent viscosity term is approximated with:

$$\nu_t = \rho C_\mu \frac{k^2}{\varepsilon} \quad (4.23)$$

Table 4.1: Model coefficients used in the standard formulation of the $k - \varepsilon$ model, according to Launder and Sharma [70]

C_μ	σ_k	σ_ε	$C_{\varepsilon 1}$	$C_{\varepsilon 2}$	$C_{\varepsilon 3}$
0.09	1.00	1.30	1.44	1.92	$\tanh \frac{ \mathbf{v}_b }{ \mathbf{u}_b }$

If compressibility is included in the analysis, the code includes an additional production term, $Y_m = -\frac{C_m k \varepsilon}{c^2}$, with c being the speed of sound and C_m is an additional model coefficient.

4.2.2 Realizable $k - \varepsilon$ model

The Realizable formulation of the $k - \varepsilon$ model contains a new transport equation for the turbulent dissipation rate. Also, a variable damping function f_μ expressed as a function of mean flow and turbulence properties is applied to C_μ , and a second damping function f_2 to $C_{\varepsilon 2}$. This procedure lets the model satisfy certain mathematical constraints on the normal stresses consistent with the physics of turbulence (realizability). This concept of a damped C_μ is also consistent with experimental observations in boundary layers.

The difference with the standard formulation is also expressed in the production term P_k and P_ε by the adoption of the curvature correction function f_c , and also the damping functions f_2 and f_μ such that

$$P_k = f_c \left(\nu_t \mathcal{S}^2 - \frac{2}{3} k (\nabla \cdot \bar{\mathbf{v}}) - \frac{2}{3} \nu_t (\nabla \cdot \bar{\mathbf{v}})^2 \right) + \beta \frac{\nu_t}{Pr_t} (\nabla \bar{T} \cdot \mathbf{g}) \quad (4.24)$$

$$P_\varepsilon = f_c \mathcal{S} k + C_{\varepsilon 3} \beta \frac{\nu_t}{Pr_t} (\nabla \bar{T} \cdot \mathbf{g}) \quad (4.25)$$

$$f_c = \min \left(C_{\max}, \frac{1}{C_{r1} (|\eta| - \eta) + \sqrt{1 - \min(C_{r2}, 0.99)}} \right) \quad (4.26)$$

$$\eta = \left(\frac{\varepsilon}{k} \right)^2 (\mathbf{S} : \mathbf{S} - \mathbf{W} : \mathbf{W}) \quad (4.27)$$

where \mathbf{W} is the mean vorticity tensor, $\mathbf{W} = \frac{1}{2} (\nabla \bar{\mathbf{v}} - \nabla \bar{\mathbf{v}}^T)$.

The damping functions in the turbulent transport equations read

$$f_2 = \frac{k}{k + \sqrt{\nu \varepsilon}}, \quad (4.28)$$

and

$$f_\mu = \frac{1}{C_\mu \left\{ 4 + \sqrt{6} \cos \left[\frac{1}{3} \cos^{-1} \left(\sqrt{6} \frac{\mathbf{S}^*}{\sqrt{\mathbf{S}^* : \mathbf{S}^*}} \right) \right] \frac{k}{\varepsilon} \sqrt{\mathbf{S} : \mathbf{S} + \mathbf{W} : \mathbf{W}} \right\}}, \quad (4.29)$$

with $\mathbf{S}^* = \mathbf{S} - \frac{1}{3} \text{tr}(\mathbf{S}) \mathbf{I}$, applied to

$$\nu_t = \rho f_\mu C_\mu \frac{k^2}{\varepsilon}. \quad (4.30)$$

The constants used are equal to the default values presented in the standard formulation of the model, with the additional coefficients tabulated below. This model is substantially better than the Standard $k - \varepsilon$ model for many applications, and can generally be relied upon to give answers that are at least as accurate. Both the standard and realizable models are available in STAR-CCM+ with the option of using a two-layer approach, which enables them to be used with fine meshes that resolve the viscous sublayer, which is explained in more detail in Section 4.4

Table 4.2: Model coefficients used in the realizable formulation of the $k - \varepsilon$ model

$C_{\varepsilon 1}$	$C_{\varepsilon 2}$	σ_{ε}	C_{r1}	C_{r2}
$\max(0.43, \frac{\eta}{\eta+5})$	1.9	1.2	0.05	0.25

4.2.3 SST $k - \omega$ model

Another two-equation model is based on the *specific* rate of dissipation, ω , instead of the turbulent dissipation rate, ε , which is sometimes referred to as the mean frequency of the turbulence ($\omega \propto \frac{\varepsilon}{k}$). In general, the kinetic energy and specific turbulent dissipation can be written in the form

$$\frac{Dk}{Dt} = \nabla \cdot [(\nu + \sigma_k \nu_t) \nabla k] + P_k - \beta^* f_{\beta^*} (\omega k - \omega_0 k_0) + S_k \quad (4.31)$$

$$\frac{D\omega}{Dt} = \nabla \cdot [(\nu + \sigma_{\omega} \nu_t) \nabla \omega] + P_{\omega} - \beta f_{\beta} (\omega^2 - \omega_0^2) + S_{\omega} \quad (4.32)$$

The modification factors in the dissipation terms, f_{β^*} and f_{β} , are the free-shear modification factor and vortex-stretching modification factors, further discussed in the Appendix. The so-called shear-stress transport (SST) formulation adds an additional non-conservative cross-diffusion term $\nabla k \cdot \nabla \omega$, as shown in the production term of ω . The addition of this term is triggered by a blending function F_1 , which acts as a trigger for the cross-diffusion term far from the walls but not near the wall. The blending functions F_1 and F_2 (blending function in the formulation of the turbulent viscosity shown in Eq.(4.34)) are given in the Appendix, along with the corresponding auxiliary relations necessary for their definition. The turbulent kinetic energy production is identical to the $k - \varepsilon$ model, whereas the production term of the specific dissipation rate is given as:

$$P_{\omega} = \gamma \left[\left(S^2 - \frac{2}{3} (\nabla \cdot \bar{\mathbf{v}})^2 \right) - \frac{2}{3} \omega \nabla \cdot \bar{\mathbf{v}} \right] + 2(1 - F_1) \sigma_{\omega 2} \frac{1}{\omega} \nabla k \cdot \nabla \omega \quad (4.33)$$

The kinematic eddy viscosity is then calculated as:

$$\nu_T = k \min \left(\frac{\alpha^*}{\omega}, \frac{a_1}{S F_2} \right) \quad (4.34)$$

The model coefficients used are the default ones, shown in the table below.

Table 4.3: Model coefficients used in the SST $k - \omega$ model

α_1	α^*	β^*	C_t	β_1	β_2	σ_{k1}	$\sigma_{\omega 1}$	σ_{k2}	$\sigma_{\omega 2}$
0.31	1	0.09	0.6	0.075	0.0828	0.85	0.5	1	0.856

4.3 Calculation of heat transfer coefficients

Several heat transfer coefficients are available within the code, all shown in Eq.(4.40)-(4.39). These include:

1. Heat transfer coefficient
2. Virtual local heat transfer coefficient
3. Local heat transfer coefficient
4. Specified y^+ heat transfer coefficient

For turbulent flows, the heat flux vector coming from the RANS equations is analogously calculated using the Boussinesq approximation as shown below.

$$\bar{\mathbf{q}} = - \left(\lambda_f + \frac{\mu_t C_p}{Pr_t} \right) \nabla \bar{T} \quad (4.35)$$

The **wall** local value of the heat flux scalar is computed using the relevant scalars at the wall, such as:

$$q_w = |\mathbf{q}_w| = \rho_f c_{p,f} u_\tau \frac{T_w - \bar{T}_c}{\bar{T}_c^+} \quad (4.36)$$

The u_* represents the velocity scale, which is calculated in accordance to the wall treatment method chosen, as explained in the next section. This also holds for the RANS-averaged cell temperature \bar{T}_c^+ . The wall friction velocity is calculated using the non-dimensional tangential velocity component of the velocity vector and the RANS averaged tangential velocity vector such that:

$$u_\tau = \frac{u_*}{u^+} |\bar{\mathbf{v}}_{\text{tangential}}| \quad (4.37)$$

with

$$\mathbf{v}_{\text{tangential}} = (\mathbf{v}_c - \mathbf{v}_w) - [(\mathbf{v}_c - \mathbf{v}_w) \cdot \mathbf{n}] \mathbf{n} \quad (4.38)$$

where subscript c indicates cell centroid value, \mathbf{v}_w is the velocity at the wall (e.g. zero for no slip stationary wall) and \mathbf{n} is the wall-normal vector. The value of u^+ is also found using wall functions (see next section on wall functions).

The first and most fundamental heat transfer calculation approach calculates the surface heat flux using Eq.(4.41) with $T_{ref} = \bar{T}_c$, and then recasts for the heat transfer coefficient term such as:

$$h_{bulk} = \frac{q_w}{T_w - T_{ref,h}} \quad (4.39)$$

The heat transfer coefficient is calculated using a preselected reference temperature $T_{ref,h}$. Therefore, it is worthwhile noting that this approach does not guarantee a positive value for the heat transfer coefficient (i.e. negative for regions where the specified temperature is higher than the local wall temperature).

All other turbulent heat transfer coefficients mentioned earlier stem from the standard wall functions (SWF). The second option is calculated without solving the energy equation in the fluid. Instead, only flow information is used such that:

$$h_{virtual} = \frac{\rho_f(y_c) c_{p,spec} u_*}{\bar{T}_c^+(y^+(y_c))} \quad (4.40)$$

The value of \bar{T}_c^+ is calculated using SWF. Since thermal material properties using this approach are not available, a reference value for the specific heat $c_{p,spec}$ is specified, along with the molecular Prandtl number Pr and the specified turbulent Prandtl number $Pr_{t,spec}$. The necessity for such large number of specified values makes this approach more ambiguous than the ones to follow. The wall surface heat flux in Eq. 4.36 can be rewritten in the typical form of Newton's cooling law:

$$q_w = h_{local} \cdot (T_w - T_{ref}) \quad (4.41)$$

The local heat transfer coefficient is hence always calculated and used internally in the code using SWF, and $T_{ref} = \bar{T}_c$ from Eq. 4.41 above.

$$h_{local} = \frac{\rho_f(y_c) c_{p,f}(y_c) u_\tau}{\bar{T}_c^+(y^+(y_c))} \quad (4.42)$$

A similar alternative option is the specified y^+ heat transfer coefficient, which is the HTC usually used in the decoupled approach, since it allows to be exported to external codes. This is also the HTC used in the decoupled approach for the turbulent offset jet (using a $y^+ = 10$). It is defined as:

$$h_{y^+} = \frac{\rho_f(y_c)c_{p,f}(y_c)u_\tau}{\overline{T}_c^+(y_{spec}^+)}. \quad (4.43)$$

The value is calculated at a explicitly specified value for y^+ , which then allows for finding the reference temperature T_{ref,y^+} by using the value for the local heat flux and solving Newton's law for cooling for T_{ref} :

$$T_{ref,y^+} = T_w - \frac{q_w}{h_{y^+}} \quad (4.44)$$

This definition of the reference temperature does not guarantee that it lies within the minimum and maximum temperature range of the local fluid region. If T_{ref,y^+} lies outside this temperature range, then either the minimum or maximum temperature is used in its place, and the heat transfer coefficient is recalculated accordingly.

A brief comprehensive comparison of the main differences of all four HTC approaches is given in Table 4.4.

Table 4.4: Summary of available heat transfer coefficients.

HTC Approach	Definition	Reference temperature	Comment
Virtual local HTC	$h_{virtual} = \frac{\rho_f(y_c)c_{p,spec}u_*}{\overline{T}_c^+(y^+(y_c))}$	Reference Pr , Pr_t , and c_p values are specified manually	Does not require energy model to be activated; can be used as an approximation of the Local HTC
Local HTC	$h_{local} = \frac{\rho_f(y_c)c_{p,f}(y_c)u_\tau}{\overline{T}_c^+(y^+(y_c))}$	$T_{local} = T_w + \frac{q_w}{h_{local}}$	Evaluated at the centroid of the cell next to the boundary, that is $h(y = y_c)$
Specified y^+ HTC	$h_{y^+} = \frac{\rho_f(y_c)c_{p,f}(y_c)u_\tau}{\overline{T}_c^+(y_{spec}^+)}$	$T_{y_{ref}^+} = T_w + \frac{q_w}{h_{y^+}}$	Evaluated at a custom-specified value of y^+
HTC	$h_{bulk} = \frac{q_w}{T_w - T_{ref,h}}$	Manually specified on a rather empirical basis	Does not guarantee a positive HTC value, choice of reference temperature is somewhat uncertain

4.4 Wall treatment functions

The importance of the boundary layer on the heat transfer characteristics of the flow has been well-established throughout the years, particularly in the vicinity of the viscosity-affected region (viscous sublayer and buffer layer, see Figure 4.2). Therefore, an accurate prediction of the flow across the boundary layer is essential, particularly for conjugate heat transfer problems.

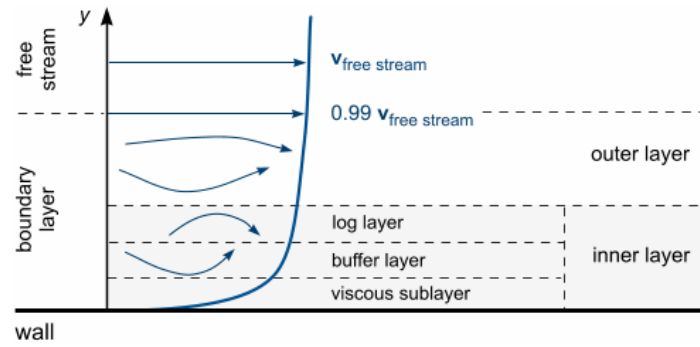


Figure 4.2: Typical velocity profile of a turbulent boundary layer

Wall functions provide an algebraically approximated value for main flow field quantities. The following functions can be hence attributed:

1. Calculation of the wall shear stress (according to $\tau_w = \rho u_\tau^2 \frac{\overline{v}_{\text{tangential}}}{|\overline{v}_{\text{tangential}}|}$)
2. Calculation of the wall heat flux (as in eq.(4.41))
3. Imposition of values for non-dimensional turbulence quantities (ε^+ or ω^+ , and P_k^+) on the centroids of the near-wall cells. Note that no wall treatment is available for the turbulent kinetic energy term k^+ as it is strongly dependent on the Reynolds number of the flow. The definition is given as $k^+ = \frac{k}{u_\tau^2}$, and k is calculated from the initial conditions at the boundaries.

The following three approaches are used in this thesis for the investigation of the conjugation effects in turbulent flow: (i) High- y^+ treatment, (ii) All- y^+ treatment, and (iii) Two-layer all- y^+ . Within the code used, the Two-layer all- y^+ treatment, which is available for the two-layer turbulence models, uses an approach that is identical to the all-wall treatment. However, specific values of turbulence dissipation rate are imposed at the centroids of the near-wall cells to make it consistent with the two-layer formulation of the underlying turbulence model. The high- y^+ approach relies on the assumption that the near-wall cell lies within the log layer of the boundary layer, compared to the all- y^+ treatment which provides a blending function, evaluating the field quantity depending on the region inside the inner layer (thus blending the viscous sublayer and the log layers).

It should be noted that, however, not all wall treatments are available with every RANS model or model variant. High Reynolds number models do not contain the ability to attenuate the turbulence in the viscosity-affected regions and therefore only include a high- y^+ wall treatment. Low Reynolds number models are offered only with a low- y^+ wall treatment and an all- y^+ wall treatment. The two-layer all- y^+ wall treatment is only available with the two-layer $k - \varepsilon$ model.

Two key non-dimensional variables are used, commonly referred to as *wall units*, namely the non-dimensional wall-tangential velocity and the non-dimensional wall distance:

$$y^+ = \frac{y u_*}{\nu} \quad (4.45)$$

$$u^+ = \frac{\bar{u}}{u_*} \quad (4.46)$$

Each respective wall treatment approach proposes a formulation for five non-dimensional variables: velocity, temperature, turbulent dissipation, turbulent kinetic energy, and production of turbulent kinetic energy. The respective functions used for the High y^+ approach read:

$$u_* = c_\mu^{1/4} k^{1/2} \quad (4.47)$$

$$u^+ = \frac{1}{\kappa} \ln(E' y^+) \quad (4.48)$$

where

$$E' = \frac{E}{f} \quad (4.49)$$

with $E = 9$ being the log law offset, f is the roughness function, and $\kappa = 0.42$ is the von Kármán constant. CFD roughness is an important parameter which is touched upon in the TP cooling analysis due to the AM-related constraints of the cooling channels. The full formulation is given in the appendix as well. The function for temperature similarly reads, with an additional term P :

$$T^+ = \text{Pr} \left[\frac{1}{\kappa} \ln(E' y^+) + P \right] \quad (4.50)$$

with the function P governing the velocity at which the log layer and the viscous sub-layer of the thermal profiles intersect [53]:

$$P = 9.24 \left[\left(\frac{\text{Pr}}{\text{Pr}_t} \right)^{3/4} - 1 \right] 1 + 0.28 \exp \left(-0.007 \frac{\text{Pr}}{\text{Pr}_t} \right) \quad (4.51)$$

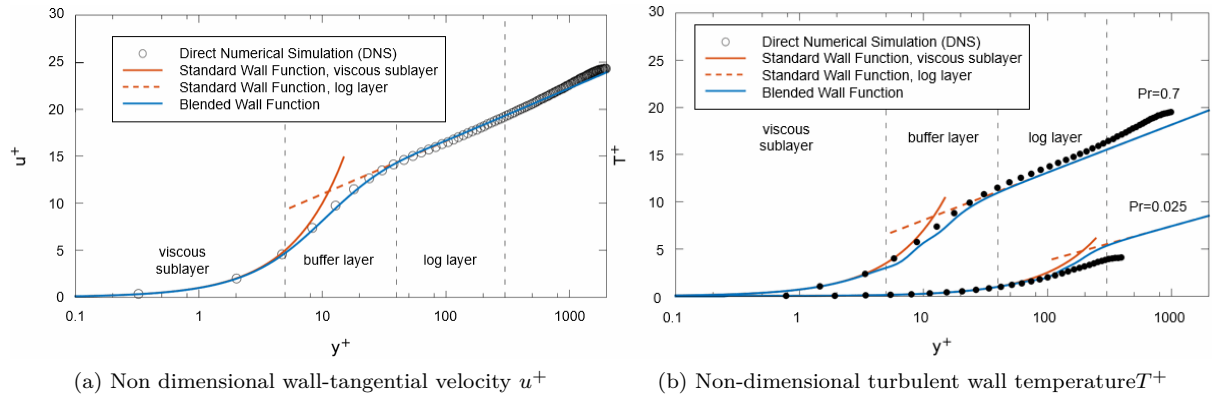


Figure 4.3: Velocity (a) and temperature (b) as a function of non dimensional wall distance displaying wall treatment for viscous sub-layer, log layer, and the blending approach covering the buffer layer

$$u^+ = \frac{1}{\kappa} \ln(1 + \kappa y^+) + C \left(1 - e^{-y^+/y_m^+} - \frac{y^+}{y_m^+} e^{-by^+} \right) \quad (4.52)$$

$$C = \frac{1}{\kappa} \ln \left(\frac{E'}{\kappa} \right), \quad b = 0.5 \left(y_m^+ \frac{\kappa}{C} + \frac{1}{y_m^+} \right) \quad (4.53)$$

$$y_m^+ = \max [3, 267(2.64 - 3.9\kappa)E^{0.0125}] - 0.987 \quad (4.54)$$

The temperature wall function is based on Kader's law [58]:

$$T^+ = \exp(-\Gamma) \text{Pr} y^+ + \exp \left(-\frac{1}{\Gamma} \right) \text{Pr}_t \left[\frac{1}{\kappa} \ln(E y^+) + P \right] \quad (4.55)$$

$$\Gamma = \frac{0.01c (\text{Pr} y^+)^4}{1 + \frac{5}{c} \text{Pr}^3 y^+} \quad (4.56)$$

$$c = \exp(f - 1) \quad (4.57)$$

The velocity scale needed for the shear stress calculation reads

$$u_* = \gamma \frac{\mu |\mathbf{v}_{\text{tangential}}|}{\rho y} + (1 - \gamma) C_\mu^{1/4} k^{1/2} \quad (4.58)$$

with

$$\gamma = \exp\left(-\frac{Re_d}{11}\right) \quad (4.59)$$

$$Re_d = \frac{\sqrt{k}y}{\nu}. \quad (4.60)$$

Table 4.5: Wall functions for both approaches for turbulence parameters required by the RANS model

Parameter	High y^+	Blended approach
Turbulent dissipation, ε^+	$\frac{1}{\kappa y^+}$	$\gamma \frac{2k^+}{(y^+)^2} + (1 - \gamma) \frac{1}{\kappa y^+}$
Specific turbulent dissipation, ω^+	$\omega^+ = \frac{1}{\sqrt{\beta^* \kappa y^+}}$	$\sqrt{\frac{6}{\beta_1 (y^+)^2} + \frac{1}{\beta^* \kappa y^+}}$
Production of TKE, P_k^+	$\frac{1}{\kappa y^+}$	$P_k^+ = \gamma \left(\mu_t^+ \frac{\partial u^+}{\partial y^+} \right) + (1 - \gamma) \frac{1}{\kappa y^+}$

Both high- y^+ and blended wall functions for velocity and temperature are illustrated in Fig.4.3. The dashed lines are used to indicate the log-layer, i.e. modelling for $y^+ \gtrsim 30$ (high- y^+ function). The respective functions for the turbulence variables are tabulated above in Table4.5.

Part I

Canonical cases

Chapter 5

Numerical validation cases

The computational code used in this projects needs to be compared with analytical solutions or experimental data to test its validity and add to its credibility before embarking onto the optimization case. Thereby, the physical modelling errors are quantified and carried over. Such errors may come from simplifications in the mathematical model of the physical problem, assumptions in the analytical solutions, or uncertainties in the experimental procedure. Hence, an ample evaluation of the program accuracy is imperative prior to carrying out predictive simulations.

The chapter also includes the numerical comparison between the decoupled and conjugate heat transfer approach, with the use of two types of boundary conditions on the wall for the decoupled approach, specific to the flow case considered.

5.1 Laminar flat plate

As previously mentioned in literature, the problem of the conjugate heat transfer of flows over flat plates, in particular, flows exhibiting laminar characteristics, presents a good suitability for solver validation purposes due to the existence of analytical solutions presented in literature.

Hence, the direct applicability and accuracy of numerical methods for conjugate heat transfer is tested against solutions, the boundary conditions of which most often include isothermal or adiabatic wall conditions, and often a variety of simplifications around the velocity and temperature fields (as shown later). In this study, the chosen analytical solution is given by Luikov [81] and is presented broadly in the upcoming section, proceeded by the results and discussion.

5.1.1 Analytical solution

The analytical solution proposed by Luikov [81] comprises of two separate approaches:

- The direct solution of the partial differential heat transfer equation;
- The solution of the laminar boundary-layer equations, both applied in two dimensions (x-y).

For both cases the boundary conditions include a solid plate with a constant temperature of the bottom surface set to T_b , and a free-stream of perfectly uniform temperature $T_a = T_\infty$ and velocity u_a , both imposed at the domain inlet ($x = 0, y \in [0, \infty]$) and far field ($x \in [0, \infty], y = \infty$). It is also worthwhile mentioning that the plate has a length l , which considerably higher than its thickness b . This allows for the temperature profile within the plate region to be assumed linear (for small values of b). The governing equations and their respective (shortened where deemed adequate) derivations are presented below. The notations that are used in this chapter are also illustrated in Fig. 5.1 below.

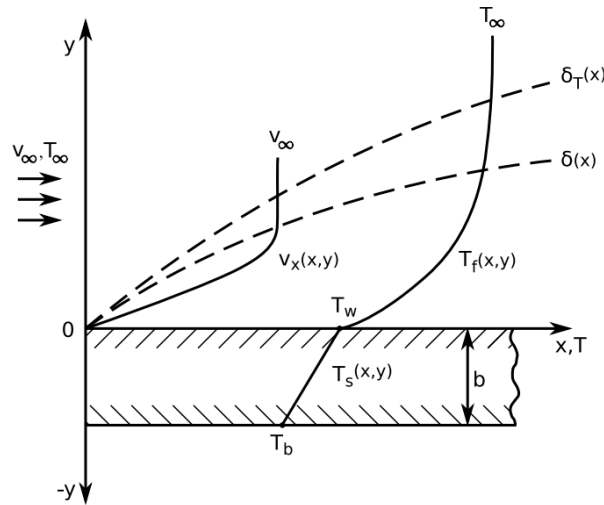


Figure 5.1: Schematic of boundary conditions and respective notation used for the analytical solution of Luikov.[81]

Differential heat transfer equation (DHT) approach

For an incompressible fluid, the steady state differential heat-conduction equation in a laminar boundary layer reads:

$$v_x \frac{\partial T_f(x, y)}{\partial x} + v_y \frac{\partial T_f}{\partial y} = \alpha \frac{\partial^2 T(x, y)}{\partial y^2}. \quad (5.1)$$

The thermal diffusivity, α , is the ratio of the thermal conductivity and the product of the specific heat capacity with the density of the fluid ($k/\rho C_p$). For a full, more detailed derivation of the differential heat transfer equation, the reader can refer to [85].

The boundary conditions illustrated in Fig. 5.1, are expressed as:

$$x = 0; T_f(0, y) = T_\infty, \quad (5.2a)$$

$$y = -b; T_s(-b, x) = T_b = \text{const}, \quad (5.2b)$$

$$y = 0; -\lambda_f \frac{\partial T_f(x, 0)}{\partial y} = -\lambda_s \frac{\partial T_s(x, 0)}{\partial y}, \quad (5.2c)$$

$$T_f(x, 0) = T_s(x, 0), \quad (5.2d)$$

$$y = \infty; T_f(x, \infty) = T_\infty = \text{const}. \quad (5.2e)$$

The previously mentioned linear temperature distribution within the plate can be used from the heat interface balance:

$$-\frac{\partial T_f(x, 0)}{\partial y} + \frac{\lambda_s}{b\lambda_f} [T(x, 0) - T_b] = 0. \quad (5.3)$$

Another key assumption used by Luikov is that the local longitudinal and transverse velocities are equal to their mean values:

$$v_x = \bar{v}_x = \text{const}, \quad (5.4a)$$

$$v_y = \bar{v}_y = \text{const}. \quad (5.4b)$$

The solution of (5.1) is published in [1] and [82], and reads:

$$\begin{aligned} \frac{T(x, y) - T_b}{T_\infty - T_b} &= \frac{K - \frac{1}{2}B}{K - B} \exp \left[(K^2 - BK) \frac{\lambda_s y}{\lambda_f b} \right] \cdot \operatorname{erfc} \left(K - \frac{1}{2}B + \frac{1}{2} \frac{\lambda_s y}{\lambda_f Kb} \right) \\ &+ \frac{1}{2} \operatorname{erfc} \left(\frac{1}{2}B - \frac{1}{2} \frac{\lambda_s y}{\lambda_f Kb} \right) \\ &- \frac{1}{2} \frac{\exp[(B/K)(\lambda_s/\lambda_f)(y/b)]}{1 - (B/K)} \cdot \operatorname{erfc} \left(\frac{1}{2}B + \frac{1}{2} \frac{\lambda_s y}{\lambda_f Kb} \right). \end{aligned} \quad (5.5)$$

The constants are presented in the Appendix, along with other constants related to the boundary layer approach. and the local mean velocities in the streamwise and vertical directions in the boundary layer, respectively, are given as:

$$\bar{v}_x = 0.66v_\infty \quad (5.5a)$$

$$\bar{v}_y = 0.43v_\infty \left(\frac{xv_\infty}{\nu} \right)^{(-\frac{1}{2})} \quad (5.5b)$$

The constants of 0.66 and 0.43 are derived using the similarity solution method from the corresponding limit values of the auxiliary function $f(\zeta = (y/x)Re_x^{1/2})$, which transforms the PDE-s system into an ODE system. For more details on the analysis, one can refer to [1] (namely formula 3.1.19 and Fig. 3.3.). This is a key assumption in the process of deriving an analytical solution for (5.1) using the conditions in (5.2a)-(5.2e), and is one of the major differences between the numerical and analytical method, which is discussed later.

The quantity of the local average Reynolds number, \overline{Re}_x , is expressed using (5.5a), which yields:

$$\overline{Re}_x = \frac{x\bar{v}_x}{\nu} = 0.66 \frac{xv_\infty}{\nu} \quad (5.6)$$

and using the standard definition of the Prandtl number, Pr :

$$Pr = \frac{\mu C_p}{\lambda_f} \quad (5.7)$$

Boundary layer (BL) approach The analytical solution of heat transfer for laminar boundary layers can be regarded more as an approximation, compared to the DHT method, and begins from the integral heat transfer equation of a boundary layer:

$$\int_0^{\delta_t} (T_\infty - T_f)v_x(y)dy = \alpha \left(\frac{\partial T_f(x, 0)}{\partial y} \right) \quad (5.8)$$

Luikov uses the following assumption for the laminar boundary layer velocity distribution:

$$\frac{v_x}{v_\infty} = \frac{3y}{2\delta} - \frac{1}{2} \left(\frac{y}{\delta} \right). \quad (5.9)$$

The temperature distribution in the fluid and solid regions is assumed to have linear and cubic expressions, respectively as:

$$\theta_1 = T_f - T_b = a_1 + b_1y + c_1y^2 + d_1y^3, \quad (5.10a)$$

$$\theta_2 = T_s - T_b = a_2 + b_2y. \quad (5.10b)$$

The boundary conditions are similar to (5.2a)-(5.2e), but in the form of θ_1 and θ_2 , such that:

$$y = \delta_t, \theta_1 = \theta_\infty = (T_\infty - T_b); \frac{\partial \theta}{\partial y} = 0, \quad (5.11a)$$

$$y = 0, \theta_1 = \theta_2 = \theta_w; \lambda_f \frac{\partial \theta_1}{\partial y} = \lambda_s \frac{\partial \theta_2}{\partial y}, \quad (5.11b)$$

$$y = -b, \theta_2 = 0. \quad (5.11c)$$

Hence, from (5.11a)-(5.11c), (5.10a), and (5.10b):

$$T_f(x, y) = T_w + \frac{3}{2} \frac{T_\infty - T_w}{\delta_t} \cdot y - \frac{1}{2} \frac{T_\infty - T_w}{\delta_t^3} \cdot y^3, \quad y \in [0, \delta_t] \quad (5.12a)$$

$$T_s(x, y) = T_w + \frac{T_w - T_b}{b} \cdot y, \quad y \in [-b, 0]. \quad (5.12b)$$

The wall surface temperature is denoted by T_w and reads

$$T_w(x) = T_b + (T_\infty - T_b) \frac{z}{1+z} \quad (5.13)$$

where the quantity z is:

$$z = \frac{3}{2} \frac{\lambda_f}{\lambda_s} \frac{b}{\delta_t}, \quad (5.14)$$

with δ_t being the thermal boundary layer thickness. Equations (5.9) and (5.12a) can be subsequently substituted into (5.8) which eventually yields:

$$\frac{\delta_t}{\delta} = \sqrt[3]{\frac{13}{14}} \cdot \sqrt[3]{\frac{1}{Pr}}, \quad (5.15)$$

which is identical to the solution also presented in [28]. Similarly, the velocity boundary layer thickness is expressed using the known relation, first derived by Blasius [106], using the similarity solution approach:

$$\frac{\delta}{x} = \sqrt{\frac{280\nu}{13v_\infty} x} = \frac{4.64}{\sqrt{Re_x}}. \quad (5.16)$$

The Biot number is another important nondimensional number. Hereby, the respective expression is shown used for the analysis in this chapter. Using the Luikov's boundary layer approach, which allows for an analytical expression of the Biot number from the heat transfer coefficient h . To find the heat transfer coefficient, one can first express the wall heat flux (using the derivative w.r.t y of (5.12a))

$$q = -\lambda_f \frac{\partial T_f(x, 0)}{\partial y} \quad (5.17)$$

$$= -\lambda_f \frac{3}{2} \frac{(T_\infty - T_w)}{\delta_t} \quad (5.18)$$

$$= h \cdot (T_w - T_\infty), \quad (5.19)$$

where (5.19) is from Newton's Law of cooling. The convention used is a positive sign for expressing heat entering the fluid domain. Further equating (5.18) to (5.19), and substituting δ_t with (5.15), yields:

$$h = \lambda_f \frac{3}{2} \cdot \frac{1}{\delta_t}, \quad (5.20a)$$

$$= 0.332 \cdot \lambda_f \sqrt[3]{Pr} \frac{\sqrt{Re_x}}{x}, \quad (5.20b)$$

which is also identified in [106], where an ordinary heat transfer flat plate problem with a constant wall temperature is considered (without taking into account for conjugation). Thereby, the effect of conductivity of the solid is ignored. However, this assumption only holds for $z \ll 1$, which was also applied in the derivation of the thermal boundary layer from eq.(B.1g) (N.B. the limit value in the denominator). Such a condition is satisfied by having a solid region conductivity considerably higher than that of the fluid, which corresponds namely to cases with a low Biot number

$$Bi = \frac{h \cdot b}{\lambda_s}. \quad (5.21)$$

One of the benefits of using the simplified boundary layer approach, is that the heat transfer coefficients and hence the Biot number can be easily derived analytically. Due to the constant conductivity and

plate thickness, the Biot number is proportional to $(\sqrt{x})^{-1}$.

A limitation of this approach that is worthwhile mentioning is the required thermal conductivity of the solid for the method to be counted accurate. In the scope of this project, the averaged Biot number is used, which takes the averaged heat transfer coefficient:

$$\bar{h} = \frac{1}{L} \int_0^L h dx = \quad (5.22)$$

$$= \frac{0.664}{L} \lambda_f \sqrt[3]{Pr} \sqrt{Re_L}, \quad (5.23)$$

where Re_L is the Reynolds number at the plate trailing edge ($x = L$). The averaged Biot number thus becomes:

$$\overline{Bi} = \frac{\bar{h} \cdot b}{\lambda_s} \quad (5.24)$$

$$= 0.664 \cdot \left(\frac{b}{L}\right) \left(\frac{\lambda_f}{\lambda_s}\right) \cdot \sqrt[3]{Pr} \sqrt{Re_L}. \quad (5.25)$$

Referring back to (5.15), the calculation of the mean Biot number using the boundary layer approximation holds only for $z \ll 1$ (i.e. values where the thermal conductivity of the solid region is considerable higher than that of the fluid region). The results from the evaluated cases are presented in the following sections and the fulfilment of this criterion is briefly discussed.

5.1.2 CFD setup and boundary conditions

The computational domain consists of a plate ($0.2m \times 0.01m$), and two additional extensions with a length of $5b$ at the entrance and outlet of the domain in order to ensure valid flow behaviour and convergence. The fluid domain extends of a height of $10b$.

For the purpose of this study, two values of Biot number were used, $\overline{Bi} = 0.1$ and $\overline{Bi} = 1$, in order to investigate the applicability of the two analytical methods mentioned above and, respectively the solver's accuracy to be validated at two separate physical conditions.

Air is simulated as an ideal gas at 1.03bar, where the the necessary properties are calculated at 1000K, with the respective values tabulated below.

The boundary conditions are applied and corresponding equations discretized and solved by using the commercial CFD code in STAR-CCM+, for both fluid and solid domains.

Table 5.1: Calculated properties of air at 1000K. [65]

R (J/kgK)	ρ (kg/m ³)	c_p (J/kgK)	γ	μ (Ns/m ²)	λ_f (W/mK)	Pr
282	0.3525	1142.6	1.335	3.95e-5	0.06808	0.66

Table 5.2: Resultant solid thermal conductivity from the two average Biot numbers

\overline{Bi}	0.1	1
λ_s (W/mK)	2.786	0.2786

A freestream boundary condition normal to the inlet plane is imposed using a velocity of 12m/s. The

resultant Reynolds number is hence:

$$Re_L = \frac{\rho_{air} u_{\infty} L_{plate}}{\mu_{air}} = 21,418 \quad (5.26)$$

According to [106], where for a plate with a sharp leading edge, the laminar–turbulent transition occurs at a critical Reynolds number, $Re_{crit} = 320,000$, and hence one can safely conclude that a laminar flow is present, which was a deliberate choice, and no turbulence modelling will be needed as a part of this study.

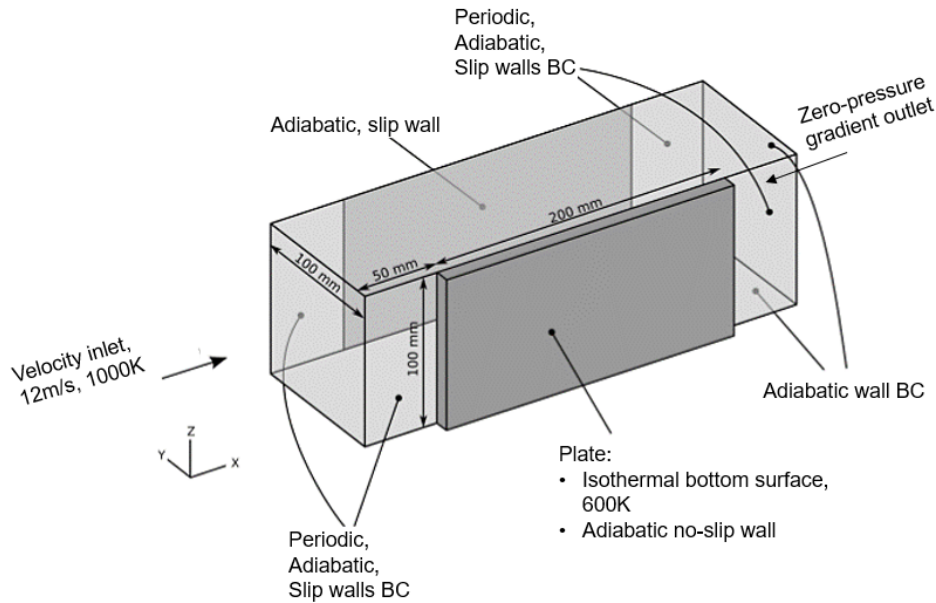


Figure 5.2: Problem domain schematic and boundary conditions.

Using the equation for the average heat transfer coefficient (5.23), one can obtain $\bar{h} = 28.76 \text{ W/m}^2\text{K}$. and rearrange (5.25) for λ_s with the specified averaged Biot numbers and obtain the values in Table 5.2. However, as previously mentioned, the criterion of $z \ll 1$ is not met for $\overline{Bi} = 1$ ($z = 0.631$). The difference in the heat transfer coefficients calculated for both Biot number settings (and hence z) for each solution approach, are plotted in Figure (5.3), which is created by using the formulae in [81] for the local Nusselt numbers (given in the Appendix B).

Comparing the two solutions, the values for the heat transfer coefficient from the boundary layer approach, using $\overline{Bi} = 1$ are greatly underestimated compared to the differential heat transfer approach, in which the thermal conductivity of the solid is taken into account. For the latter, the two Biot number settings lead to almost matching solutions. The mismatch for the boundary layer approach holds particularly well in the region after the leading edge approximately between $x/L \in (0.05, 0.25)$. One can thus find that the average Biot number in the BLE is in fact above one. For the sake of consistency in this study however, the notation $\overline{Bi} = 1$ is kept.

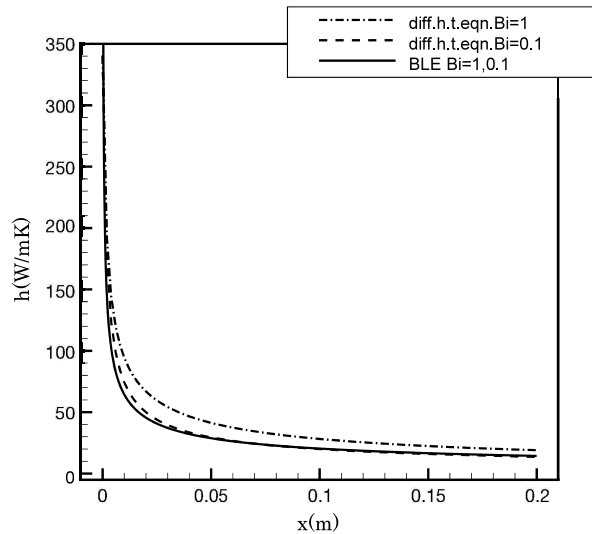


Figure 5.3: Heat transfer coefficient along the plate surface for $\overline{Bi} = 0.1$, and $\overline{Bi} = 1$ for each of the two solution methods by Luikov [81].

Expanding on the boundary conditions applied to the domain (Figure 5.2), periodic wall boundary conditions are applied on the surface in front of the plate and after the trailing edge. This is done in the attempt to replicate as close as possible the boundary conditions applied in the studies of turbomachinery components, such as the case of the transition, described in Section 7.1. All surfaces of the plate, except for the fluid/structure interface are treated as adiabatic no-slip walls. The side walls of the fluid domain, along with the top surface are also treated as slip-adiabatic walls.

The fluid/solid interface is the only surface where the no-slip boundary condition is present. The type of interface used was a mapped contact interface, since it allows for data mapping when a conformal match between the fluid and solid meshes is lacking. Such instances occur when different resolutions are necessary on both sides of this interface. Such is the case for instance in this problem, where the heat conduction in the solid region requires a coarser mesh compared to resolving the boundary layer in the fluid domain. For further details on the choice of the CHT interface settings, one can refer to Appendix B.

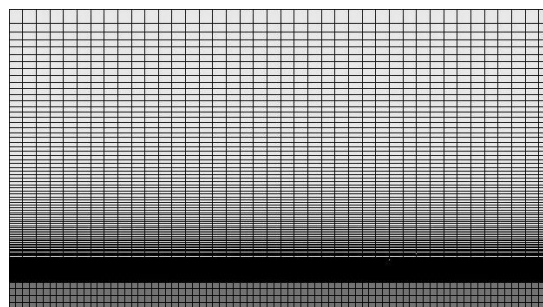


Figure 5.4: Mesh used in the validation and HT methodology comparison. Grid is of size 60x120 and a first cell height of $\Delta y_{\min} = 7.2e-05\text{m}$ with a logarithmic stretching factor of 1.061

The fluid region was modelled on a finite volume method domain using a laminar solver and a segregated fluid enthalpy model (temperature is calculated from enthalpy using the equation of state) in accordance with the SIMPLE algorithm. Variable gradients are calculated using the Hybrid Gauss-Least Squares Method. The limiter of choice for the reconstruction gradients was Venkatakrishnan. Second-order upwind differencing was employed for the convection scheme. The reader can refer to the theory of

FV discretization, including transport equations, differencing schemes and gradient calculation methods in the Appendix, where a brief derivation and explanation of key terms is included.

A steady state finite element solver was applied to the solid region in order to solve for the solid temperature. A nearest neighbour interpolation method was used to map data (temperature and heat transfer coefficient) onto the solid domain. This method, compared to other methods such as the higher-order stencil (alternative option in STAR-CCM+, which makes use of a distance-weighted, least-square approach) provides a quicker interpolation at the expense of accuracy. Due to the simplicity of the problem and hence resultant meshes, it proves to be a reasonable choice. The shortened read on the numerics of FEM is also included in the Appendix.

The convergence criteria for the simulation used were based on minimum residual values of the Continuity equation, Energy equation, and the Momentum equation (all directions). For all 5 equations the value was set to 10^{-5} . A fully converged solution is thus achieved in 260 iterations for the finest mesh.

A structured mesh approach was used for both cases of $\overline{Bi} = 1$, and $\overline{Bi} = 0.1$. A mesh refinement was strongly recommended in a similar study by Verstrate [117], and hence the resolution of the mesh was chosen based on a mesh independence, which took both refinement in the -x and -y directions into account. The chosen mesh is shown above in Fig. 5.4, along with the respective resolution at the wall.

5.1.3 Results and discussion

The results presented in this section consist of temperature in both solid and fluid domain and a comparison of the velocity in the laminar boundary layer to analytical solution. As previously mentioned, two values of the averaged Biot number are used, 0.1 and 1. The comparison of the two simulation methodologies (decoupled and CHT) are discussed later in Section 6.

An important remark regarding all post-processed figures presented below: the plots includes interface quantities measured only from the FVM mesh, the reason being that it coincides with the interpolated data on the FEM and thus avoiding confusion in the plots. Figure 5.8 presents the interface temperatures and heat transfer coefficients at $Bi = 0.1$. The leading edge is primarily where discontinuities exist with the analytical solution. This error tends to decrease downstream but remains firmly at an offset of $\approx 8\text{K}$, even at the trailing edge. This discontinuity is less apparent in the heat transfer coefficient calculation where almost no difference is found after roughly $x/L = 0.3$. The large change in temperature that is required over such a small length is the reason why such a difference is to be expected, particularly for low Biot numbers. Additionally, a similar observation is reported by Verstraete [117], where the steep temperature change is also predicted inaccurately.

An interesting observation coming from Figure 5.6 is present. The gradients of the thermal profiles agree well with the analytical solution, despite the small difference. The difference however, tends to become more pronounced in the downstream direction, which is contrary to what one might expect given the results in Figure 5.8. The peak differences between the differential heat transfer approach for all three locations in the downstream direction are 1.95%, 3.3%, and 3.6%, respectively.

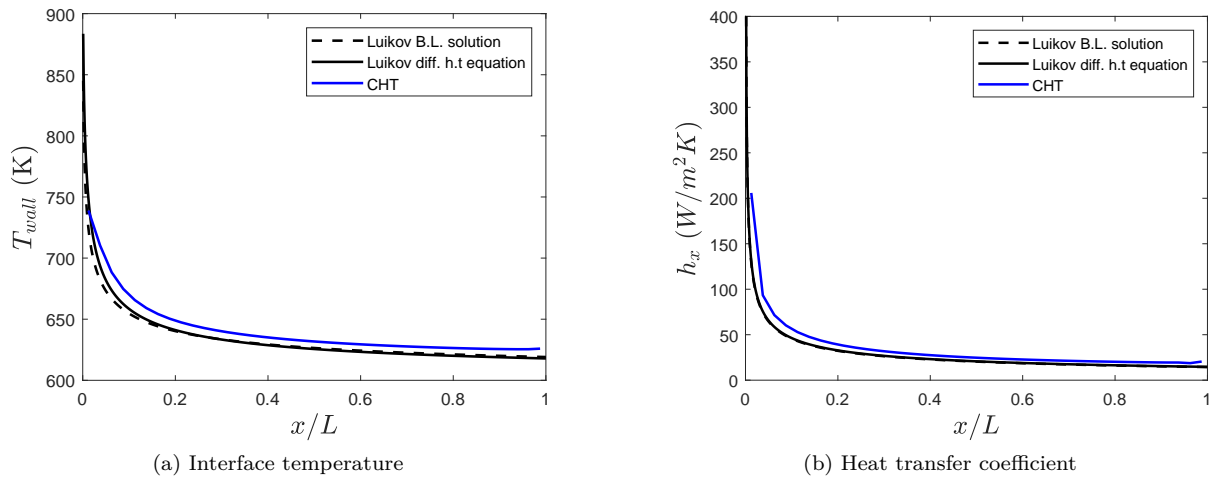


Figure 5.5: Interface temperature and heat transfer coefficient comparison with the differential heat transfer approach [81], at $\overline{Bi} = 0.1$

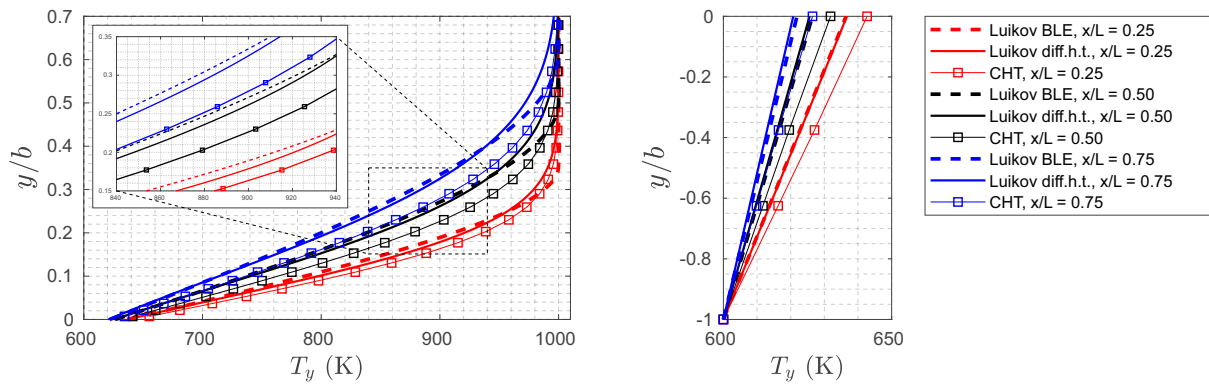


Figure 5.6: Temperature distribution across the fluid region (left) and solid (right) and comparison to Luikov solution, with a $\overline{Bi} = 0.1$

The velocity profiles of the CFD results are compared to the Blasius solution [106] at the previously used locations downstream for both Biot number settings. The quantity η corresponds to the nondimensional distance from the plate, given in correspondence with the coordinates in Fig. 5.1:

$$\eta = y \sqrt{\frac{v_{\infty}}{\nu x}}, \quad (5.27)$$

in which y and x are the normal distance from the wall and the distance from the leading edge. Hence, the velocity boundary layers are shown in Figure 5.7 and Figure 5.10, respectively.

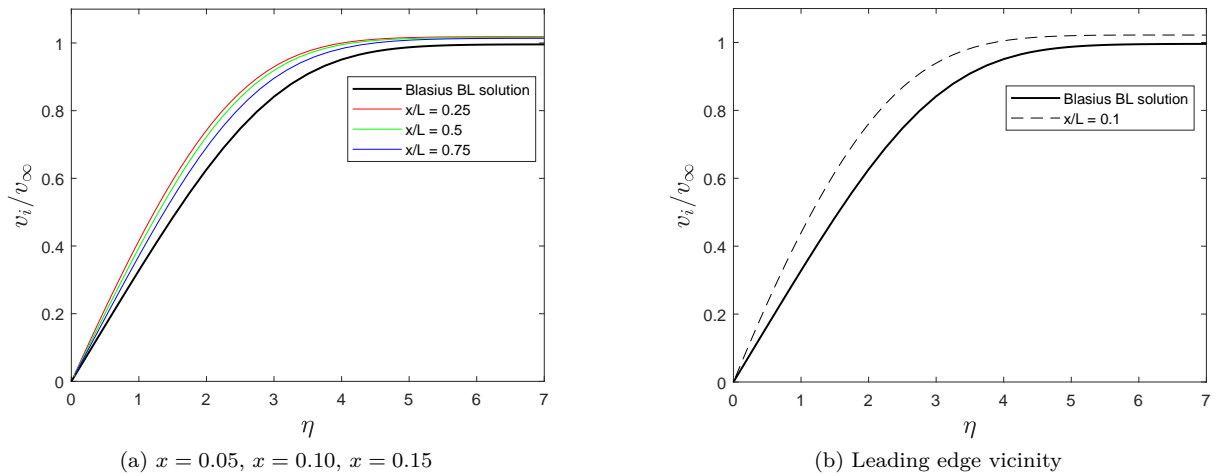


Figure 5.7: Comparison of velocity profiles to Blasius solution [106], at $\overline{Bi} = 0.1$

The velocity boundary layer thickness is found to be lower than the one proposed by Blasius, with the tendency for the error to decrease downstream. This coincides with the interface temperature profiles, but is contradicting the findings of the thermal boundary layer, which are displaying exactly the opposite behaviour downstream.

When it comes to the computation of the case at Biot number equal to 1, the temperature and heat transfer quantities from STAR-CCM+ are presented in 5.9 along with the direct solution of Luikov of the differential heat transfer equation. In general, a good agreement is found with the CHT solution. The largest difference is observed at the trailing edge, where the temperature is overpredicted by the numerical method, and also in the vicinity of the first quarter of the plate upstream, where the value is lower. The former is also where the maximum difference of 11K occurs.

Such phenomenon is also observed by Verstraete in [117] and Racca [99], where the former author reported a similar increase of temperature in the second half of the plate in his attempts to study the stability of various coupling algorithms. Coincidentally, this observation also happens for the CHT coupling algorithm which is similar to what is used in this numerical study (Table B.1), namely the heat transfer coefficient forward temperature back method (hFTB) method. In [117], the difference was explained by the remaining heat flux difference between solid and fluid domain at convergence. For a more detailed read on the main differences between coupling schemes the reader can refer to the Appendix.

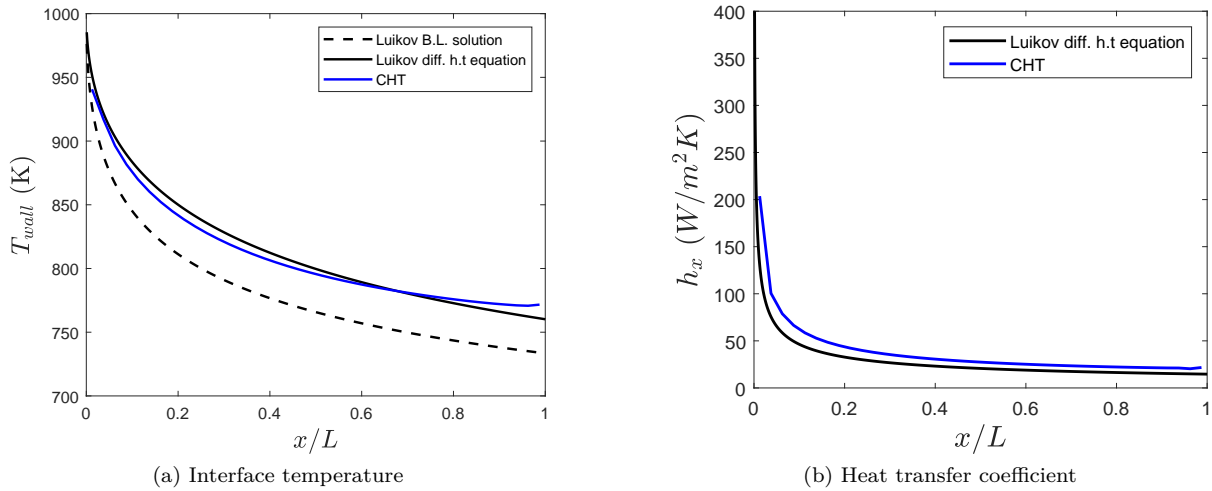


Figure 5.8: Interface temperature and heat transfer coefficient comparison with the differential heat transfer approach [81], at $\overline{Bi} = 1$

The temperature profiles in the y -direction for both fluid and solid region is again plotted in Figure 5.9 at the three previously mentioned downstream locations. The difference with the solution of the differential approach is rather small. Overall the thermal boundary layer thickness is similar. An interesting observation is that the temperature difference for $x/L = 0.25$ is the highest near the wall (i.e. $y/b < 1$), and close to zero as the end of the boundary layer is approached. This is contrary to the CHT prediction for $x/L = 0.5$ and $x/L = 0.75$, where the difference is close to zero near the wall, but the thickness is underevaluated. This could partially explain the temperature profile at the interface, in which case the gap with the Luikov solution is the smallest for the two aforementioned x -locations. The difference, however, remains negligible. A similar observation is present in the solid region as well: the gradient of the CHT solution is lower than the analytically calculated one as the leading edge is approached, and virtually corresponds precisely to the Luikov solution further downstream.

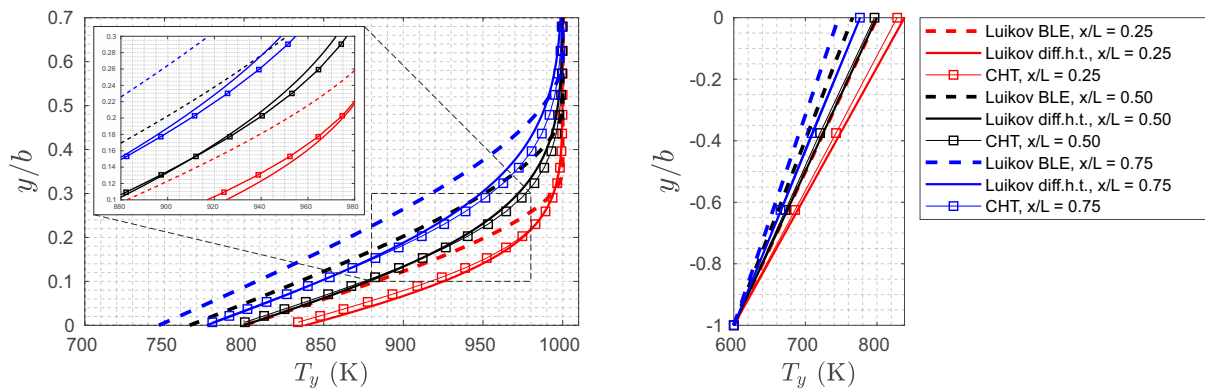


Figure 5.9: Temperature distribution across the fluid region (left) and solid (right) and comparison to Luikov solution, with a $\overline{Bi} = 1.0$

The good fit of the thermal profiles with the analytical solutions can also be related to the velocity boundary layer. The velocity profiles again at three distinct regions, similarly to the analysis at $\overline{Bi} = 0.1$ above, are plotted in Figure 5.10. An overall good prediction is achieved by STAR-CCM+ when it comes to the slope of the velocity within the boundary layer. The difference tends to increase upstream, where the gradients are the highest. The close temperature fit at $x/L = 0.1$ in Fig. 5.8) can also be traced down in Fig. 5.10(b): the difference in this case is smaller than in Fig.5.7, where a comparatively larger

divergence with the analytical solution was found in terms of interface temperature for the respective location. The exact reason as to why this happens in conjugate heat transfer terms for both $\overline{Bi} = 0.1$ and $\overline{Bi} = 1$, however, is inconclusive and difficult to determine. A possible reasoning is the inherently large gradients as previously discussed for $\overline{Bi} = 0.1$.

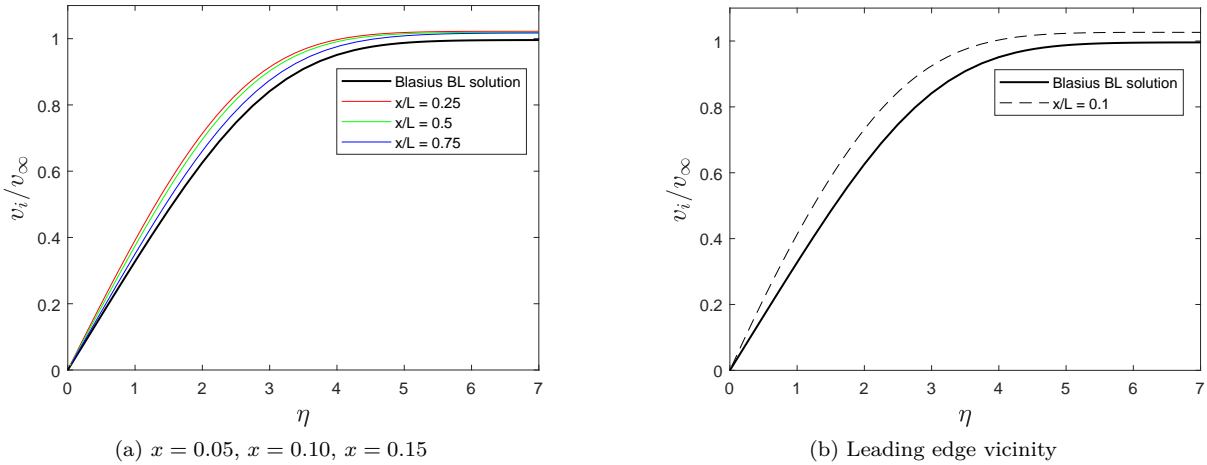


Figure 5.10: Comparison of velocity profiles to Blasius solution [106], at $\overline{Bi} = 1$

The averaged values of the quantities on the centerline (not of the entire 2D surface) of the solid interface are summarized in Table 5.3 below.

Table 5.3: Summary of average values for temperature and heat transfer coefficient from both simulations and the analytical solution [81].

	$\overline{Bi} = 0.1$		$\overline{Bi} = 1$	
	$\overline{T}_{wall}(K)$	$\overline{h}(w/m^2K)$	$\overline{T}_{wall}(K)$	$\overline{h}(w/m^2K)$
CHT	641.2765	35.02	810.915	38.06
Luikov (diff.h.t.eq.)	634.7062	28.76	813.493	28.76

In both Biot number settings, the average values differ from the analytical solution, the larger error being in the heat transfer coefficient.

The average heat transfer is overpredicted in both cases. The change in the average temperature for $\overline{Bi} = 1$, however, is smaller than the resultant increase for $\overline{Bi} = 0.1$, given that $\Delta T(\%)$ is $\approx 0.3\%$ and 1% , respectively.

5.1.4 Summary

The numerical validation study investigated the accuracy of the STAR-CCM+ solver at two physical conditions on a simple flow problem where an analytical solution is present. Following the mesh independence study (computed on a low Biot number setting), the following was observed:

- For the computation of the low Biot number setting, small differences were present in terms of the interface temperature and heat transfer coefficient with the Luikov solution.
- The results of the Biot number of unity were comparatively better in terms of the interface temperature prediction. It is assumed that this is primarily due to the lack of high temperature gradients near the leading edge, owing to the high thermal conductivity of the solid region.

- In terms of velocity and thermal boundary layers, the case of high Biot number was also more consistent with the analytical solution. On the other hand, the low Biot number computation yielded thermal profiles that contradict the velocity profiles behaviour (boundary layer thickness).
- The exact reasons why the difference (never mind little) exist can be partially explained by the assumptions used in the derivation of the analytical solution. The problem formulation (especially in cases of low Biot numbers) introduces large gradients in the vicinity of the leading edge which the solver finds hard to predict and opens room for further analysis as to why this happens even with refinements in the x-directions (shown in the mesh study - see Figure B.5).
- However, for the purposes of this study the STAR-CCM+ CHT solver does a good job in predicting the temperature profiles in both fluid and solid regions for both settings. The accuracy achieved in terms of average values is also satisfactory to the prediction of thermal stresses and hence allows for adequate lifeing analysis, especially in cases of MDOs, where the focus lies on overall trends and tradeoffs rather than exact solutions.

The introduction of turbulence in the upcoming section increases the complexity of the problem and addresses different aspects more relevant to a turbine transition piece, presented in the sections to follow.

5.2 Turbulent offset jet

5.2.1 CFD setup and boundary conditions

As for the validation of the turbulent offset jet a different procedure was followed: experimental data for flow and temperature fields, as opposed to semi-empirical relations or solutions.

As a first step of the validation process was, similarly to the case with the flat plate, a mesh study in which, the flow was validated against measurement velocity data presented by Pelfrey and Liburdy [95], thus eliminating the effect of the mesh and boundary conditions as much as possible before conducting the numerical study. A code validation step followed in which the experimental interface temperature on the plate was compared to the one predicted by the CHT solver in STAR-CCM+.

The computational domain that was initially utilised for this part of the validation process comprised of a simple rectangular domain, using a structured directed mesh in both y- and x- directions. The domain was very closely replicating the one used in the study by Vishnuvardhanarao [118], as mentioned in Section 2.2.2, where no inlet duct was added for the jet itself.

The velocity profiles however were unsatisfactory in terms of accuracy with the experimental data. Therefore, despite the inherent simplicity of the domain to discretize and solve using such a mesh, both fluid and solid, an unstructured polyhedral grid was chosen for the fluid region in order to be consistent with methodologies applied in turbomachinery applications, e.g. a combustor transition piece, which most often cannot be discretied in a structured way due to the complexity of geometry and the complex flow field. Additionally, the computational domain was altered so that it was attempted that it replicate the experimental setup, described in the paper, using boundary conditions that would reproduce the experimental boundary conditions with the highest possible fidelity, allowing room for assumptions, where information was lacking.

The entirety of the computational domain used in this study is displayed in Figure C.2, followed by a close-up of the region where the offset plate is contained within the plexiglass sidewalls. The dimensions used are identical to those in the experimental domain. The pressure outlet boundary conditions were placed at a large distance from the jet discharge region so that they do not interfere with the numerical results and to diminish the likelihood of reversed flow.

The schematic shown below in Figure C.1 provides information with regards to the experimental setup by Pelfrey and Liburdy. The setup allows for a multitude of offset ratios using an adjustable plate. The numerical study described here was computed using $OR = 7$. The choice of the setting was made arbitrarily. The width of the exit nozzle is $t = 12.5\text{mm}$.

Similarly to the laminar flat plate case study, the FVM is used for the fluid region along with a tetrahedral FEM mesh for the solid region. The zero-pressure gradient boundary condition (blue annotation in Figure 5.11) was applied on all faces which do not correspond to walls or inlets. The interpolation stencil and settings used for data transfer across the interface on the plate are identical to the ones used in the laminar flat plate study (see Table B.1). An under-relaxation factor of 0.7, 0.3 and 0.9 are used for the velocity, pressure and energy in the fluid region. A turbulence intensity I of 2% is specified at the inlet for the kinetic energy equation, along a turbulent viscosity ratio (μ_T/μ_L) of 10 for the dissipation equation. The temperature specified is $\theta = 1$, where θ is the nondimensionalized quantity:

$$\theta = \frac{T - T_\infty}{T_j - T_\infty}, \quad (5.28)$$

with T_∞ and T_j being the ambient (300K) and jet outlet temperatures (385K), respectively. An additional distinction between the continua set-up of the flat plate study is the calculation of the properties of air. In this case, variable air properties are used and are calculated using Sutherland's Law. This holds for dynamic viscosity, thermal conductivity and molecular weight. The properties of the solid region were all set to constant values. Due to the problem definition of the optimization task, which is intended for a combustion component, an additional step was taken for the choice of the Turbulent Prandtl number. The number changes from 0.9 at the wall to 0.4 in the free stream flow with a specified wall distance of 1.0mm and free stream distance of 5.0mm, using a linear interpolation for the in-between region. Such manipulation of the Turbulent Prandtl Number is common for combustion flows in which the effects on the resultant low turbulent scalar transport is to some extent mitigated. In a RANS combustion simulation this is also done by decreasing the Turbulent Schmidt number, Sc_t , thus artificially increasing the turbulent diffusion coefficient, D_t . Many studies confirm such considerations using a variety of turbulence models. Examples of some are the works of He et al. [43], Ivanova et al. [51], and Baurle [10].

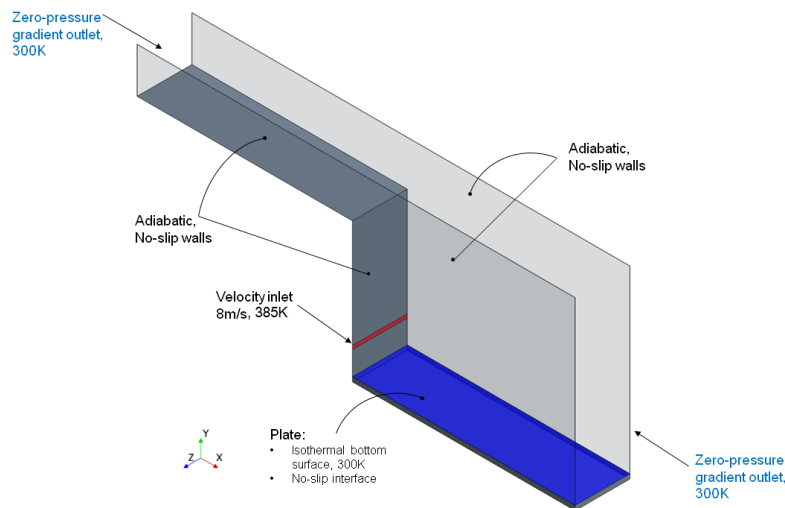


Figure 5.11: Close-up of dark gray region in Figure C.2: schematic of boundary conditions used in the turbulent offset jet problem. Domain width is 150mm (identical to experiment)

The value of 0.9 for the turbulent Prandtl number in the near-wall region is entirely based on turbulence theory, which is consistently used in literature for air [67], [126]. However, it is widely known that

it varies significantly within a turbulent boundary layer [64]. The usage of a constant value nonetheless is common for numerical simulations.

It is worthwhile mentioning that the thickness of the solid region was set to 0 for the mesh study, where an adiabatic wall boundary condition was used, since the study of Pelfrey & Liburdy, used to validate the mesh does not include conjugate heat transfer measurements, but only flow characteristics. The thickness of the plate is 0.635cm and the material is balsa wood⁴. The chosen turbulence model was the realizable $k - \varepsilon$ model with the blended WF approach. Parameters used for the mesh independence study were reattachment length, X_{cr} , the maximum value of the coefficient of friction along the middle of the interface, and a comprehensive comparison of the velocities with the experimental data from Pelfrey. For the full analysis of the mesh independence study and results, refer to Appendix C.

In the following subsection, a comparison of the three turbulence models of choice will be discussed (realizable $k - \varepsilon$, standard $k - \varepsilon$, SST $k - \omega$), in which two wall-treatment methods are used: All- y^+ (or Two-layer y^+) and High- y^+ wall functions for a fine and coarse mesh, respectively. This procedure is also followed later in the comparison of the conjugate heat transfer approach to the decoupled approach, where of interest is the effect of flow properties and wall-treatment methods on conjugation and under what conditions is the difference between the decoupled (adiabatic) and conjugate method minimized/maximised.

5.2.2 Results and discussion

Given the experimental apparatus used in [47], the paper lacks a multitude of important details around key parameters. The parameters are presented in Table 5.4 below. The results from all cases with the respective measures taken are presented in 5.12, where the nondimensional wall temperature is given.

The results correspond to the expectations and there is no noticeable change in the behaviour of the profile (no change of turbulence model). The temperature gradient in the recirculation, impingement, and wall jet regions are almost identical. The difference consists only in a *shift* of the profile higher or lower. The increase of the inlet velocity and also turbulence intensity lead to a seemingly identical level of heat transfer augmentation. Further refinement of the solid mesh leads to an increase in heat flux and respectively to wall temperature possibly due to the resultant interpolation at the interface. The opposite effect is manifested by an increase in the thermal conductivity which lowers the temperature gradients within the solid, explainable by the increase in heat flux across the boundary.

Table 5.4: Sources of errors and unknowns in the numerical procedure followed for the CHT validation.

Unknown parameter	Experiment (Holland, 1990)	Countermeasure
Turbulence intensity, I (%)	Only Reynolds number and discharge coefficient present	Sweep of various values for I (%)
Thermal conductivity of plate	Only thickness and material name	Two values of thermal conductivity of the given material
Velocity inlet data	No velocity data available for CHT experiment, only Re	Velocity scaled down accordingly from Re number
Solid plate mesh	-	Mesh refinement in the solid reigon

Therefore, for further analysis, the baseline settings described in the previous subsection will be used. This includes a thermal conductivity of 0.0339W/mK, no mesh refinement (mesh presented in Figure

C.3e), turbulence intensity of 2%, and jet outlet velocity of 8m/s.

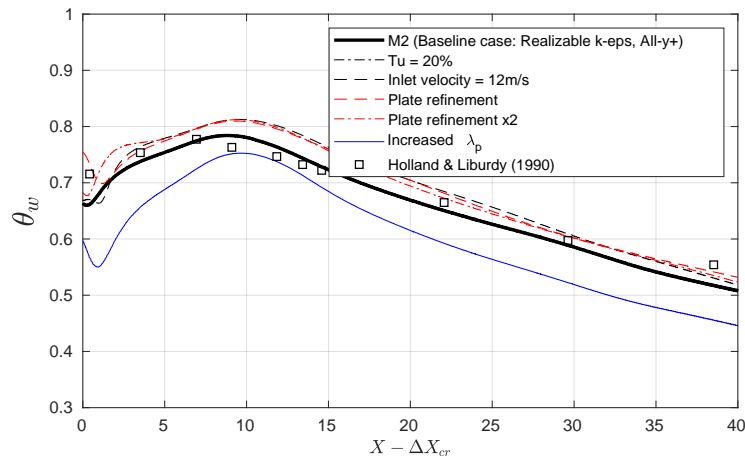


Figure 5.12: Interface temperature variation using countermeasures on the realizable $k - \epsilon$ model

Figure 5.14 indicates the results from all four computations on mesh M2, where a blended or low- y^+ wall function modelling is applied to all three turbulence models investigated. The aerodynamic characteristic of the results are discussed later, hence the averaging on the plot x-axis: ΔX_{cr} is intended to take care of difference between the reattachment lengths for all models. Thereby, focus is put mainly on the behaviour of the temperature before and after the reattachment point without emphasising on the exact prediction, but rather on average temperatures. Thus, if one assumes that all computations result in a reasonable match with X_{cr} , the results lie within a satisfactory region off the experimental data.

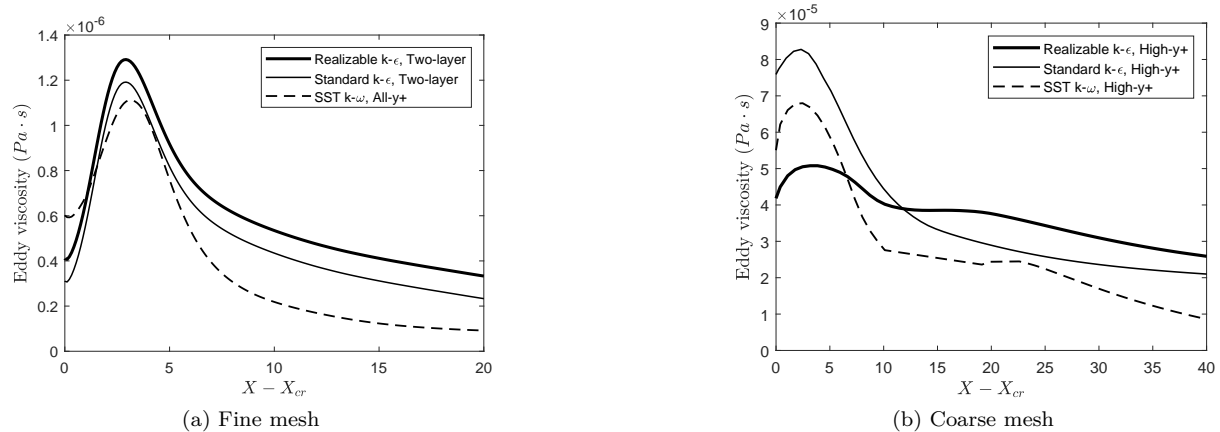


Figure 5.13: Comparison of eddy viscosity for all three models

In nominal terms, the difference at the peaks for the standard and realizable $k - \epsilon$ models is $\approx 2K$ and $\approx 4.2K$, which considering the temperature difference of 85K between the bottom surface of the plate and the jet outlet from the problem boundary conditions, is in good agreement. A more realistic fit is achieved by both realizable and standard formulations of the $k - \epsilon$ models, compared to SST $k - \omega$. The difference with the SST $k - \omega$ model is larger by $\approx 7.34K$. The reason for this can be traced back to the formulation of the turbulent viscosity term in the model equations. The respective turbulent viscosities along the interface are given in Figure 5.13. For all models, μ_t is at a local minimum at the reattachment

point, similar to other flow quantities (see friction coefficient in Figure C.4c), followed by a sharp increase in the impingement region.

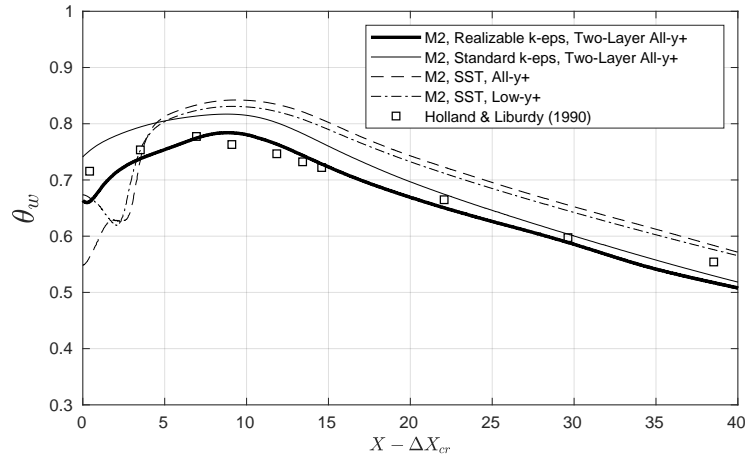


Figure 5.14: Comparison of interfacial temperature profile for all three models using finer mesh (M2) and blended wall function approach

The values of the turbulent viscosity term from the $k - \varepsilon$, particularly in the near wall region, are higher than the values computed by the SST $k - \omega$. The difference is not overwhelming but is the reason why the temperature increase on the surface is lower for the former model. When the turbulent viscosity is low in the vicinity of the wall, the velocity of the flow in the region will become lower, which will inherently lead to a drop the heat transfer rate. This results in in lower temperatures at the wall and low heat fluxes through the solid walls. The alternative formulation of the turbulent viscosity term in the SST turbulence model did not lead to a better prediction for this particular problem. However, this greatly depends on the type of flow and its features, since the model has been reported to perform better than the (realizable) $k - \varepsilon$ model in multiple studies involving conjugate problems, [21] [48].

As it can be seen in Figure 5.15, where the temperature profiles in the wall-normal directions at two separate recirculation locations are compared to the experimental results of Holland and Liburdy [47], there is no major difference in the predictions in the core of the flow for all computations. The similarity in the results is due to the two-zonal behaviour of the SST model, which switches to the standard $k - \varepsilon$ model in the free-stream region. The difference in the temperature profiles however becomes more pronounced near the wall, where the $\omega - SST$ model leads to large gradients, not present in the experimental data.

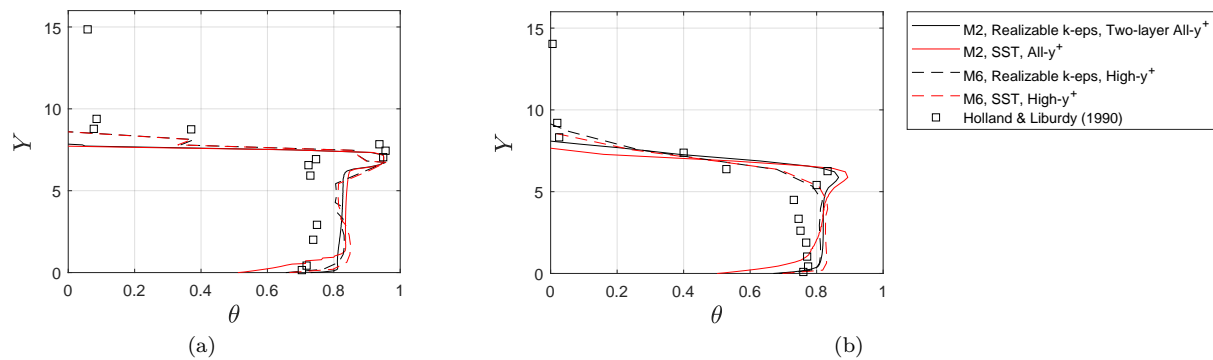


Figure 5.15: Nondimensional temperature in the wall-normal direction at (a) 3mm in front of the exit nozzle and (b) $X = 6.69$ (midway in the recirculation region in the experiment).

Another important parameter is the thermal decay of the jet, which is presented as the decrease of the maximum jet temperature downstream. The computed value is compared to the experimental data in Fig.5.16. Evidently, neither of the models studied satisfy the real rate of decay. This is in accordance to the expectations following also the slower rate of velocity decay compared to the experiment, as shown previously in the mesh independence study. The realizable $k - \varepsilon$ model tends to perform slightly better in this regard. The difference however remains large.

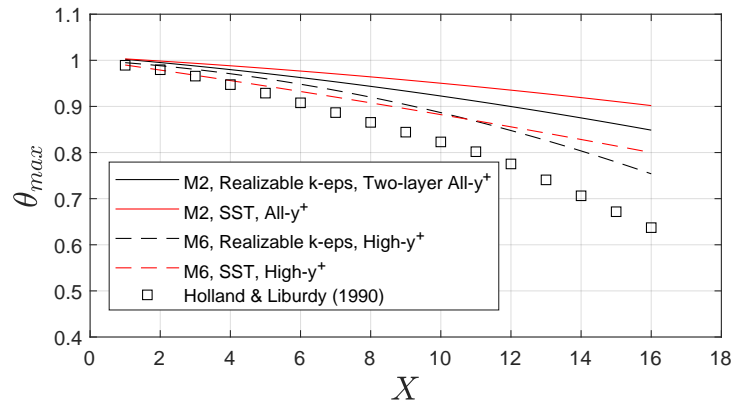


Figure 5.16: Decay of the maximum jet temperature downstream (SST model in red and $k - \varepsilon$ model in black).

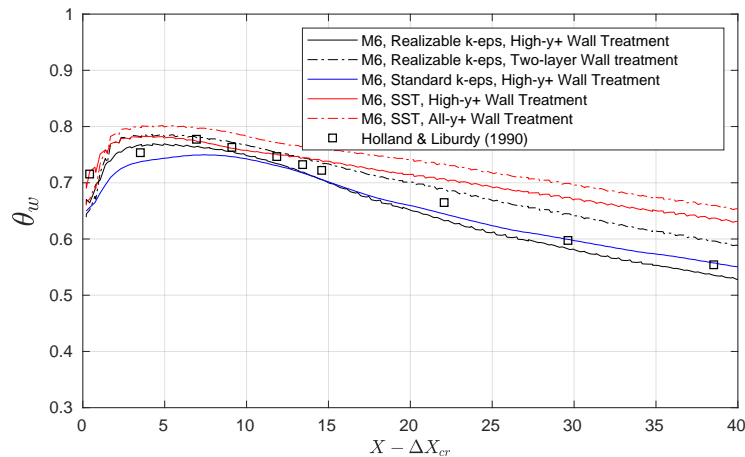


Figure 5.17: Comparison of interfacial temperature profile for all three models using coarse mesh (M6) and high- y^+ wall function approach

Referring back to the temperature plot Figure 5.14, the temperature gradient in the x-direction is similar for all models, where temperature tends to dissipate quicker than in the experiment. A significant divergence from the physical result is the underprediction of the results for the SST $k - \omega$ model in the recirculation region. The gradients, as a result, are much steeper for both types of wall function treatment. As previously mentioned, the SST model does provide superior computations where adverse pressure gradients and separations are present. However, it has been reported that the model can lead to overpredicted turbulence levels in regions with large normal strain, i.e. stagnation zones and zones with high acceleration [92], such as the recirculation zone in a offset-jet.

When it comes to the temperature profiles on the coarse grid, shown in Figure 5.17, the overall va-

lidity of the previous findings remain: the SST model leads to higher interface temperature and the dissipation downstream does not match the one in the experiment. Varying the wall function treatment leads to less visible effects on the SST model compared to the realizable $k - \varepsilon$. When the two-layer formulation is used on the coarse grid in the latter, the model tends to predict the experimental data fairly well in all regions. The difference, however, between the realizable and standard $k - \varepsilon$ models is diminished on the coarse grid. Additionally, the SST model does not display such large gradients upstream in the recirculation region, and the curve is much more 'flatter' than in the computations performed on M2, particularly in the wall jet region. For future computations it is therefore recommended to investigate the effect of different discretization schemes of the convection term, in order to address this issue. Moreover, no resources in open literature have been found discussing numerical dissipation sensitivity of the $k - \omega$ and $k - \varepsilon$ models.

5.2.3 Summary

In general, The exact boundary conditions are unknown and could have a noticeable effect on the reattachment length. The goal of this study is to validate the CHT solver in STAR-CCM+ and by doing so to choose the best option in terms of a RANS turbulence model and a wall treatment method. Predicting an accurate reattachment length was not part of the objectives (RL could be predicted with fine turbulence modelling tuning). The key findings from this validation case thereby include:

- Attempt was made to eliminate effect of BCs, by reproducing the experimental domain as closely as possible. If the reattachment points are artificially matched (by shifting the results on the plot), the CHT solver was a good agreement with the data in general.
- The resultant temperature profile for all computation cases considered is in very good agreement with the experimental data from Holland & Pelfrey. The temperature profiles in the recirculation, impingement, and wall jet regions are within the acceptable accuracy implying that the presented turbulence models are suitable for predicting flows similar to the case of an offset jet flows.
- Coarser mesh study results in a more accurate solution in terms of both CHT and RL, which is however due to numerical (not physical) dissipation
- A comparison between SST and realizable $k - \varepsilon$ shows that it is more diffusive in the solid region than the SST $k - \omega$
- Both models displayed similar thermal dissipation downstream in the wall jet region

In general, the realizable $k - \varepsilon$ model showed comparatively better agreement particularly in the impingement region where the maximum temperature is found, and therefore will be used for the upcoming study presented in Section 6 and also the optimization study of the combustion transition cooling.

Chapter 6

Heat transfer methodology comparison

The section addresses the impact of conjugation on the computed results by performing a sensitivity study comparing the decoupled and CHT approaches. The sensitivity includes changing thermal conductivity ratio. $\lambda^* = \lambda_s/\lambda_f$. In addition, the problem of the turbulent offset jet also includes an investigation of two key turbulence settings, namely the turbulent Prandtl number, Pr_t and the turbulence intensity, Tu(%). The total amount of simulations for the case of the turbulent offset jet equals 13 cases for each HT methodology. The study was conducted for both coarse and fine wall mesh setting. For each thermal conductivity ratio ($\lambda^* = 1 - 50$), the turbulent Prandtl number, Pr_t , and Turbulent intensity were kept at constant values of 0.9% and 2%, respectively, and vice versa, thermal conductivity ratio was constant at 1 when varying $Pr_t = 0.4 - 1$, and Tu = 2% - 15%. In order to study the heat transfer characteristics, results are presented in both interface profiles and averaged quantities, and the effect of each parameter has been discussed.

The reasons for choosing the turbulent Prandtl number can be traced back to the definitions of the wall treatment functions. There is also substantial relevance in reacting flows as explained in the appendix, and the applicability of Reynolds analogy in additively-manufactured channels, similarly to the ones that will be used for the internal cooling of the TP. Hence, the effect that this parameter has on the conjugation effects is of great interest. Moreover, inlet turbulence intensity provides a simplistic approach into quantifying the effect of turbulence at the inlet. The transported variables at the flow boundary are estimated using (for all $k - \varepsilon$ models)

$$k = \frac{3}{2} (Iv^2) \quad (6.1)$$

$$\varepsilon = \frac{\rho C_\mu k^2}{(\mu_t/\mu) \mu} \quad (6.2)$$

The last parameter in the study is, as aforementioned, the conductivity ratio, which is an alternative approach to using the Biot number. The use of the Biot number presents a somewhat level of vagueness as explained in the next section.

6.1 Flat plate

In the present work, all computations are performed at the Reynolds number used for the validation of the code, $Re = 21,418$.

An alternative for the conventional Biot number is introduced: the mesh Biot number. The importance of such a modification is justified for the following reason: in CHT problems, it is known that

the ratio of the thermal conductivities plays a role (as previously established in the literature study, also with the Brun number). The drawback of this approach however is, first, the use of a reference temperature for calculating the heat transfer coefficient, and the characteristic lengths of the two media is not taken into account. Hence, the mesh Biot number reads:

$$Bi_{(\Delta)} = \frac{K_f}{K_s} = \frac{(\lambda_f/\Delta y_f)}{(\lambda_s/b)} \quad (6.3)$$

with Δy_f being the cell centroid wall-normal distance of the fluid region (FVM).

Table 6.1: Resultant Biot numbers from heat conductivity ratios

λ^*	\overline{Bi}^1	\overline{Bi}_{CHT}	Error(%)	$Bi_{(\Delta)}$
1	4.22	5.65	-34	275.86
5	0.84	1.11	-32	55.17
10	0.42	0.54	-28	27.59
20	0.32	0.26	-24	13.79
50	0.08	0.10	-20	5.52

The error tends to decrease as expected with increasing solid conductivity, which is traceable back to the requirement of $z \ll 1$. Figure 6.1 provides the solution for the interface temperature characterized by the variation of the conductivity ratio λ^* . The decoupled flow solution, where an *isothermal* wall condition was used is also plotted for reference with a broken line. The fluid film temperature ($T_f = \frac{T_\infty + T_b}{2}$) was used as a reference temperature for the wall. Hence, one decoupled flow simulation is used to subsequently map the heat transfer coefficient on the FEM solid solver.

The profile of the heat transfer coefficient achieved from a decoupled simulation (purely isothermal CFD) closely replicates the one that is also visible from the boundary layer approach from Luikov (see Figure 5.3), in which steep gradients are present in the leading edge and the profile tends to remain flat downstream. It should be noted that this profile is indeed unique for the fluid studied, and is hence dependent on the conductivity, Prandtl and Reynolds numbers, none of which are altered.

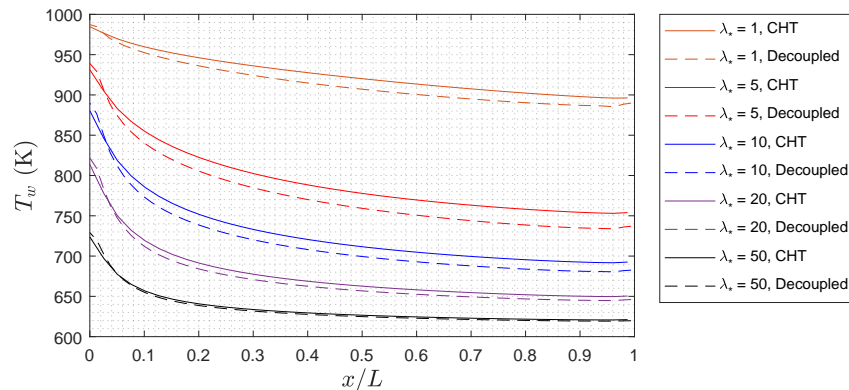


Figure 6.1: Wall interface temperature (solid side) as a function of all conductivity ratios consider.

It is clear that the difference between the two methodologies increases as the conductivity of the solid increases, which is in accordance to the theory of the lumped-capacitance analysis. The mean error along the interface is then 0.4%, 1.1%, 1.8%, 2.4% for $\lambda^* = 50 - 5$. For $\lambda^* = 1$, however the mean error is again reduced to 1.3%. The results comprise of surprisingly well predicted decoupled temperatures even

¹The value is calculated using the assumption that the average heat transfer coefficient stays constant (equation 5.23).

for large values of the Biot number well $\gg 0.1$. On the other hand, the decrease in the difference for low thermal conductivities (i.e. $Bi \gg 1$) is due to the fact that the wall temperature gradient decreases and local values approximate the value of the free stream temperature. This simplifies the boundary condition for the problem so that the usage of a constant temperature on the wall in a decoupled simulation (isothermal wall) is justifiable. The mesh Biot number underlines this observation: all values of $Bi_{(\Delta)} \gg 1$.

The velocity profiles are presented in Figure 6.2. The difference tends to increase downstream for larger conductivities, but remains negligible. This can be more clearly seen when the nondimensionalized velocity boundary layer thickness Δ_u is plotted, as presented in Figure 6.3. The two boundary layers, temperature and velocity, δ and δ_t are nondimensionalized as:

$$\Delta_u = \frac{\delta}{L} \sqrt{Re_\infty}, \quad (6.4)$$

$$\Delta_t = \frac{\delta_t}{L} \sqrt{Re_\infty} \quad (6.5)$$

where δ and δ_t are numerically estimated from the computation using the 99% rule (location where 99% of the respective field quantity value is reached). To reduce the potential for user error, the estimation was performed using a Java macro within STAR-CCM+. The limitation however of this method comes with the refinement of the mesh in y-direction, as the exact location where the criterion is met is rather substituted with the last cell centroid location where $\phi \leq 0.99\phi$. The nondimensional thermal boundary layer is also shown in Figure 6.3, along with the value obtained from the Boundary Layer approach from Luikov, see Eq.(5.16) and (5.15).

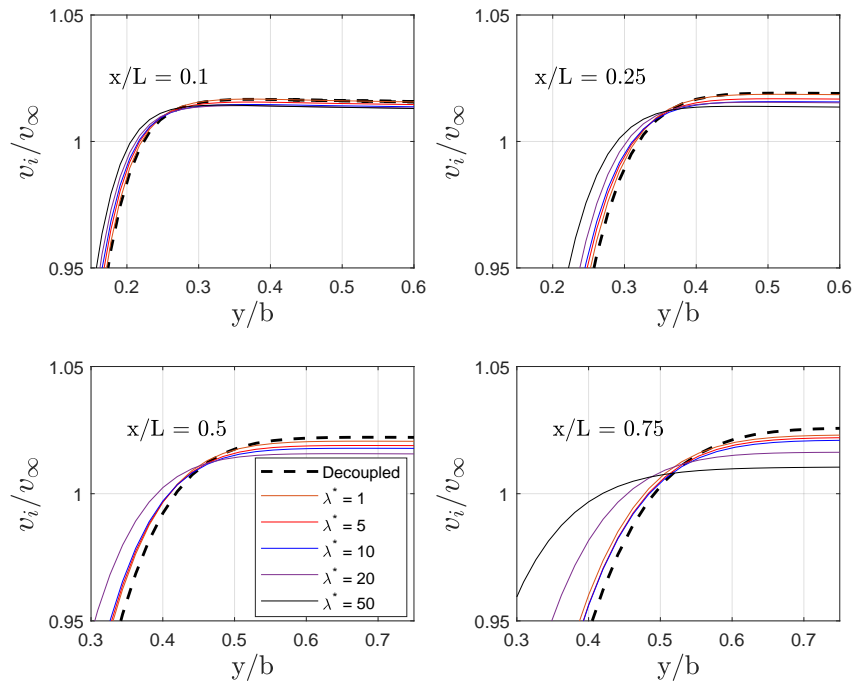


Figure 6.2: Velocity profile comparison for all thermal conductivity ratios at four different axial locations.

If one focuses solely on surface temperatures, then indeed, the two methodologies yield similar results. However, when it comes to the convective boundary layer, the effect of conjugation clearly becomes more prominent. Thermal conductivity of the solid begins to have a similar effect on the fluid behaviour as the Prandtl number. The thermal boundary layer decreases with decreasing conductivity and diverges from a CFD computation with an isothermal wall BC, partly tracable to the z criterion mentioned earlier.

The plot of the value of z (Eq.(5.14)) is shown below. The criterion of $z \ll 1$ is matched for all settings except $\lambda^* = 1$ and thus explains the increasing difference with the boundary layer obtained from the analytical solution with decreasing solid conductivity ($z \propto (\lambda^*)^{-1}$). Hence, the conductivity ratio does in fact provide some insight into the applicability of the decoupled method.

The effect is more clearly depicted as the ratio of the two boundary layers (ζ), shown in Figure 6.6. Theoretically, the ratio is a function of the Prandtl number (see eq.(5.15)), as outlined in the above paragraph. According to the Luikov BL method, it equals 1.12 for $Pr=0.66$. The value tends to be asymptotically reached with increasing λ^* . This however is purely due to the assumption taken for z necessary for deriving the Luikov relationship, which does not necessarily hold a physical basis, but is rather purely empirical.

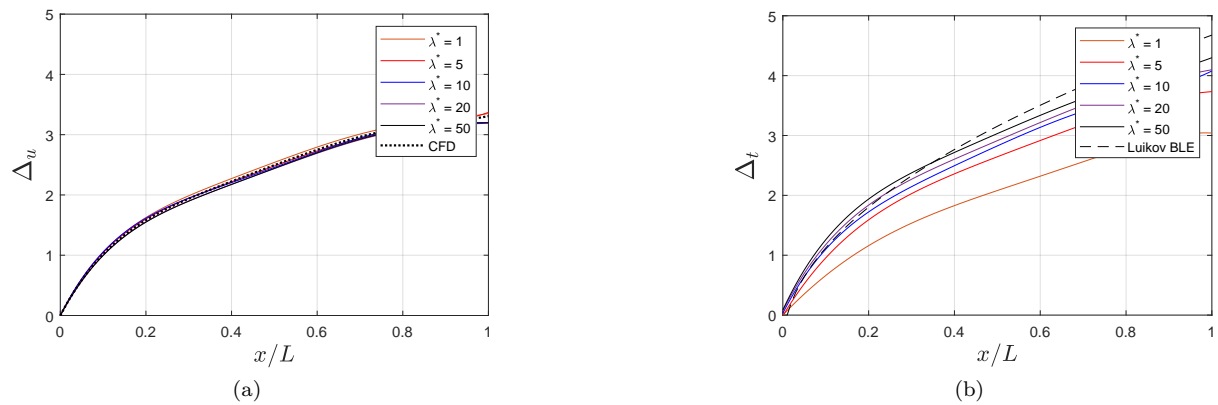


Figure 6.3: Nondimensional (a) velocity and (b) thermal boundary layers for all cases.

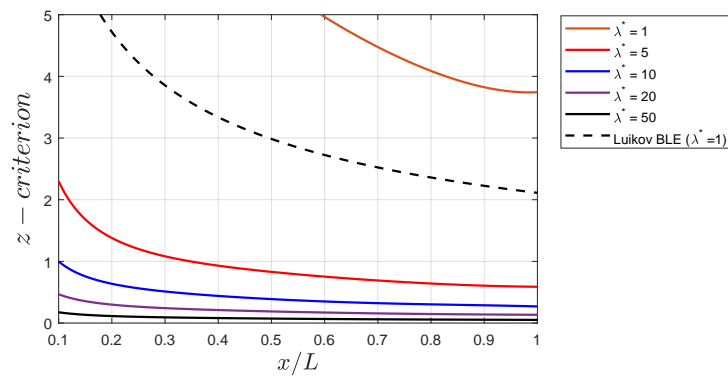


Figure 6.4: Critical z criterion for all cases

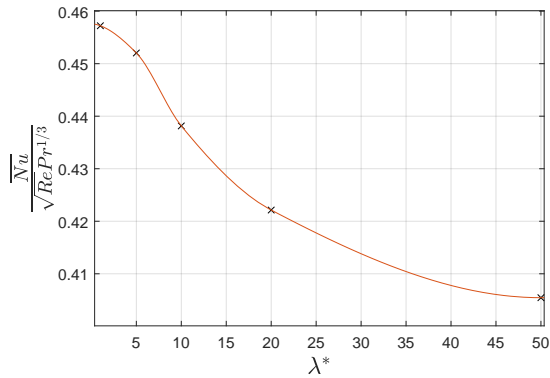


Figure 6.5: Averaged Nusselt number, derived from Eq.5.23 (shape-preserving interpolant)

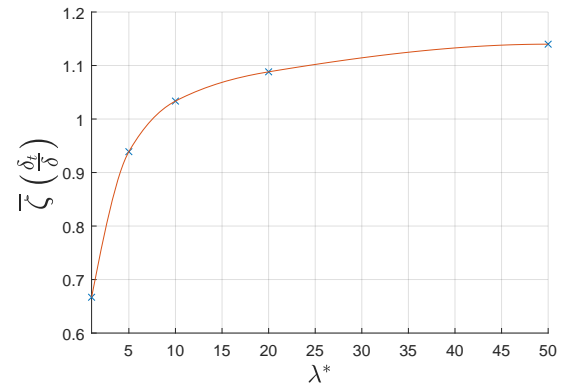


Figure 6.6: Effect of thermal conductivity ratio on boundary layer ratio (shape-preserving interpolant)

As demonstrated by the study, the resultant Nusselt number is larger in cases where the heat flux to the plate is accounted for (CHT). The increase is explainable by the decreasing surface temperature of the wall $T(x,0) = T_w$ along x , from ∞ to T . The temperature driving force (i.e. temperature differential between free-stream value and interface $\Delta T = T_\infty - T_b$) is hence increasing with x . From basic theory of heat transfer it is known that this differential increases in the direction in the flow, and thus the heat transfer coefficient (presented in the form of Nusselt numbers) also increases. For the case of isothermal decoupled simulations where the heat flux into the plate is not accounted for, $\Delta T = \text{const}$. One drawback of the approach in the study, however, is the *critical* temperature difference, $\Delta T_{cr} = T_\infty - T_b = 400K = 0.4 \cdot T_\infty$. This can also partially be used to explain the small difference between the methods even for $0.1 \ll 1$. Figure 6.7 presents the interface temperatures at a lowered bottom surface temperature, $T_b = 300K$ ($\Delta T_{cr} = 700K$), which clearly indicates that accuracy of the decoupled approach for a laminar flow case is dependent not solely on the thermal conductivity ratio but also on the critical temperature difference of the problem. A summary of the data is presented in Table 6.2.

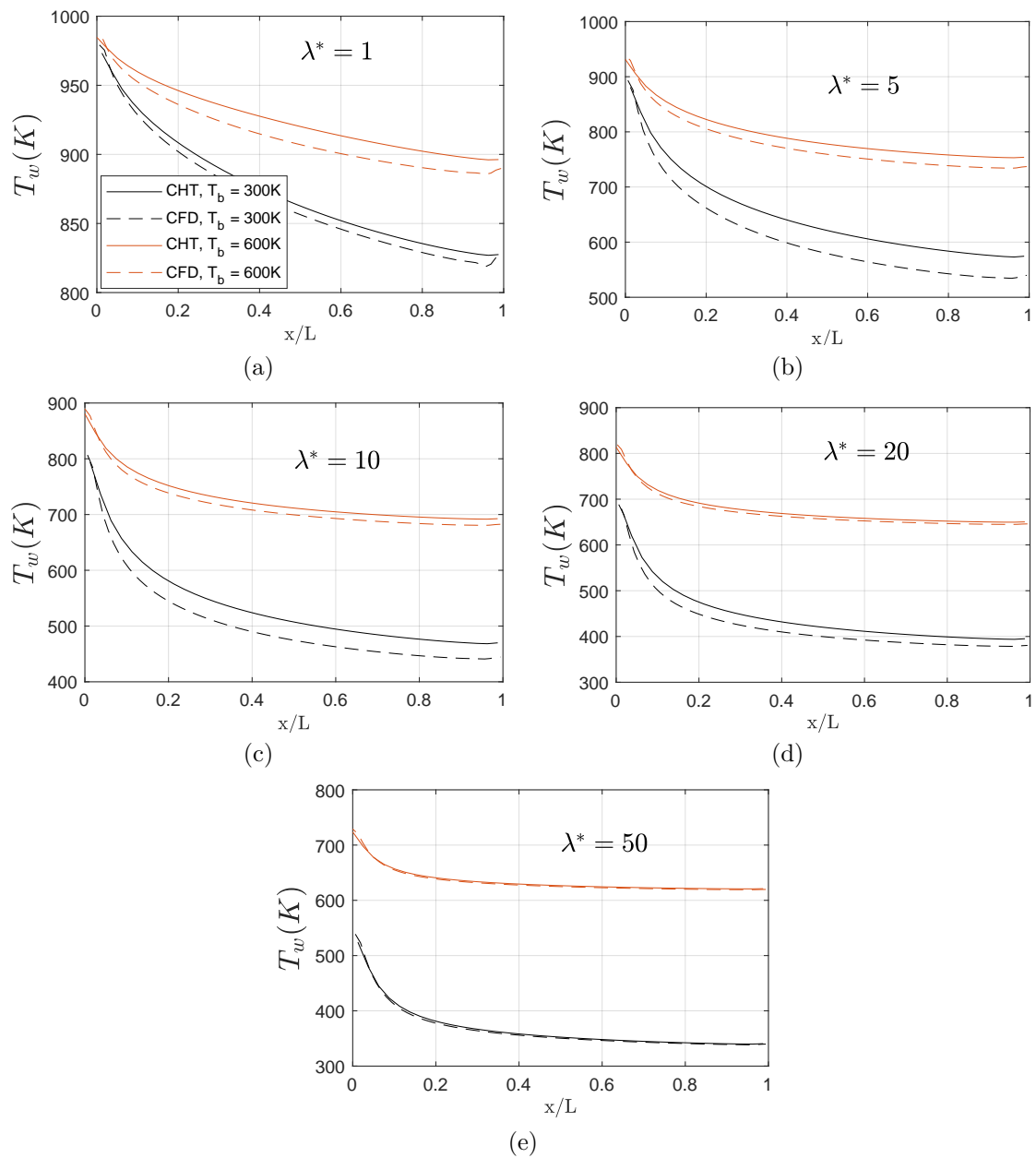


Figure 6.7: Comparison of interface temperatures using a decreased bottom plate surface temperature, for all conductivities (a) - (e).

Table 6.2: Summary of average heat transfer coefficient, and boundary layers comparison for all conductivities at $T_b = 600K$.

λ^*	Average HTC, \bar{h}			$\Delta_u(x=L)$			$\Delta_t(x=L)$		
	CFD	CHT	Error (%)	CFD	CHT	Error (%)	CFD	CHT	Error (%)
1	32.58	38.44	-17.98	3.58	3.59	-0.28	4.05	2.93	27.65
5	32.58	37.85	-16.15	3.58	3.59	-0.28	4.05	3.73	7.90
10	32.58	36.88	-13.21	3.58	3.38	5.59	4.05	4.08	-0.74
20	32.58	35.76	-9.76	3.58	3.39	5.31	4.05	4.09	-0.99
50	32.58	34.52	-5.97	3.58	3.39	5.31	4.05	4.29	-5.93

Table 6.3: Error comparison for average interface temperature for baseline and increased critical temperature difference ($T_\infty - T_b$)

λ^*	Average temperature, \bar{T}_w			
	CHT	CFD	Error (%)	Error $_{T_b=300K}$ (%)
1	925.62	914.59	-1.21	-0.66
5	794.20	776.39	-2.30	-6.27
10	728.89	716.73	-1.70	-6.14
20	677.11	670.92	-0.92	-4.77
50	635.13	633.21	-0.30	-0.48

Investigating however only the interface temperature distribution is a rather simplistic approach to comparing the two methodologies. The thickness of the thermal boundary layer showed that, the conductivity ratio does in fact have influence, and it is imperative that CHT is used for the conductivity envelop studied.

6.2 Turbulent offset jet

The common procedure followed in the case of turbulent flows is to employ an adiabatic wall boundary condition for a decoupled simulation, extract the specified- y^+ heat transfer coefficient and map it onto the FEM solid only solver (**n.b.**, an isothermal wall in the laminar plate case).

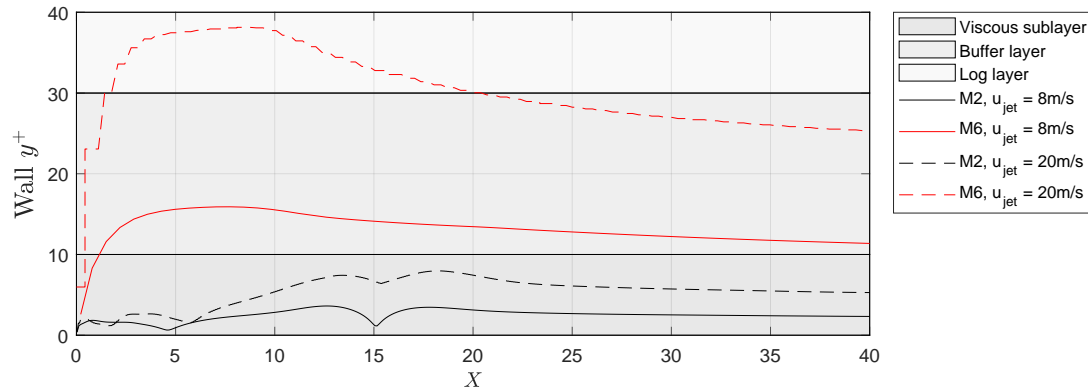


Figure 6.8: Comparison of resultant wall y^+ profiles from the validation case and the methodology comparison with increased jet velocity. The value of the wall y^+ is still ≤ 10 for the blended WF approach, which is beneficial for the consistency of the study.

Another important adjustment is in the increase in the jet nozzle velocity to 20m/s. This was done with the sole purpose of addressing the uncertainty of using the high- y^+ approach without the criterion of $y^+ > 30$ being satisfied, and ensuring that the full range of the blended approach is tested (i.e. the first cell is in the viscous sublayer at $y^+ < 10$). An example of the resultant first-cell y^+ values in the two cases is shown Fig.6.8 above.

Prior to investigating the effects of the aforementioned parameters in the sensitivity study, it is useful to compute the resultant difference in the validation study using the experimental data from Pelfrey, should the decoupled approach was used instead.

The resulted temperature profiles on the wall are shown in Fig.6.9 and Fig.6.10. A comparatively low difference is found between the two methodologies. For both, the temperature using the CHT approach is higher than the decoupled approach in the recirculation and impingement regions. The opposite holds for the blended WF approach in the wall jet region. The difference for both WF, however, is marginal. It could be argued that it is due to the comparatively low thermal conductivity material of the solid plate in the experiment ($\lambda^* = 1.04$). From the previous laminar flow sensitivity study, it has been found that conjugation plays no role in the HT process due to the low temperature gradients in the flow direction. The same can also be assumed for the case of a turbulent flow. A more detailed discussion is made in the upcoming sections where the previous λ^* envelop is also applied for this problem.

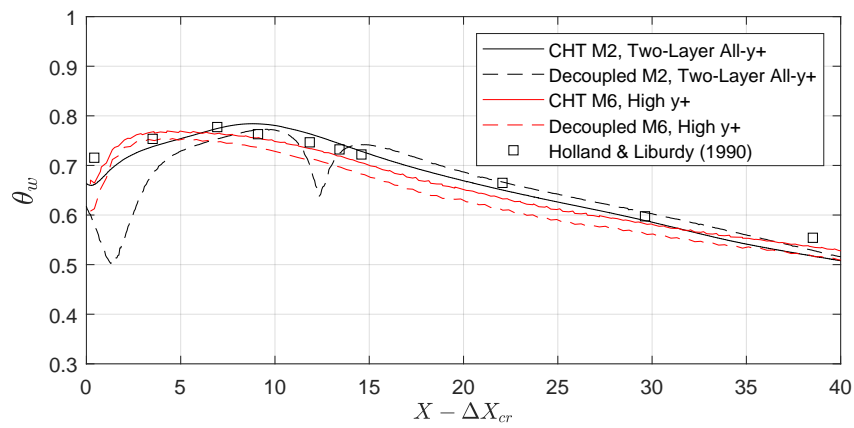


Figure 6.9: Local wall interface temperature (solid side) as a function of Pr_t .

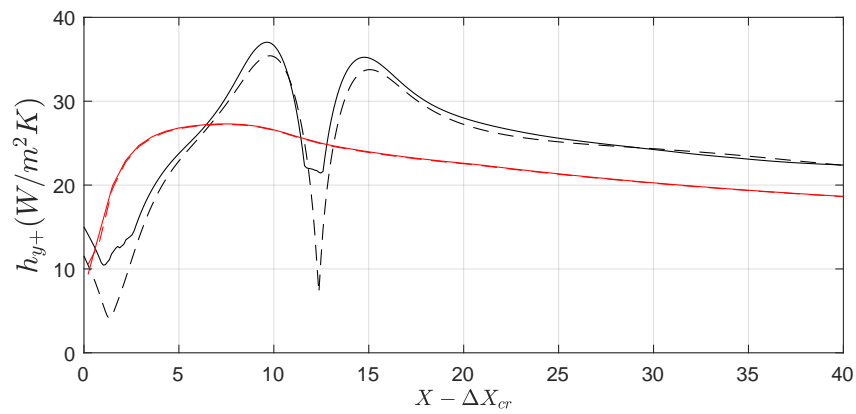


Figure 6.10: Local wall interface temperature (solid side) as a function of Pr_t .

6.2.1 Turbulent Prandtl number

The resultant temperature and specified y^+ heat transfer coefficient for the two-layer all- y^+ wall function are plotted in Fig. 6.11 and Fig. 6.12 below. As expected and noticed in literature, interface temperature tends to decrease with decreasing Turbulent Prandtl number (i.e increasing thermal eddy diffusivity). Similarly to the laminar flat plate case, the temperature is higher along the entirety of the plate length when using CHT approach. The divergence between the two methods is more pronounced in the turbulent wall jet region (i.e. $X > 20$). With regards to heat transfer coefficients, the difference is less visible. The values for both methods tend to remain identical for all regions, except for the impingement. The decoupled approach slightly overpredicts the HTC and also results in a reattachment length which is slightly lower than the one obtained from the conjugate method.

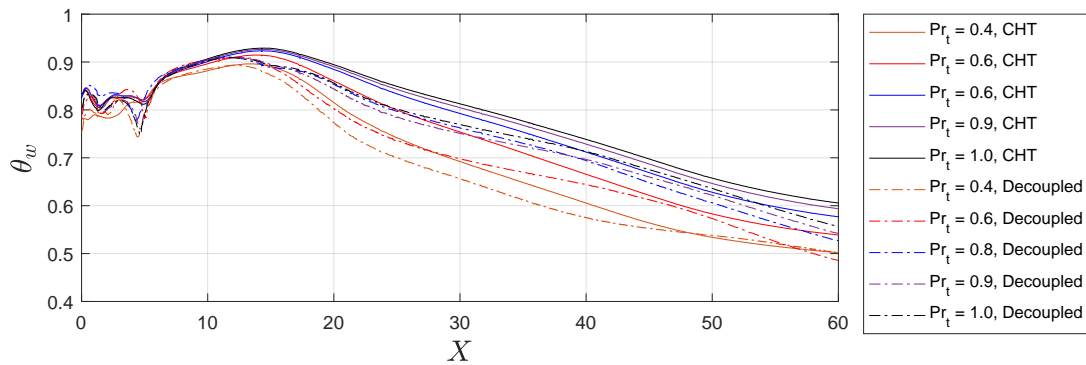


Figure 6.11: Local wall interface temperature (solid side) as a function of Pr_t .

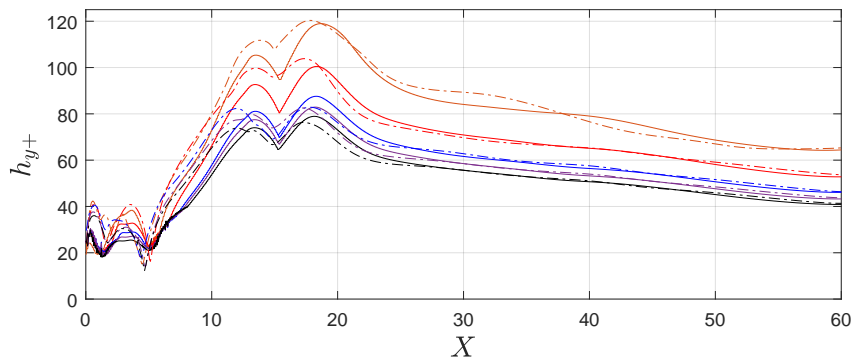


Figure 6.12: HTC as a function of Pr_t .

Analogously, the observations mentioned above also hold for the high- y^+ approach, shown in Fig.6.13 and Fig 6.14: the temperature difference is higher in the wall jet region, whereas in the impingement region, it tends to zero. The opposite is found for h_{y^+} and interestingly, the difference is augmented in the impingement, in comparison to the blended wall treatment approach.

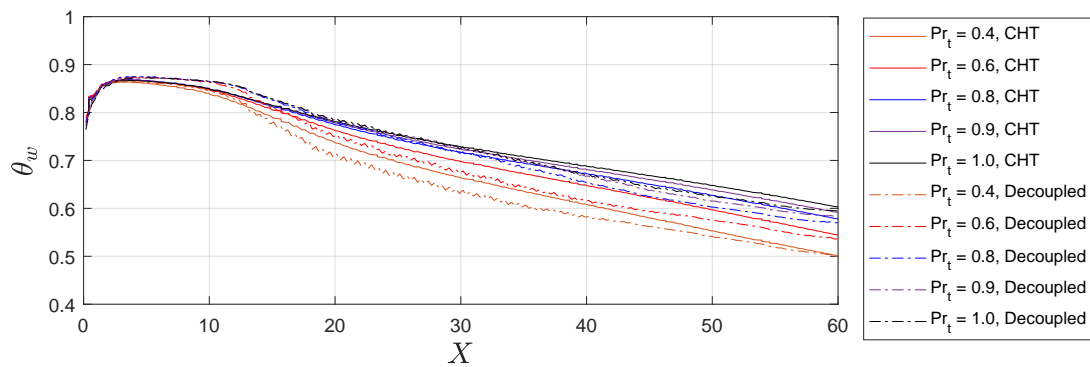


Figure 6.13: Local wall interface temperature (solid side) as a function of Pr_t .

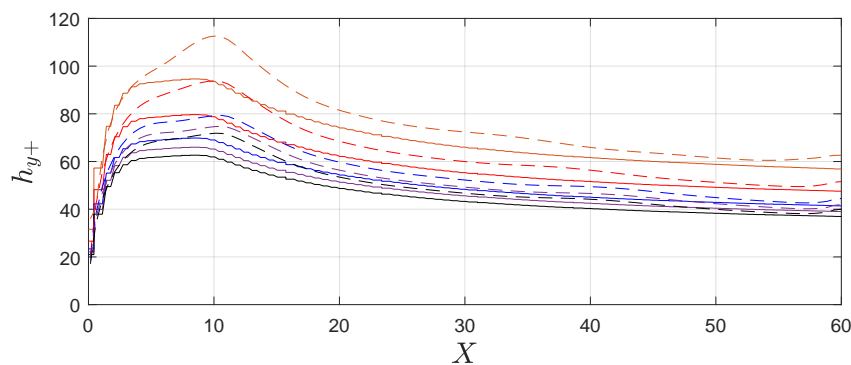


Figure 6.14: HTC as a function of Pr_t .

In order to compare the conjugate and decoupled approach more broadly, the surface averaged temperature, $\bar{\theta}_w$, reattachment point, X_{cr} , and the surface averaged specified- y^+ heat transfer coefficient are shown in Fig. 6.15 across all Pr_t values.

Looking at the resultant difference between the HT methodologies, a concrete relationship with the turbulent Prandtl number seems to be missing. The only evident variation is in the averaged surface temperature. The absolute value however for all settings remains negligible and cannot therefore be attributed solely to the effect of conjugation.

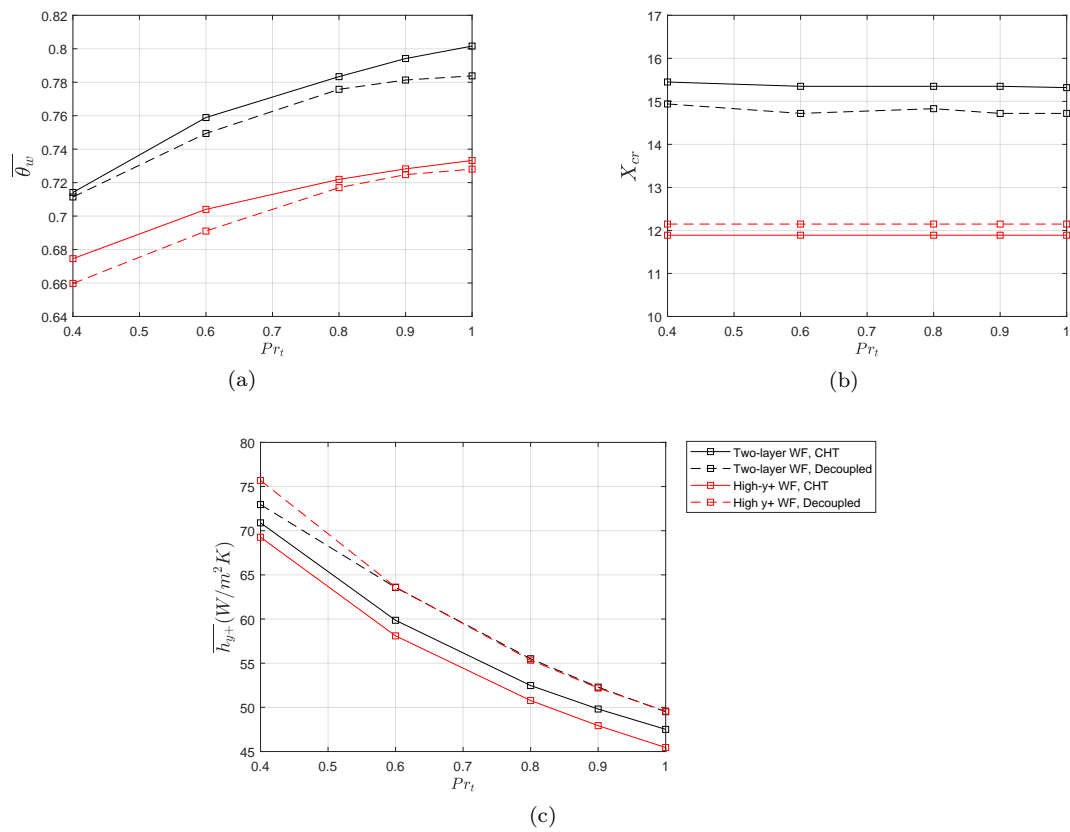


Figure 6.15: Influence on surface averaged values of (a) temperature, (b) reattachment length, (c) specified- y^+ heat transfer coefficient

6.2.2 Turbulence intensity

Similar approach in the comparison is followed for the effect of turbulence intensity on conjugation as well. As shown in Fig.6.16 and Fig.6.17, no clear influence on temperature and HTC, respectively is present. The maximum absolute difference percentagewise for θ_w and h_{y^+} equals 18%($X = 60$) and 66%($X = 11.5$) at $Tu=2\%$ and $Tu=15\%$, respectively for the Blended WF. Similarly, for the high- y^+ WF treatment the values are 19.3%($X = 34$) and 29.7%($X = 9.8$) both at $Tu=15\%$.

The small difference in the interface scalars is due to the inherent quick dissipation of the turbulence intensity characteristic for such a flow problem. As it can be seen in Fig. 6.18 and Fig.6.19, where, although not available for post-processing directly in a RANS model, one can trace back to turbulence intensity via the turbulent kinetic energy (see eq. 6.1). The value of the TKE is little influenced particularly in the vicinity of the wall, and hence the heat transfer process is not affected. The value is maximum in the impingement region, and when high turbulence intensity is considered ($Tu= 15\%$), near the jet exit region where the jet interacts with stationary fluid. Turbulence intensity tends to remain constant in both inner and outer shearing layers for all cases.

On the other hand, if one considers the case of the high- y^+ treatment, the resultant distribution of turbulent kinetic energy differs substantially. This however is not due to the wall treatment but rather the numerical dissipation from the needed coarse mesh settings, pinpointing to one of the drawbacks of this methodology, as shown earlier in the chapter. The resultant effect of $Tu(\%)$ is more pronounced throughout the entirety of the jet near the nozzle and not exclusively at the shear layers. The turbulent kinetic energy is also higher at the reattachment point compared to the case of low turbulent intensity.

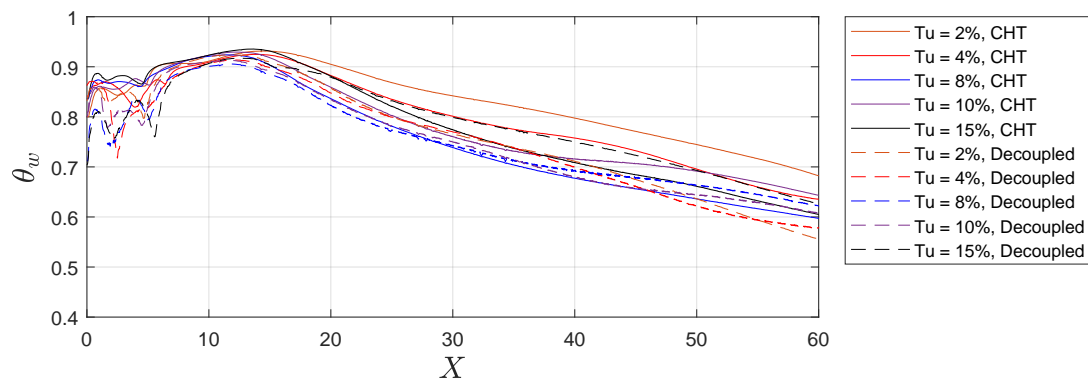


Figure 6.16: Local wall interface temperature (solid side) as a function of $Tu(\%)$.

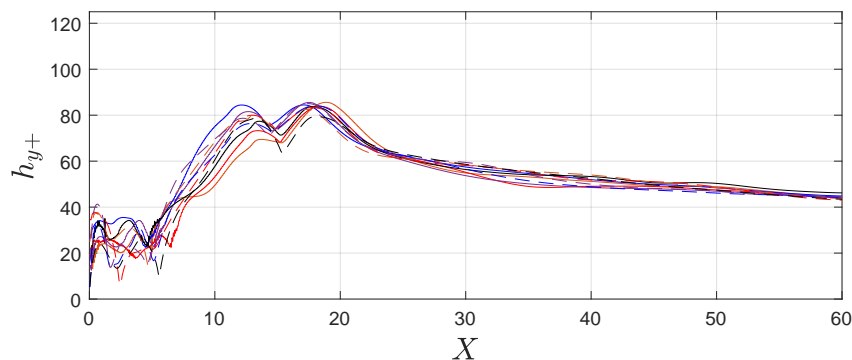


Figure 6.17: HTC as a function of $Tu(\%)$.

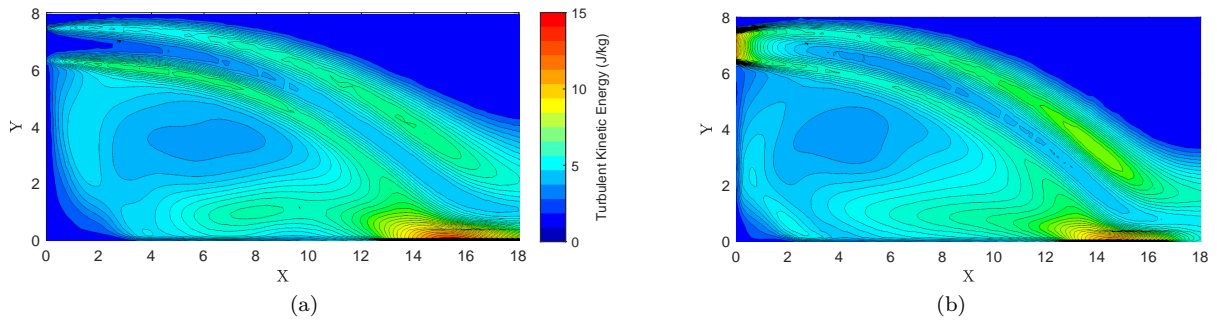


Figure 6.18: Turbulent kinetic energy for (a) $Tu = 2\%$, (b) $Tu = 15\%$ using a fine mesh (M2) and the blended wall function approach.

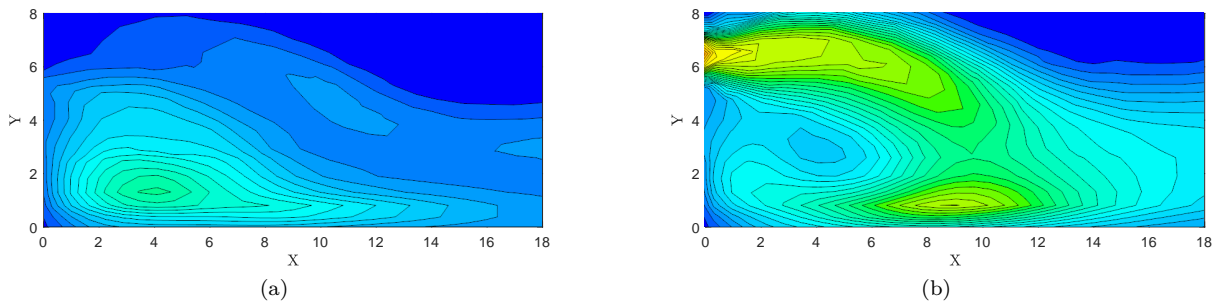


Figure 6.19: Turbulent kinetic energy for (a) $Tu = 2\%$, (b) $Tu = 15\%$ using a coarse mesh (M6) and the high- y^+ wall function.

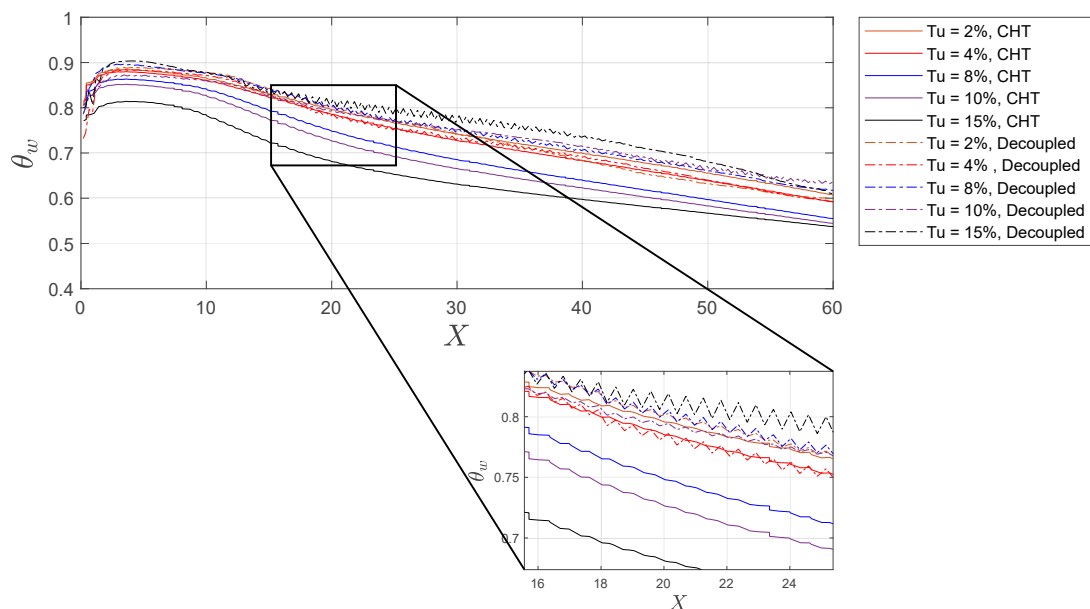


Figure 6.20: Local wall interface temperature (solid side) as a function of $Tu(\%)$.

Thereby, the resultant effect of turbulence intensity is more pronounced when a coarse mesh is used, from which the following observation is found: the difference between the heat transfer methodologies

tends to increase with increasing turbulence intensity. This more visible in the resultant average surface temperatures, where a clear divergence is found between the solid and broken red lines in Figure 6.22a. The same hold also for the reattachment length, indicating that conjugation could play a role on the aerodynamic characteristics of the flow should a coarse mesh be used. No clear trend of the heat transfer coefficient can be established: the value tends to fluctuate between ≈ 53 and ≈ 50 with standard deviations of 0.763 and 1.188 for the decoupled and conjugate approach, respectively.

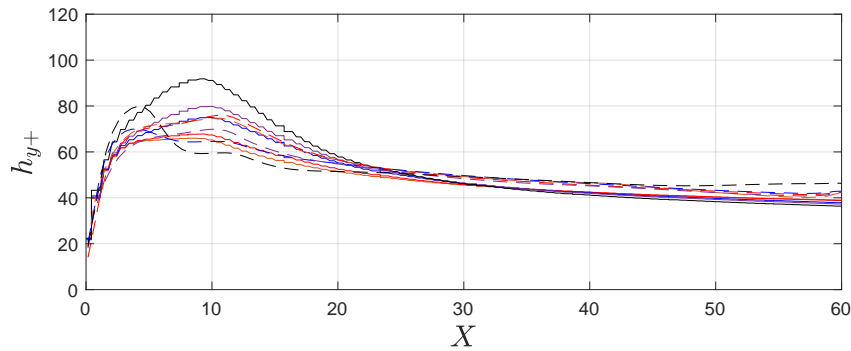


Figure 6.21: HTC as a function of Tu(%).

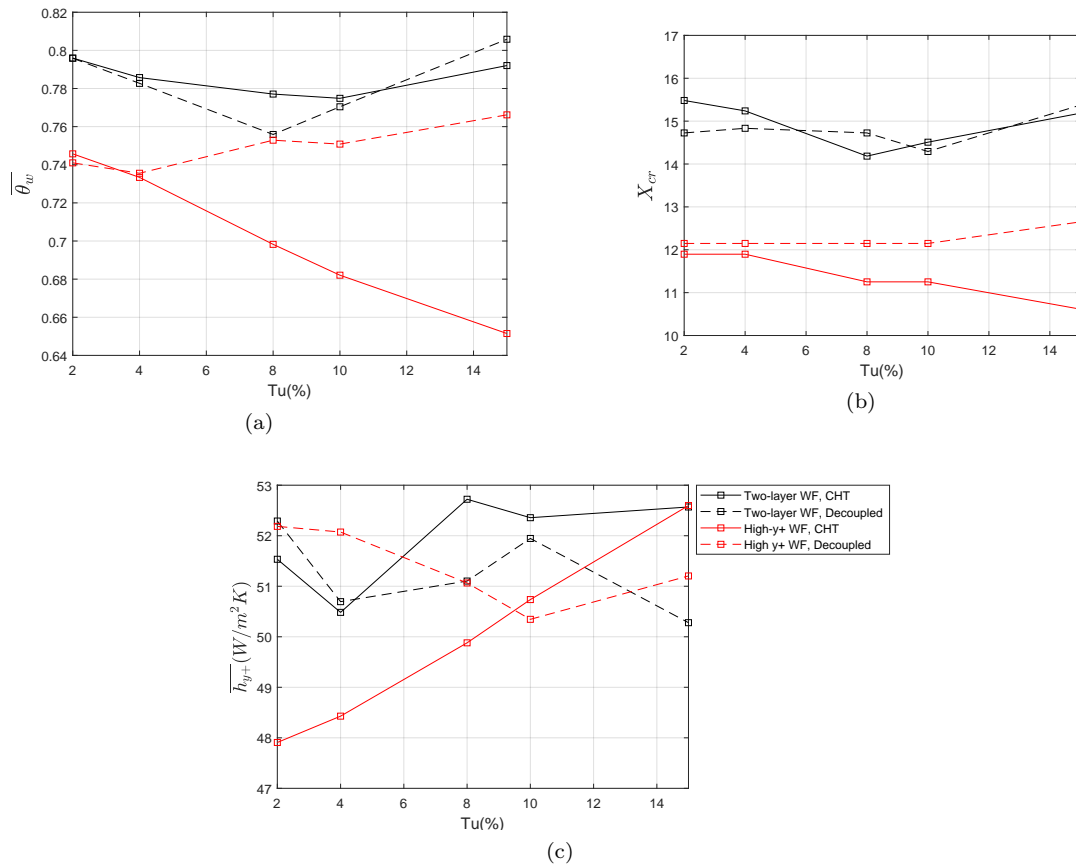


Figure 6.22: Influence on surface averaged values of (a) temperature, (b) reattachment length, (c) specified- y^+ heat transfer coefficient

Overall, the sensitivity study on turbulence intensity showed little to no influence on the effect of conjugation particularly for a blended WF approach. The influence was more prominent when a coarse mesh was used, where the the two HT methodologies yielded different results with increasing Tu(%). According to author's assumption however, this is also partially due to the effects of a coarse mesh setting on computed flow parameters.

6.2.3 Thermal conductivity ratio

The results from the thermal conductivity ratio sensitivity study to an extend contradict the established expectations from the laminar flat plate sensitivity study. In the latter it was established that increasing the solid thermal conductivity to values of $\ll 0.1$, lessens the effect of conjugation. This was established not to be the case when considering turbulent conjugate heat transfer as shown in the interface temperature at the wall in Fig.6.23 below. It is also worth emphasising on the difference in the decoupled approach used in the two cases: an *isothermal* wall for the laminar plate and an *adiabatic* wall in the case of the turbulent offset jet.

The difference between the two methodologies is mostly present in the impingement region and tends to decrease in the wall jet region. The difference in the impingement seems to be dependent on the thermal conductivity ratio with the tendency to increase at the peak values ($X = X_{cr}$), whereas the wall jet region values are irrespective of the solid conductivity.

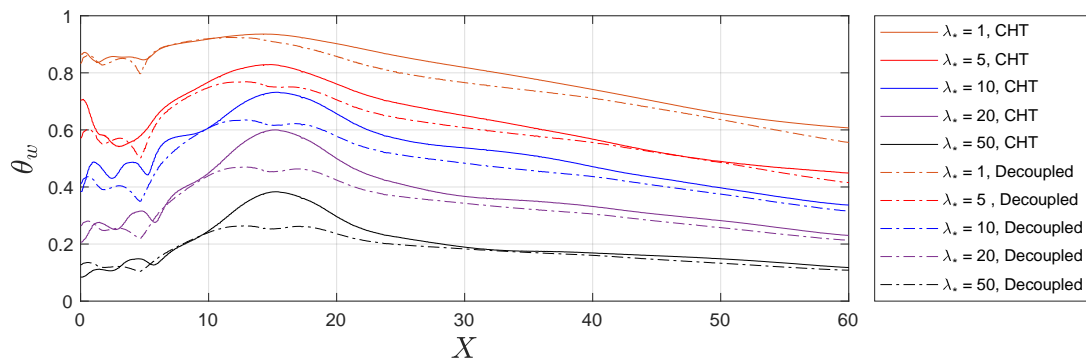


Figure 6.23: Local wall interface temperature (solid side) as a function of λ^* .

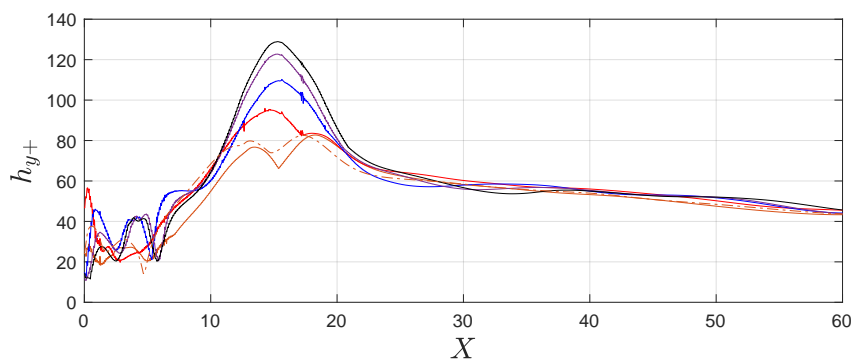


Figure 6.24: HTC as a function of λ^* .

The difference is diminished and close to virtually zero when a coarse mesh is used, as shown in Fig.6.25. The influence of increasing thermal conductivity is also negligible when considering the heat transfer coefficients, presented in Fig.6.24. The difference in the wall temperature is again the highest

near the impingement region and this time roughly remains constant. Again, these findings can be attributed to the high numerical dissipation of the coarse mesh

For both mesh settings the difference between the two HT methodologies can be explained in an identical fashion. In both cases, blended and high- y^+ , an identical heat transfer coefficient is exported and mapped onto the FEM solver. Thereby, the temperature profiles for all decoupled computations are inherently similar. The effect of the heat transfer coefficient augmentation for example, obtained in the blended approach (see Fig.6.24) is not transferred onto the solid region, since the heat transfer coefficient that is exported (no conjugation - broken orange line) is comparatively 'flat' in the vicinity of the impingement, which is in turn also visible in the wall temperature profile. The same applies to the coarse mesh, with the exception of little influence on the heat transfer coefficient with increasing solid conductivity.

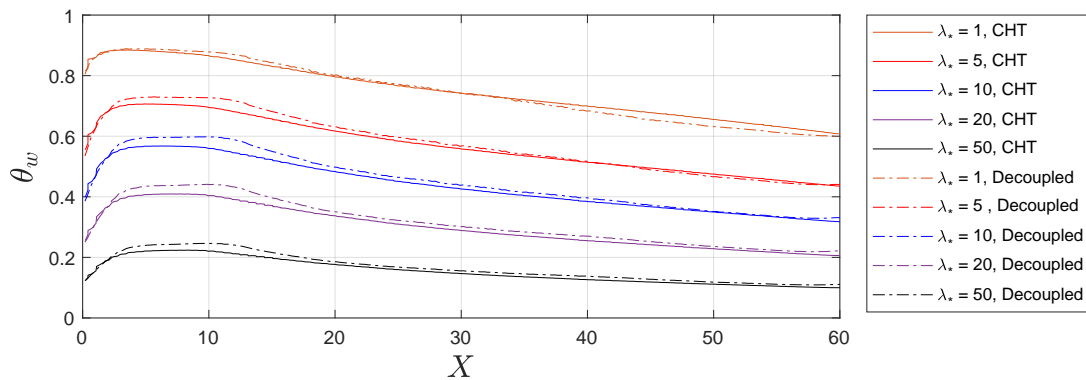


Figure 6.25: Local wall interface temperature (solid side) as a function of λ^* .

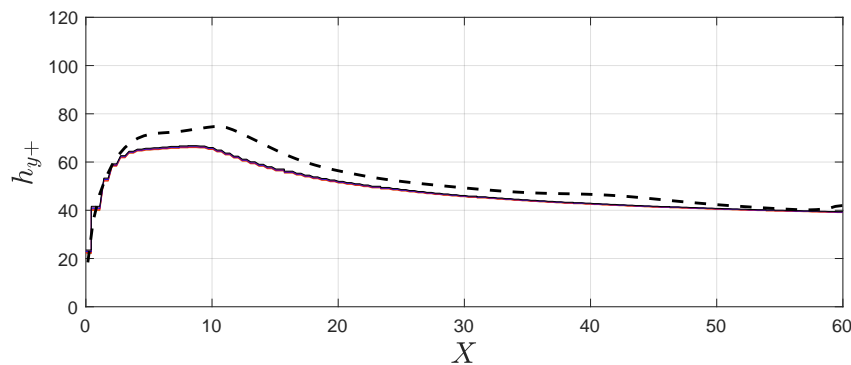


Figure 6.26: HTC as a function of λ^* .

Another important finding is that, in fact, the CHT approach results in a higher temperature profile when a fine mesh is used, whereas the opposite holds for a coarse mesh setting: the decoupled HT approach results in higher temperatures. The difference is as mentioned more pronounced for the fine mesh settings, but in both cases it remains negligibly small. This is also visible in the surface average profiles in Fig.6.27a. The averaged values of the heat transfer coefficient scalar and the reattachment length also reflects the abovementioned analysis.

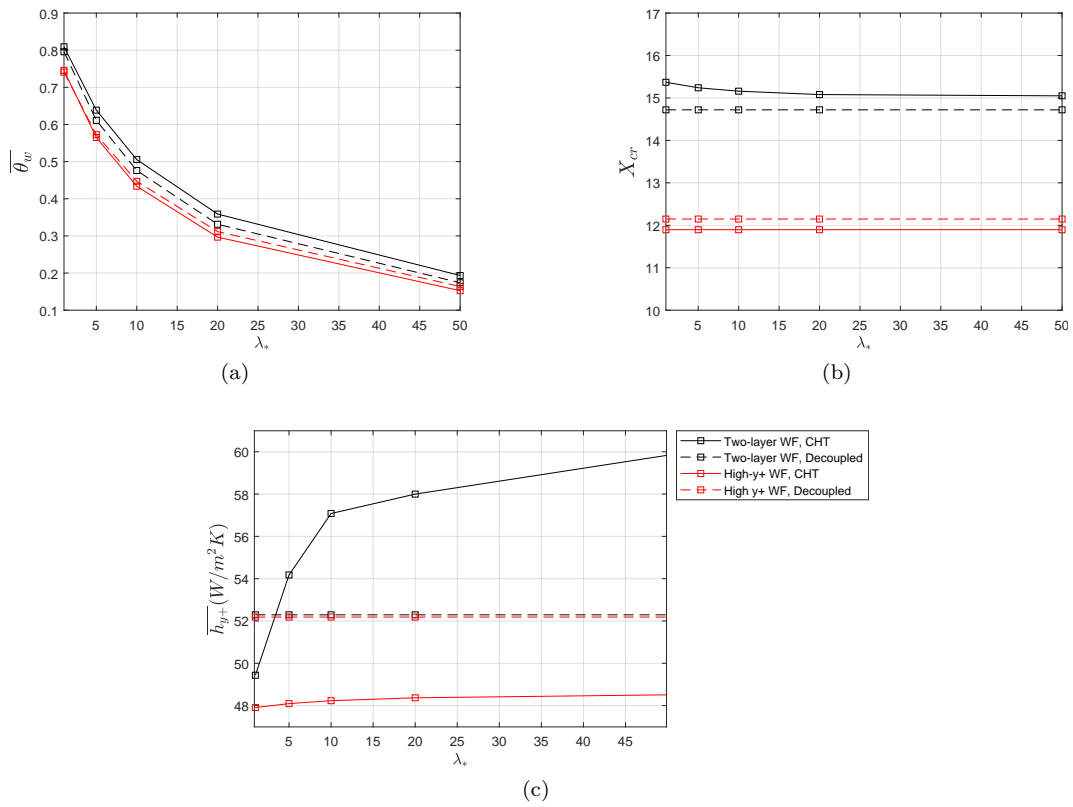


Figure 6.27: Influence on surface averaged values of (a) temperature, (b) reattachment length, (c) specified- y^+ heat transfer coefficient

6.3 Summary

The chapter included a comprehensive validation procedure and analysis of both laminar and turbulent flow conjugate heat transfer methodologies, that ought to be followed in the upcoming part, where an optimization is performed, followed by a comprehensive sensitivity study on both problems.

The laminar flow CHT solver in STAR-CCM+ was successfully validated and yielded results comparable to an analytical solution within an acceptable accuracy for two Biot number settings. The difference was discussed and concluded that it is due to the assumption used in the laminar solutions (incl. the velocity from Blasius and temperature profiles from Luikov).

The validation study of the turbulent CHT problem showed that the realizable $k - \varepsilon$ model resulted in the most accurate solution when compared to experimental data, explainable by the different formulation of the eddy viscosity term. The temperature profile for all turbulence models studied was otherwise within an 8% difference from the experimental data (SST $k - \omega$ and standard formulation of the $k - \varepsilon$ models). This difference was shown to decrease to less than $\approx 5\%$ when a coarser mesh was used with a high- y^+ wall treatment, an effect attributable to the numerical dissipation from the mesh.

Moreover, the sensitivity study addressed two decoupled approaches: isothermal wall and adiabatic walls for the laminar and turbulent flow problem, respectively. Contrary to the popular guideline for conjugation use for $\overline{Bi} \ll 0.1$ and $\overline{Bi} \gg 1$, the study showed the error with the decoupled approach is in fact negligible for the entire envelope, particularly for $\lambda^*(\lambda_s/\lambda_f) > 1$, i.e. a solid region with a thermal conductivity considerably larger than that of the fluid region. The study pointed the importance of the critical temperature difference ($T_\infty - T_b$) and proved that it is another important parameter that has to be taken into account when choosing a HT methodology. With respect to the turbulent offset jet, no firm dependency of the conjugation effect was found with respect to Turbulent Prandtl number and turbulence intensity. The only visible apparent increase in the necessity for CHT was established at increasing solid conductivities, contrary to the findings of the laminar flat plate, where increasing λ^* yielded to essentially no difference. The difference was shown to be pronounced solely in the impingement regions of the jet. The difference in the wall jet and recirculation regions were also negligible.

The specific findings of the validation study are carried over to the optimization case of the transition piece cooling. In it, the realizable $k - \varepsilon$ model is used along with a blended WF approach. Due to the presence of internal cooling inside the GT component, the analysis employs the CHT approach, in order to take the heat pick-up inside the cooling channels into account. The use of the decoupled approach for internal cooling is hence strictly not recommended as it will result in grossly overestimated cooling performance (channel wall temperature being higher than in reality). As discussed in the upcoming chapter, the reasons for using the blended WF approach is pointed out too.

Part II

GT Transition Piece

Chapter 7

Gas Turbine Transition Piece Analysis

As initially mentioned in the introductory chapter of this report, the study does not include the full-scale transition. The reasons are explained in further detail in the upcoming sections, but they can be overall summarized as a hedge against high computational costs of optimization studies of large components. The drawback of this approach is mentioned as well. The chapter is comprised of a thorough description of the computational domains used, description of the rib parameters, followed by a brief comparison of the baseline flow fields of the baseline cases and a discussion on the findings.

7.1 Computational domain

Due to the size of the full transition piece, using a 1:1 scale model for the computational domain would make the optimization task infeasible from a computational cost point of view. Therefore, the component was simplified into two separate parts: top and bottom panels, as shown in Fig. 7.1. The drawback of such approach is its inability to predict the lifting enhancement of an actual transition piece. However, it allows for easy parametrization and an insight into potential cooling improvement that can be re-applied into a full-scale transition model, depending on the findings.

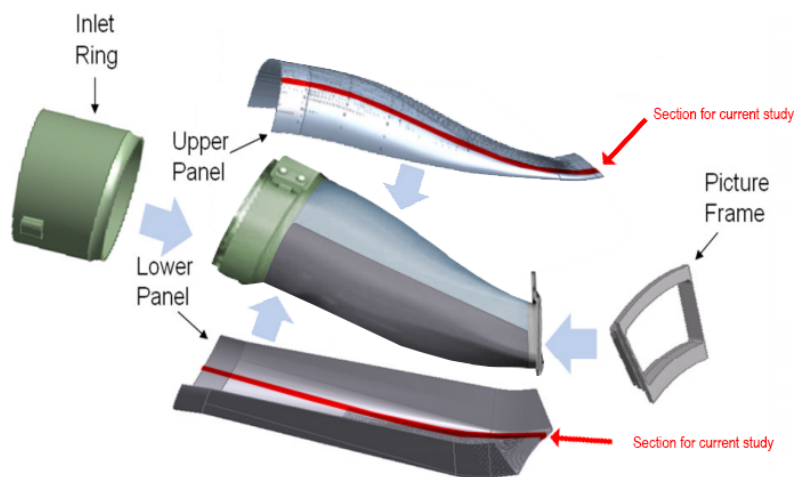


Figure 7.1: Illustration of approach used for discretizing the transition piece geometry into a parametric *slice* (shown in red), consisting of two counter-current channels. Original unedited (author's TP is replaced with the Siemens 8000H TP) picture is obtained from [93]. The figure has an illustrative purpose only, and components are not to scale.

The shape of the cooling channels and the shape of the panel are fully parametrized (with parameters shown in the Appendix) allowing for both different channel designs and adaptable to accommodate the entire range of transition shapes as well as TBC thickness. Each panel was made using a spline CAD feature and consists of no curvature in the tangential direction (z -coordinate in the coordinate frame shown in Figures 7.2-7.3 below). The key dimensions are also shown in the domain schematics.

As visible in Figures 7.2-7.3, the cooling consists of a pair of counter-current channels with a circular cross section. The channels extract cool dump diffuser (i.e. compressor shell/plenum) air of temperature T_{diff} from top and bottom parts of each transition panel and dump the coolant air in the hot gas mixture from the combustion process, with a temperature of T_g , Fig. 1.4 presents a simplified overall arrangement similar to the one used in the study. For confidentiality reasons, temperature and pressure values are respectively nondimensionalised using:

$$\theta = \frac{T - T_{diff}}{T_g - T_{diff}}, \quad (7.1)$$

$$\Pi = \frac{p}{p_{comp}}, \quad (7.2)$$

$$U^* = \frac{\langle u \rangle}{u_\infty}, \quad (7.3)$$

where p_{comp} is the dump diffuser pressure, and u_∞ is the free-stream velocity from the combustor liner exit, as displayed in Fig. 7.2. The computational domain has a constant thickness in all regions of 6mm, with the baseline case (circular channels) using a channel pitch distance of 3mm (equidistant from the domain side walls). An additional extrusion is included at the end of the domain for convergence reasons.

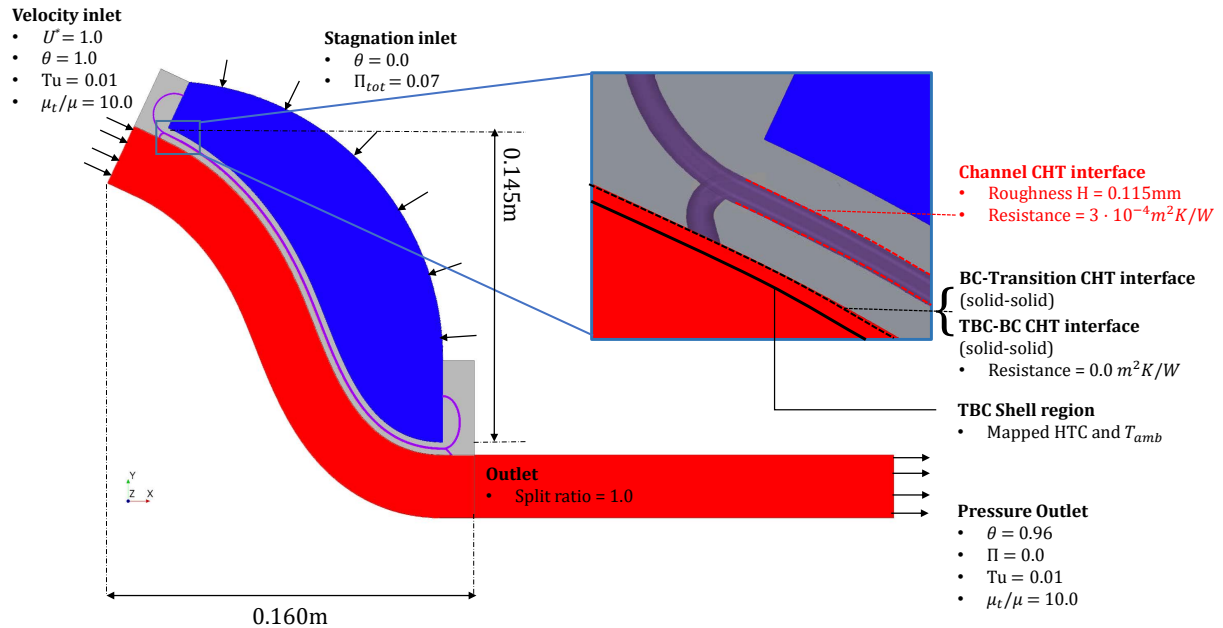


Figure 7.2: Top panel schematic and boundary conditions used, along with a close-up view of the channels, where relevant interfaces are illustrated using dashed lines. Red and blue are used to indicate fluid region (hot and cold flows, respectively), whereas gray is the transition metal region. Channel flow is shown in purple.

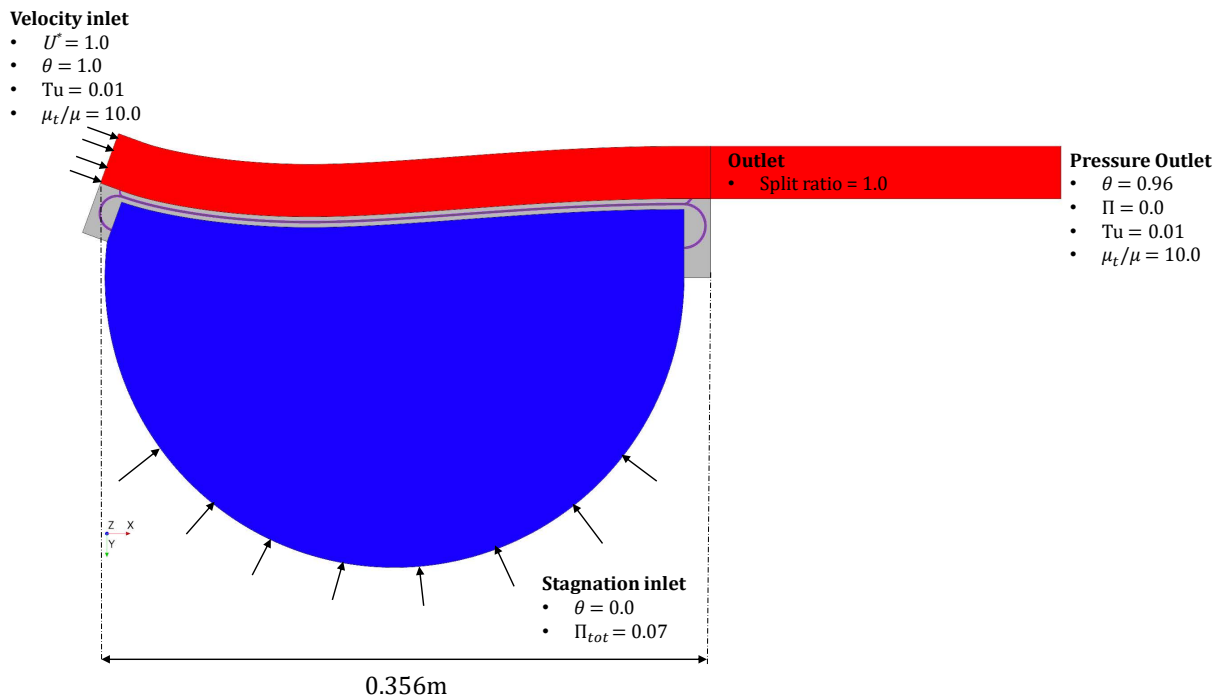


Figure 7.3: Bottom panel schematic and boundary conditions used.

In the numerical set-up used, only the channel wetted area is a conjugate (fluid-solid) interface (red broken line in Fig. 7.2). The solid-solid interface between the TBC and BC is also a CHT interface, and since no thermal resistance is added to the BC-TP interface, the BC essentially has no effect on the HT performance. The figure below presents a simplified schematic of the types of BCs on the TP walls: it can be said that the analysis hence uses a combined approach: decoupled HT (mapped h_{bulk} and T_{amb}) on the walls, and a CHT on the walls of the cooling channels.

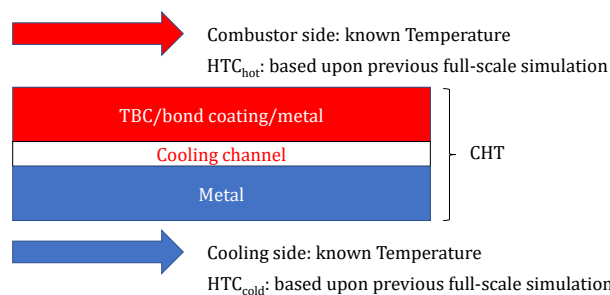


Figure 7.4: Types of HTC BCs and interfaces in the transition piece set-up.

The outlet BC at the start of the additional extension downstream in the hot region arises from the fluid-fluid interface with the original one. Using an outlet BC allows the outflow conditions to not be prescribed, but rather determined by the flow upstream of the outlet boundary. The split ratio of 1 indicates the fraction of the total outflow leaving at the given outlet boundary (i.e. entire flow) before eventually reaching the pressure outlet.

The domain side walls for both cases are modelled using a translational periodicity boundary condition. This also applies to the area of the TBC shell region and transition piece at the end of the domain. The hot and cold sides are mapped from a full GT mid-frame system model, allowing different *regions* of the transition to be evaluated without extensive turning of the boundary conditions, i.e. only the values

of the heat transfer coefficients. The heat transfer coefficient is mapped at three locations along the hot and cold sides and interpolated using a linear function. The distribution for both top and bottom panel is shown in the Fig. 7.14 below.

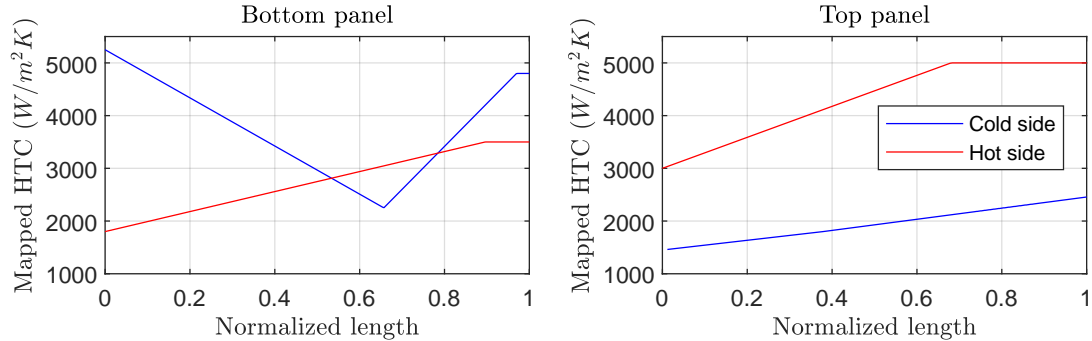


Figure 7.5: Mapped HTC on hot and cold sides of the top and bottom panels, extracted from a full midframe simulation.

The origin and reasons for using such HTC values for extrapolating a convective BC is beyond the scope of the project. Therefore, the values are not discussed and directly used in the current analysis. The potential impact of the resultant distribution, however, on the cooling performance is touched upon in the upcoming subsections. Due to lack of proprietary data on temperature profiles of the transition piece, the temperature profiles are not validated. The flow inside the circular cooling channels is compared to experimental data with a similar Reynolds number found in literature as a potential compromise for a validation of the resultant temperature fields.

The table below examines the CFD-predicted effective area of the transition piece and compares it to previously experimentally measured values using a test rig at Pennsylvania State University (PSU). The bottom and top panel estimates are obtained by simply taking the submodel effective area and multiplying by total channels for that panel.

Table 7.1: Non-dimensionalized transition channels effective area (A_{eff}/A_{ch}): validation of pressure drop calculation versus test measurements.

Bottom Panel	69.5
Top Panel	84.2
Total	153.7
Measured (experimental)	152.5

The channel effective area was approximated using the Bernoulli principle, i.e.:

$$A_{eff} = \frac{N_{ch} \dot{m}_c}{\sqrt{2\Delta p/\rho_c}} \quad (7.4)$$

with Δp , the pressure drop across the transition, calculated using the explicitly calculated values at the stagnation inlet and transition outlet (not the specified BCs values), and N_{ch} is the number of channels in the respective panel.

The assumptions made for building the computational model can be summarized as follows:

- Fluid flow is modelled using the 3D steady-state RANS equations;
- The model used is the realizable formulation of the $k - \varepsilon$ model, in accordance with the CHT validation studies presented earlier;

- The turbulence model employs the isotropic turbulence assumption for calculating the eddy viscosity;
- A blended-wall y^+ approach is used for near-wall calculation of velocity, temperature and turbulent flow field quantities;
- The model does not take radiation heat losses into account;
- The working fluid in the transition is considered as an ideal gas.

Additionally, an important distinction with the previously shown methodology has to be made:

A comparison between a FEM-FVM interpolation and a FVM-FVM conformal mesh interpolation showed that there is no reduction in the accuracy of the results. There was, however, a small reduction in the computational speed of a fully-converged simulation, which compounded into hundreds of runs in an optimization task would potentially lead to a faster solution. Therefore, for the sake of the computational cost of this study, **a FVM mesh is used for the calculation of the temperatures in the solid region.**

Table 7.2: Thermal conductivities used in the model.

Region	Material	Function	Value (W/mK)
TBC	Proprietary YSZ compound	Custom $f(T)$	Confidential
Transition metal	Ni-based super alloy	Constant	25
Coolant	Air	Sutherland's law	0.026 ($T_{ref} = 20^\circ\text{C}$)

With regards to solver settings, a segregated fluid enthalpy with second order upwind convection differencing scheme are used for the fluid region. As mentioned earlier, the Turbulent Prandtl number is set according to the field function in the validation study: value is set at 0.9 near the wall, and 0.4 in the free-stream. With regards to the thermal conductivities used, for all three regions, the value is tabulated above in Table 7.2. The proprietary field function for the TBC is omitted to avoid a conflict of interest.

7.2 Reynolds Analogy

Further addressing the (rough) channel effective area, attention has to be paid to the addition of the thermal resistance at the channel CHT interface, shown in red in Fig. 7.2. The results of previous flow tests conducted Pennsylvania State University [112] indicate a relative roughness value of 0.31 for horizontally-printed cylindrical holes. Considering the measured hydraulic diameter of the cooling channels of the TP, this results in a equivalent sand grain roughness of $175\mu\text{m}$. The numerical relationship between the equivalent (CFD) roughness height and the roughness function applied in the respective wall treatment method is briefly explained in Appendix E.3. Normalizing both friction factor and Nusselt number to smooth-wall values, it becomes apparent that friction factor augmentation is significantly higher than the Nusselt number augmentation, i.e. the penalty for added roughness is 2x higher than the heat transfer benefit in AM-channels. Therefore, the addition of a thermal resistance is used as a compromise in the heat transfer enhancement from the metal to the coolant, while still accounting for the penalty in the friction coefficient. The addition of thermal resistance at the interface hence leads to a reduction in the heat flux to the coolant, which results in an artificially reduced cooling effectiveness (i.e. higher temperatures on the channel walls). This can also be regarded as an adjustment for the non-applicability of the Reynolds analogy, which states:

$$St = \frac{h}{\rho u c_p} = \frac{C_f}{2} \quad (7.5)$$

with St , called the Stanton number. The non-proportionality between Nusselt number augmentation and skin friction increase in rough channels has been widely reported and literature, whereas the above-mentioned flow tests were validated against the data presented by Snyder [112]. The reason for the disproportionality is well-put by Bons [14] where he assess the applicability of the Reynolds analogy in GT flows and states that surface roughness introduces a large pressure drag component on the individual roughness elements to the net skin friction measurement with only a modest corresponding increase in heat transfer, which corresponds to a dramatic decrease of the Reynolds analogy factor (i.e. $2St/C_f$). The respective increase in both skin friction and Nusselt numbers reported in the paper for various AM-build directions are shown in Fig. 7.6(a)-(b), while Fig. 7.6 displays the trade-off between the two.

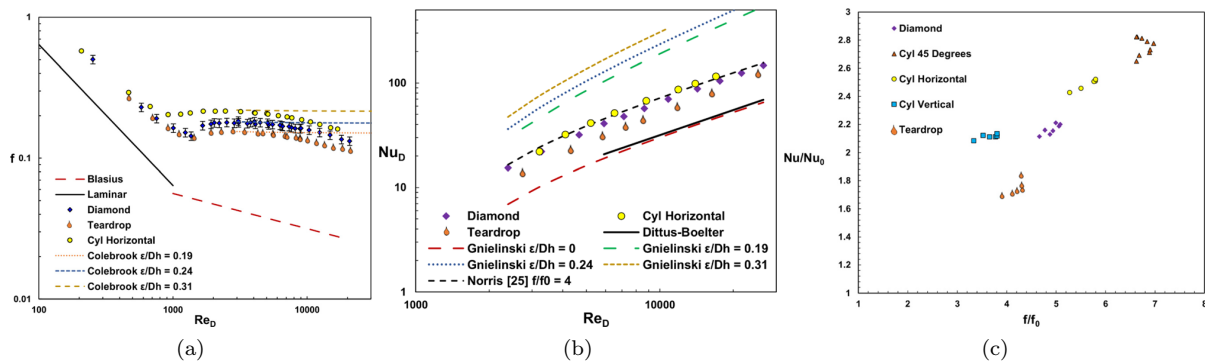


Figure 7.6: Roughness benchmarking for AM-channels of various build directions: friction factor f , Nusselt number (b) as a function of Re , and f and heat transfer augmentation for all tested channels (c) from Snyder [112].

The validation of this approach, which is beyond the scope of this project, has been performed a priori in-house at Siemens AG, where the resultant Nusselt numbers and friction factors are compared to the experimental results from [112] shown in Fig 7.6, using a range of equivalent sand grain roughness and the $k - \omega$ SST model. The exact results, however, are confidential and remain an intellectual property of Siemens AG, only the final value of the added heat resistance of $3 \cdot 10e-4m^2K/W$ is reported and used in this study.

7.3 Parametrization of cooling topology

As mentioned in Section 2.3.1 and pointed out in Fig. 2.12, various rib arrangements have displayed the best performance in terms of the trade off between friction factor and heat transfer enhancement. Thus, for the sake of this study, a rectangular rib turbulence geometry will be used. The parametrization is shown in the figure below.

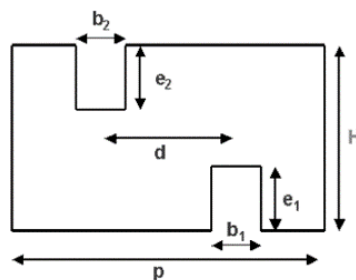


Figure 7.7: Schematic representation of key parameters used in the rib geometry

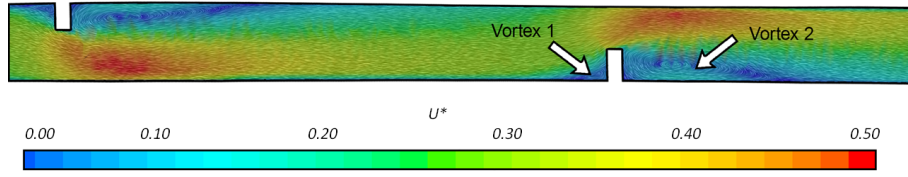


Figure 7.8: Resultant flow structure in the rib geometry used (top panel used for illustrative purposes). The structure closely resembles the flow structure commonly found in literature, see Fig.2.11, with the exception of a recirculation region on top of the rib structure.

For the sake of this study the height and width of each rib is equal, as opposed to the schematic, i.e. $e_1 = e_2 = e$, and $b_1 = b_2 = b$. The pitch of a rib on one side is denoted with p whereas the distance between two ribs on the opposite sides of the channels is denoted with d , and later referred to as the *periodicity ratio*. Hence, four key parameters are defined: rib height-to-channel height ratio, rib pitch-to-rib height, distance-to-pitch ratio, and the aspect ratio of the rib (height-to-width). The values chosen for each parameter, respectively, are shown below:

$$e/H = 0.35 \quad (7.6)$$

$$p/e = 40 \quad (7.7)$$

$$d/p = 0.5 \quad (7.8)$$

$$e/b = 2 \quad (7.9)$$

The reasoning behind the chosen values, is so that they lie in the middle of the design space exploration later used for the optimization, as it will be shown. This, however, is not a requirement by the optimizer, and does not guarantee a better performance. Hence, the procedure followed is to a certain degree arbitrary.

The same consideration applies to the width and height of the channel itself too. The full range of heights and widths considered are presented later in Chapter 6. The values chosen are shown in Table 7.3, along with a comparison to the resultant hydraulic diameter ($d_h = 4P/A$, with P being the channel circumference) for both cases: baseline circular channel and ribbed rectangular channel.

Table 7.3: Cross section of baseline (circular) and ribbed baseline (rectangular) channels used. All values are nondimensionalised, as a fraction w.r.t to the respective circular channel value.

Channel aspect ratio (H/w)	$A_{ch,rec}^*$	$A_{ch,circ}^*$	$d_{h,rec}^*$	$d_{h,circ}^*$
0.53	0.78	1.0	0.69	1.0

As it can be found from the height ratio and aspect ratio of each rib, a large proportion of the ribs that will be generated in the design space for the optimization are beyond the manufacturing tolerance capabilities of AM. This was done in order to increase the size of the design space and establish whether the Pareto-optimal solutions perform better than the current design. The task is hence, more theoretical rather than practical in the sense that concluding whether rib geometries can be *adjusted* to mitigate the effect of friction was more important than the derivation of a set of a rib geometry that can be used straight into manufacturing.

7.3.1 Mesh study

As mentioned above, no mesh independence study was performed for the domain with circular channels, due to the simpler flow, which was expected to be captured well with the use of the wall function. Hence,

the resolution of the mesh was chosen based solely on the author's experience, and the expectation that a finer resolution would have little to no influence on the key parameters incl. average metal (BC) temperature and coolant mass flow rate. When ribs are added however, the flow features are more complicated as shown in the Literature study chapter earlier. Therefore, a mesh independence study was deemed indispensable. Explain briefly settings and how they help with optimization task here

Table 7.4: Mesh settings used for the top panel study. The channel with an inlet upstream is denoted with 1, and vice versa.

Mesh ID	Element count	Average y^+		TSZ ¹	PLT ²
		Channel 1	Channel 2		
M1	79.94M	8.09	8.29	0.03	0.075
M2	24.61M	11.06	11.36	0.05	0.1
M3	11.82M	11.29	11.38	0.07	0.1
M4	6.09M	10.92	11.21	0.1	0.1
M5	3.74M	15.7	16.0	0.125	0.15

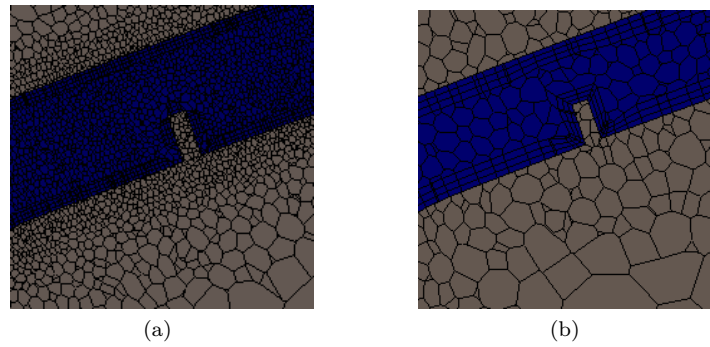


Figure 7.9: Comparison of mesh resolution: M1 (a) and M5 (b), channel shown in blue.

Three critical surface average temperatures are used to track the computational cost of each grid, shown below in Fig. 7.10. Standard surface averaging is used as shown in the equation below:

$$\text{Surface Average} \equiv \frac{1}{a} \int \theta_f da = \frac{\sum_f \theta_f A_f}{\sum_f A_f} \quad (7.10)$$

where θ_f is the cell face value of the temperature and A_f is the face area. Increasing the domain element count, particularly in the fluid region has no influence on the averaged temperatures on all three key surfaces. The deviation for the bond coating, thermal barrier coating, and channel walls is merely 0.174%, 0.09%, and 0.276%, respectively. The velocity profiles inside the channel also did not display a large difference, contrary to the expectation of numerical dissipation from the turbulent offset jet study. The profiles are available to the reader in the Appendix.

¹Target surface size (mm)

²Prism layer thickness (mm)

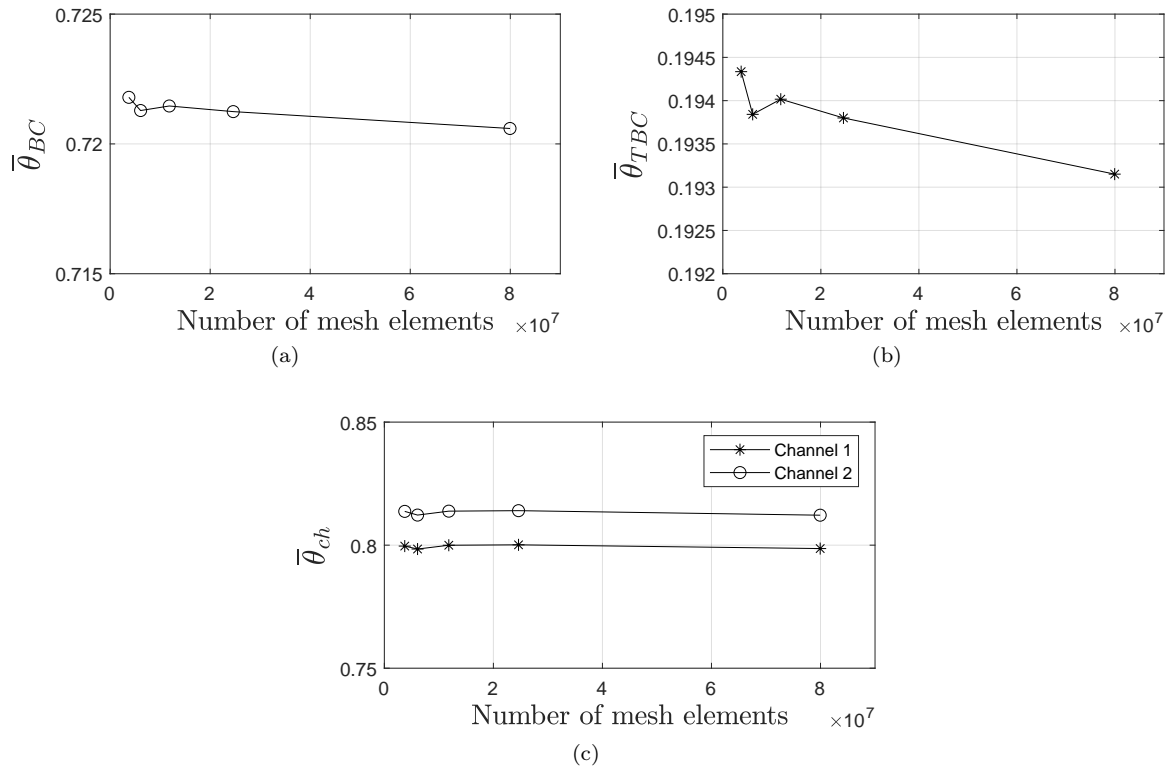


Figure 7.10: Mesh convergence tracked in surface averaged temperatures: Bond coating (i.e. hot side of transition metal) (a), thermal barrier coating (b), channel surface (c).

With changing rib parameters, the mesh size would have to be adjusted in the automated mesh generation process in the optimization. The result of the mesh independence study also provided a guideline for choosing a wall mesh resolution inside the channels as a function of the size of the rib. This provides a good compromise for conducting the optimization study, as recirculation regions are the only flow structure that can be captured with an isotropic RANS approach, and with the low numerical dissipation, it can be expected that they are well captured for a wide envelop of rib configurations. This approach, however, lacks physical basis to some extent, since mesh size and a mesh-independent solution does not guarantee an accurate solution.

Table 7.5: Computational cost comparison between all meshes.

Mesh ID	Number of CPUs	Wallclock (min)
M1	72	1465
M2	72	452
M3	24	435
M4	48	111
M5	24	129

The computational time as mentioned earlier has also been tracked to accelerate the optimization process, with the computation wallclock time tabulated above. Thereby, based on cost and results it can be concluded that mesh M4 is the best option for further analysis and a wall resolution of $\mathbf{TSZ} = \mathbf{PLT} = \mathbf{0.7b}$ is chosen for the optimization run. The average wall y^+ values also help validate the choice for the blended WF approach.

7.4 Flow validation

As mentioned above, due to the lack of experimental apparatus and data, a rather crude approach was followed for the validation of the flow field in the two cases. The velocity profile in the outer-layer (buffer and logarithmic regions) were scaled in accordance to the defect law, shown on the y-axis. The data was then compared to the Townsend's (1976) outer flow similarity hypothesis for rough-wall flows first presented in [46]. The term U_{cl} is used to denote the centerline velocity, i.e. $U(y = D_h/2)$. The velocity scaling collapses well, except at the inlet and outlet of the cooling channel, which is precisely after and before the inlet and outlet *rings*, shown in Fig.7.3 which can be used to explain the non uniformity in the velocity profiles. The slight curvature of the panel is an additional difference with a typical pipe flow.

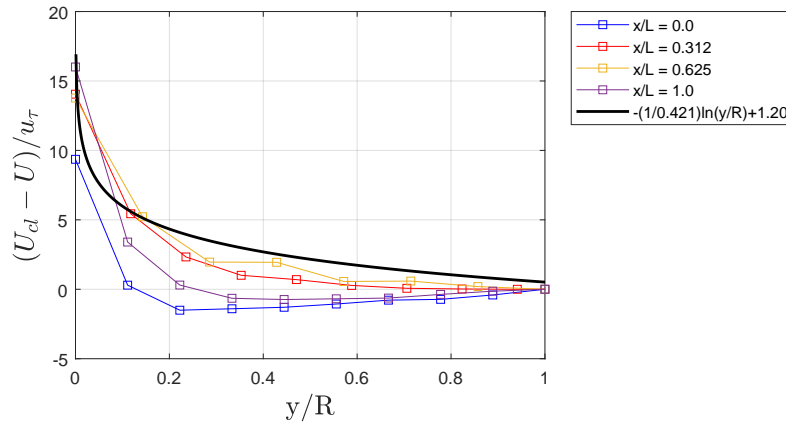


Figure 7.11: Outer-layer scaling at four locations downstream in one of the cooling channels inside the bottom panel. Townsend's similarity equation presented in the legend.

As shown by the mesh independence study, the exact solution of the flow inside the channels has little impact on the overall cooling performance measurement, which in terms of the cooling performance numbers (η , Phi , HLP) is measured using the surface-averaged temperature. Thereby, the small deviations from the defect law observed in the validation are expected to have a minimal impact the subsequent results (baseline comparisons and rib optimization).

The procedure followed for the ribbed case is similar, where the velocity profiles are compared to DNS data from Wang [84]. The author used a blockage ratio of 0.2 and a Reynolds number based on the average bulk mean velocity over the streamwise direction of the ribbed duct (U_b), $Re_b = 5600$. The bulk velocity (also used in the cooling comparison presented subsequently) is calculated as:

$$U_b = \frac{\int_V \rho \vec{v} dV}{\int_V \rho dV} = \frac{\sum_c \rho_c \vec{v} V_c}{\sum_c \rho_c V_c} \quad (7.11)$$

where subscript c is used to indicate the value over a single cell.

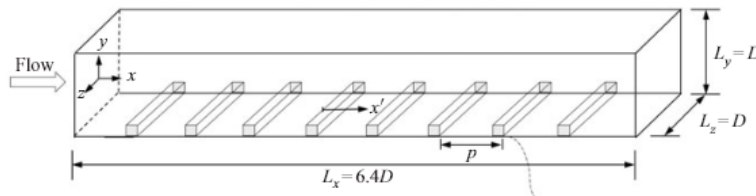


Figure 7.12: Schematic of a square duct with transverse ribs used by Wang [84]. The duct uses a blockage ratio of 0.2 and pitch-to-height ratio of 4.

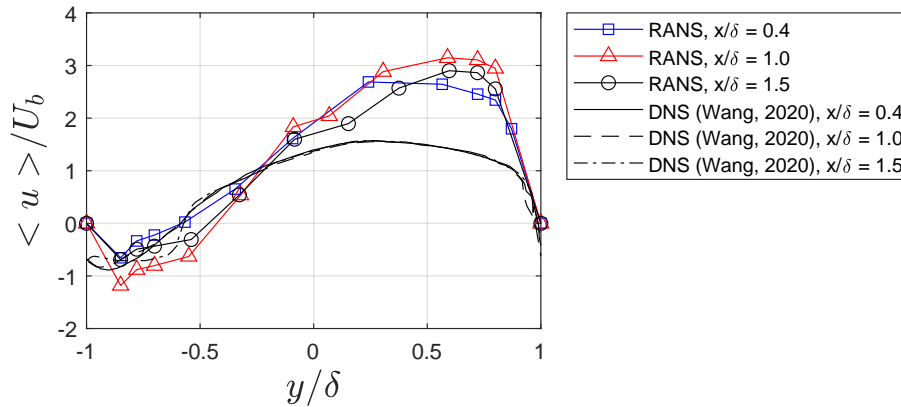


Figure 7.13: Comparison to DNS data of nondimensional streamwise velocity at three downstream locations of the rib.

The axial locations were nondimensionalized using $\delta = H/2$, where $x/\delta = 0$ is at the trailing edge of the rib. A substantial difference is present with the DNS-solution. The reasons for the difference discussed above however also hold in this case. An overview of the geometry used by Wang is shown in Fig. 7.12. Additionally, the disagreement in the two cases in the rib geometry and Reynolds numbers, particularly the latter ($\approx 12,000$ in the ribbed channels of the bottom panel, based on the mean inlet velocity), supplement the difference and explain why the streamwise velocity is considerably higher in the region above the rib ($y/\delta > -0.3$). The difference in the recirculation region in the lower half of the channel is negligible.

7.5 Preliminary baseline comparison

Prior to conducting the comparative analysis of the two cooling schemes, multiple important parameters have to be introduced first, which are not present to classical heat exchanger performance curves.

For transition piece heat transfer analyses the Heat Load Parameter (HLP) is an important parameter that has to be adapted first to include technologies that are common in combustion hardware, but not present in heat exchangers. Such includes TBC, and the presence of heat transfer to the midframe flow. The heat addition from the hot gas path is equal to the sum of the heat picked up by the cooling features in the component and the heat transferred from the part to the midframe flow:

$$q_g = q_c + q_{cs} \quad (7.12)$$

Subsequently, a thermal resistance network between the hot gas and the bond coat can be used to account for the performance of the TBC:

$$q_g = \frac{T_g - T_m}{\left(\frac{1}{A_g h_g} + \frac{t_{TBC}}{k_{TBC} A_g} \right)} \quad (7.13)$$

where the heat transfer coefficient on the hot side is h_g and k_{TBC} and t_{TBC} are used for the thermal conductivity and thickness of the thermal barrier coating, and T_m is the transition metal temperature. Conversely, on the cold side of the transition, the heat transfer rate reads:

$$q_{cs} = A_{cs} h_{cs} (T_{cs} - T_{diff}) \quad (7.14)$$

using a simple heat transfer expression for the heat transfer pick-up inside the channels $q_c = \dot{m} c_{p,c} (T_{c,o} - T_{c,i})$, substituting in (7.12) and rearranging, yields:

$$\text{HLP}_{\text{aug}} = \left[m_c c_{p,c} + A_{cs} h_{cs} \frac{(T_{cs} - T_{diff})}{(T_{c,o} - T_{c,i})} \right] \left(\frac{1}{A_g h_g} + \frac{t_{TBC}}{k_{TBC} A_g} \right) = \frac{T_g - T_m}{T_{c,o} - T_{c,i}}, \quad (7.15)$$

where the subscript *aug* is used to denote *augmented*. Historically, the HLP has been used to represent a nondimensional coolant mass flow rate. The **augmented HLP** incorporates the heat transfer from combustion parts to the midframe as well as the mass flow through the cooling features. As a result, the augmented HLP represents a nondimensional cooling rate.

Another important term is the Cooling Effectiveness, defined as:

$$\Phi = \frac{T_g - T_m}{T_g - T_{c,i}} \quad (7.16)$$

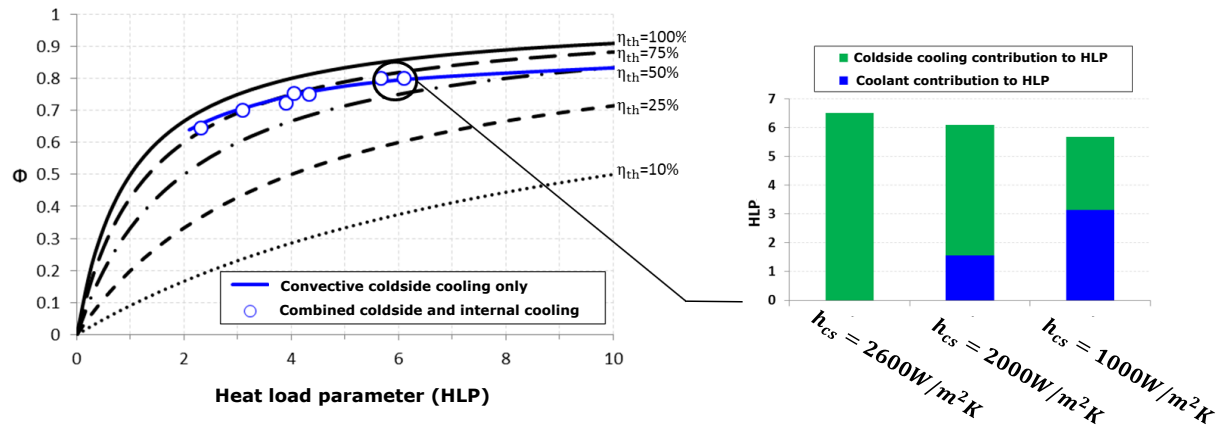


Figure 7.14: Effect of HLP on cooling effectiveness, and the ratio of passive to active cooling requirement as a function of the cold side convective heat transfer coefficient. The internal cooling efficiency is indicated using $\eta_{th} = (T_{c,o} - T_{c,i}) / (T_m - T_{c,i})$, i.e. the actual channel heat pick-up to the theoretical maximum

The figure above illustrates the cumulative nature of the augmented HLP. The thermal efficiency curves for heat exchangers are plotted in the main figure on the left. The solid curves represent the optimal designs where the part is cooled entirely by convective heat transfer to the midframe. The symbols represent designs for the same range of cooling effectiveness (Φ) values which use channel cooling as well as convective cooling. Since the augmented HLP captures the combined cooling effect of the various technologies used in combustion hardware, the cooling designs collapse onto a single curve regardless of the presence of channel cooling, the thickness of the TBC, or the amount of convective cooling to the midframe. The inset in the figure shows the breakdown between the part of the augmented HLP that corresponds to the midframe convective cooling (in green) and that of the channel cooling flow (in blue). Each design meets a Φ value of roughly 0.8 and has a similar value of augmented HLP. However, each design uses a vastly different amount of cooling air to do it. If the convective cooling to is sufficient, no internal cooling features are required to meet the required Φ value. However, more cooling air is required as the available midframe convective cooling decreases.

This adds up to the expectations of the cooling performance of the cooling channels inside both to and bottom panels of the geometry considered in this study. Referring back to Fig. 7.14 it is clear that the bottom panel might require less coolant air despite its larger length. On the other side, the heat transfer coefficient of the top panel on the cold side is considerably lower, and hence, *passive* cooling will be grossly insufficient, as visible in Fig.7.14.

The temperature design limits of the materials of the TP also need to be specified. They are driven by a combination of material properties and design requirements. They would normally be set at the beginning of the design cycle.

Table 7.6: Maximum allowable temperatures and design margins

	Cold side	Bond coating	TBC
$\theta_{w,max}$	0.22	0.35	0.96
θ_{margin}	-0.39	-0.37	-0.4

The non-dimensional interface temperatures on the bond coating, TBC, and cold side surfaces of the transition are shown below. The respective design limits are displayed with shaded areas.

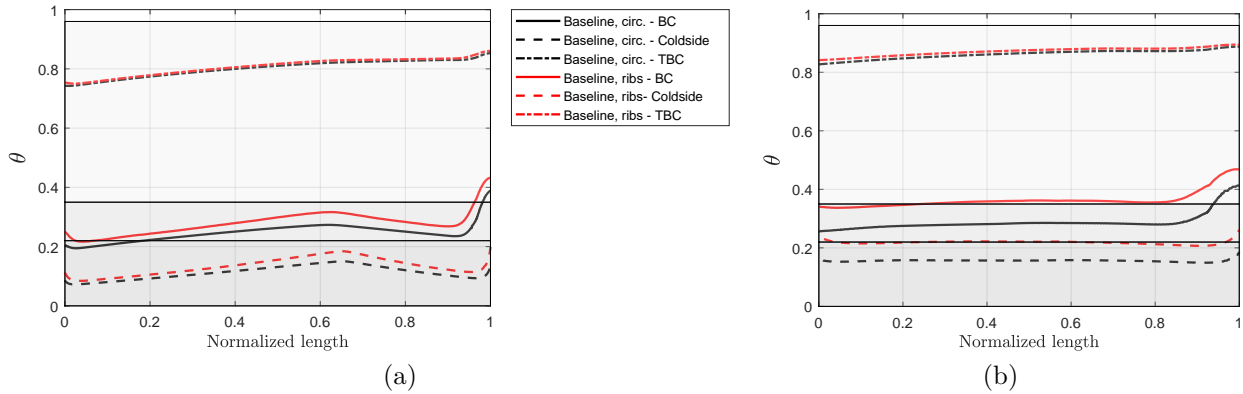


Figure 7.15: Local wall temperatures for bottom (a) and top (b) panels, with and without rib turbulators.

In accordance to the expectations from the effect of the heat transfer coefficient on the cold sides, the difference between the two cooling schemes is augmented for the bottom panel, where the HTC on the cold side is considerably lower. In the top panel, the temperatures of the cold side and bond coating are at or above the critical design limits for the majority of their length. For further investigation into the reasons behind the lack of enhanced cooling, the bulk channel velocities is presented below along with the nondimensional bulk temperatures of the cooling air.

As seen in the plot of bulk coolant temperature, a cross-over occurs at approximately $x = 0.6$ and $x = 0.7$, for the ribbed and smooth channels of the bottom channels respectively. A region of extremely low HTC on the cold side of the panel is present. As a result, not a lot of passive cooling and channels pick up heat. Further downstream the channel, the cold-side HTC increase again, and the passive cooling drops the metal temperature lower than the channel air temperature. This is also apparent on the metal temperature plot, i.e. the location where the BC and cold side temperatures reach a maximum values. The observation underlines the importance of effective cold side HTC. With regards to the top panel, coolant stagnation where in reality, the channels only pick up heat but due to the low velocity, is the reason behind the high panel temperatures. The considerable drop in the bulk velocity due to the presence of ribs is also visible in the figure.

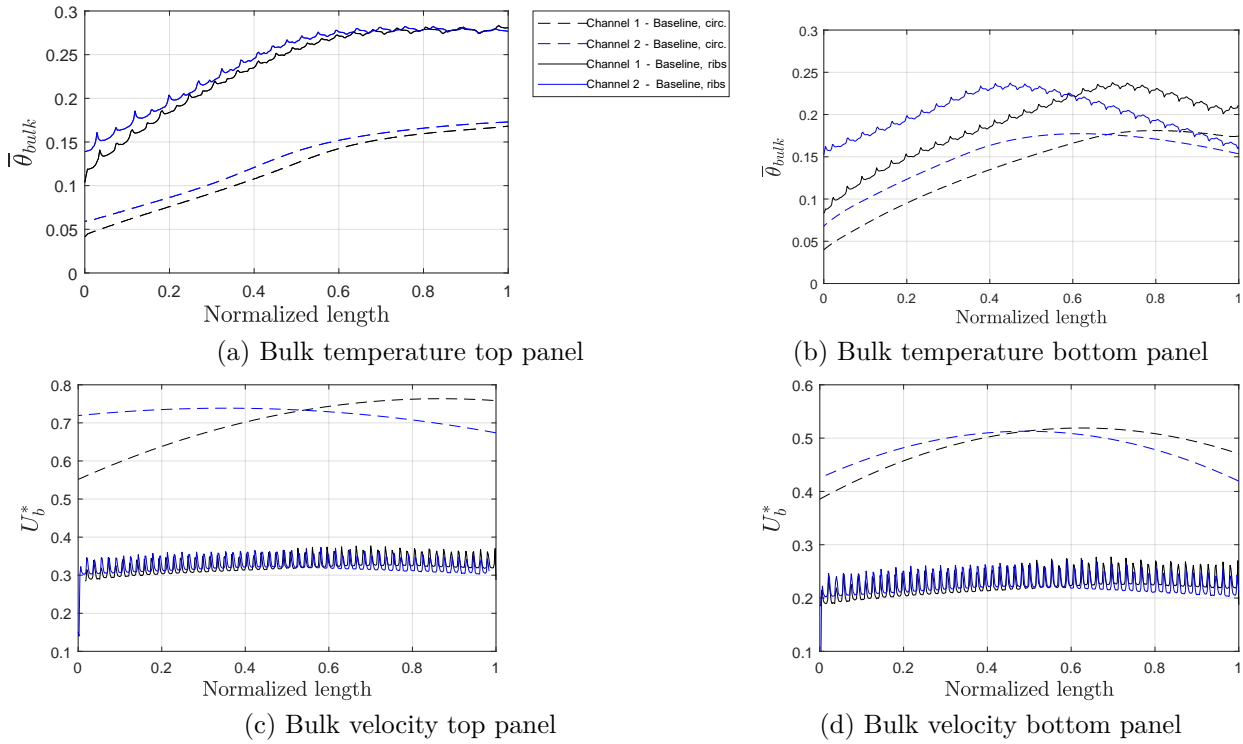


Figure 7.16: Nondimensional bulk velocity and bulk nondimensional temperature along the two channels for both geometries.

The bulk heat transfer coefficient, calculated according to Eq. 4.39, are also presented below. Following the formulation of the turbulent wall heat flux in eq. 4.36, the resultant values of the bulk HTC approach zero downstream and are negative on the cold side for both top and bottom panels, i.e. the wall temperature of the channel is higher than the temperature of the RANS-averaged cell temperature, \overline{T}^+ , computed from the respective wall treatment (despite choosing a value for $\theta_{ref} = 0.0$). The difference between the smooth and ribbed channels is the largest at the channel inlet, and tends to decrease downstream the channel. This observation holds particularly well for the bottom panel. The augmentation due to the rib structures (in the presence of spikes) also tends to diminish downstream, putting an emphasis on the effectiveness of turbulators for the given problem.

A summary of the obtained mass flow rates from the stagnation BC and key non-dimensional parameters are presented in Table 7.7 below. The coolant mass flow is nondimensionalized due to confidentiality reasons, such that

$$\dot{m}^* = \frac{\dot{m}}{\dot{m}_{circ.}} \quad (7.17)$$

A direct comparison between the top and bottom panels indicate that a smaller decrease in the Nusselt numbers and friction coefficients for the top panel is present, when compared to the smooth circular channel. A look at the wall temperature profiles, however, displays that the performance is worse than in the bottom panel. This is due to the worse passive cooling in the form of mapped HTCs, which has a more pronounced effect on cooling and hence despite the better internal cooling it is overwritten by the HTCs.

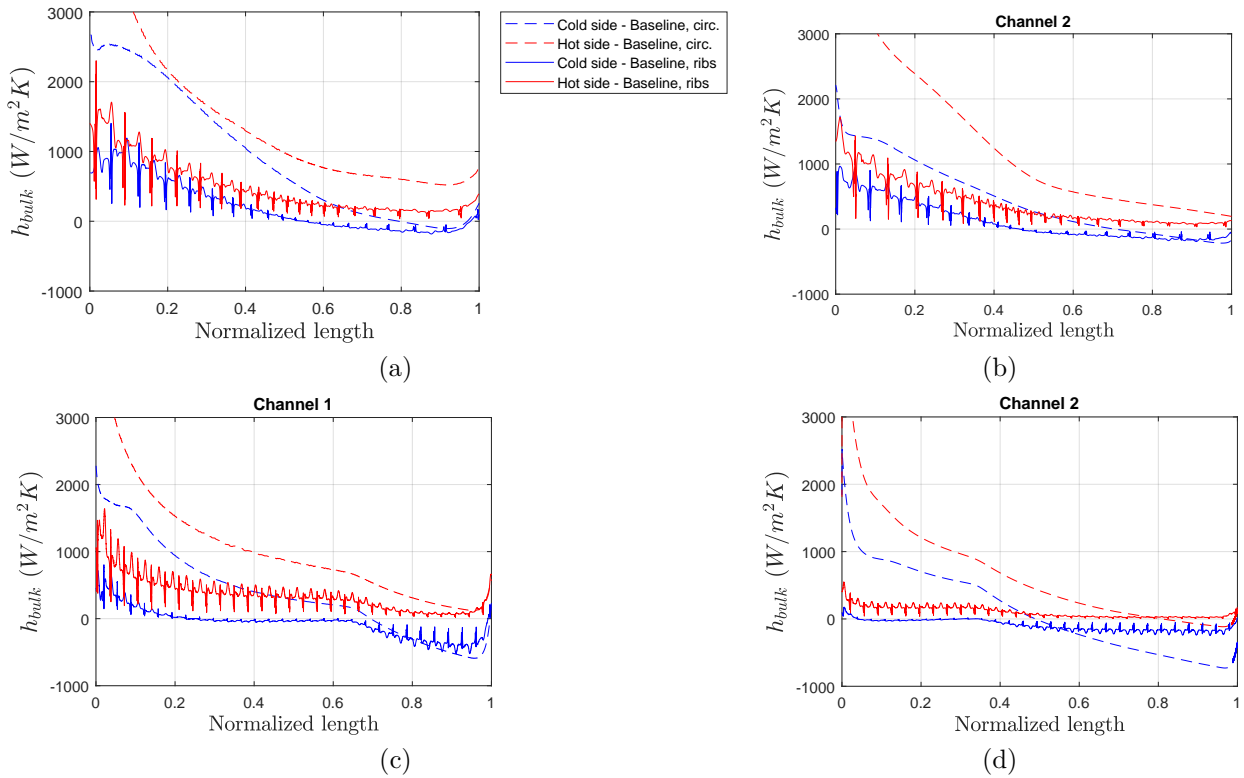


Figure 7.17: Bulk heat transfer coefficients on both panels for each channel: (a)-(b) top panel, (c)-(d) bottom panel.

Table 7.7: Comparison of two baseline cooling schemes

	Bottom		Top	
	Smooth	Ribbed	Smooth	Ribbed
\dot{m}^*	1.0	0.29	1.0	0.34
Re_{ch}	43,932	12,501	19,187	6,493
\overline{Nu}_{ch}	519.69	113.72	244.56	86.88
$\overline{C}_{f,ch}$	351.29	55.33	488.4	92.5
Φ	0.76	0.73	0.71	0.64
HLP	4.42	3.56	3.41	2.18
$\bar{\theta}_{BC}$	0.25	0.28	0.29	0.36
θ_{BC}^{\max}	0.39	0.43	0.41	0.47

It is thus safe to conclude that the chosen rib geometry as a turbulence feature inside the channel is not effective for such channel lengths at such pressure drops. The performance is hence influenced mainly by the following three parameters:

- Amount of passive cooling and heating, i.e. cold and hot sides HTC's respectively
- Channel length
- Channel curvature

Channel curvature has a less pronounced effect however in this case, since the channel length of the top panel (despite its strong curvature) is almost half of the bottom one. It is worth noting that the results

are only preliminary. The full picture and potential HT improvements will be achieved upon completion of the optimization loop, presented in the following Chapter.

Chapter 8

Ribs Optimization Study

The present chapter introduces the optimization problem of the transition piece and discusses the findings, by considering the thermal performance in terms of the previously-introduced nondimensional parameters used in combustion hardware, and the absolute value of the coolant air consumption. The potential drawbacks of using this approach are also pointed out.

8.1 Optimization set-up

8.1.1 Optimization objectives

The optimization presented in the study is, as previously mentioned, a multi-objective unconstrained optimization. Minimizing the average surface temperature, along with minimizing the requirement for cooling mass flow comprise the two objectives, whereas the constraints are related to the feasibility (i.e. parameters) of the rib geometry. The CHT method and required boundary conditions have been described in detail in section 7.1.

Temperature (lifetime) objective

Ideally, in a full-scale transition, where appropriate BCs can be applied, the objective can be set to maximizing the LCF lifetime. Due to the simplified geometry, such structural constraints cannot be used, and as an alternative the average surface bond coating temperature is to be minimized. This is also in accordance to the works of Chi et al. [22], in which was established that the most appropriate objective function is the averaged outer wall temperature of a turbine rotor blade. The objective consists of a target average surface temperature of the bond coating, θ_{tar} , set to 0.2 for both panels, which is considerably low given the high inlet temperatures. Thereby, the objective function in Eq. 8.1 becomes zero only if the target temperature value is met.

$$f_{\theta}(\vec{\mathbf{x}}) = \max(\theta(\vec{\mathbf{x}}) - \theta_{\text{tar}}, 0) \quad (8.1)$$

Minimizing f_{θ} thereby corresponds to minimizing the surface temperature.

Cooling channel mass flow objective

A similar approach is also followed for the cooling mass flow objective. An increase in the consumption of cooling air results in a lower cycle efficiency.

$$f_{\dot{m}} = \max\left(\frac{\dot{m}(\vec{\mathbf{x}}) - \dot{m}_{\text{offset}}}{\dot{m}_{\text{offset}}}\right) \quad (8.2)$$

The objective hence increases when the mass flow rate is higher than a specified offset, set at a non-dimensional value of 0.015 and 0.017 for the top and bottom panels, respectively. The OF is therefore

minimized. The use of such target and offset values is not a firm requirement, but is rather used for convenience and the avoidance of the SHERPA proposing a possible solution of m for example equal to zero.

8.1.2 Optimization parameters & range

In the optimization, the geometry parameters included in the study relate only to the channel cross section and ribs. The choice of the parameter values defining the rib geometry in the previous section was based on the mid values of the design space. The exact range is set as:

$$0.86 \leq H/H_{baseline} \leq 1.44, \quad (8.3a)$$

$$0.5 \leq w/w_{baseline} \leq 1.17, \quad (8.3b)$$

$$0.2 \leq e/H \leq 0.4, \quad (8.3c)$$

$$10 \leq p/e \leq 70, \quad (8.3d)$$

$$0.3 \leq d/p \leq 0.7, \quad (8.3e)$$

$$1 \leq e/b \leq 4. \quad (8.3f)$$

The maximum allowable value for the width of the channel was set such that the minimal resultant metal difference (nondimensionalised as a fraction of the baseline hydraulic diameter, $d_{h,rec}$) is 1, whereas the minimum and maximum value of the height was to a certain degree arbitrary, while still keeping some broad degree of manufacturability into consideration (e.g. $H/H_{baseline} = 0.125$ height with a 0.2 blockage ratio, will result in unrealistically low rib geometry even for the most sophisticated equipment). All parameters were discretized as continuous in an interval of 50 values.

The comparatively low number of parameters (six) included presents a feasible opportunity to establish whether the increase in friction factor can be mitigated for an optimized rib geometry. Possible additional parameters are the x- and y- coordinates of multiple points used in the definition of the spline for each panel. Such an approach will potentially yield a panel shape that is less or more sensitive to pressure drop. However, optimization methods suffer from what is called “*the curse of dimensionality*”, which is a term introduced by R. Bellman in 1961 [13] to describe the problem arising by the exponential increase in volume associated with additional dimensions to a mathematical space. Thereby, with a bigger number of parameters, the optimization problem tends to converge to an optimum design more slowly and the requirement for number of evaluations due to the increased design space increases. Given that on average a CHT computation in STAR-CCM+ takes ≈ 2 hours to complete (see Table 7.5), it is therefore desirable to obtain a better design in a number of evaluations as little as possible.

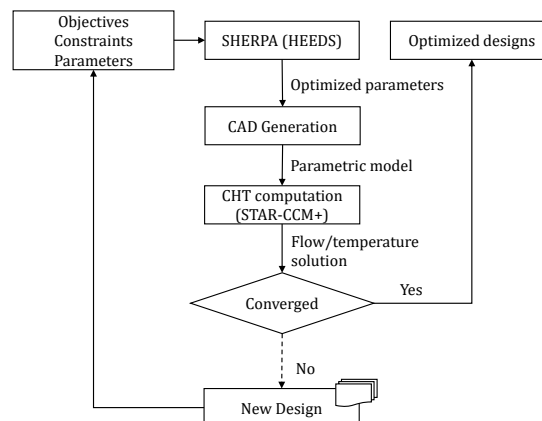


Figure 8.1: Flowchart of the automated design workflow in the MDO software HEEDS. The variables are modified in input (.in) files, which are read by the solver running in batch mode. The results are then obtained from an output (.out) file.

Due to the trade-off nature of the optimization algorithm, i.e. a Pareto optimization, SHERPA selects the optimal designs based on whether they dominate other designs. A design is considered dominant over another in cases where it has showed better performance in at least one of the objectives, and not worse in all others. Thereby, SHERPA yields a so-called rank to such designs equal 1. Rank 2 is given to the remaining designs and those that are dominated by any other design in that group. The remaining designs are established under ranks of 3, 4, etc. following the same procedure. The full automated workflow is presented in Fig. 8.1 above.

The settings used in the SHERPA optimization algorithm are listed as:

- The size of the **archive set**, which is maximum number of designs that are stored at any time is set to 12 designs, based on the algorithm requirement if $N_{\text{parameters}} < 10$, otherwise the nearest multiple of 4 ($N_{\text{parameters}} = 6$) is recommended; the archive set in the algorithm can be basically interpreted as a certain *cycle* of designs, upon completion of which the algorithm learns and the next cycle begins based on a new set of parameter values.
- Number of evaluations = 200, minimum requirement of SHERPA is that it equals at least 15 $N_{\text{parameters}}$
- The entire archive set of 12 designs is evaluated in parallel on a computational multiprocessor cluster using 48 CPUs each, to speed up the process.

8.2 Results & analysis

The particular evolution history of both objective functions per iteration is of great interest for understanding the full scope of the results and deriving a coherent set of conclusions. This is presented in Fig 8.3 and Fig 8.4 for the temperature and cooling flow objectives, respectively. Another important parameter to track is the measured performance index of each design, shown in Fig. 8.2. During the optimization, SHERPA provides each design with a performance rating, which is determined by the extend to which the constraints are met, along with the value of the objective function. In the case when no constraints are presented, the performance is only based on the objective value. Hence, the weighted-sum performance can be then theoretically used to return the best designs (see eq. 8.4)

$$\text{Performance} = \sum_{i=1}^{N_{\text{obj}}} \left(\frac{w_i S_i f_i(\vec{x})}{\text{norm}_i} \right) \quad (8.4)$$

The sign of the objective is indicated with S_i , i.e. value of +1 for maximization problem and -1 for minimization, and w_i is the linear weight for the i^{th} objective (default value is 1).

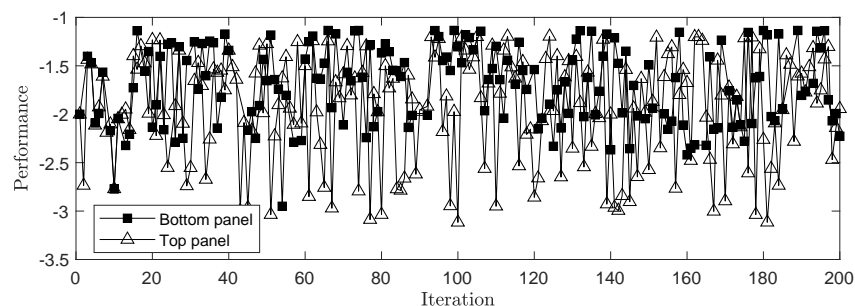


Figure 8.2: SHERPA Design performance.

It is worth mentioning, however, that the performance rating is not used as a criterion by SHERPA for choosing the values in subsequent designs during the search. The normalization coefficient therefore

plays a key role in calculating the performance. The value in this study was chosen to be the baseline values (responses from the ribbed case in 7.5), and can explain the lack of convergence towards -1.

No clear convergence to a minimized value for both temperature and cooling flow is present either. The temperature value for the top panel displays oscillations between 0.4 and 0.325, a range higher than the average temperature of the baseline case with circular 1.5mm channels. The same applies to the bottom panel. The fluctuations are less pronounced and the difference with the baseline case is lower. Similar results are found with regards to the cooling flow. Interestingly, the value is successfully minimized by a factor of almost 30 (the lowest nondimensionalized value from the optimization is $\approx 0.035\text{g/s}$ compared to the baseline value). These observations lay down a comprehensive introduction to the full picture of the results of the optimization.

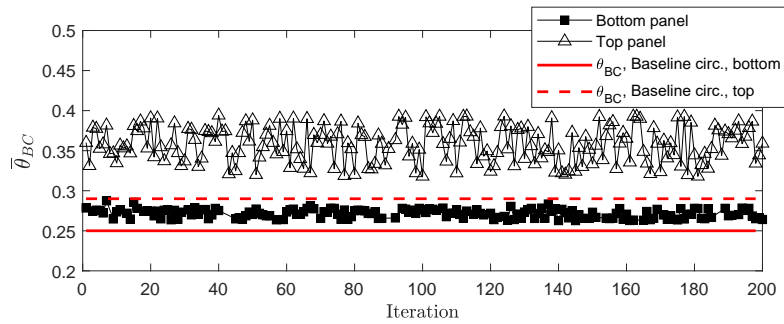


Figure 8.3: Evolution of temperature OF

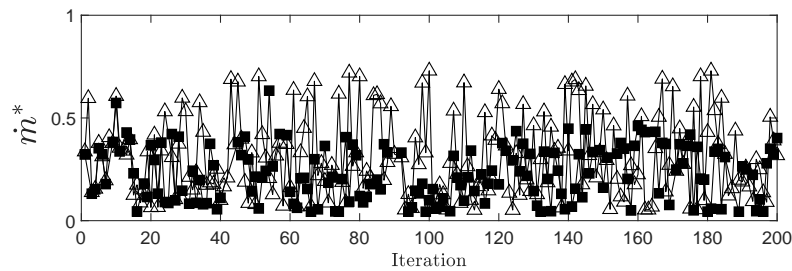


Figure 8.4: Evolution of nondimensionalized cooling mass flow

The average temperature objective versus the cooling mass flow rate objective is shown in Figure 8.5 and Fig. 8.6 for both bottom and top panels, respectively below. The envelop of all CHT results successfully form a well-defined Pareto front in both cases. The colorbar on the right of the figures is used to show the cooling effectiveness Φ of each design point. Results are in agreement with the expectations that reducing the bond coating temperature (increasing the lifetime) requires a higher coolant mass flow.

Table 8.1: Comparison of maximum and minimum values achieved by SHERPA for both panels to the values with baseline channel configuration (BR - baseline ribbed, BCIRC - baseline circular).

	OF	min	max	BR	BCIRC ¹
Top panel	f_{θ}	0.12	0.19	0.16	0.09
	$f_{\dot{m}}$	2.4	47.4	21.4	65.4
Bottom panel	f_{θ}	0.06	0.09	0.08	0.05
	$f_{\dot{m}}$	1.4	35.4	17.4	56.2

As already established from the evolution plots above, none of the optimized geometries managed to achieve an improved cooling system in terms of the averaged bond coating temperature. However, a thorough design exploration is achieved and the reduction in mass flow rate is considerably large, particularly when compared to the lower range of resultant values of the temperature objective. Hence, as it can be seen in the Appendix, the histogram distribution of the values used for all design parameters indicate that the majority of the design space is successfully explored. The highest and lowest values of the two OFs are presented above in Table 8.1, where the values are compared to the ribbed and smooth baseline geometries. In terms of the OFs on the other hand, the optimized geometries lie within 3% and 1% from the currently used channels in the TP (baseline circular), for the top and bottom panels, respectively. The cooling mass flow rate OF corresponding to the minimum of the computed temperatures is lower by a factor of 1.4 and 1.6, respectively, which is a considerable improvement and can help reduce overall GT emissions, only if however the entirety of the temperature profile of the BC is below the material temperature limit.

The high negative values of the Pearson correlation coefficient (PCC) can be interpreted as Pareto set, in which the majority of the designs are close to the Pareto front (assuming a linear Pareto front). The PCC value is commonly calculated as:

$$\rho(x, y) = \frac{\text{cov}(x, y)}{\sigma_x \sigma_y}, \quad (8.5)$$

where cov is the covariance and σ_x and σ_y are the standard deviations of the predictor x and predictant y , respectively. The Pearson correlation coefficient is then used to calculate the slope of the linear regression line:

$$\beta = \rho(x, y) \frac{\sigma_y}{\sigma_x} \quad (8.6)$$

which is ultimately used for the full equation of the linear regression:

$$y_i = \beta_0 + \beta x_i, \quad (8.7)$$

with the y-intercept denoted $\beta_0 = \bar{y} - \beta \bar{x}$.

¹Intentional abbreviation to avoid confusion with bond coating (BC).

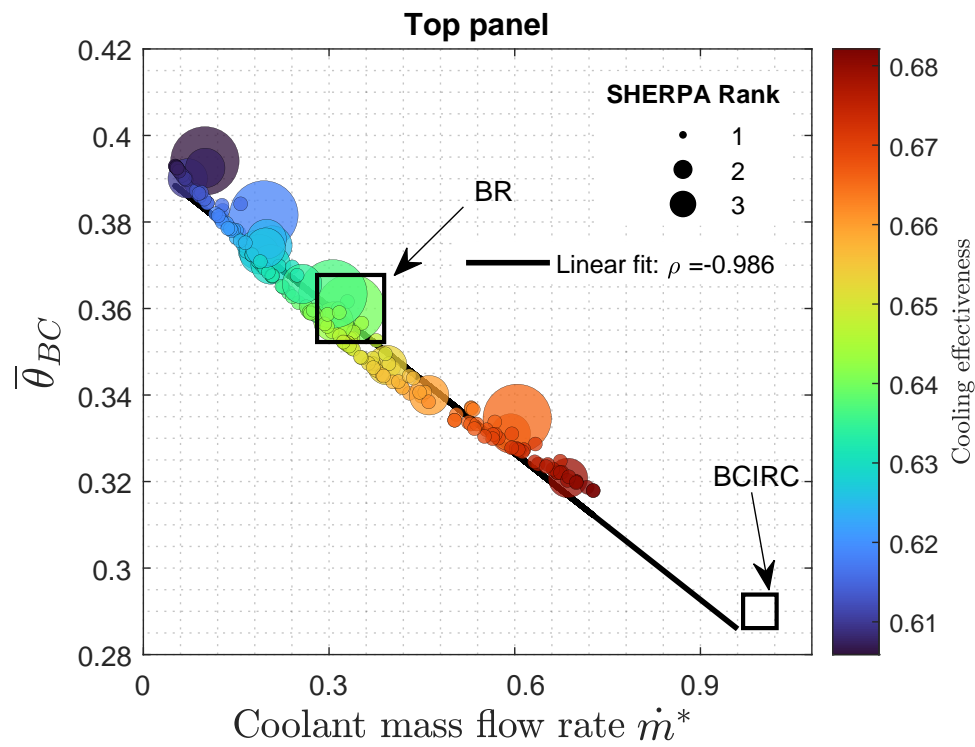


Figure 8.5: Pareto front of top panel. Note: $\theta_{BC}^{max} = 0.35$.

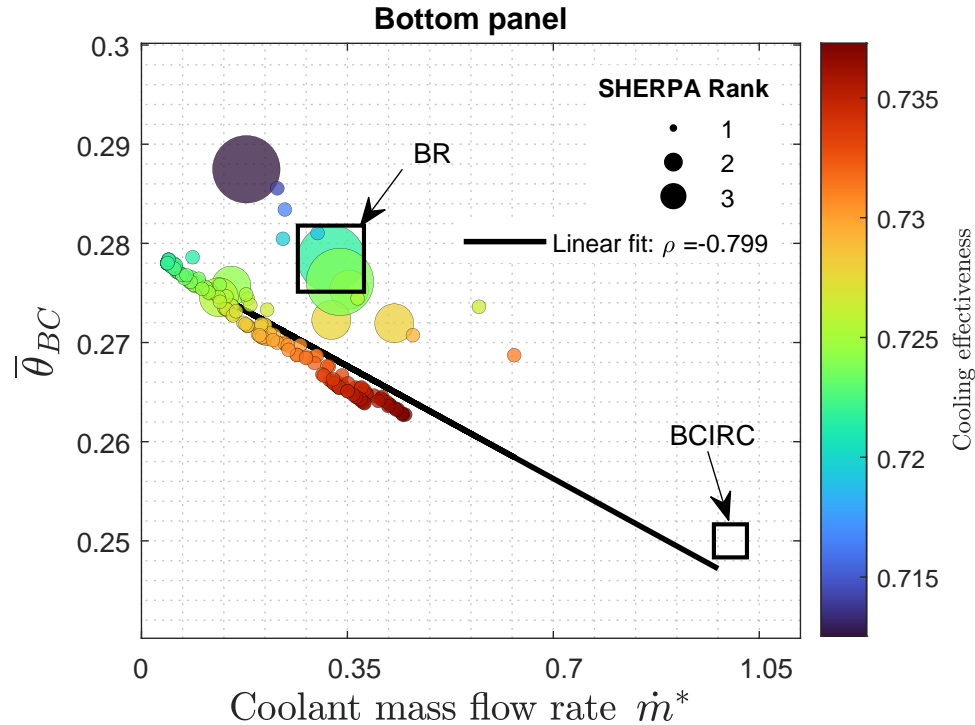


Figure 8.6: Pareto front of bottom panel. Note: $\theta_{BC}^{max} = 0.35$.

To investigate the effects of the independent rib parameters, the value of the computed $\bar{\theta}_{BC}$ and coolant

are plotted against each parameter individually. The plots are shown in Fig. 8.7 and Fig. 8.8. The two panels do display slight differences in the PCC values, but the overall trends remain the same: blockage has a negative effect on the temperature OF (i.e. temperature is increased with increasing blockage), and positive effect on the coolant mass flow rate OF. The increase in size of the recirculation regions inside the channels, resulting from the higher ribs, contribute to higher friction, which explains the observation mentioned above. Basically, with lower blockage ratios, the two OFs tend to converge to a single region: see values for $e/H < 0.225$ below. The opposite holds for the pitch ratio, which is to be expected. The two OFs tend to converge after a $p/e > 50$. Increasing pitch ratio can also be interpreted as decreasing the total number of ribs inside the channel. This reduces the skin friction losses and increases the mass flow rate. An interesting observation is that the correlation in these two parameters is less pronounced in the top panel. This can be attributed to the bigger effect passive cooling has on this panel and also the strong curvature. Further investigation needs to be done to confirm this assumption however. On the other hand, the periodicity and thickness ratio of the rib has a considerably less clear effect on the two OFs, analogous to low PCC values, visible in the two abovementioned figure.

The results of both objectives are almost perfectly antisymmetric: the correlation coefficients $\rho(\text{OF}_i)$ are approximately equal but with a negative sign, emphasizing on the strong coupling and trade-off between the two objectives. This however should not be considered as a lack of improvement from the optimization run. In a realistic problem setup, where the lifing is calculated using the appropriate boundary conditions and full geometry, then the results will be more decoupled due to the introduction of non-linearities from LCF (local stress regions, application of external loads, etc.). The results, however, are still indicative that heat transfer can be enhanced using varying turbulation features without a considerable penalty in friction (in the form of low mass flow rate). A clearer picture is painted when the HTC augmentation in the form of Nusselt number is plotted against the Skin friction, presented below. Moreover, the plots are also beneficial for displaying the presence of outliers (i.e. high Nu numbers against a low value of C_f) from the linear fit, which is desirable. Such data was recorded for the top panel only and is shown below in Figures 8.9-8.11.

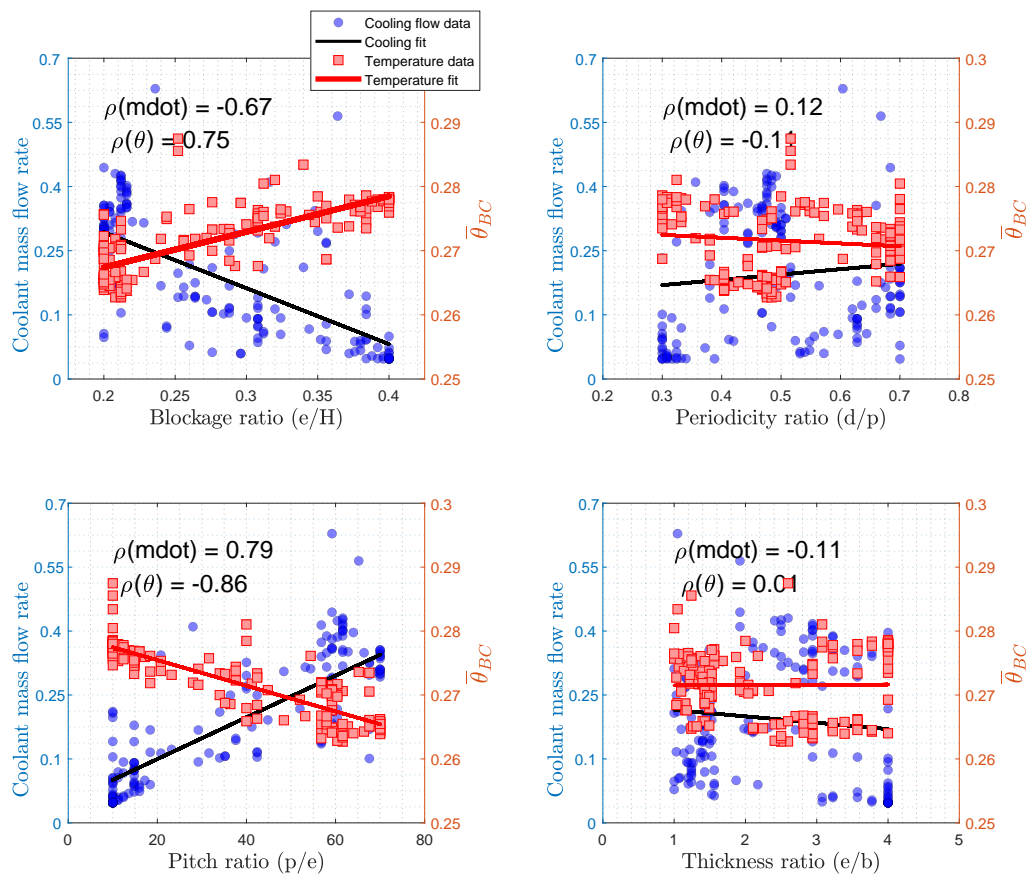


Figure 8.7: Influence of rib parameters on bottom panel temperature and cooling

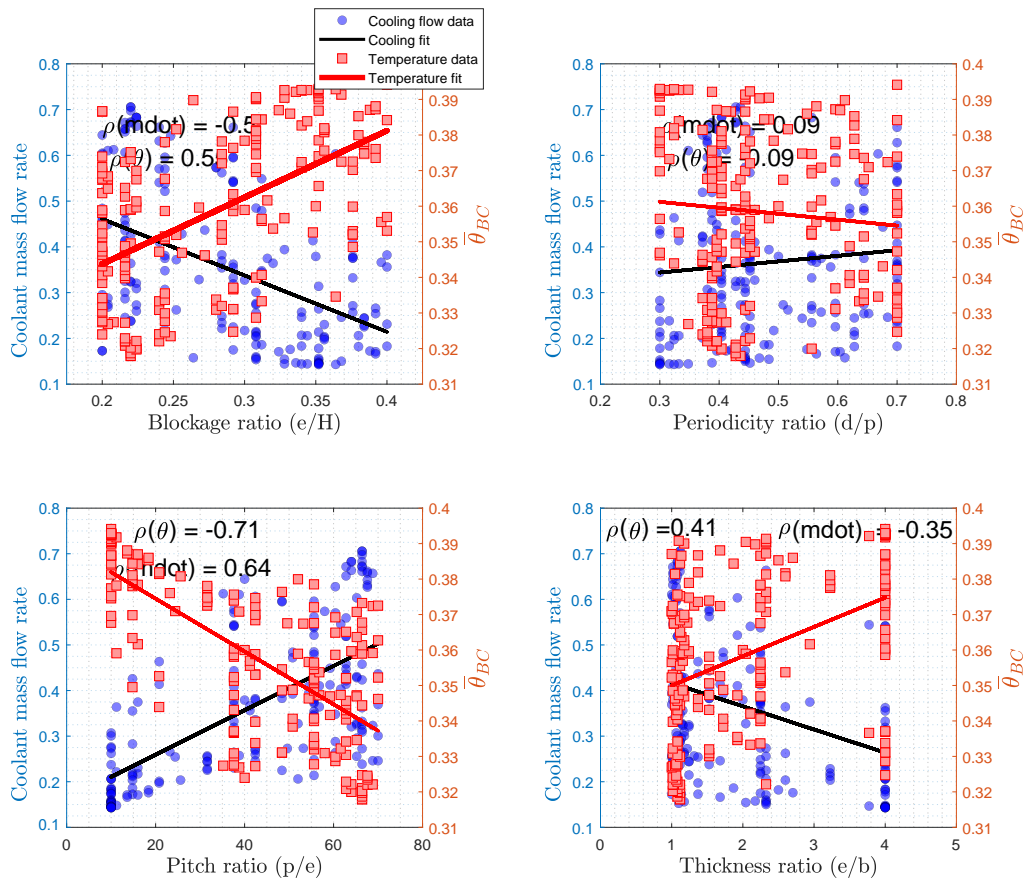


Figure 8.8: Influence of rib parameters on top panel temperature and cooling

The range of values for Φ was split into four ranges, and then used to indicate the marker size of all three plots to aid in the understanding of the results. The Nusselt number was calculated using the average wall values for both specified- y^+ heat transfer coefficient and conductivity, the latter being calculated using the average channel temperature and Sutherland's law. A small difference between the two channels in terms of variation with Reynolds number is present, but the data points eventually converge as visible in Fig. 8.11. For all designs a strong linear trend is present, particularly for the skin friction coefficient. For the case of cooling performance however, a lower correlation coefficient is actually beneficial, as it can be used to display an increase in HTC, without a corresponding increase in skin friction losses. The presence of such outliers can also be quantified with the so-called Z-score:

$$Z_x = \frac{x - \mu_x}{\sigma_x} \quad (8.8)$$

A distribution of the z-score of the difference between the predicted value (i.e. linear regression line) and the computed value from the optimization run, which is more skewed or with a higher σ is therefore desirable. The z-score of the skin friction difference however, is advantageous for the rib performance to remain uniformly distributed with a very low σ as a countermeasure. The z-score for both Nu number and C_f are shown below in Fig.8.12.

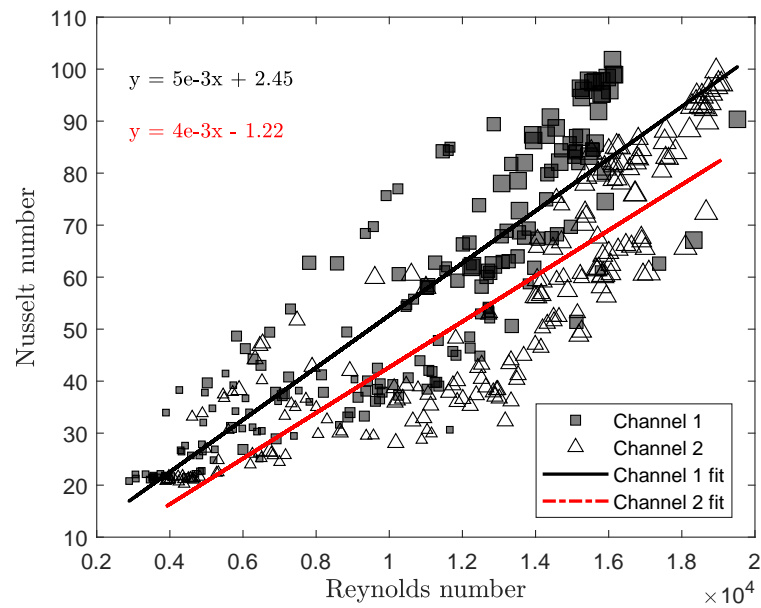


Figure 8.9: Nusselt number increase with Reynolds number

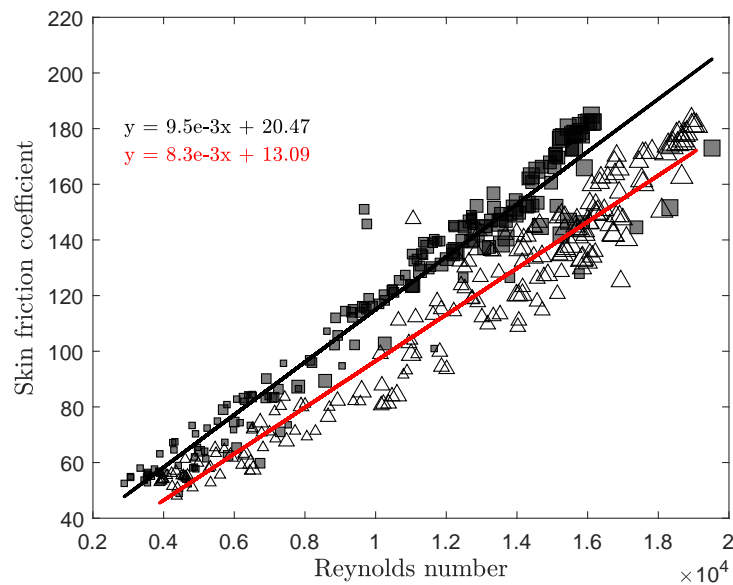


Figure 8.10: Skin friction increase with Reynolds number

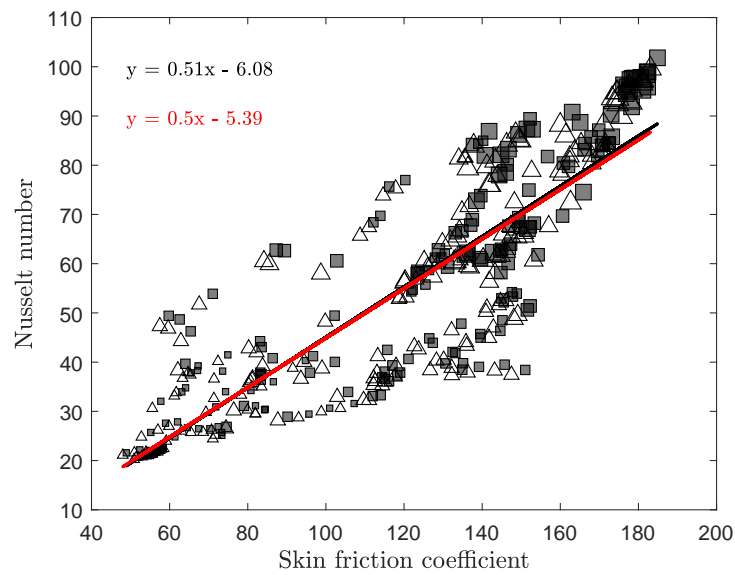


Figure 8.11: Nusselt number against skin friction

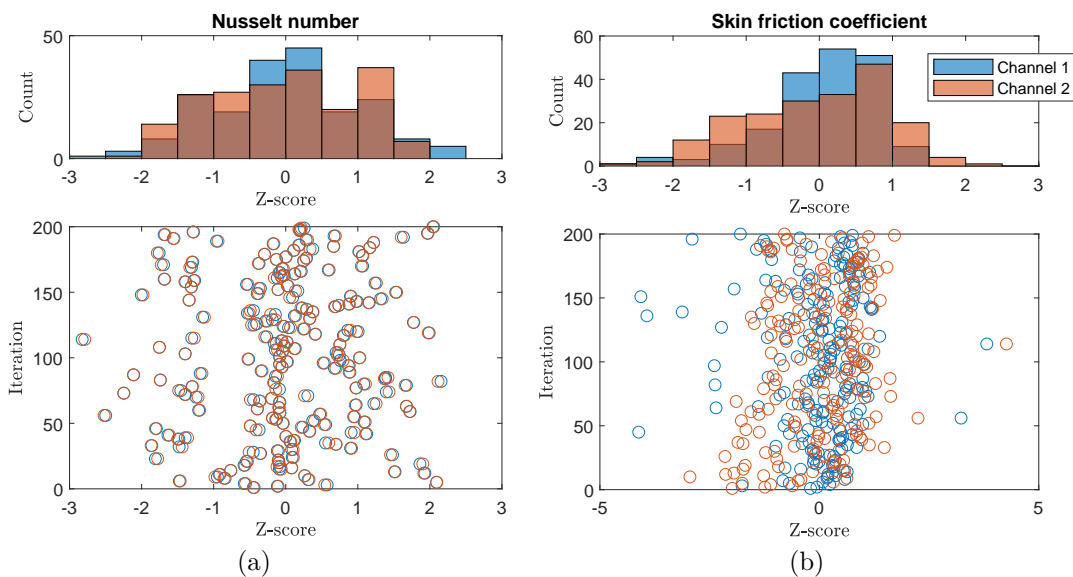


Figure 8.12: Z-score (scatter and distribution) of (a) Nusselt number and (b) Skin friction coefficient.

Figure 8.11 is hence a good summary of the objective of this optimization run. The plot displays a low PCC $\rho = 0.87$, which is due to the wide combinations of rib parameters. A wide range of Nusselt numbers for both channels are well above the linear regression line, proving that a rib geometry can be customized in accordance of the given flow problem.

The overall cooling performance, however, of equipment used in gas turbines, does not depend solely on the internal cooling HTC. As pinpointed previously, the issue of low cold side HTC on the TP is of high impact on the cooling. Therefore, additional cooling adjustments are necessary to further decrease the effect of skin friction as discussed in the next section.

8.3 Recommendations

It was observed that the surface average temperatures of the bond coating (i.e. transition metal) on the top panel are above the maximum allowable design constraint of the material (see Table 7.6). The maximum BC temperatures were not recorded during the optimization process, but considering the results in Section 7.5 and particularly Fig. 7.15, one can assume that they are proportionally above the average value and hence above the material limit for some of the designs on both panels. The optimization, however, displayed a promising opportunity that such turbulation features can in fact be tailored and help reduce the mass flow rate drastically, with a smaller penalty on temperature. Thereby, the study points to the assumption that the temperature penalty can be further reduced, given the cooling design is adjusted carefully. A possible adjustment is presented in Appendix D, where additional inlets downstream are added, while their respective inlet cross-section area is progressively reduced to artificially throttle the flow downstream. Recommendations arising from that study led to the conclusion that a large potential improvement in overall cooling (both in Φ and HLP values) is expected if in addition to inlets, separate channel outlets are added as well, thus effectively reducing the channel length. A further study in which the number of additional contracted inlets is matched with contracted outlets can help validate this assumption.

The analysis presented the overwhelming effect cold-side cooling actually has on the transition piece. Therefore, another recommendation is designers' attempt to maximise the passive cold-side convective cooling along with the use of internal cooling techniques. This is achievable, by maximising cold air circulation in the plenum, and avoiding stagnation regions around the combustor inlet ring and the picture frame on the turbine side.

Additionally, from the correlation plots it was found out that the periodicity and aspect ratio of the ribs play approximately no role in the effectiveness of the cooling geometry. The range of values provided for the parameters with the highest influence, however, i.e. rib blockage and pitch were relatively low. Therefore, a further study can increase the range for the abovementioned parameters along with a higher maximum value of the channel height (the maximum value of the channel width chosen here does not allow further increase for structural reasons). As previously explained the range of values provided for some parameters was rather arbitrary. Therefore, in the current study, the maximum $D_h = 1.38\text{mm}$ is still lower than the circular channels currently used by Siemens ($D_h = 1.5\text{mm}$), and matching D_h in both cases, circular baseline and the maximum value for the ribbed channel can eventually help conclude whether the gap with the temperature value from the circular baseline case can be further reduced (an approach that can be interpreted as an attempt to extend the Pareto front - see linear regression line in Fig. 8.5 and Fig. 8.6).

Chapter 9

Conclusion

This final chapter of the report summarizes the approach followed in the study and the main key findings. It also lays out further recommendations for potential fields of research that can shed light on a broader spectrum of topics related to the objectives of the study

The study objectives were to validate the conjugate heat transfer methodology in a commercial software for two canonical cases, and compare the conjugate heat transfer results with the uncoupled solution under a wide envelope of conditions. The study also aimed at providing an insight whether an optimization methodology, using a proprietary optimization algorithm, can lead to an optimized rib-turbulated internal cooling channel geometry of the transition piece of an industrial gas turbine, such that lifing is enhanced with the lowest mass flow rate possible.

9.1 Conclusions

Firstly, the conjugate heat transfer methodology in the commercial code package was successfully validated. It included first a laminar flat plate case, the results of which were compared to an analytical solution under two physical settings ($\overline{Bi} = 0.1$ and $\overline{Bi} = 1$). The model employed a finite element mesh on the solid side in order to quantify the resultant difference when a mapped interface is used. The results showed better convergence with the higher Biot number with the analytical solution, primarily due to the lower temperature gradients at the leading edge. For both cases, the assumptions used in the derivation of the analytical solution are in part the main cause of the discrepancy.

The validation of the turbulent flow field case (a turbulent offset jet) helped remove uncertainty between the available Reynolds-Averaged turbulence models, and also types of wall treatment. The study showed that the resultant temperature profile from the realizable $k - \varepsilon$ model yields the closest results to an experimental measurement from literature. The reason for the better computation is the different formulation of the turbulent viscosity, which was overpredicted for the $k - \omega$ model, particularly in the stagnation regions, which led to higher temperature values. The runs using a high- y^+ treatment on a coarser mesh suffered from high numerical dissipation, which artificially led to results being closer to the experimental values. This artefact from the coarse grid points to the possible inappropriacy of the chosen experimental setup: the low jet velocity in the experiment did not allow for robust testing of the high- y^+ approach as the resultant solution is mesh dependent. Moreover, the resultant y^+ value on the wall was in the buffer layer which is strongly advised against when using this wall function. It is worth mentioning however that the difference between the two approaches (blended and high- y^+) however remained small in terms of maximum and minimum interface quantities and the overall interface temperature profile on the plate.

Secondly, the subsequent part of the study: quantifying the relevance of the uncoupled approach showed the following. When the thermal conductivity of the solid region was altered on the laminar flat plate

case, the error between the two heat transfer methodologies remained relatively low, with the tendency to increase with lower solid conductivities, in accordance with the Lumped Capacitance theory. The difference however remained negligible, particularly for averaged temperature values. Additionally it was shown that increasing the difference between the cold (bottom wall of the plate) and hot temperatures in the domain ($T_\infty - T_b$), can yield to an increase in the errors of the decoupled approach. The maximum error however, remained small at $\approx 6\%$. More prominent differences were observed in the thermal boundary layers.

When the heat transfer methodology was compared using a turbulent flow case on an offset jet, the sensitivity study with the Turbulent Prandtl number (range between 0.4 - 1) showed no noticeable effect for both wall treatments, and the difference between the conjugate heat transfer and decoupled heat transfer tended to remain constant. The second parameter studied was the turbulence intensity at the jet inlet. The blended wall approach seemed to be independent of turbulence intensity. The only parameter investigated that showed larger fluctuations was the reattachment length (the difference remained small however at 3%). The lack of established tendency is even more pronounced for a high- y^+ approach. An important observation is that the difference between conjugate heat transfer and the decoupled approach seemingly increased with increasing Tu(%) for the high- y^+ approach. This observation, however, can be solely an artefact from the coarse mesh size, rather than a result coming from the WF itself. The third parameter was again, same as in the laminar flat plate case, the thermal conductivity of the solid (presented as a conductivity ratio with the fluid region). In terms of average values, the difference in temperature is negligible for both wall treatments. The largest divergence was at stagnation regions but only apparent in the blended wall approach. For the high- y^+ treatment, the difference was artificially *softened*, because of numerical dissipation, as discussed in the validation case, and remained rather small even for intermediate solid conductivities. Hence, the effect of the solid thermal conductivity was negligible for both local and averaged values on the wall when a coarse grid approach was used. In general, a consistent observation for all sweeps tested on the blended wall function, showed that the interface temperature and was higher when conjugation was included accounted for.

Finally, the last part of the Masters Thesis surrounded around the cooling study and optimization of a gas turbine transition piece. A simplified domain was proposed, in order to reduce computational costs, and analyse cooling performance only on the most thermally loaded parts of the transition. This was done by, instead of calculating a full-scale mid-frame combustor model every time, the heat transfer coefficients and ambient temperatures were mapped on the hot and cold sides of the transition piece. The walls of the channels were the only conjugate heat transfer interface in the study. The addition of turbulators (in the form of straight rectangular ribs perpendicular to the flow) resulted in a decrease in the cooling performance for both top and bottom panels, with a more pronounced deterioration on the top panel. This was due to the comparatively low cold side cooling on the panel, and the large role that this component of the total cooling plays on the performance. Numerically, the increase in the average bond coating temperature was 12% and 24% for the bottom and top panels, respectively, when compared to the case of circular channels without turbulators. On the other hand, the improvement in the consumption of coolant was reduced by a factor of 3.1 and 2.9. Since the temperature profiles for the turbulated channels were very close to the temperature design limits, the performance of the baseline ribbed geometry was deemed unsatisfactory and the possible improvement of the turbulated cooling is only fully visible in after the optimization routine.

The optimization procedure helped further reduce the bond coating temperature for both panels compared to the results from the initial rib configuration, specifically a reduction of 11% and 6.25% for top and bottom panels, respectively. The resultant penalty for the mass flow rate was augmented by approximately a factor of 2, but still remained considerably lower than the non-turbulated channel design used currently in the transition piece. In summary, the average temperature of the bond coating were still unsatisfactory and higher than the non-turbulated channels, but the reduction in the coolant mass flow rate was considerably higher. The results put an emphasis on the possibility to optimize turbulence features and reduce the penalty on the pressure drop (expressed in mass flow in this study),

without solely relying on the experience of the designer. The ultimate cooling design choice is based on the following: unless the average bond coating temperature has to be strictly lower than the previous configuration, one can use the lowest achievable value of the temperature, and considerably lower the coolant consumption. A complete improvement in both mass flow rate and temperature profiles and, thus, lifing, however, is only possible, however, with an additional measures in the cooling design, e.g. additional inlets and outlets downstream, which will most likely lead to a temperature value close to the nonturbulated circular channel at a reduced mass flow rate.

9.2 Recommendations

A list of further developments and improvements proposed for the methodology implemented in this project potentially include:

- A different experimental set-up might yield different recommendations of a model and WF: the results presented above are in no way binding to all flows, and in case of a different flow structure, the appropriate model should be then re-chosen based on assumptions, and available literature (unless validation data is present). A validation of the conjugate heat transfer methodology at different settings is imperative to confirm or deny the finding that the realizable $k - \epsilon$ is the best for conjugate heat transfer problems.
- The comparison between the two heat transfer methodologies can be expanded into sensitivity studies including other nondimensional numbers or parameters. For example, it was briefly mentioned that the Turbulent Prandtl number study is relevant for reacting flows. The flows studied in this project however were not reacting, and hence, a more interesting parameter to study is the ratio between the turbulent Schmidt and turbulent Prandtl numbers.
- Additionally, with the advent of high performance computing, Large Eddy Simulations (LES) and also Detached Eddy Simulations (DES) can be used to quantify the difference between the conjugate heat transfer and decoupled approach. It can be, thus, found whether the behaviour of such large flow structures, in an unsteady setup, omitted in the steady Reynolds-Averaged approach, plays a big role on conjugation.
- With regards to the optimization study, a further step into addressing the trade-off between pressure drop and temperature is using a more complex rib geometry. In literature various rib configurations were presented, such as wedge-shaped ribs, or backward-aligned ribs. The parametrization of such ribs and a similar optimization analysis can shed more light on the turbulence technique offering the lowest friction/heat transfer coefficient ratio.
- Finally, from the correlation plots of the rib parameters of this study, it was established that the rib thickness and periodicity ratio play almost no role in both objectives. Therefore, one can run additional computations with an extension of the specified range of blockage and pitch ratios to establish whether the Pareto front also extends and achieves also better temperatures, and not only mass flow, compared to the nonturbulated circular channel.

Appendices

Appendix A

Gas turbine basics

Derivation of the thermodynamic efficiency (at optimum pressure) of the Joule-Brayton cycle is herein presented. The thermodynamic efficiency of the cycle is defined as the ratio of the extracted work to the added heat (assuming no losses, i.e. ideal cycle):

$$\eta_{th-dynamic} = \frac{\text{Net work}}{\text{Heat added}} = \frac{(T_4 - T_5) - (T_3 - T_2)}{T_4 - T_3}, \quad (\text{A.1})$$

where T_5 is the temperature at the end of the expansion process, and T_3 is the compressor outlet temperature. The expression can be further rearranged to

$$\eta_{th-dynamic} = 1 - \frac{T_2}{T_3}. \quad (\text{A.2})$$

The net work (or the specific gas power, *sgg*, i.e. work per unit mass) is hence:

$$W_{s,gg} = c_p(T_4 - T_5) = c_p[(T_4 - T_5) - (T_3 - T_2)], \quad (\text{A.3})$$

and using the isentropic gas equation:

$$\text{PR}^{\frac{\kappa-1}{\kappa}} = \frac{T_3}{T_2} = \frac{T_4}{T_5}, \quad (\text{A.4})$$

$$W_{s,gg} = c_p \left(T_4 - \frac{T_4 T_2}{T_3} - T_3 + T_2 \right). \quad (\text{A.5})$$

Differentiating w.r.t T_3 and equated to zero to find the peak value of specific power for a given temperature ratio (T_4/T_2), called the optimum pressure ratio, yields:

$$\frac{dW_{s,gg}}{dT_3} = c_p \left(\frac{T_4 T_2}{T_3^2} - 1 \right) = 0 \quad (\text{A.6})$$

hence,

$$T_3^2 = T_2 T_4, \quad (\text{A.7})$$

which yields

$$T_3 = \sqrt{T_2 T_4}, \quad (\text{A.8})$$

and finally substituting into eq.A.2:

$$\eta_{th-dynamic} = 1 - \sqrt{\frac{T_2}{T_4}}.$$

Appendix B

Luikov solution

B.1 Direct heat transfer solution method

The constants used in Eq. 5.5 (K and B) are given below:

$$K = \frac{\lambda_s}{\lambda_f} \frac{x}{b} (Pr)^{(-\frac{1}{2})} (\overline{Re}_x)^{(-\frac{1}{2})} \quad (\text{B.1a})$$

$$B = \frac{\bar{v}_y}{\bar{v}_x} \sqrt{Pr \overline{Re}_x} \quad (\text{B.1b})$$

The exact formulation of the Nusselt number, and hence HTC is calculated using:

$$Nu_x^{DHT} = \frac{1}{\pi} Pr^{\frac{1}{2}} (\overline{Re}_x)^{\frac{1}{2}} N(K, B), \quad (\text{B.1c})$$

where

$$N(K, B) = \frac{\varphi(K, B) - \frac{1}{2} \sqrt{\pi} B \operatorname{erfc} B}{\left(1 - \frac{B}{K}\right) - \frac{1}{K \sqrt{\pi}} \varphi(K, B) + \frac{1}{2} \frac{B}{K} \operatorname{erfc} \frac{1}{2} B}, \quad (\text{B.1d})$$

$$\begin{aligned} \varphi(K, B) &= \left(1 - \frac{1}{2} \frac{B}{K}\right) (\pi) K \exp(K^2 - BK) \\ &\times \operatorname{erfc}\left(K - \frac{1}{2} B\right). \end{aligned} \quad (\text{B.1e})$$

B.2 Boundary layer approximation

The procedure omitted in the derivation of the thermal boundary layer thickness in Chapter 5 includes the evaluation of the following integral:

$$\begin{aligned} \frac{\partial}{\partial x} \int_0^{\delta_t} v_\infty \left[1 - \frac{3}{4} \frac{y}{\delta_t} + \frac{1}{2} \left(\frac{y}{\delta_t}\right)^3\right] (\theta_\infty - \theta_w) \\ \times \left[\frac{3}{2} \frac{y}{\delta} - \frac{1}{2} \left(\frac{y}{\delta}\right)^3\right] dy = \alpha \left(\frac{\partial \theta_1(x, 0)}{\partial y}\right), \end{aligned} \quad (\text{B.1f})$$

By evaluating the integral and applying some mathematical operations ultimately yields:

$$\frac{\partial}{\partial x} \left[\frac{1}{(1+z)z^2\delta} \right] = \left(\frac{1}{z\delta_t}\right)^3 \frac{10\alpha z}{v_\infty(1+z)}, \quad (\text{B.1g})$$

Given the limit value of the equation, $\lim_{z \rightarrow 0}$, (B.1g) becomes:

$$\frac{\partial}{\partial x} \left(\frac{1}{z^2 \delta} \right) = \left(\frac{1}{\delta_t} \right)^3 \frac{10\alpha z}{v_\infty} \quad (\text{B.1h})$$

The Biot number can be calculated analytically, using the approximation of the HTC, such that:

$$Bi = 0.332 \cdot b \left(\frac{\lambda_f}{\lambda_s} \right) \sqrt[3]{Pr} \frac{\sqrt{Re_x}}{x}. \quad (\text{B.1i})$$

The Nuselt number is calculated as:

$$Nu_x^{BLE} = \frac{x}{(T_\infty - T_w)} \left(\frac{\partial T}{\partial y} \right) = \frac{3}{2} \frac{x}{\delta_t} \quad (\text{B.1j})$$

B.3 Numerical solution

The energy coupling setting was chosen to explicit, since it allows for coupling of FVM-FEM meshes. This includes a mapped static temperature on the fluid mesh interface, and mapped reference temperature and mapped local heat transfer coefficient on the solid interface. The types of solvers for each domain are briefly presented in the main part of the report. A summary of the boundary conditions settings is given in Table B.1 A compact interpolation stencil was selected for connection method for the mesh faces on the two sides of the interface. The interpolation stencil method on interfaces is briefly discussed in Appendix E.1, including a short comparison with the alternative methods available in the code.

Table B.1: Interface boundary condition settings

Type	Mapped Contact
Energy coupling	Explicit
Energy source	None
Contact resistance	None
Solid side	Mapped local HTC Mapped ref. temp.
Fluid side	Mapped static temp.
Interpolation stencil	Compact
Interpolation method	Nearest Neighbour

The mesh study included five sizes tabulated below. The naming convention used for each mesh is based on the resultant minimum y^+ value on the fluid/solid interface. To the author's knowledge, the y^+ is exclusively a turbulence based parameter, but will be solely used in this study for the sake of convenience for addressing the level of mesh refinement in the vicinity of the wall. The results of each mesh are compared in the following section. The number of elements in the z-direction was kept constant at 10 for all five meshes. The mesh study focuses only on $\overline{Bi} = 0.1$. A value for the Biot number of 1 will only be used for the studies in Section 5.1.3, in which the findings of the validation study are discussed.

Table B.2: Properties of meshes used for laminar flat plate study

Grid size	$\Delta y_{min}@wall$ (m)	Stretching factor	Approx. min. y^+
60x120	7.2e-05	1.061	0.5
60x60	1.4e-04	1.115	1
60x40	7.2e-04	1.129	5
60x20	1.4e-03	1.235	10
60x5	1.4e-02	1.467	100

The results, indicating the accuracy of each mesh are shown below. From the resultant interface quantities, it is clear that accuracy is gained, as expected, with increasing (logarithmic) refinement near the interface. Since the difference between the first and second finest meshes ($y^+ = 1$ and $y^+ = 0.1$) is essentially intangible and the computational speed gain is negligible (Figure B.2, for the sake of the results of this study, presented in Section 5.1.3, and all upcoming studies, including the comparison of the conjugate heat transfer method with the decoupled approach on this study case, are based on the finest mesh (60×120 cell elements).

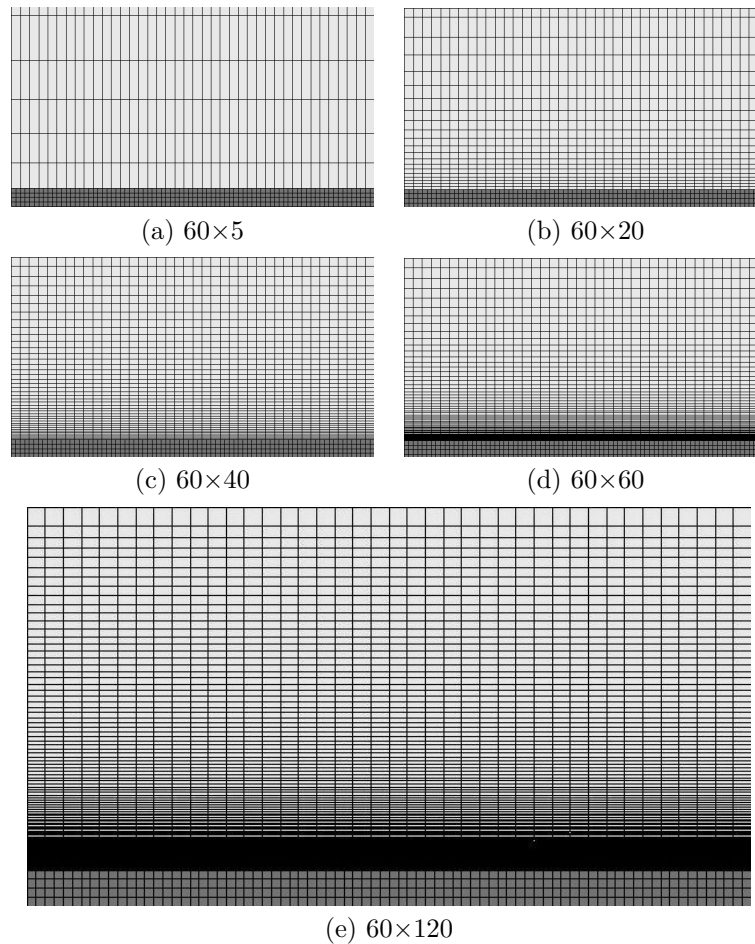


Figure B.1: All five meshes used for the independence study of the flat plate problem, in the vicinity above the plate (no rear and front fluid extensions)

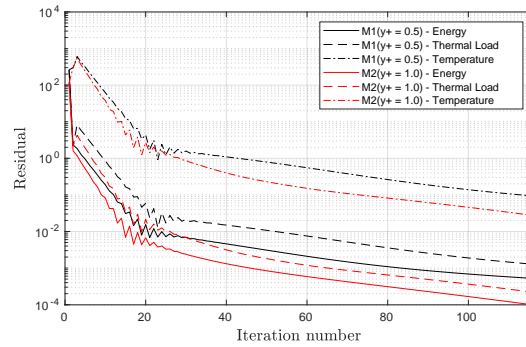


Figure B.2: Temperature, energy, and thermal load residual values from M1 and M2, until iteration number 120 (convergence for M1 reached at 260 iterations)

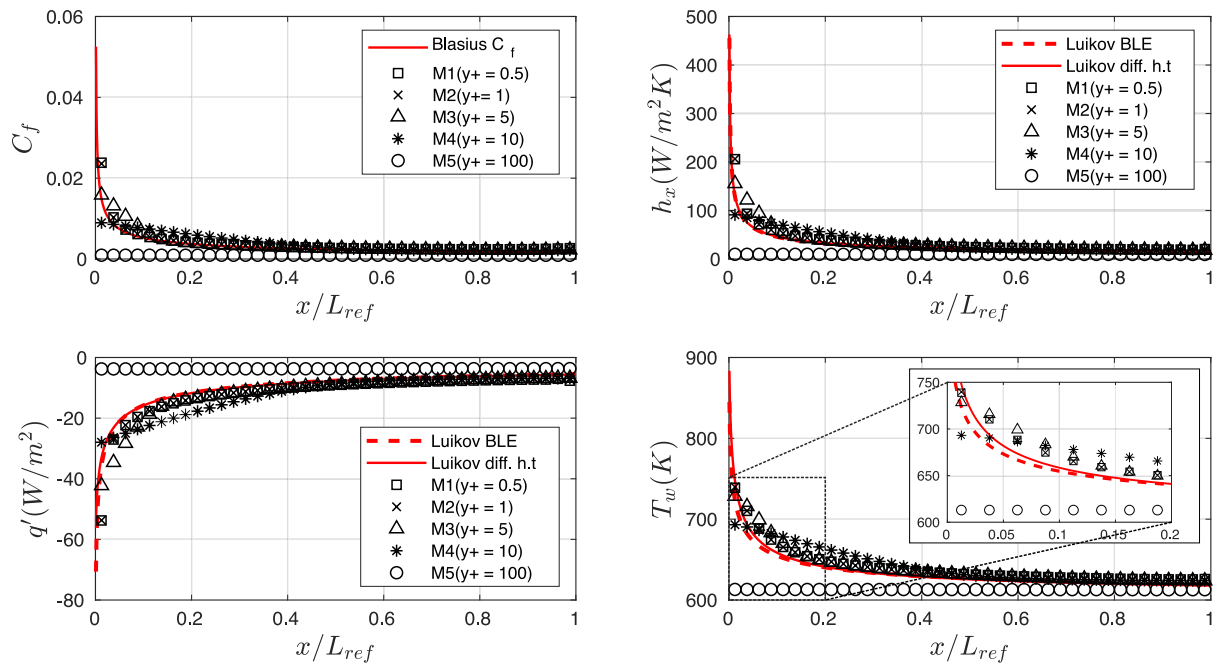


Figure B.3: Comparison of friction coefficient to Blasius analytical solution, along with heat transfer coefficient, heat flux, and temperature at the interface with Luikov analytical solution ($\overline{Bi} = 0.1$).

Expanding on the mesh study results, it is evident that for M1 and M2, in particular, the difference between the numerical solution and the analytical one is the highest in the vicinity of the leading edge, where the gradients are the highest. The error hence grows from $\approx 1\%$ to $\approx 2.5\%$ upstream from $x/L_{ref} = 0.25$ to $x/L_{ref} = 0.0$, respectively, for both M1 and M2. Therefore, an additional step taken towards minimizing this error was adding mesh stretching also downstream in the x-direction (in a similar fashion such that $x^+ = y^+$) in both solid and fluid regions. The resulting mesh is presented below.

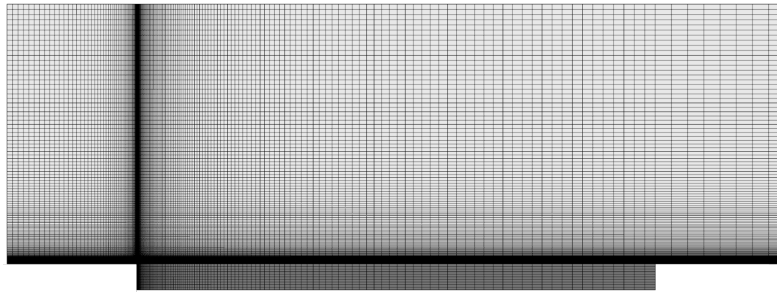


Figure B.4: Mesh M1 with x-refinement (incl. extensions in fluid region).

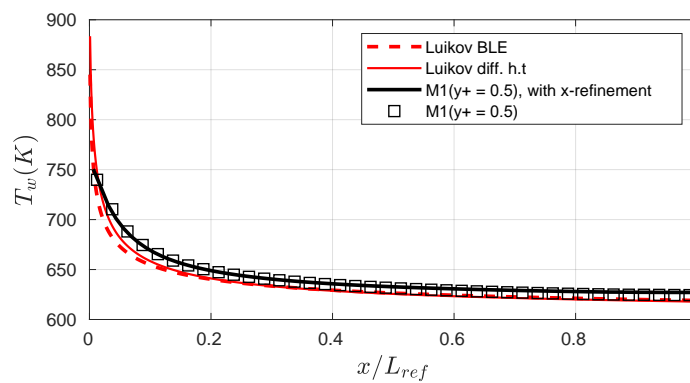


Figure B.5: Comparison of interface temperature obtained from refined mesh in the x-direction w.r.t mesh without refinement and the analytical solution from Luikov ($\overline{Bi} = 0.1$).

However, the refinement near the leading edge did not lead to any benefit in terms of convergence with the steep gradients present in the analytical solution, as shown in Figure B.5. The only noticeable difference is the slight increase in the temperature downstream, however, it still remains negligible. Hence, due to the lack of improvement in the vicinity where the difference is the highest, the subsequent studies are done on mesh M1, as previously mentioned, having ensured that the solution is independent on the mesh fineness.

Appendix C

Turbulent offset jet mesh study

The experimental domain that was attempted to be replicated is shown in Fig. C.1.

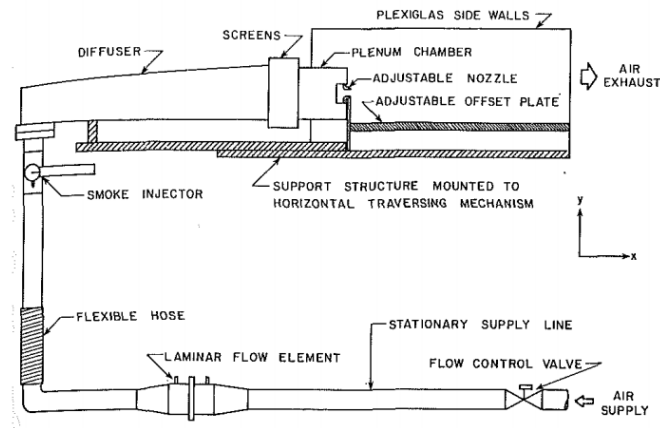


Figure C.1: Schematic of experimental arrangement, extracted from [95]

The entire CFD domain is shown below.

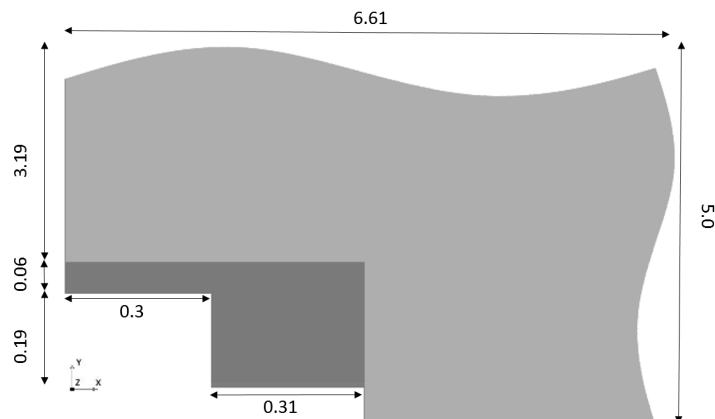


Figure C.2: Entire CFD domain with relevant dimensions (m) (light gray region is not included in Figure 5.11, i.e. ambient room region in the experimental domain, having a width of 3.0m)

Table C.1: Specification of mesh settings on target surfaces for M2

Surface (region)	Control value		
	TSS ¹ (mm)	GR ²	PLT ³
Ambient	250	1.05	N/A
Plexiglass walls	10	1.05	3
Interace	0.5	1.05	5
Plenum chamber walls	0.5	1.1	N/A

A short description of some key attributes of all meshes used for the study is shown in the table below, followed by a set of comprehensive plots, to illustrate the mesh convergence. The meshes and a table containing the respective mesh settings along all surfaces (table contains data only for mesh M2) are illustrated in Figure C.3 and Table C.1, respectively. Clearly, the solution tends to be independent around an mesh size of $\approx 8 \times 10^6$. Figure C.4 displays the convergence of the peak value of the friction coefficient along the centreline of the interface and the measured reattachment length.

Table C.2: Mesh attributes of all meshes in the mesh independence study

Reference ID	Cell count	y_{max}^+	y_{ave}^+	$\overline{C_f}$	X_{cr}
M1	15.9M	2.25	1.63	1.16	16.64
M2	10.3M	3.59	2.62	1.22	16.32
M3	4.9M	4.62	3.26	1.24	16.00
M4	2.4M	6.14	3.83	1.11	15.28
M5	1.5M	8.56	5.31	1.13	14.48
M6	226K	15.91	11.65	1.01	11.91

The red horizontal line represents the experimental reattachment length for OR=7 in the study by Pelfrey, equal to 12.42. In the current study, it was measured by taking the axial location of the minimum friction coefficient. All meshes overpredicted the reattachment length, which was found to be one of the key differences between the studies in the results in Section 5.2.2. Later, it will be shown that this finding is independent on the choice of RANS model, but mostly on the mesh size.

Meshes M1-M3 display very similar velocity and interface friction profiles. The resultant reattachment lengths for meshes M4-M6 are visible lower and friction profiles are inherently more dissipative, which in particular becomes evident in the region downstream ($\Delta X \approx 7$), using the friction profile as an example. This observation can also be traced back to the normalized axial velocity profiles plotted in Figure C.5 for four regions - two for recirculation region ($X = 3, 6$), impingement ($X = 9$), and wall jet region ($X = 15$).

¹Target surface size (mm)

²Growth rate factor

³Prism layer thickness (mm)

⁴No thermal conductivity is given in the paper.

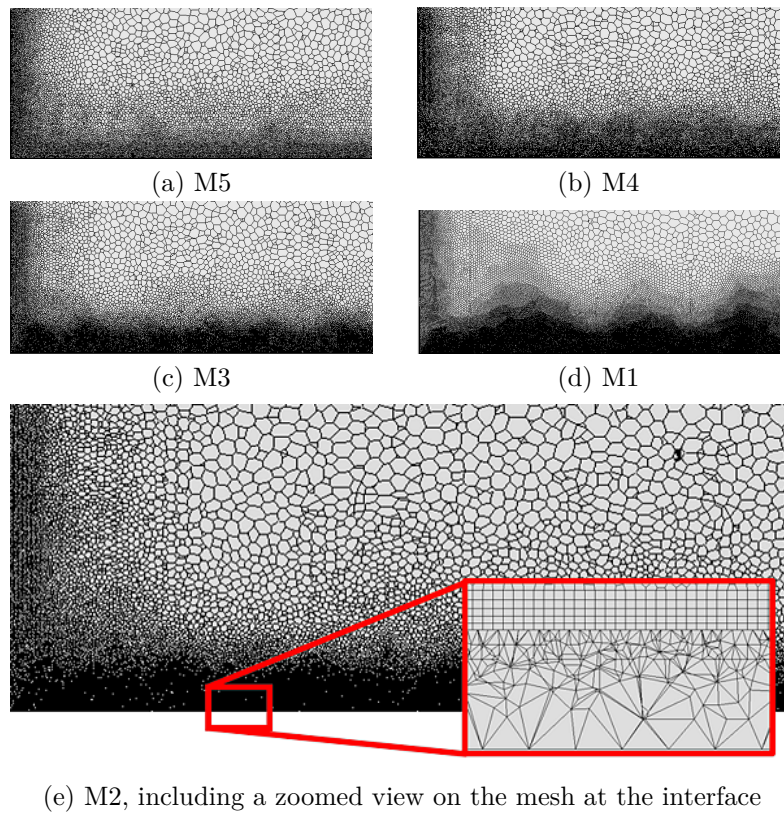


Figure C.3: All five meshes used for the independence study of the flat plate problem, in the vicinity above the plate (no rear and front fluid extensions)

The dissipative effect of M5 is less apparent in velocity: the peak axial value is lower by between 5% to 10% in the impingement and wall jet regions, respectively. A more striking difference is that despite the relatively good fit with experimental data for the friction coefficient along the plate, the axial velocity for all finer meshes is higher than in the experiments following the recirculation region. Only mesh M6 seems to match the physical dissipation of the problem based on velocity data and is the closest to the experimental attachment point.

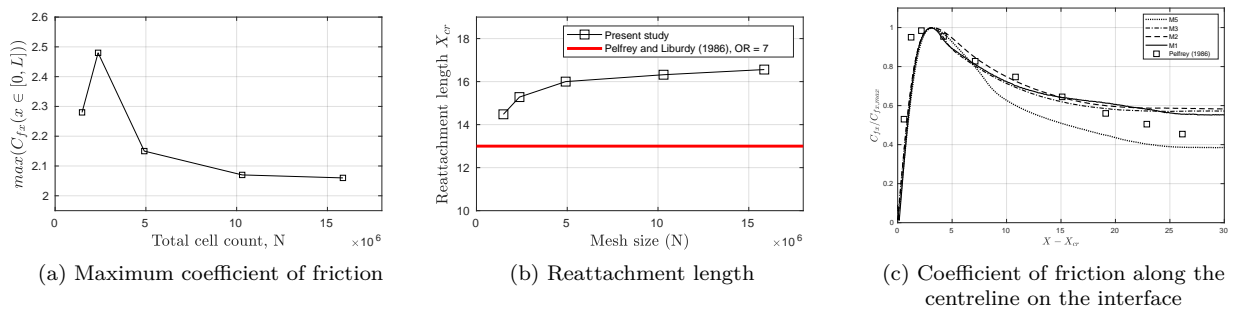


Figure C.4: Convergence for M1, M2, M3, M4 and M5

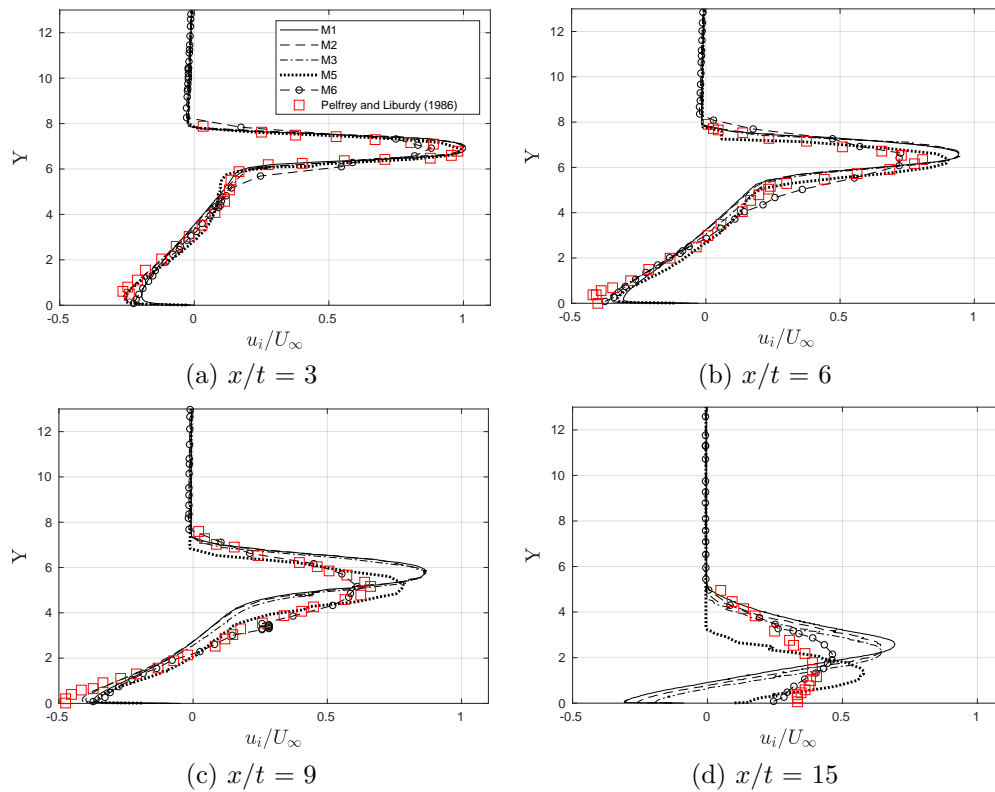


Figure C.5: Axial velocity component convergence with experimental data at five downstream location

Thereby, based on the brief analysis done above, mesh M2 was chosen for the purpose of the upcoming studies for all computations involving All- or low- y^+ wall functions. The grid size provides satisfactory results and very close to to M1, and ensures a grid-independent solution. The fine discretization around the near wall region is also beneficial for the analysis of scalar fields in the subsequent studies.

Multiple additional measures were taken in terms of solver type/settings and parameters to address the mismatch of experimental and numerical reattachment length, and hence axial velocities downstream. Such include:

- **Turbulence intensity sweep (no CHT enabled)** - Constant air properties were applied to the fluid; the jet temperature at the outlet was set equal to that of the ambient air; the free-stream and near-wall turbulent Prandtl number were both set to a constant value of 0.9.
- **Prandtl Number** - Various values for the Prandtl number were also tested, under the assumption that the varying thermal and momentum diffusivity would tangibly change the velocity profiles used for validating the mesh and settings.
- **Multi-component mixture, along with variable properties** - Thermal conductivity and dynamic viscosity were both algebraically modelled using Sutherland's formulation.

All three abovementioned methods yielded no improvement in the accuracy of the simulations. This is partially documented in the Appendix, where the different RL values are tabulated along with axial velocities at the four aforementioned locations downstream.

Appendix D

Auxiliary contracted inlets study

D.1 Concept introduction

Since no improvement in the cooling was achieved, a proposed method was keeping the length of the cooling channel the same as in the baseline, but with additional inlets positioned equidistantly downstream. The cross section of the generated aux. inlets was kept identical to the main original inlets of the ribbed component inlets with $d_{h,aux}^*$. Initially, the number of aux. inlets is swept from 1 to 3, at 5 different angles, $\alpha = 30^\circ, 45^\circ, 60^\circ, 90^\circ$, for each number, leading to 15 evaluations in total. An illustration is shown below.

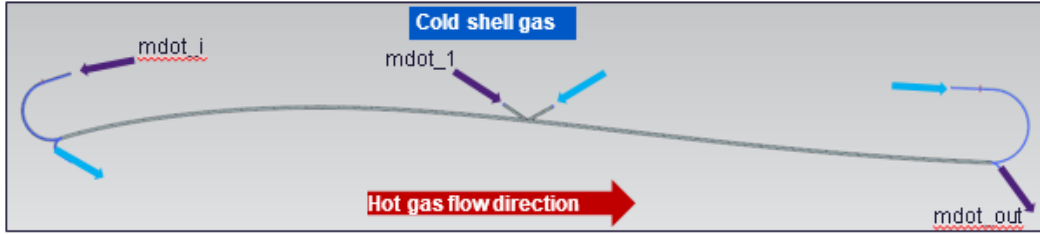


Figure D.1: Schematic of the setup: auxiliary inlets are placed downstream for both counter current channels.

The results of this approach are presented in Section D.2. Subsequently, a new parametrization on the inlets was proposed with the goal of further reducing the BC temperature. By decreasing the area of the channels downstream closer to the outlet, the inlet velocity will be higher and hence the coolant can be artificially throttled, mitigating for the velocity decrease (arising from the pressure drop at the end). The inlet area of the aux. inlets was parametrized and related to the main inlets using:

$$A_i = C_{adjusted}^i A_{main} . \quad (B.1a)$$

The power of the area factor is equal to the number of the aux. inlet, e.g. the 2nd inlet downstream uses an exponent equal to 2. Two aux. inlets per channel were used (i.e. only a quadratic relationship). Three hydraulic diameters (of the main inlet), $d_h^* = 0.7, 0.9, 1$ for each correction factor are used. A schematic is shown below, to illustrate the concept of such artificial throttling.

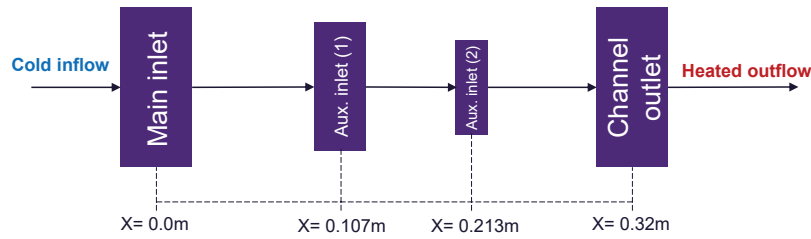


Figure D.2: Illustrative depiction of the idea of contracting the inlets downstream.

D.2 Constant cross-section

The influence on the average and maximum temperatures, along with the nondimensional coolant mass flow (as a fraction of the mass flow in the circular smooth bottom panel). Clearly, temperature fields are virtually independent on the number of inlets downstream. The effect of inlet angle is even smaller. There seems to be a minimum for the average temperature but the difference is however negligible. Interface temperatures showed that the decrease in temperature from the inlet angle is strongly localized exclusively at the respective inlet location. The profile everywhere else was virtually identical.

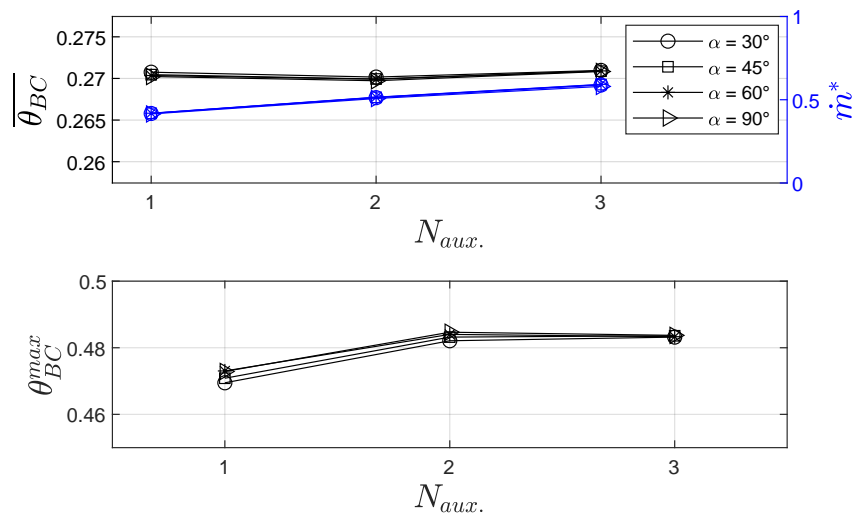


Figure D.3: Effect of number of inlets and inlet angle on average, maximum temperatures and coolant consumption (nondimensionalized).

Pumping more air downstream does not influence cooling performance (when the outlet number is kept constant). Longitudinal gradients are actually introduced on the BC and cold side which will likely have a negative/neutral effect on lifing. Improvement on average temperatures is negligible.

D.3 Adjusted cross-section

The results for each contraction factor and hydraulic diameter are shown below. The effect of area reduction becomes more pronounced for larger hydraulic diameters when it comes to \dot{m}^* . Same phenomenon is observed for the average BC temperature, $\bar{\theta}_{BC}$. The maximum temperature near the exit frame is reduced when flow is ‘more’ throttled’ (i.e smaller areas), thus the correlation b/w \dot{m}^* and θ_{BC}^{max} : the area-adjustment factor effect becomes negligible for small channel diameters, similarly to the maximum temperature where the increase is also higher for larger diameter. However, the maximum temperature is in fact lower, with a lower mass flow, which is the main benefit from this study. The

influence of area reduction however is still negligible for $\overline{\theta_{BC}}$ when it comes to small hydraulic diameter, $d_{h,aux} = 0.7$. Additionally, the maximum difference between the obtained values for the average temperatures are within the range of only 0.01 in nondimensional terms.

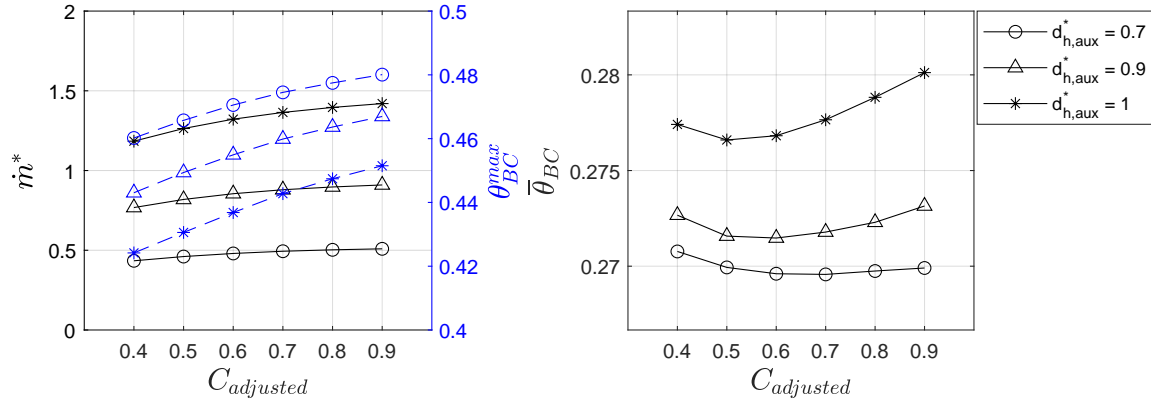


Figure D.4: Influence of the amount of contraction on the average, maximum temperatures and coolant consumption (nondimensionalized).

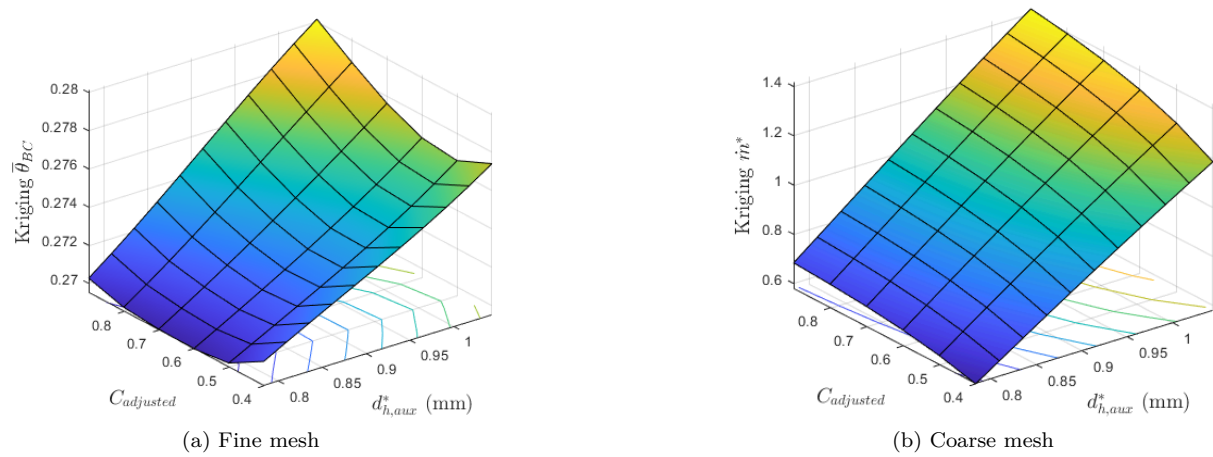


Figure D.5: Kriging fits of numerical data: (a) nondimensionalized mass flow and (b) average bond coating temperature.

Referring back to the constant channel length, the results prove that unless the channel length is reduced, i.e. include at least more channel outlet, the achievable reduction in temperature and mass flow from such artificial throttling is still limited. The benefit of reducing the maximum temperature near the turbine inlet however, presents a promising path into a potential full (both mass-flow- and temperature-wise) HT enhancement of the cooling system in the future.

Appendix E

More on numerical methodology

E.1 Interpolation methods & coupling

E.1.1 Interpolation stencils

Interpolation stencil properties and values from STAR-CCM+ Interpolation, as previously mentioned, is required at the fluid-solid interface, where data is mapped from the FVM fluid mesh to the FEM solid mesh and vice versa. Data interpolation is not solely limited to interface calculations however: remeshing operations require interpolation of existing solution data onto a new mesh, or additionally, mapping external (tabular) data onto a mesh, such as the case in the decoupled HT approach. The available interpolation algorithms in STAR-CCM+ include

- Nearest Neighbor Interpolation
- Least Squares Interpolation
- Exact Imprinting Interpolation
- Approximate Imprinting Interpolation
- Shape function Interpolation

The choice of interpolation method is determined by the type of mesh from which data is interpolation (source stencil) to the mesh points on which the data is interpolated (target stencil), as shown in the table below.

		Source stencil		
		Vertex	Face	Cell
Target stencil	Vertex	Shape Function Least Squares Nearest Neighbor	Least Squares Nearest Neighbor	Least Squares Nearest Neighbor
	Face	Shape Function Least Squares Nearest Neighbor	Least Squares Nearest Neighbor Exact Imprinting Approximate Imprinting	Least Squares Nearest Neighbor
	Cell	Shape Function Least Squares Nearest Neighbor	Least Squares Nearest Neighbor	Least Squares Nearest Neighbor

Table E.1: Different interpolation methods in accordance to the source and target stencils.

The available methods are briefly explained in the subsections to follow.

It is also worthwhile mentioning the mechanism used for connecting the mesh faces on the two sides of the interface. Two options are given within the code: (i) compact and (ii) imprinted. The compact scheme builds a connectivity map by finding the nearest neighbour of a face on the opposite side of the interface, and then sets the interpolation weights based on the face area ratios from the map. The imprinted scheme uses a connectivity map by finding all the faces on the opposite side of the interfaces that overlap with a face. The method however, is less tolerant to mesh irregularities and poor mesh quality, compared to the compact method.

In addition, the Explicit energy coupling was used for both laminar and turbulent offset jet studies, in which the fluid interface boundary is automatically set to a temperature thermal boundary condition (i.e. static temperature), while the solid side of the CHT interface uses a convection thermal boundary condition. When the Laminar Flow model is selected, either the Mapped Local Heat Transfer Coefficient method (for no time averaging) is used or the Mapped Averaged Local Heat Transfer Coefficient method (for time averaging). When the Turbulent Flow model is selected, the default is set to the Mapped Specified Y+ Heat Transfer Coefficient method.

Nearest Neighbour Interpolation

The nearest neighbor method sets the data on a target face to the data on the nearest source face. In the following diagram, the centroid of the source face *k* is the closest point to the centroid of the target face *n*. The data from face *k* is assigned to face *n* as the mapped value.

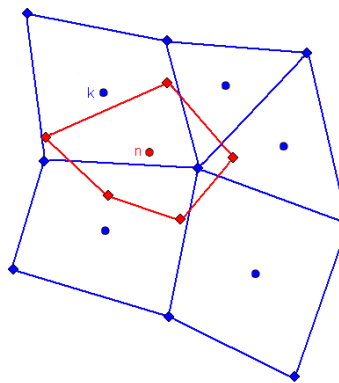


Figure E.1: Nearest neighbour interpolation method illustration.

Since the interface tolerance is manually set, the search algorithm is activated and tolerances that the algorithm uses to find the neighbors to the cells have to be specified. The following properties are set:

- Proximity Check - when activated, the minimum proximity check occurs.
- Minimum Proximity - the relative distance (based on cell size) to the target cell. 1 is equivalent to 100%.
- Normal Directions check - when activated, the normal direction check occurs.
- Minimum Angle - the angle, in degrees, between the source and target face normals. When the minimum angle is 0, the two normals point in the same direction, when 180, the normals point toward each other.

The values used are tabulated below.

Proximity check	Enabled
Minimum proximity	0.05
Normal directions check	Enabled
Minimum angle	110.0

Table E.2: Values and settings of the mapped interface tolerance

Least Squares Interpolation

A cost function is implemented in the least squares method to approximate the solution field distribution near a target location. In the following diagram, the solution field has known values f_i at the face centroids i on the source stencil.

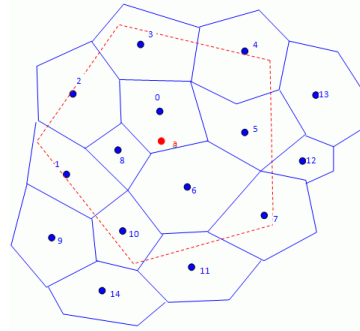


Figure E.2: Least square interpolation schematic.

The solution of the solution field is approximated to find the mapped value at the target point \mathbf{a} by first-order Taylor's expansion:

$$f(\mathbf{x}) \approx f(\mathbf{x}_a) + (\mathbf{x} - \mathbf{x}_a) \cdot \nabla f(\mathbf{x}_a). \quad (\text{B.1a})$$

The sum of the squared of the residuals to calculate $f(\mathbf{a})$:

$$S = \sum_{i \in F(c)} r_i^2, \quad (\text{B.1b})$$

where the residual is the difference between the predicted value at the source locations i and their known values f_i

$$r_i = f(\mathbf{x}_i) - f_i. \quad (\text{B.1c})$$

Exact Imprinting Interpolation

The exact imprinting name comes from the fact that the target cell face is imprinted on the source mesh. The value at the target \mathbf{a} is hence found from the resultant (from the imprint operation) normalized facelet areas as interpolation weights:

$$f_a A_a = \sum_{i \in F(c)} A_i f_i. \quad (\text{B.1d})$$

The difference with the least square method comes from the fact that all faces on the imprint surface contribute, as opposed to the least square interpolation where only the cells neighbouring the cell closest to the target cell centroid contribute (i.e. 2, 3, 4, 5, 6, and 8 in Fig. E.2)

Approximate Imprinting Interpolation

The method is a variation of the exact imprint method, which makes it less computationally expensive. The difference is that the method uses a proximity method instead of an exact intersection of the cells. A drawback of the method is that it is not flux-preserving, and is hence only recommended if the target mesh is considerably coarser than the source mesh.

Shape Function Interpolation

This interpolation method is only available for triangle and quadrilateral elements in 2D and tetrahedral and hexahedral elements in 3D for a source mesh, mapping to a FVM mesh. To evaluate the mapped value at the target point \mathbf{n} , the solution is interpolated at the vertices of element \mathbf{k} using nodal shape functions $N(k)$:

$$f_n = \sum_{l \in N(k)} f_l N_l(\xi_n, \eta_n, \chi_n), \quad (\text{B.1e})$$

where N_l is the shape function at vertex l , f_l is the solution value at vertex l , and denotes the local coordinates (ξ_n, η_n, χ_n) of point \mathbf{n} in the element \mathbf{k} . The sum is over the set of vertices of element \mathbf{k} , $N(k)$.

E.1.2 CHT coupling algorithms

Several explicit coupling algorithms are available according to literature. Explicit coupling accentuates on the need for interpolation between the two sides of the interface. However, it allows for conjugate heat transfer between two different mesh types (e.g. FVM for fluid and FEM for solid region), whereas the implicit energy coupling option is only available when both source and target meshes are FVM, and preferably the time-scales of both solid and fluid regions are similar. The drawback of the implicit energy coupling is that in order to calculate the thermal stresses in a solid, the component has to be meshed twice. In the subsections to follow, the most commonly used coupling algorithms are briefly discussed.

FFTB

The naming convention of all methods follow the quantities transferred relative to the fluid domain. In the flux forward temperature back method (FFTB), the wall temperature distribution is imposed to the fluid solver and the resulting heat flux distribution is imposed as a boundary condition to the solid conduction solver. The heat flux imposition on the solid then predicts a new temperature for the fluid region. The procedure is then iterated until convergence (i.e. the heat flux across the interface meets the specified convergence criteria). Hence, at the i -th iteration:

$$q_{wall}^{fem^i} = q_{wall}^{fvm^i} \quad (\text{B.1f})$$

The subsequent iteration then interpolates the previously obtained FEM temperature on the FVM side:

$$T_{wall}^{fvm^{i+1}} = T_{wall}^{fem^i} \quad (\text{B.1g})$$

For stability, an alternative formulation of the method can also employ under-relaxation factors. The equations of this techniques are omitted in this report.

TFFB

The temperature forward flux back method (TFFB) is the inverse method in which the heat flux distribution is imposed as a boundary condition for the fluid computation and the resulting wall temperature to the solid conduction solver. The updated heat flux is then returned as a boundary condition to the fluid solver:

$$q_{wall}^{fvm^i} = q_{wall}^{fem^i} \quad (\text{B.1h})$$

$$T_{wall}^{fem^{i+1}} = T_{wall}^{fvm^i} \quad (\text{B.1i})$$

Convergence is obtained when the exchanged temperatures and heat fluxes are not changing anymore.

hFTB

The third explicit coupling uses Newton’s law of cooling to calculate the HTC to update the boundary conditions on the solid FEM side and then reimpose the newly found temperature on the fluid FVM side. The method is thus named the the heat transfer coefficient forward temperature back method (hFTB).

The method is initialized with an imposed temperature on the FVM boundary. The adiabatic flow solver then estimates the local HTC and the ambient fluid temperature according to

$$q_{wall} = h \cdot (T_{wall} - T_{fluid})$$

Thereby, an implicit relation is provided between T_{wall} and q_{wall} that can be used as a boundary condition for the solid conduction computation. By using this method, the heat flux at the wall is automatically adjusted by the wall temperature which is the advantage of this algorithm. The boundary condition after the i -th iteration are hence:

$$q_{wall}^{fvm^i} = h \left(T_{wall}^{fvm^i} - T_{fluid}^i \right) \tag{B.1j}$$

$$q_{wall}^{fem^i} = h \left(T_{wall}^{fem^i} - T_{fluid}^i \right) \tag{B.1k}$$

$$T_{wall}^{fvm^{i+1}} = T_{wall}^{fem^i} \tag{B.1l}$$

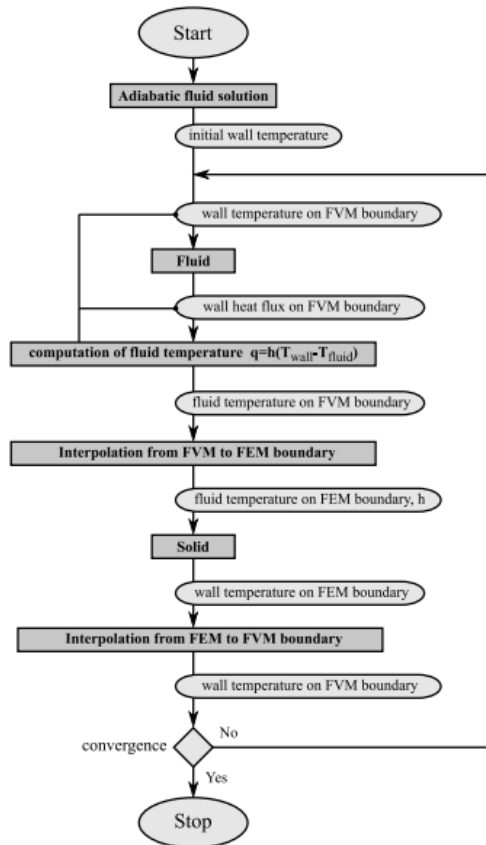


Figure E.3: Flow chart of the hFTB method.

The first equation is used to compute, for a fixed value of h , the value of T_{fluid} in function of the value T_{wall}^{fvm} and q_{wall}^{fvm} wall defined by the fluid computation. The second equation is the boundary condition

for the conduction calculation in the solid. This results in a new T_{wall}^{fem} and q_{wall}^{fem} on the solid wall. The third equation defines the boundary condition for the next iteration of the fluid computation. The flowchart above presents schematically the hFTB algorithm.

hFFTB

The heat transfer coefficient forward flux back method (hFFTB) is an alternative to HFTB where, instead of temperature, the quantity returned to the FVM domain can be a heat flux. This results in a new method with different stability properties and is called the hFFB method. The boundary conditions can be re-written as:

$$q_{wall}^{fvm^i} = h \left(T_{wall}^{fvm^i} - T_{fluid}^i \right) \quad (\text{B.1m})$$

$$q_{wall}^{fem^i} = h \left(T_{wall}^{fem^i} - T_{fluid}^i \right) \quad (\text{B.1n})$$

$$q_{wall}^{fvm^{i+1}} = q_{wall}^{fem^i} \quad (\text{B.1o})$$

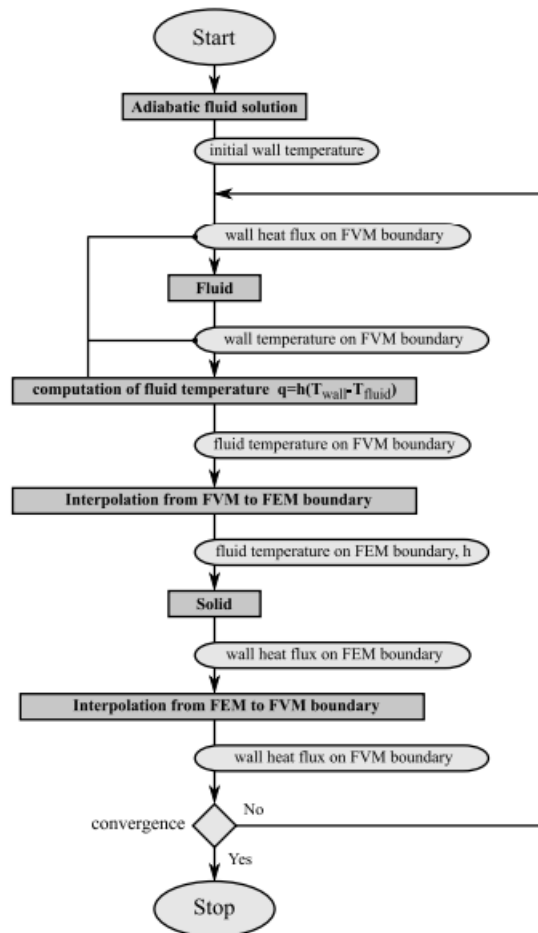


Figure E.4: Flow chart of the hFFTB method.

The flowchart above presents schematically the hFFTB algorithm.

E.2 More on turbulence models

E.2.1 Derivation of the RANS equations

In Chapter 4, the derivation of the Reynolds stress term, which arises due to the non-linearity of the convective term was not included. This subsection of the appendix addresses the derivation of the new term in the RANS equations, by showing explicitly the time-averaging procedure followed. In this subsection Cartesian tensor notation is used as it provides a short-hand that is widely used in fluid dynamics, especially in the context of classical turbulence analyses. Hence, the velocity vector for example is expressed as

$$\vec{v} = (u, v, w)^T = u_i, \quad \text{where } i = 1, 2, 3 \quad (\text{B.1p})$$

The NS equations (for an incompressible Newtonian fluid) are hence expressed as (the expression of the divergence and gradient operators using the Cartesian tensor notation, one can refer to in any standard turbulence textbook):

$$\frac{\partial u_i}{\partial x_i} = 0, \quad (\text{B.1q})$$

$$\frac{\partial u_i}{\partial t} + u_j \frac{\partial u_i}{\partial x_j} = f_i - \frac{1}{\rho} \frac{\partial p}{\partial x_i} + \nu \frac{\partial^2 u_i}{\partial x_j \partial x_j}. \quad (\text{B.1r})$$

Splitting the instantaneous field quantities (pressure, velocity, and body forces) into a mean and fluctuating component $u(\mathbf{x}, t) = \bar{u}(\mathbf{x}) + u'(\mathbf{x}, t)$, plugging into the original set of NS equations yields:

$$\frac{\partial (\bar{u}_i + u'_i)}{\partial x_i} = 0, \quad (\text{B.1s})$$

$$\frac{\partial (\bar{u}_i + u'_i)}{\partial t} + (\bar{u}_j + u'_j) \frac{\partial (\bar{u}_i + u'_i)}{\partial x_j} = (\bar{f}_i + f'_i) - \frac{1}{\rho} \frac{\partial (\bar{p} + p')}{\partial x_i} + \nu \frac{\partial^2 (\bar{u}_i + u'_i)}{\partial x_j \partial x_j}. \quad (\text{B.1t})$$

and knowing that the mean of the fluctuating component $\overline{u'_i} = 0$, and the double average of $\bar{u}_i = \overline{\bar{u}_i}$:

$$\frac{\partial \bar{u}_i}{\partial t} + \bar{u}_j \frac{\partial \bar{u}_i}{\partial x_j} = \bar{f}_i - \frac{1}{\rho} \frac{\partial \bar{p}}{\partial x_i} + \nu \frac{\partial^2 \bar{u}_i}{\partial x_j \partial x_j} - \frac{\partial \overline{u'_i u'_j}}{\partial x_j}. \quad (\text{B.1u})$$

Then, using the definition of the mean-strain tensor, \mathbf{S} , expressed in Cartesian tensor notation

$$\mathbf{S} = S_{ij} = \frac{1}{2} \left(\frac{\partial \bar{u}_i}{\partial x_j} + \frac{\partial \bar{u}_j}{\partial x_i} \right), \quad (\text{B.1v})$$

the equation becomes

$$\rho \frac{\partial \bar{u}_i}{\partial t} + \rho \bar{u}_j \frac{\partial \bar{u}_i}{\partial x_j} = \rho \bar{f}_i + \frac{\partial}{\partial x_j} \left[-\bar{p} \delta_{ij} + 2\mu \bar{S}_{ij} - \rho \overline{u'_i u'_j} \right], \quad (\text{B.1w})$$

where δ_{ij} is the Kronecker delta function. The Reynolds averaged conservation, momentum and energy equations, hence, in vector form (the default notation of this report) are:

$$\frac{\partial \rho}{\partial t} + \nabla \cdot (\rho \bar{\mathbf{v}}) = 0, \quad (\text{B.1x})$$

$$\frac{\partial}{\partial t} (\rho \bar{\mathbf{v}}) + \nabla \cdot (\rho \bar{\mathbf{v}} \otimes \bar{\mathbf{v}}) = -\nabla \cdot \bar{p} \mathbf{I} + \nabla \cdot \bar{\boldsymbol{\tau}} + \mathbf{f}_b, \quad (\text{B.1y})$$

$$\frac{\partial}{\partial t} (\rho \bar{E}) + \nabla \cdot (\rho \bar{E} \bar{\mathbf{v}}) = -\nabla \cdot \bar{p} \bar{\mathbf{v}} + \nabla \cdot \bar{\boldsymbol{\tau}} \bar{\mathbf{v}} - \nabla \cdot \bar{\mathbf{q}} + \mathbf{f}_b \bar{\mathbf{v}}. \quad (\text{B.1z})$$

E.2.2 Realizable $k - \varepsilon$ Damping function

The damping function used in the realizable $k - \varepsilon$ model of the coefficient C_μ follows the standard formulation found in literature. It is expressed as a function of mean flow and turbulence properties, so that certain mathematical constraints on the normal stresses are consistent with the physics of turbulence (hence term realizable).

E.2.3 Two-layer modification of the $k - \varepsilon$ model

When the blended wall function approach is used, a two-layer model modification is used and solves for k but prescribes ε algebraically with distance from the wall in the viscosity dominated near-wall flow regions. The dissipation rate near the wall is simply prescribed as

$$\varepsilon = \frac{k^{3/2}}{l_\varepsilon}, \quad (\text{B.1})$$

where l_ε is the length scale function calculated according to the Wolfstein variant:

$$c_l d \left[1 - \exp\left(-\frac{\text{Re}_d}{2c_l}\right) \right], \quad (\text{B.1})$$

with d being the wall normal distance and $c_l = 0.42C_\mu^{-3/4}$. As per the suggestion of Jongen, a wall-proximity indicator is used to combine the two-layer formulation with the full two-equation model, such that:

$$\lambda = \frac{1}{2} \left[1 + \tanh\left(\frac{\text{Re}_d - \text{Re}_y^*}{A}\right) \right], \quad (\text{B.1})$$

with $\text{Re}_y^* = 60$, and $A = 4.35$. More importantly, a blending function for the turbulent viscosity on the wall is used to implement the formulation according to Wolfstein such that:

$$\mu_t = \lambda \mu_t|_{k-\varepsilon} + (1 - \lambda) \mu \left(\frac{\mu_t}{\mu} \right)_{2\text{-layer}}, \quad (\text{B.1})$$

$$\left(\frac{\mu_t}{\mu} \right)_{2\text{-layer}} = 0.42 \text{Re}_d C_\mu^{1/4} \left[1 - \exp\left(-\frac{\text{Re}_d}{70}\right) \right] \quad (\text{B.1})$$

E.2.4 Shear and stretching modification in the $k - \omega$ SST model

The blending functions F_1 and F_2 in Eq.4.33-4.34, needed in the formulation of the turbulent viscosity and production of ω are defined as:

$$F_1 = \tanh\left(\left[\min\left(\max\left(\frac{\sqrt{k}}{0.09\omega d}, \frac{500v}{d^2\omega}\right), \frac{2k}{d^2 CD_{k\omega}}\right)\right]^4\right), \quad (\text{B.1})$$

$$F_2 = \tanh\left(\left(\max\left(\frac{2\sqrt{k}}{\beta^*\omega d}, \frac{500v}{d^2\omega}\right)\right)^2\right). \quad (\text{B.1})$$

with d being the wall-normal distance and $CD_{k\omega} = \max\left(\frac{1}{\omega} \nabla k \cdot \nabla \omega, 10^{-20}\right)$ is the cross-diffusion coefficient. By definition the SST model includes free shear-modifications including:

$$f_{\beta^*} = \begin{cases} 1 & \text{for } \chi_k \leq 0 \\ \frac{1+680\chi_k^2}{1+400\chi_k^2} & \text{for } \chi_k > 0 \end{cases}, \quad (\text{B.1})$$

which is often referred to as the dissipation limiter, and cross-diffusion limiter:

$$CD_\omega = \sigma_d \frac{\rho}{\omega} \frac{\partial k}{\partial y} \frac{\partial \omega}{\partial y}, \quad (\text{B.1})$$

where

$$\sigma_d = \begin{cases} 0, & \frac{\partial k}{\partial y} \frac{\partial \omega}{\partial y} \leq 0 \\ \frac{1}{8}, & \frac{\partial k}{\partial y} \frac{\partial \omega}{\partial y} > 0 \end{cases} \quad (\text{B.1})$$

E.3 CFD roughness

The effect of added wall roughness is implemented in the wall functions by using the wall roughness function f . The roughness parameter R^+ is first defined as:

$$R^+ = \frac{r\rho u^*}{\mu} \quad (\text{B.1})$$

with r being the sandgrain roughness height used in the computation. The roughness function f used is then calculated given three conditions:

$$f = \begin{cases} 1 & ; R^+ \leq R_{\text{smooth}}^+ \\ \left[B \left(\frac{R^+ - R_{\text{smooth}}^+}{R_{\text{rough}}^+ - R_{\text{smooth}}^+} \right) + CR^+ \right]^a & ; R_{\text{smooth}}^+ < R^+ < R_{\text{rough}}^+ \\ B + CR^+ & ; R^+ > R_{\text{rough}}^+ \end{cases} \quad (\text{B.1})$$

The exponent a is simply

$$a = \sin \left[\frac{\pi}{2} \frac{\log(R^+/R_{\text{smooth}}^+)}{\log(R_{\text{rough}}^+/R_{\text{smooth}}^+)} \right] \quad (\text{B.1})$$

and the model coefficients $C = 0.253$, $R_{\text{smooth}}^+ = 2.25$, and $R_{\text{rough}}^+ = 90$.

Bibliography

- [1] A. Predvoditelev A. V. Luikov, A. Pomerantsev, and V. Bubnov. “Heat and Mass Transfer (Handbook)”. In: *International Journal of Heat and Mass Transfer* 16 (1973), pp. 1062–1063.
- [2] Theodore Allen. *Introduction to Engineering Statistics and Lean Six Sigma: Statistical Quality Control and Design of Experiments and Systems*. Jan. 2019. ISBN: 978-1-4471-7419-6. DOI: 10.1007/978-1-4471-7420-2.
- [3] F. E. Ames and R. J. Moffat. *Heat Transfer With High Intensity, Large Scale Turbulence: The Flat Plate Turbulent Boundary Layer and the Cylindrical Stagnation Point*. 1990.
- [4] Forrest E. Ames. “Turbulence Effects on Convective Heat Transfer”. In: *Handbook of Thermal Science and Engineering* (2018), pp. 391–423. DOI: 10.1007/978-3-319-26695-4_17.
- [5] Mark Anderson and Patrick Whitcomb. “Design of Experiments”. In: Sept. 2010. ISBN: 9780471238966. DOI: 10.1002/0471238961.0405190908010814.a01.pub3.
- [6] Mehdi Bahador, T Nilsson, and Bengt Sundén. “On heat load calculations in gas turbine combustors”. eng. In: *Computational Studies*. Vol. 5. WIT Press, 2004, pp. 345–357. DOI: 10.2495/HT040321. URL: <http://dx.doi.org/10.2495/HT040321>.
- [7] J. W. Baughn et al. “Local Heat Transfer Downstream of an Abrupt Expansion in a Circular Channel With Constant Wall Heat Flux”. In: *Journal of Heat Transfer* 106.4 (1984), pp. 789–796. DOI: 10.1115/1.3246753.
- [8] C. E. Baukal and B. Gebhart. “A Review of Flame Impingement Heat Transfer Studies Part 2: Measurements”. In: *Combustion Science and Technology* 104.4-6 (1995), pp. 359–385. DOI: 10.1080/00102209508907728.
- [9] C.E. Baukal and B. Gebhart. “Surface condition effects on flame impingement heat transfer”. In: *Experimental Thermal and Fluid Science* 15.4 (1997), pp. 323–335. ISSN: 0894-1777. DOI: [https://doi.org/10.1016/S0894-1777\(97\)00036-8](https://doi.org/10.1016/S0894-1777(97)00036-8). URL: <http://www.sciencedirect.com/science/article/pii/S0894177797000368>.
- [10] R. A. Baurle. “Hybrid Reynolds-Averaged/Large-Eddy Simulation of a Cavity Flameholder: Modeling Sensitivities”. In: *AIAA Journal* 55.2 (2017), pp. 524–543. DOI: 10.2514/1.J055257. eprint: <https://doi.org/10.2514/1.J055257>.
- [11] T.L. Bergman et al. *Fundamentals of Heat and Mass Transfer*. Wiley, 2011. ISBN: 9780470501979.
- [12] Dimitris Bertsimas and John N. Tsitsiklis. *Introduction to linear optimization*. Athena Scientific, 1997.
- [13] L. Bittner. “R. Bellman, Adaptive Control Processes. A Guided Tour. XVI + 255 S. Princeton, N. J., 1961. Princeton University Press. Preis geb. \$ 6.50”. In: *ZAMM - Journal of Applied Mathematics and Mechanics / Zeitschrift für Angewandte Mathematik und Mechanik* 42.7-8 (1962), pp. 364–365. DOI: <https://doi.org/10.1002/zamm.19620420718>. eprint: <https://onlinelibrary.wiley.com/doi/pdf/10.1002/zamm.19620420718>. URL: <https://onlinelibrary.wiley.com/doi/abs/10.1002/zamm.19620420718>.

-
- [14] J. Bons. “A Critical Assessment of Reynolds Analogy for Turbine Flows”. In: *Journal of Heat Transfer* 127.5 (2005), pp. 472–485. ISSN: 0022-1481. DOI: 10.1115/1.1861919. eprint: https://asmedigitalcollection.asme.org/heattransfer/article-pdf/127/5/472/5734392/472_1.pdf. URL: <https://doi.org/10.1115/1.1861919>.
- [15] R.s. Bunker. “Innovative gas turbine cooling techniques”. In: *Thermal Engineering in Power Systems WIT Transactions on State of the Art in Science and Engineering* (2008), pp. 199–229. DOI: 10.2495/978-1-84564-062-0/07.
- [16] H.l. Cao and J.l. Xu. “Thermal performance of a micro-combustor for micro-gas turbine system”. In: *Energy Conversion and Management* 48.5 (2007), pp. 1569–1578. DOI: 10.1016/j.enconman.2006.11.022.
- [17] Luca Casarsa, Murat Çakan, and Tony Arts. “Characterization of the Velocity and Heat Transfer Fields in an Internal Cooling Channel With High Blockage Ratio”. In: Jan. 2002. DOI: 10.1115/GT2002-30207.
- [18] Marco Cavazzuti. *Optimization methods from theory to design ; scientific and technological aspects in mechanics*. Springer, 2013.
- [19] Tuncer Cebeci and Peter Bradshaw. In: *Physical and Computational Aspects of Convective Heat Transfer* (1988). DOI: 10.1007/978-1-4612-3918-5.
- [20] Subhash Chander and Anjan Ray. “Flame impingement heat transfer: A review”. In: *Energy Conversion and Management* 46.18-19 (2005), pp. 2803–2837. DOI: 10.1016/j.enconman.2005.01.011.
- [21] Yuming Chen, Frederik Arbeiter, and Georg Schlindwein. “A Comparative Study of Turbulence Models for Conjugate Heat Transfer to Gas Flow in a Heated Mini-Channel”. In: *Numerical Heat Transfer, Part A: Applications* 61.1 (2012), pp. 38–60. DOI: 10.1080/10407782.2012.638524. eprint: <https://doi.org/10.1080/10407782.2012.638524>. URL: <https://doi.org/10.1080/10407782.2012.638524>.
- [22] *Cooling Structure Optimization for a Rib-Roughed Channel in a Turbine Rotor Blade*. Vol. Volume 3B: Heat Transfer. Turbo Expo: Power for Land, Sea, and Air. V03BT11A009. June 2013. DOI: 10.1115/GT2013-94527. eprint: <https://asmedigitalcollection.asme.org/GT/proceedings-pdf/GT2013/55157/V03BT11A009/4225298/v03bt11a009-gt2013-94527.pdf>. URL: <https://doi.org/10.1115/GT2013-94527>.
- [23] Young Cho. “Handbook of Heat Transfer”. In: Jan. 1997.
- [24] G. S. Corman et al. “Rig and Engine Testing of Melt Infiltrated Ceramic Composites for Combustor and Shroud Applications”. In: *Journal of Engineering for Gas Turbines and Power* 124.3 (2002), pp. 459–464. DOI: 10.1115/1.1455637.
- [25] Riccardo Da Soghe et al. “Thermo Fluid Dynamic Analysis of a Gas Turbine Transition-Piece”. In: June 2014. DOI: 10.1115/GT2014-25386.
- [26] P. A. Dellenback, D. E. Metzger, and G. P. Neitzel. “Heat Transfer to Turbulent Swirling Flow Through a Sudden Axisymmetric Expansion”. In: *Journal of Heat Transfer* 109.3 (1987), pp. 613–620. DOI: 10.1115/1.3248132.
- [27] Tarek Echekki and Epaminondas Mastorakos. *Turbulent combustion modeling: Advances, new trends and perspectives*. Vol. 95. Jan. 2011. ISBN: 978-94-007-0411-4. DOI: 10.1007/978-94-007-0412-1.
- [28] E.R.G. Eckert, R.M.J. Drake, and R.M. Drake. *Heat and Mass Transfer*. International student edition. McGraw-Hill, 1959.
- [29] Vishnuvardhanarao Elaprolu and Manab Das. “Conjugate heat transfer study of incompressible turbulent offset jet flows”. In: *Heat and Mass Transfer* 45 (July 2009). DOI: 10.1007/s00231-009-0486-9.
- [30] F. A. Ficken. *Simplex method of linear programming*. Dover Publications Inc., 2015.

-
- [31] Chen Fu, Mesbah Uddin, and Alex Curley. “Insights derived from CFD studies on the evolution of planar wall jets”. In: *Engineering Applications of Computational Fluid Mechanics* 10.1 (2016), pp. 44–56. DOI: 10.1080/19942060.2015.1082505.
- [32] Hideo Futami, Ryoichi Hashimoto, and Hiroshi Uchida. “The development of new catalyst and heat transfer design method for steam reformer. (I).” In: *Journal of the Fuel Society of Japan* 68.3 (1989), pp. 236–243. DOI: 10.3775/jie.68.236.
- [33] VDI Gesellschaft. *VDI-Wärmeatlas* -. Wiesbaden: Springer Berlin Heidelberg, 2005. ISBN: 978-3-540-25503-1.
- [34] D.E. Goldberg. “Genetic algorithms in search, optimization, and machine learning”. In: *Choice Reviews Online* 27.02 (1989). DOI: 10.5860/choice.27-0936.
- [35] Graham Goldin et al. “HEEDS Optimized HyChem Mechanisms”. In: *Volume 4B: Combustion, Fuels and Emissions* (2017). DOI: 10.1115/gt2017-64407.
- [36] P Gosselin, A De Champlain, and D Kretschmer. “Prediction of wall heat transfer for a gas turbine combustor”. In: *Proceedings of the Institution of Mechanical Engineers, Part A: Journal of Power and Energy* 213.3 (1999), pp. 169–180. DOI: 10.1243/0957650991537527.
- [37] J. Griswold. *Fuels, Combustion, and Furnaces*. Chemical engineering series. McGraw-Hill Book Company, Incorporated, 1946.
- [38] U. Gruschka et al. “ULN System for the New SGT5-8000H Gas Turbine: Design and High Pressure Rig Test Results”. In: Jan. 2008. DOI: 10.1115/GT2008-51208.
- [39] Mohammad R. Hajmohammadi and S. S. Nourazar. “Conjugate Forced Convection Heat Transfer From a Heated Flat Plate of Finite Thickness and Temperature- Dependent Thermal Conductivity”. In: *Heat Transfer Engineering* 35.9 (2014), pp. 863–874. DOI: 10.1080/01457632.2014.852896.
- [40] Je-Chin Han, Sandip Dutta, and Srinath Ekkad. *Gas turbine heat transfer and cooling technology*. Taylor Francis, 2013.
- [41] Je-Chin Han, J. Joy Huang, and Ching-Pang Lee. “Augmented Heat Transfer in Square Channels with Wedge-Shaped and Delta-Shaped Turbulence Promoters”. In: *Journal of Enhanced Heat Transfer* 1.1 (1993), pp. 37–52. DOI: 10.1615/jenhheattransf.v1.i1.40.
- [42] M. N. A. Hawlader, S. K. Chou, and K. J. Chua. “Development of design charts for tunnel dryers”. In: *International Journal of Energy Research* 21.11 (1997), pp. 1023–1037. DOI: 10.1002/(sici)1099-114x(199709)21:11<1023::aid-er309>3.0.co;2-a.
- [43] G. He, Y. Guo, and A. Hsu. “The effect of Schmidt number on turbulent scalar mixing in a jet-in-crossflow”. In: *International Journal of Heat and Mass Transfer* 42 (1999), pp. 3727–3738.
- [44] *High Intensity Combustors - Steady Isobaric Combustion*. Wiley-VCH Verlag GmbH Co. KGaA, 2002. ISBN: 9783527277315,9783527601998. URL: <http://gen.lib.rus.ec/book/index.php?md5=6ba76199f62ca5e2413baecff2e26103>.
- [45] J. Hoch and L. M. Jiji. “Two-Dimensional Turbulent Offset Jet-Boundary Interaction”. In: *Journal of Fluids Engineering* 103.1 (1981), pp. 154–161. DOI: 10.1115/1.3240766.
- [46] M. Hoffmeister. “Townsend, A. A., The Structure of Turbulent Shear Flow, Second Edition, Cambridge. Cambridge University Press. 1976. 429 S., £ 15.50 A. Cambridge Monographs on Mechanics and Appl. Mathematics”. In: *ZAMM - Journal of Applied Mathematics and Mechanics / Zeitschrift für Angewandte Mathematik und Mechanik* 56.9 (1976), pp. 448–448. DOI: <https://doi.org/10.1002/zamm.19760560921>. eprint: <https://onlinelibrary.wiley.com/doi/pdf/10.1002/zamm.19760560921>. URL: <https://onlinelibrary.wiley.com/doi/abs/10.1002/zamm.19760560921>.
- [47] J.T. Holland and J.A. Liburdy. “Measurements of the thermal characteristics of heated offset jets”. In: *International Journal of Heat and Mass Transfer* 33.1 (1990), pp. 69–78. ISSN: 0017-9310. DOI: [https://doi.org/10.1016/0017-9310\(90\)90142-H](https://doi.org/10.1016/0017-9310(90)90142-H).

-
- [48] Matjaz Hriberšek et al. “Numerical computation of turbulent conjugate heat transfer in air heater”. In: vol. 51. Jan. 2005, pp. 470–475. DOI: 10.1615/ICHMT.2004.IntThermSciSemin.980.
- [49] J. E. Hustad and O. K. Sonju. “Heat Transfer to Pipes Submerged in Turbulent Jet Diffusion Flames”. In: *Heat Transfer in Radiating and Combusting Systems* (1991), pp. 474–490. DOI: 10.1007/978-3-642-84637-3_30.
- [50] L. Ingber. “Simulated annealing: Practice versus theory”. In: *Mathematical and Computer Modelling* 18.11 (1993), pp. 29–57. DOI: 10.1016/0895-7177(93)90204-c.
- [51] Elizaveta M Ivanova, Berthold E Noll, and Manfred Aigner. “A numerical study on the turbulent Schmidt numbers in a jet in crossflow”. In: *Journal of Engineering for Gas Turbines and Power* 135.1 (2013).
- [52] Muhammad Javed, Naseem Irfan, and Muhammad Ibrahim. “Combustion Kinetic Modeling”. In: July 2010. ISBN: 9783527628148. DOI: 10.1002/9783527628148.hoc007.
- [53] Chandra Laksham Vaidyaratna Jayatilleke. “The influence of Prandtl number and surface roughness on the resistance of the laminar sub-layer to momentum and heat transfer”. In: 1966.
- [54] Bibin John, P. Senthilkumar, and Sreeja Sadasivan. “Applied and Theoretical Aspects of Conjugate Heat Transfer Analysis: A Review”. In: *Archives of Computational Methods in Engineering* 26.2 (2018), pp. 475–489. DOI: 10.1007/s11831-018-9252-9.
- [55] W. P. Jones and B. Launder. “The prediction of laminarization with a two-equation model of turbulence”. In: *International Journal of Heat and Mass Transfer* 15 (1972), pp. 301–314.
- [56] Shariatzadeh Joneydi. “Analytical solution of conjugate turbulent forced convection boundary layer flow over plates”. In: *Thermal Science* 20.5 (2016), pp. 1499–1507. DOI: 10.2298/tsci140115062j.
- [57] Charles E. Baukal Jr. “Heat Transfer in Industrial Combustion”. In: (2000). DOI: 10.1201/9781420039757.
- [58] B.A. Kader. “Temperature and concentration profiles in fully turbulent boundary layers”. In: *International Journal of Heat and Mass Transfer* 24.9 (1981), pp. 1541–1544. ISSN: 0017-9310. DOI: [https://doi.org/10.1016/0017-9310\(81\)90220-9](https://doi.org/10.1016/0017-9310(81)90220-9). URL: <https://www.sciencedirect.com/science/article/pii/0017931081902209>.
- [59] L. V. Kantorovich. “Mathematical Methods of Organizing and Planning Production - English Transcript”. In: *Management Science* 6.4 (1960), pp. 366–422. DOI: 10.1287/mnsc.6.4.366. eprint: <https://doi.org/10.1287/mnsc.6.4.366>. URL: <https://doi.org/10.1287/mnsc.6.4.366>.
- [60] J. S. Kapat, A. K. Agrawal, and T. Yang. “Air Extraction in a Gas Turbine for Integrated Gasification Combined Cycle (IGCC): Experiments and Analysis”. In: *Journal of Engineering for Gas Turbines and Power* 119.1 (1997), pp. 20–26. DOI: 10.1115/1.2815551.
- [61] J. S. Kapat et al. “Cold Flow Experiments in a Sub-Scale Model of the Diffuser-Combustor Section of an Industrial Gas Turbine”. In: *Volume 3: Coal, Biomass and Alternative Fuels; Combustion and Fuels; Oil and Gas Applications; Cycle Innovations* (1996). DOI: 10.1115/96-gt-518.
- [62] R. Karvinen. “Note on conjugated heat transfer in a flat plate”. In: *Letters in Heat and Mass Transfer* 5.3 (1978), pp. 197–202. ISSN: 0094-4548. DOI: [https://doi.org/10.1016/0094-4548\(78\)90005-X](https://doi.org/10.1016/0094-4548(78)90005-X). URL: <http://www.sciencedirect.com/science/article/pii/009445487890005X>.
- [63] Reijo Karvinen and Antti Lehtinen. “Analytical Solution For A Class Of Flat Plate Conjugate Convective Heat Transfer Problems”. In: *Frontiers in Heat and Mass Transfer* 2.4 (2011). DOI: 10.5098/hmt.v2.4.3004.
- [64] William Morrow Kays. *Convective heat and mass transfer*. Tata McGraw-Hill Education, 1993.
- [65] J.H. Keenan and J. Kaye. *Thermodynamic Properties of Air, Including Polytropic Functions*. Wiley, 1945.

-
- [66] J.C Ku and K.H. Shim. “The effects of refractive indices, size distribution, and agglomeration on the diagnostics and radiative properties of flame soot particles”. In: *Heat and Mass Transfer in Fires and Combustion Systems* 148.3 (1997), pp. 105–115.
- [67] L.D. Landau and E.M. Lifshits. *Fluid Mechanics, by L.D. Landau and E.M. Lifshitz*. Teoreticheskaya fizika. Pergamon Press, 1959.
- [68] S. C. Lau, R. D. Mcmillin, and J. C. Han. “Heat Transfer Characteristics of Turbulent Flow in a Square Channel With Angled Discrete Ribs”. In: *Volume 4: Heat Transfer; Electric Power; Industrial and Cogeneration* (1990). DOI: 10.1115/90-gt-254.
- [69] S. C. Lau, R. D. Mcmillin, and J. C. Han. “Turbulent Heat Transfer and Friction in a Square Channel With Discrete Rib Turbulators”. In: *Journal of Turbomachinery* 113.3 (1991), pp. 360–366. DOI: 10.1115/1.2927884.
- [70] B.E. Launder and B.I. Sharma. “Application of the energy-dissipation model of turbulence to the calculation of flow near a spinning disc”. In: *Letters in Heat and Mass Transfer* 1.2 (1974), pp. 131–137. ISSN: 0094-4548. DOI: [https://doi.org/10.1016/0094-4548\(74\)90150-7](https://doi.org/10.1016/0094-4548(74)90150-7). URL: <https://www.sciencedirect.com/science/article/pii/0094454874901507>.
- [71] A. H. Lefebvre and M. V. Herbert. “Heat-Transfer Processes in Gas-Turbine Combustion Chambers”. In: *Proceedings of the Institution of Mechanical Engineers* 174.1 (1960), pp. 463–478. DOI: 10.1243/pime_proc_1960_174_039_02.
- [72] Arthur H. Lefebvre. “Design Considerations In Advanced Gas Turbine Combustion Chambers”. In: *Combustion in Advanced Gas Turbine Systems* (1968), pp. 3–19. DOI: 10.1016/b978-0-08-013275-4.50007-6.
- [73] Arthur H. Lefebvre. “Flame radiation in gas turbine combustion chambers”. In: *International Journal of Heat and Mass Transfer* 27.9 (1984), pp. 1493–1510. DOI: 10.1016/0017-9310(84)90262-x.
- [74] Arthur H. Lefebvre and Dilip R. Ballal. “Gas Turbine Combustion”. In: (2010). DOI: 10.1201/9781420086058.
- [75] J. H. Lienhard IV and J. H. Lienhard V. *A Heat Transfer Textbook*. 5th. Mineola, NY: Dover Publications, Dec. 2019. 784 pp. ISBN: 9780486837352. URL: <http://ahtt.mit.edu>.
- [76] Timothy C. Lieuwen and Vigor Yang. *Combustion instabilities in gas turbine engines operational experience, fundamental mechanisms and modeling*. eng. Progress in astronautics and aeronautics ; v. 210. Reston, Va: American Institute of Aeronautics and Astronautics. ISBN: 1-60086-680-8.
- [77] Phil Ligrani. “Heat Transfer Augmentation Technologies for Internal Cooling of Turbine Components of Gas Turbine Engines”. In: *International Journal of Rotating Machinery* 2013 (2013), pp. 1–32. DOI: 10.1155/2013/275653.
- [78] Matti Lindstedt and Reijo Karvinen. “Conjugate heat transfer in a plate – One surface at constant temperature and the other cooled by forced or natural convection”. In: *International Journal of Heat and Mass Transfer* 66 (Nov. 2013), pp. 489–495. DOI: 10.1016/j.ijheatmasstransfer.2013.07.052.
- [79] Mordor Intelligence LLP. “Industrial Gas Turbine Market - Growth, Trends, and Forecast (2020-2025)”. In: May 2020.
- [80] Morten Løvbjerg. “Improving particle swarm optimization by hybridization of stochastic search heuristics and self-organized criticality”. PhD thesis. 2002.
- [81] A.V. Luikov. “Conjugate convective heat transfer problems”. In: *International Journal of Heat and Mass Transfer* 17.2 (1974), pp. 257–265. ISSN: 0017-9310. DOI: [https://doi.org/10.1016/0017-9310\(74\)90087-8](https://doi.org/10.1016/0017-9310(74)90087-8).
- [82] A.V. Luikov. “Heat and Mass Transfer in Capillary-Porous Bodies”. In: Oxford: Pergamon, 1966, pp. 305–340. ISBN: 978-1-4832-0065-1. DOI: <https://doi.org/10.1016/B978-1-4832-0065-1.50011-8>.

- [83] *Wall Temperature Effects on Heat Transfer Coefficient*. Vol. Volume 3C: Heat Transfer. Turbo Expo: Power for Land, Sea, and Air. V03CT14A003. June 2013. DOI: 10.1115/GT2013-94291. eprint: <https://asmedigitalcollection.asme.org/GT/proceedings-pdf/GT2013/55164/V03CT14A003/2420664/v03ct14a003-gt2013-94291.pdf>. URL: <https://doi.org/10.1115/GT2013-94291>.
- [84] S. V. Mahmoodi-Jezeh and Bing-Chen Wang. “Direct numerical simulation of turbulent flow through a ribbed square duct”. In: *Journal of Fluid Mechanics* 900 (2020), A18. DOI: 10.1017/jfm.2020.452.
- [85] A.F. Mills. *Heat Transfer*. Irwin, 1992, pp. 402–404. ISBN: 9780256076424.
- [86] Narendernath Miriyala, Anthony Fahme, and Mark Van Roode. “Ceramic Stationary Gas Turbine Program: Combustor Liner Development Summary”. In: *Volume 4: Manufacturing Materials and Metallurgy; Ceramics; Structures and Dynamics; Controls, Diagnostics and Instrumentation; Education; IGTI Scholar Award* (2001). DOI: 10.1115/2001-gt-0512.
- [87] M. Mosaad. “Laminar forced convection conjugate heat transfer over a flat plate”. In: *Heat and Mass Transfer* 35.5 (1999), pp. 371–375. DOI: 10.1007/s002310050338.
- [88] J. A. Nelder and R. Mead. “A Simplex Method for Function Minimization”. In: *The Computer Journal* 7.4 (1965), pp. 308–313. DOI: 10.1093/comjnl/7.4.308.
- [89] W. A. Nelson and R. M. Orenstein. “TBC experience in land-based gas turbines”. In: *Journal of Thermal Spray Technology* 6.2 (1997), pp. 176–180. DOI: 10.1007/s11666-997-0009-5.
- [90] P. Y. Nizou. “Heat and Momentum Transfer in a Plane Turbulent Wall Jet”. In: *Journal of Heat Transfer* 103.1 (1981), pp. 138–140. DOI: 10.1115/1.3244407.
- [91] Gordon C. Oates. *The Aerothermodynamics of aircraft gas turbine engines*. National Technical Information Service, 1978.
- [92] Mohamed Hatim Ouahabi, Mohamed Ichenial, and F. Benabdelouahab. “Evaluation of the turbulence models at low Reynolds number for wind turbine blade design”. In: Aug. 2017.
- [93] Jun Su Park et al. “Thermal Analysis of Cooling System in a Gas Turbine Transition Piece”. In: vol. 5. Jan. 2011. DOI: 10.1115/GT2011-45961.
- [94] Sunil Patil et al. “Study of Flow and Convective Heat Transfer in a Simulated Scaled Up Low Emission Annular Combustor”. In: *Journal of Thermal Science and Engineering Applications* 3.3 (2011). DOI: 10.1115/1.4004531.
- [95] J. R. R. Pelfrey and J. A. Liburdy. “Mean Flow Characteristics of a Turbulent Offset Jet”. In: *Journal of Fluids Engineering* 108.1 (Mar. 1986), pp. 82–88. ISSN: 0098-2202. DOI: 10.1115/1.3242548.
- [96] T.L. Perelman. “On conjugated problems of heat transfer”. In: *International Journal of Heat and Mass Transfer* 3.4 (1961), pp. 293–303. ISSN: 0017-9310. DOI: [https://doi.org/10.1016/0017-9310\(61\)90044-8](https://doi.org/10.1016/0017-9310(61)90044-8).
- [97] Siemens PLM.
- [98] Jeffrey Price. “Advanced Materials for Mercury 50 Gas Turbine Combustion System”. In: (2008). DOI: 10.2172/991117.
- [99] A. Racca, T. Verstraete, and L. Casalino. “Radial Turbine Thermo-Mechanical Stress Optimization by Multidisciplinary Discrete Adjoint Method”. In: *International Journal of Turbomachinery, Propulsion and Power* 5 (2020). DOI: <https://doi.org/10.1016/j.ijheatmasstransfer.2016.05.041>.
- [100] D. Radaj and M. Vormwald. *Ermüdungsfestigkeit: Grundlagen für Ingenieure*. Springer Berlin Heidelberg, 2007. ISBN: 9783540714590. URL: <https://books.google.bg/books?id=MAgeBAAAQBAJ>.
- [101] Bürgel Ralf, Maier Hans Jürgen, and Thomas Niendorf. *Handbuch Hochtemperatur-Werkstofftechnik Grundlagen, Werkstoffbeanspruchungen, Hochtemperaturlegierungen und -beschichtungen ; mit 66 Tabellen*. Vieweg Teubner, 2011.

-
- [102] D. Ramirez. “Heat Transfer and Flow Measurements in an Atmospheric Lean Pre-Mixed Combustor”. In: 2016.
- [103] Takeo Saitou, Yasuyuki Watanabe, and Shouhei Yoshida. *Gas turbine combustor including a transition piece flow sleeve wrapped on an outside surface of a transition piece*. May 2012.
- [104] Tareq Salameh and Bengt Sunden. “Comparison of Continuous and Truncated Ribs on Internal Blade Tip Cooling”. In: *Volume 4: Heat Transfer, Parts A and B* (2012). DOI: 10.1115/gt2012-68028.
- [105] K. Schittkowski. “NLPQL: A fortran subroutine solving constrained nonlinear programming problems”. In: *Annals of Operations Research* 5.1-4 (1986), pp. 485–500. DOI: 10.1007/bf02739235.
- [106] H. Schlichting (Deceased) and K. Gersten. “Boundary–Layer Equations in Plane Flow; Plate Boundary Layer”. In: *Boundary-Layer Theory*. Berlin, Heidelberg: Springer Berlin Heidelberg, 2017, pp. 145–164. ISBN: 978-3-662-52919-5. DOI: 10.1007/978-3-662-52919-5_6.
- [107] A. Schumacher. *Optimierung mechanischer Strukturen: Grundlagen und industrielle Anwendungen*. SpringerLink: Springer e-Books. Springer, 2005. ISBN: 9783540218876. URL: https://books.google.bg/books?id=PaE%5C_21AYJj4C.
- [108] N. Selcuk, R. G. Siddall, and J. M. Beer. “Prediction of the effect of flame length on temperature and radiative heat flux distributions in a process fluid heater”. In: *J. Inst. Fuel; (United Kingdom)* 48 (June 1975).
- [109] *SGT6-8000H: H-class Gas Turbine: Gas Turbines: Manufacturer: Siemens Energy Global*. URL: <https://www.siemens-energy.com/global/en/offerings/power-generation/gas-turbines/sgt6-8000h.html>.
- [110] Robert Siegel et al. *Thermal Radiation Heat Transfer*. CRC Press, Dec. 2020. DOI: 10.1201/9780429327308.
- [111] Sin Chien Siw, Mary Anne Alvin, and Minking Chyu. “Heat Transfer Enhancement of Internal Cooling Passage With Triangular and Semi-Circular Shaped Pin-Fin Arrays”. In: *ASME Turbo Expo 2012: Turbine Technical Conference and Exposition* (2012), pp. 493–503. DOI: GT2012-69266.
- [112] Jacob Snyder et al. “Build Direction Effects on Additively Manufactured Channels”. In: *Journal of Turbomachinery* 138 (Dec. 2015). DOI: 10.1115/1.4032168.
- [113] Manohar S. Sohal and John R. Howel. “Determination of plate temperature in case of combined conduction, convection and radiation heat exchange”. In: *International Journal of Heat and Mass Transfer* 16.11 (1973), pp. 2055–2066. ISSN: 0017-9310. DOI: [https://doi.org/10.1016/0017-9310\(73\)90108-7](https://doi.org/10.1016/0017-9310(73)90108-7). URL: <http://www.sciencedirect.com/science/article/pii/S0017931073901087>.
- [114] M. Soliman and H. A. Johnson. “Transient Heat Transfer for Turbulent Flow Over a Flat Plate of Appreciable Thermal Capacity and Containing Time-Dependent Heat Source”. In: *Journal of Heat Transfer* 89.4 (1967), pp. 362–370. DOI: 10.1115/1.3614398.
- [115] R.I. Stephens et al. *Metal Fatigue in Engineering*. A Wiley-Interscience publication. Wiley, 2000. ISBN: 9780471510598. URL: <https://books.google.bg/books?id=B2aAPVa1Tl0C>.
- [116] Red Cedar Technology. 2015.
- [117] Tom Verstraete and Sebastian Scholl. “Stability analysis of partitioned methods for predicting conjugate heat transfer”. In: *International Journal of Heat and Mass Transfer* 101 (2016), pp. 852–869. ISSN: 0017-9310. DOI: <https://doi.org/10.1016/j.ijheatmasstransfer.2016.05.041>.
- [118] E. Vishnuvardhanarao and Manab Kumar Das. “Computation of Mean Flow and Thermal Characteristics of Incompressible Turbulent Offset Jet Flows”. In: *Numerical Heat Transfer, Part A: Applications* 53.8 (2007), pp. 843–869. DOI: 10.1080/10407780701715760. eprint: <https://doi.org/10.1080/10407780701715760>.
- [119] E. Vishnuvardhanarao and Manab Kumar Das. “Study of Conjugate Heat Transfer from a Flat Plate by Turbulent Offset Jet Flow”. In: *Numerical Heat Transfer, Part A: Applications* 53.5 (2007), pp. 524–542. DOI: 10.1080/10407780701678331.

-
- [120] R Viskanta and M.P. Menguc. “Radiation heat transfer in combustion systems”. In: *Progress in Energy and Combustion Science* 13.2 (1987), pp. 97–160. DOI: 10.1016/0360-1285(87)90008-6.
- [121] M. Vynnycky et al. “Forced convection heat transfer from a flat plate: the conjugate problem”. In: *International Journal of Heat and Mass Transfer* 41.1 (1998), pp. 45–59. ISSN: 0017-9310. DOI: [https://doi.org/10.1016/S0017-9310\(97\)00113-0](https://doi.org/10.1016/S0017-9310(97)00113-0). URL: <http://www.sciencedirect.com/science/article/pii/S0017931097001130>.
- [122] Liang Wang and Ting Wang. “Investigation of the Effect of Perforated Sheath on Thermal-Flow Characteristics Over a Gas Turbine Reverse-Flow Combustor: Part 1 — Experiment”. In: *Volume 3C: Heat Transfer* (2013). DOI: 10.1115/gt2013-94474.
- [123] Liang Wang and Ting Wang. “Investigation of the Effect of Perforated Sheath on Thermal-Flow Characteristics Over a Gas Turbine Reverse-Flow Combustor: Part 2 — Computational Analysis”. In: *Volume 3C: Heat Transfer* (2013). DOI: 10.1115/gt2013-94475.
- [124] T. Wang et al. “Effect of Air Extraction for Cooling and/or Gasification on Combustor Flow Uniformity”. In: *Volume 3: Coal, Biomass and Alternative Fuels; Combustion and Fuels; Oil and Gas Applications; Cycle Innovations* (1998). DOI: 10.1115/98-gt-102.
- [125] Yu Wen-Shing, Lin Hsiao-Tsung, and Hwang Tsung-Yuan. “Conjugate heat transfer of conduction and forced convection along wedges and a rotating cone”. In: *International Journal of Heat and Mass Transfer* 34.10 (1991), pp. 2497–2507. ISSN: 0017-9310. DOI: [https://doi.org/10.1016/0017-9310\(91\)90091-R](https://doi.org/10.1016/0017-9310(91)90091-R). URL: <http://www.sciencedirect.com/science/article/pii/001793109190091R>.
- [126] Victor Yakhot, Steven A. Orszag, and Alexander Yakhot. “Heat transfer in turbulent fluids - I. Pipe flow”. In: *International Journal of Heat and Mass Transfer* 30.1 (1987), pp. 15–22. ISSN: 0017-9310. DOI: [https://doi.org/10.1016/0017-9310\(87\)90057-3](https://doi.org/10.1016/0017-9310(87)90057-3).
- [127] Mehmet Yilmaz et al. “Heat transfer and friction characteristics in decaying swirl flow generated by different radial guide vane swirl generators”. In: *Energy Conversion and Management* 44.2 (2003), pp. 283–300. DOI: 10.1016/s0196-8904(02)00053-5.
- [128] F. Yin and A. Gangoli Rao. “Performance analysis of an aero engine with inter-stage turbine burner”. In: *The Aeronautical Journal* 121.1245 (2017), pp. 1605–1626. DOI: 10.1017/aer.2017.93.
- [129] Wen-Shing Yu and Hsiao-Tsung Lin. “Conjugate problems of conduction and free convection on vertical and horizontal flat plates”. In: *International Journal of Heat and Mass Transfer* 36.5 (1993), pp. 1303–1313. ISSN: 0017-9310. DOI: [https://doi.org/10.1016/S0017-9310\(05\)80099-7](https://doi.org/10.1016/S0017-9310(05)80099-7). URL: <http://www.sciencedirect.com/science/article/pii/S0017931005800997>.
- [130] Parviz Mohammad Zadeh and Mohadeseh Alsadat Sadat Shirazi. “5 - Multidisciplinary Design and Optimization Methods”. In: *Metaheuristic Applications in Structures and Infrastructures*. Ed. by Amir Hossein Gandomi et al. Oxford: Elsevier, 2013, pp. 103–127. ISBN: 978-0-12-398364-0. DOI: <https://doi.org/10.1016/B978-0-12-398364-0.00005-X>. URL: <http://www.sciencedirect.com/science/article/pii/B978012398364000005X>.
- [131] Yan Zhao et al. “Numerical and Experimental Study of Geometry Effects on Fuel/Air Mixing and Combustion Characteristics of a DLN Burner”. In: Oct. 2020. DOI: 10.1115/POWER2020-16371.
- [132] Dadong Zhou, Ting Wang, and William R. Ryan. “Cold Flow Computations for the Diffuser-Combustor Section of an Industrial Gas Turbine”. In: *Volume 3: Coal, Biomass and Alternative Fuels; Combustion and Fuels; Oil and Gas Applications; Cycle Innovations* (1996). DOI: 10.1115/96-gt-513.